

UNIVERSIDADE FEDERAL DE SANTA CATARINA CENTRO TECNOLÓGICO PROGRAMA DE PÓS-GRADUAÇÃO EM ENGENHARIA MECÂNICA

Vinícius Vigolo

ENHANCING ENERGY EFFICIENCY AND ROBUSTNESS IN PNEUMATIC ACTUATION SYSTEMS: A DESIGN AND SETUP FRAMEWORK

Vinícius Vigolo

ENHANCING ENERGY EFFICIENCY AND ROBUSTNESS IN PNEUMATIC ACTUATION SYSTEMS: A DESIGN AND SETUP FRAMEWORK

Tese submetida ao Programa de Pós-Graduação em Engenharia Mecânica da Universidade Federal de Santa Catarina como requisito parcial para a obtenção do título de Doutor em Engenharia Mecânica.

Orientador: Prof. Victor Juliano De Negri, Dr. Eng. Coorientador: Prof. Antonio Carlos Valdiero, Dr. Eng. Coorientador: Univ.-Prof. Jürgen Weber, Dr.-Ing.

Ficha catalográfica gerada por meio de sistema automatizado gerenciado pela BU/UFSC. Dados inseridos pelo próprio autor.

Vigolo, Vinícius

Enhancing Energy Efficiency and Robustness in Pneumatic Actuation Systems: A Design and Setup Framework / Vinícius Vigolo; orientador, Victor Juliano De Negri, coorientador, Antonio Carlos Valdiero, coorientador, Jürgen Weber, 2025.

257 p.

_

Tese (doutorado) - Universidade Federal de Santa Catarina, Centro Tecnológico, Programa de Pós-Graduação em Engenharia Mecânica, Florianópolis, 2025.

Inclui referências.

1. Engenharia Mecânica. 2. Pneumatic systems. 3. Robustness. 4. Operating point. 5. Design framework. I. De Negri, Victor Juliano. II. Valdiero, Antonio Carlos. III. Weber, Jürgen IV. Universidade Federal de Santa Catarina. Programa de Pós-Graduação em Engenharia Mecânica. V. Título.

Vinícius Vigolo

Enhancing Energy Efficiency and Robustness in Pneumatic Actuation Systems: A Design and Setup Framework

O presente trabalho em nível de Doutorado foi avaliado e aprovado, em 08 de julho de 2025, pela banca examinadora composta pelos seguintes membros:

Prof. Eduardo André Perondi, Dr. Eng. - Relator Universidade Federal do Rio Grande do Sul

Prof. Amir Antônio Martins de Oliveira Junior, Dr. Eng. Universidade Federal de Santa Catarina

Univ.-Prof. Katharina Schmitz, Dr.-Ing.
RWTH Aachen University

Certificamos que esta é a versão original e final do trabalho de conclusão que foi julgado adequado para obtenção do título de Doutor em Engenharia Mecânica.

Prof. Henrique Simas, Dr. Eng.

Coordenação do Programa de Pós-Graduação em Engenharia Mecânica - POSMEC

Prof. Victor Juliano De Negri, Dr. Eng.
Orientador

"Do not go where the path may lead, go instead where there is no path and leave a trail." – Ralph Waldo Emerson

ACHNOWLEDGEMENTS

Among the infinite paths of life, two people guided me to choose the right one. For this, I will be eternally grateful to them, the ones I am proud to call FATHER and MOTHER.

In a very special way, I would like to thank God for giving me life and the strength to overcome the challenges I have faced along the way.

To my dear friend, partner, and wife, Simone, who has been by my side from the very beginning, encouraging me to embrace life's challenges, teaching me to become a better person, sharing ideas and dreams, and choosing to walk this path with me, pursuing knowledge, adventure, and growth. For every single moment we have spent together, thank you!

I am grateful to my family for their support, standing by my side through both challenging and joyful moments of daily life. For their trust, allowing me to pursue my dreams and follow what I believe is best for me. To all of you, muito obrigado!

I would like to thank my advisor, Professor Victor Juliano De Negri, for these invaluable years of learning, for his outstanding support in achieving the optimal operating point, for encouraging me to take on challenges, and, above all, for his friendship. Thank you.

Likewise, I would like to thank my co-advisor, Professor Antonio Carlos Valdiero, for his support, willingness to help, friendship, and for sharing knowledge that was essential for both my personal growth and the development of this thesis.

I am grateful to Professor Jürgen Weber for welcoming me as an exchange PhD student at TU Dresden and giving me the opportunity to work with the Fluidtronik pneumatics team. Many thanks to my German colleagues, Fedor, Tania, Vladimir, Thomas, Anabel, Lukas, and Benjamin, for their warm reception and friendship during my stay in Germany. Vielen Dank!

Many thanks to all my Lashipian friends, Marcos, Dimitri, Vanderlei, Keliene, Gregori, Thales, Túlio, Giuliano, Carlos, Ismael, Otávio, Yasmin, Lucas, Letícia, Job, Tales, Arthur, Ruham, Felipe, João Pedro, Ivan, Gabriel, Nelson, Rodrigo, Alexandre, Henrique, Tiago, Guilherme, Henri, Heitor, Nicodemos, Andrei, and many others. You all made a difference throughout these years, making this journey infinitely better.

Among my many Lashipian friends, special thanks to "Marquinho", Gregori, Thales, Dimitri, Vanderlei, and Kelly. You stood by my side day after day, offering friendship, support, and reasons to laugh, even when things seemed to fall apart. Thank you for always being there.

I would like to thank the UNIEDU/FUMDES Pós-Graduação Program and the Coordenação de Aperfeiçoamento de Pessoal de Nível Superior (CAPES) for the financial support provided during my doctoral studies.

ABSTRACT

Due to the growing demand for sustainable technologies and the global increase in energy consumption, energy efficiency has become a pillar of sustainable economic development. Pneumatic systems, widely used in industry due to their low cost, high power density, versatility, and robustness, face the challenge of low energy efficiency. While existing strategies aim to improve this aspect, they often involve additional components, complex control, high costs, and reduced reliability, limiting their practical application. In this context, proper sizing of pneumatic actuation systems becomes an efficient solution to enhance their energy performance. Therefore, this thesis proposes a design and setup framework for pneumatic actuation systems that balances energy efficiency and robustness, achieving an optimal operating condition. The framework comprises a set of concepts and definitions that support the optimization of sizing of pneumatic actuators and valves, provide guidelines for selecting the most effective throttling method, and integrate a real-time monitoring system for optimization of pneumatic systems during operation. The developed tools aim to eliminate uncertainties in pneumatic system design, such as determining chamber pressures in actuators, friction forces, system dynamic behavior under variable loads, and effective load force determination. To address these uncertainties, the governing equations of the system under steady-state assumptions were used to identify an optimal operating condition where energy efficiency and robustness are balanced. The analysis of the characteristic displacement times of pneumatic actuators, combined with statistical analysis of experimental data and dynamic simulations, enabled the development of analytical equations for system sizing. A hybrid machine learning (HML) model was developed to optimize pneumatic systems during operation by adjusting supply pressure and the throttle valves openings, ensuring that design requirements are met and optimizing air consumption based on the actual applied loads. The framework was extensively evaluated through dynamic simulations and experimental tests, demonstrating its ability to meet design requirements, ensure robust operation, and avoid excessive compressed air consumption. The HML system proved effective in optimizing operational conditions, enhancing robustness for undersized actuators, and reducing air consumption by approximately 50% in oversized actuators. In conclusion, the developed framework addresses the knowledge gap in pneumatic system design, offering a systematic alternative to traditional sizing methods.

Keywords: Energy Efficiency, Pneumatic systems, Robustness, Machine Learning, Design framework, Operating point.

RESUMO

Devido à crescente demanda por tecnologias renováveis e ao aumento do consumo energético global, a eficiência energética tornou-se um pilar essencial para o desenvolvimento econômico sustentável. Os sistemas pneumáticos, amplamente utilizados na indústria por seu baixo custo, alta densidade de potência, versatilidade e robustez, enfrentam o desafio da baixa eficiência energética. Embora existam estratégias para melhorar esse aspecto, elas frequentemente envolvem componentes adicionais, controle complexo, custos elevados e redução da confiabilidade, limitando sua adoção prática. Nesse contexto, o dimensionamento adequado do sistema de atuação pneumático surge como uma solução eficiente para aprimorar seu desempenho energético. Diante disso, esta tese propõe uma estrutura de projeto e comissionamento para sistemas de atuação pneumáticos que equilibra eficiência energética e robustez, alcançando uma condição ótima de operação. A estrutura consiste em um conjunto de conceitos e definições que embasam a otimização do dimensionamento de atuadores e válvulas pneumáticas, fornecem diretrizes para a seleção da alternativa mais eficaz de regulagem de vazão de ar comprimido e integram um sistema de monitoramento para otimização em tempo real durante a operação do equipamento. As ferramentas desenvolvidas visam eliminar incertezas no projeto de sistemas pneumáticos, como a determinação das pressões atuantes nas câmaras do atuador, as forças de atrito, o comportamento dinâmico do sistema sob cargas variáveis e a determinação eficaz das forças de carga. Para isso, foram utilizadas as equações que governam o comportamento do sistema, sob a hipótese de regime permanente, permitindo identificar uma condição ótima de operação, onde eficiência energética e robustez são equilibradas. A análise dos tempos característicos de deslocamento de atuadores pneumáticos, junto com a análise estatística de dados experimentais e simulações dinâmicas, possibilitou o desenvolvimento de equações analíticas para o dimensionamento desses sistemas. Um sistema de monitoramento, baseado em um modelo híbrido de aprendizado de máquina (HML), foi desenvolvido para otimizar sistemas pneumáticos durante a operação, ajustando a pressão de suprimento e a abertura das válvulas reguladoras de vazão, de forma que os requisitos de projeto sejam atendidos e o consumo de ar seja otimizado conforme a carga aplicada. A estrutura de projeto e comissionamento foi extensivamente avaliada em simulações dinâmicas e ensaios experimentais, demonstrando a capacidade do método de dimensionamento em atender aos requisitos de projeto, garantir operação robusta e evitar o consumo excessivo de ar comprimido. O sistema HML se mostrou eficaz na otimização das condições operacionais, aumentando a robustez de atuadores subdimensionados e reduzindo o consumo de ar em cerca de 50% em atuadores superdimensionados. Conclui-se que a estrutura desenvolvida preenche a lacuna de conhecimento na área de projeto de sistemas pneumáticos, oferecendo uma alternativa sistemática aos métodos tradicionalmente utilizados.

Palavras-chave: Eficiência energética, Sistemas pneumáticos, Robustez, Aprendizado de máquina, Estrutura de Projeto, Ponto de operação.

RESUMO EXPANDIDO

Introdução

A crescente demanda da sociedade pelo desenvolvimento de tecnologias sustentáveis e menos agressivas ao meio ambiente, bem como a expansão de fontes de energia renováveis, estão entre as principais estratégias para a redução dos gases de efeito estufa e o combate às mudanças climáticas. Entretanto, o consumo global de energia vem crescendo ano após ano, passando de 8.588,9 milhões de toneladas de óleo equivalente em 1995 para 13.147,3 milhões em 2015 (Dong; Dong; Jiang, 2020). Ao mesmo tempo, a pegada ecológica, que mede o impacto ambiental das ações humanas, está intrinsecamente relacionada ao consumo de energia (Destek; Sinha, 2020). Nesse cenário, Ahmad and Zhang (2020) destacam que o desempenho energético dos processos produtivos é um dos pilares para que o tão sonhado desenvolvimento sustentável possa ser alcançado.

O setor industrial, responsável por cerca de 37% do consumo energético mundial (IEA, 2022), utiliza frequentemente três tecnologias principais para automação de processos produtivos: eletromecânica, hidráulica e pneumática. Apesar de possuírem baixa eficiência energética, os sistemas pneumáticos apresentam características que os tornam difíceis de substituir, como agilidade, versatilidade, confiabilidade, robustez, elevada densidade de potência e baixo custo de aquisição e manutenção. Esses fatores fazem da tecnologia pneumática uma solução eficaz para setores com alto grau de automação.

Diante disso, a comunidade científica tem realizado esforços significativos para melhorar a eficiência energética de sistemas pneumáticos. Estratégias focadas na redução do consumo de ar comprimido, prevenção de perdas e reutilização do ar comprimido resultam em melhorias significativas nesses sistemas, com ganhos de 20% a 50% em comparação às soluções convencionais (Saidur; Rahim; Hasanuzzaman, 2010).

No entanto, Merkelbach and Murrenhoff (2015) argumentam que a aplicação de soluções de eficiência energética é incomum em ambientes industriais, um cenário que ainda é frequentemente observado nos dias atuais. Esse aspecto pode ser explicado pelo alto grau de complexidade associado a essas soluções, o que aumenta a probabilidade de paradas das máquinas e reduz a atratividade dos benefícios potenciais ligados à economia de energia.

Portanto, fica evidente que o sucesso na aplicação de soluções otimizadas não depende exclusivamente dos ganhos de eficiência energética, mas sim de uma combinação entre

possíveis reduções no consumo de energia e a garantia de equipamentos robustos, confiáveis e adaptáveis às diversas variáveis que podem surgir no ambiente operacional.

Diante desse cenário, acredita-se que o dimensionamento adequado do conjunto válvula-cilindro desempenha um papel crucial na otimização da eficiência energética e da robustez dos sistemas pneumáticos. Entretanto, os componentes pneumáticos são geralmente dimensionados com base apenas na experiência do projetista e em métodos empíricos, o que frequentemente resulta em sistemas superdimensionados (Boyko *et al.*, 2024).

Diante dos desafios apresentados, esta tese propõe equilibrar aspectos de eficiência energética e robustez em sistemas de atuação pneumáticos. Por meio de equações derivadas das leis físicas que governam o comportamento do sistema, define-se uma condição operacional de referência ótima. Um método inovador de dimensionamento e um sistema de monitoramento são propostos para projetar e comissionar sistemas de atuação pneumáticos de acordo com essa condição de referência, assegurando robustez e eficiência energética mesmo sob condições operacionais incertas.

Objetivos

O objetivo principal desta tese é desenvolver uma estrutura de projeto e comissionamento, que integre um método de dimensionamento para cilindros e válvulas, diretrizes de configuração e um sistema de monitoramento visando aprimorar a operação de sistemas de atuação pneumáticos. Essa estrutura busca garantir operações robustas e eficientes, superando as incertezas inerentes às condições operacionais, ao mesmo tempo que otimiza o consumo energético e a confiabilidade do sistema.

Para atingir o objetivo principal, os seguintes objetivos específicos são estabelecidos:

- Desenvolver um método de dimensionamento para selecionar atuadores pneumáticos, válvulas reguladoras de vazão e válvulas direcionais capazes de equilibrar o consumo de ar e a robustez do sistema;
- Analisar os efeitos de aplicações com componentes de carga distintos, como altas cargas inerciais, molas e amortecedores, e seu impacto no dimensionamento dos atuadores;
- Determinar a correlações entre as forças de atrito do cilindro e fatores como diâmetro do cilindro, velocidade do pistão e pressões das câmaras;

- Propor diretrizes para a configuração adequada dos modos de regulagem de vazão de ar comprimido pelas válvulas do sistema com base nas características da aplicação;
- Desenvolver uma estratégia de otimização online para auxiliar na configuração de sistemas de atuação pneumáticos, incluindo a otimização da pressão de suprimento e o ajuste das válvulas reguladoras de vazão;
- Validar a eficácia da estrutura de projeto e comissionamento por meio de experimentos em bancadas de teste;
- Comparar as soluções propostas com abordagens existentes na literatura e no mercado.

Metodologia

Inicialmente, foi conduzida uma revisão bibliográfica para avaliar as principais estratégias desenvolvidas para o dimensionamento de atuadores pneumáticos. Observou-se que os avanços nessa área estão predominantemente focados em estratégias de otimização numérica, as quais visam minimizar o consumo de ar comprimido e atender aos requisitos de projeto da aplicação. No entanto, tais abordagens exigem conhecimentos teóricos especializados e ferramentas computacionais avançadas, recursos que geralmente não estão acessíveis a engenheiros de aplicações industriais. Além disso, aspectos relacionados à robustez não são considerados nessas abordagens, o que pode resultar no projeto de atuadores operando no limite de sua capacidade de força e comprometer sua funcionalidade em cenários com variações na força de carga.

Diante disso, buscou-se aprofundar a compreensão dos principais fatores que influenciam o funcionamento de sistemas pneumáticos e sua relação com as decisões de projeto. Identificou-se a necessidade de prever analiticamente as pressões atuantes nas câmaras do atuador pneumático para um dimensionamento adequado do sistema. Para isso, utilizou-se um conjunto de equações que buscaram estabelecer, em regime permanente, as correlações entre as pressões nas câmaras do cilindro. Esse conjunto de equações, denominado de método do ponto de operação, tornou-se o elemento central desta estrutura de projeto.

Ademais, identificou-se a necessidade de prever as forças de atrito em atuadores pneumáticos, bem como de compreender o comportamento dinâmico das forças de carga, especialmente em aplicações onde elas são variáveis, como no deslocamento de molas e

amortecedores. Por meio de análises teóricas e experimentais, foram desenvolvidos modelos matemáticos para endereçar essas incertezas durante o projeto de sistemas de atuação pneumática.

Na sequência, foram realizados estudos para compreender o comportamento característico do sistema, possibilitando o estabelecimento de um método para o dimensionamento de válvulas direcionais e reguladoras de vazão. Além disso, esses estudos proporcionaram uma melhor compreensão dos modos de regulagem da vazão de ar comprimido, resultando em diretrizes para a seleção entre os modos *meter-in* e *meter-out*, de acordo com as características da aplicação.

Também foi identificado que a determinação da força de carga é um dos grandes desafios no projeto de sistemas de atuação pneumática, pois essa etapa frequentemente envolve diversas incertezas. Dessa forma, foi desenvolvida uma estratégia de monitoramento online, denominada *Hybrid Machine Learning* (HML) *model*. Essa estratégia possibilita a otimização da pressão de suprimento e da abertura das válvulas reguladoras de vazão durante a operação do equipamento, levando em consideração a carga real aplicada ao atuador.

A estrutura de projeto e comissionamento desenvolvida foi extensivamente avaliada em ambiente de simulação dinâmica e em ensaios experimentais realizados em laboratório. Durante as avaliações, diversas condições de carregamento foram consideradas, assim como quatro métodos de dimensionamento alternativos presentes na literatura, além de uma solução comercialmente disponível para economia de energia.

Resultados e discussões

O método de dimensionamento proposto, denominado método do ponto de operação, foi comparado com quatro métodos descritos na literatura, incluindo abordagens mais e menos conservadoras. Com base nos resultados das simulações dinâmicas e dos experimentos conduzidos em laboratório, destacam-se as seguintes características:

Uma variação menos conservadora do método empírico de dimensionamento de cilindros e válvulas, baseada em um coeficiente de rendimento (η) de 90% e na vazão requerida da válvula (Q_r), falhou em determinar a vazão nominal das válvulas em praticamente todos os cenários avaliados. Esse método também apresentou elevada sensibilidade e baixa robustez. Embora tenha consumido uma quantidade significativamente menor de ar comprimido em comparação ao método do ponto de operação, seu desempenho insatisfatório não justifica sua aplicação.

Uma variação conservadora do método empírico, que utiliza um coeficiente de rendimento (η) de 50% do cilindro e determina a vazão da válvula com base no coeficiente de vazão (C_V), demonstrou alta capacidade de atender aos requisitos de projeto e boa robustez. No entanto, esse método também resultou em um elevado consumo de ar comprimido, com um consumo médio aproximadamente 23% superior ao do método do ponto de operação.

Uma variação intermediária do método empírico, que assume um coeficiente de rendimento (η) de 70% e determina a vazão da válvula com base no modelo de condutância sônica (C_{DN}), apresentou boa robustez na maioria das aplicações avaliadas e um consumo de ar aproximadamente 9% menor que o do método do ponto de operação. No entanto, esse método também apresentou algumas limitações, como baixa robustez em determinadas aplicações e incapacidade de determinar a vazão nominal das válvulas em cerca de 50% dos cenários avaliados.

O quarto método analisado, denominado *Pneumatic Frequency Ratio* (*PFR*), apresentou, em geral, bons resultados em termos de robustez. No entanto, ele apresentou uma tendência de superdimensionar as válvulas do sistema, potencialmente induzindo os projetistas a escolher válvulas excessivamente grandes. Além disso, a principal desvantagem dessa abordagem é a regra empírica sugerida pelo autor do método, que estabelece que a força de carga da aplicação não deve exceder 50% da força máxima do cilindro. Consequentemente, o método *PFR* consumiu 3.72 % mais ar comprimido do que o método do ponto de operação e, em dois dos casos avaliados, excedeu os limites de energia cinética recomendados pelo fabricante.

Por fim, o método do ponto de operação apresentou resultados positivos nas aplicações analisadas, sendo capaz de atender aos requisitos do projeto, garantir uma operação robusta e evitar consumo excessivo de ar comprimido. Já o sistema de monitoramento HML comprovou ser eficaz na otimização das condições operacionais de sistemas pneumáticos com base em dados em tempo real, o que resultou em maior robustez para atuadores subdimensionados e reduziu o consumo de ar comprimido em aproximadamente 50% para atuadores superdimensionados.

Considerações Finais

O objetivo principal desta tese de doutorado foi desenvolver uma estrutura para o projeto e a otimização de sistemas de atuação pneumáticos. Esta estrutura integra um conjunto de ferramentas destinadas a aprimorar o dimensionamento de atuadores e válvulas pneumáticas,

auxiliar na montagem e na configuração do sistema, e viabilizar a otimização online de seus parâmetros operacionais.

Os resultados das análises teóricas e experimentais realizadas ao longo desta tese demonstraram que soluções empíricas, comumente utilizadas no projeto de sistemas pneumáticos, podem levar a efeitos indesejáveis durante a operação dos equipamentos. Tais efeitos variam desde movimentos ligeiramente mais lentos, sem impacto significativo na operação, até condições adversas ou críticas, como consumo excessivo de ar comprimido ou até mesmo a parada não planejada das máquinas.

Por meio da análise cuidadosa do comportamento do sistema, da modelagem matemática dos fenômenos operacionais, da abstração de características irrelevantes, da análise estatística de resultados e do desenvolvimento de modelos de *Machine Learning*, estabeleceuse um processo inovador para o projeto de sistemas pneumáticos. Esse processo foi validado extensivamente em diversas condições operacionais.

Os resultados apresentados nesta tese demonstram que a estrutura desenvolvida para o projeto de sistemas de atuação pneumáticos permite dimensionar esses sistemas de forma consistente, atendendo aos requisitos estabelecidos e garantindo operação robusta e eficiente. Dessa forma, esta tese foi capaz de preencher a lacuna de conhecimento existente na área de projeto de sistemas de atuação pneumáticos, oferecendo uma alternativa sistemática aos métodos empíricos tradicionalmente utilizados.

Palavras-chave: Eficiência energética, Sistemas pneumáticos, Robustez, Aprendizado de máquina, Estrutura de Projeto, Ponto de operação.

.

FIGURES LIST

Figure 2.1 – Structure of an industrial pneumatic system	22
Figure 2.2 – Examples of discrete actuation systems	24
Figure 2.3 – Example of a pneumatic positioner	25
Figure 2.4 – Optimization Strategies of Pneumatic Systems	27
Figure 2.5 – Examples of energy-saving pneumatic circuits	28
Figure 2.6 – Examples of pneumatic circuits for air consumption reduction	30
Figure 2.7 – Comparison of yield factor ranges by authors	34
Figure 2.8 – Energy analysis of a throttle valve	42
Figure 2.9 – Components of compressed air work	44
Figure 3.1 – Impact of parameters on the ISO 6358 mass flow rate model	50
Figure 3.2 – Control volumes of a pneumatic actuator	52
Figure 3.3 – Heat transfer in pneumatic cylinders	55
Figure 3.4 – Characteristic length of a pneumatic cylinder	58
Figure 3.5 – Stroke-End Heads of a Pneumatic Cylinder	63
Figure 3.6 – Steady-state friction force characteristics	64
Figure 3.7 – Test rig utilized for the model validation	68
Figure 3.8 – Validation curves for the simulation model	70
Figure 3.9 - Comparison of the full and simplified models with experimental data	72
Figure 4.1 – Operating curve	77
Figure 4.2 – Loading and operating curves	78
Figure 4.3 – Loading and operating curves with dynamic simulation data	79
Figure 4.4 – Impact of load force variations on displacement time	82
Figure 4.5 – Time-dependent results for the Ø26 mm cylinder	83
Figure 4.6 – Sensitivity results showing the impact of cylinder diameter	84
Figure 4.7 – Operating point curves	87
Figure $4.8 - (p_A/p_S)_{Opt}$ for extending movements	89
Figure $4.9 - (p_B/p_S)_{Opt}$ for retracting movements	90
Figure 4.10 – Error histogram for $(p_A/p_S)_{Opt}$ and $(p_B/p_S)_{Opt}$	91
Figure 4.11 – Test rig setup for friction measurement	
Figure 4.12 – Measured friction forces	
Figure 4.13 – Interpolated experimental results of friction force	96

Figure 4.14 – Experimental and model results for friction in extending movement	99
Figure 4.15 – Experimental and model results for friction in retracting movement	101
Figure 4.16 – Histogram of relative friction force error	102
Figure 4.17 – Correlation of friction coefficient, piston velocity, and load force	103
Figure 4.18 – Relative error histogram of the dynamic friction coefficient model	105
Figure 4.19 – Generic example of a static pneumatic application	107
Figure 4.20 – Generic example of a dynamic pneumatic application	108
Figure 4.21 – Overview of the test rig structure and load force characteristics	110
Figure 4.22 – Load forces for the gravity-dominant (G1) experiments	111
Figure 4.23 – Load forces for experiments with balanced force components (G2)	112
Figure 4.24 – Load forces for G3 experiments with minimal gravity influence	113
Figure 4.25 – Comparison of UAS model with the experiment G3.1	115
Figure 4.26 – Load forces of UAS highlighting the corrective factors at $x = 0.6L$	117
Figure 4.27 – Monte Carlo robustness analysis	118
Figure 4.28 – Example of allowable kinetic energy for CAMOZZI cylinders	124
Figure 4.29 – Pneumatic actuator sizing flow chart for discrete applications	126
Figure 5.1 – Standardized actuation system for analyzing the velocity profile	129
Figure 5.2 – Characteristic behavior of the velocity profile	129
Figure 5.3 – Analysis of the velocity profile	130
Figure 5.4 – Depressurization of the counter pressure chamber	133
Figure 5.5 – Transient-state piston velocity	135
Figure 5.6 – Exhaust flow path for meter-out throttling.	139
Figure 5.7 – Intake flow path for meter-in throttling	140
Figure 5.8 – Correlation of the flow restrictors' sonic conductance with α_f	141
Figure 5.9 – Pneumatic valves sizing flow chart	143
Figure 6.1 – Analysis of pneumatic actuation system throttling modes	146
Figure 6.2 – Spring-based experiment with meter-in/out throttling	147
Figure 6.3 – Inertial-based experiment with meter-in/out throttling	148
Figure 6.4 – Pneumatic throttling motion-load quadrants	150
Figure 6.5 – Alternative throttling configurations	151
Figure 6.6 – Flowchart for selecting the throttling method	152
Figure 6.7 – Optimal operating point and the Ld_{opt} curve	154
Figure 6.8 – Definition of the reference pair of pressure ratios	155

Figure 6.9 – Sobol's indices for the operating point parameters	158
Figure 6.10 – Diagnostic features derived from the operating point	160
Figure 6.11 – Architecture of the Hybrid Machine Learning (HML) model	161
Figure 6.12 – Confusion matrix for predicting corrective actions on test data	165
Figure 6.13 – Overview of the design and setup framework	166
Figure 7.1 – Box plot results for gravity and inertial force applications	172
Figure 7.2 – Box plot results for gravity, inertial, and spring force applications	174
Figure 7.3 – Box plot results for the gravity, inertial, and viscous force applications	175
Figure 7.4 – Box plot results for gravity, inertial, spring, and viscous force applications	177
Figure $7.5 - Box$ plot results for the relative displacement time of the simulated systems	178
Figure 7.6 – Schematic diagrams of the evaluated applications	179
Figure 7.7 – Test rig configuration for Application #1 experiments	181
Figure 7.8 – Experimental results for Application #1	182
Figure 7.9 – Test rig configuration for Application #2 experiments	184
Figure 7.10 – Experimental results for Application #2	185
Figure 7.11 – Test rig configuration for Application #3 experiments	187
Figure 7.12 – Experimental results for Application #3	188
Figure 7.13 – Test rig configuration for Application #4 experiments	190
Figure 7.14 – Experimental results for Application #4	191
Figure 7.15 – Test rig configuration for Application #5 experiments	193
Figure 7.16 – Experimental results for Application #5	194
Figure 7.17 – General overview of the test rig and its workstations	198
Figure 7.18 – Schematic diagram of the HML system setup	199
Figure 7.19 – Underloaded tests results	201
Figure 7.20 – Overloaded tests results	202
Figure 7.21 – Experiment analysis	203

TABLES LIST

Table 3.1 – General system parameters for the model validation	68
Table 3.2 – Valves parameters for the model validation	68
Table 3.3 – Friction parameters for the model validation	69
Table 3.4 – Correction coefficients for natural and forced convection	69
Table 4.1 – Flow regimes at the valve	75
Table 4.2 – Specifications of the tested cylinders	93
Table 4.3 – Range of design requirements for the Monte Carlo Analyses	118
Table 6.1 – Parameters range for Sobol's indices	157
Table 6.2 – Diagnostic features for an extending displacement	159
Table 6.3 – Design requirement ranges for machine learning dataset generation	162
Table 6.4 – RMSE performance of tested regression models	162
Table 6.5 – Accuracy of tested classification models	164
Table 7.1 – Sizing methods used for the comparative analyses	169
Table 7.2 – Design requirement ranges for evaluating the sizing methods	170
Table 7.3 – Sizing results for a Group #1 application example	171
Table 7.4 – Sizing results for a Group #2 application example	173
Table 7.5 – Sizing results for a Group #3 application example	175
Table 7.6 – Sizing results for a Group #4 application example	176
Table 7.7 – Sizing methods results for Application #1	180
Table 7.8 – Sizing methods results for Application #2	184
Table 7.9 – Sizing methods results for Application #3	187
Table 7.10 – Sizing methods results for Application #4	189
Table 7.11 – Sizing methods results for Application #5	192
Table 7.12 – Summary of observed characteristics of each sizing method	195
Table 7.13 – Description of the design requirements for the performed tests	200

LIST OF ABBREVIATIONS

ANN Artificial Neural Network

CS Control Surface

CV Control Volume

EMA Electromechanical Acuator

HML Hybrid Machine Learning Model

KNN K – Nearest Neighbors

LASHIP Laboratory of Hydraulic and Pneumatic Systems

LS Limit Switch

NTP Normal Temperature and Pressure

PFR Pneumatic Frequency Ratio

RMSE Root Mean Squared Error

PWM Pulse Width Modulation

SF Sizing Factor

SVC Support Vector Classification

SVM Support Vector Machine

UFSC Federal University of Santa Catarina

LIST OF SYMBOLS

GREEK ALPHABET

α	Slope angle of pneumatic application	[°]
α_a	Angular acceleration of the test rig	[°]
$lpha_f$	Auxiliary variable of the equivalent sonic conductance model	[1]
α_s	Stribeck curve coefficient	[1]
$lpha_V$	Volumetric thermal expansion coefficient	[1/K]
β, β'	Rotating arm angles	[°]
γ	Specific heat ratio	[1]
Δp	Pressure differential	[Pa]
δ	Angle of the Ybitú test rig	[°]
η	Pneumatic cylinder yield coefficient	[1]
η_{sis}	Energy efficiency of the system	[1]
λ	Convective heat transfer coeficient	$[W/m^2.K]$
μ_d	Dynamic friction coefficient	[1]
μ_{rol}	Rolling friction coefficient	[m]
$\mu_{\scriptscriptstyle S}$	Static friction coefficient	[1]
μ_{sli}	Sliding friction coefficient	[1]
ν	Specific volume	$[m^3/kg]$
ξ	Bristle average deflection	[m]
ho	Specific mass	$[kg/m^3]$
σ_0	Stiffness coefficient of the bristles	[N/m]
σ_1	Damping coefficient of the bristles	[N.s/m]
σ_2	Viscous friction coefficient	[N.s/m]
τ	Time constant of a first order system	[s]
$\Phi, oldsymbol{\phi}, oldsymbol{arphi}$	Angles of the Ybitú test rig	[°]
Ψ	Angle of the Ybitú test rig	[°]
ψ	Flow function of the pneumatic frequency ratio method	[1]
Ω	Pneumatic frequency ratio	[1]
ω_0	Natural frequency of the cylinder	[rad/s]
ω_f	Natural frequency of the task	[rad/s]

SYMBOL LIST

\overline{S}_{i_Sb}

S_i	Literal symbol
Sb	Subscript
_	Average value indicator
	SUBSCRIPTS LIST
0	Initial condition / Atmospheric condition / Dead volume
1	Valve upstream
2	Valve downstream
Al	Aluminum
\boldsymbol{A}	Chamber A
A0	Chamber A initial condition
В	Chamber B
<i>B</i> 0	Chamber B initial condition
С	Cylinder
Cat	Catalogue
DV	Directional valve
d	Design
e	Extending
exp	Experimental
ext	External environment conditions
i	Initial condition
inn	Inner chamber conditions
L	Load
Μ	Mean
max	Maximum
min	Minimum
opt	Optimal
R	Reference condition
r	Retracting
rob	Robustness
S	Static / Spring
SS	Steady-state

Throttle valve

TV

LATIN ALPHABET

\boldsymbol{A}	Area	$[m^2]$
A, B, C, D, E	Lengths of the test rig structure	[m]
A_A , A_B , A_r	Areas of chambers A, B, and the piston rod	$[m^2]$
A_{s}	Heat flow surface area	$[m^2]$
A_0	Pneumatic valve orifice area	$[m^2]$
а	Exponential parameter for viscous friction	[1]
a_{ang}	Angular coefficient	[1]
b	Critical pressure ratio	[1]
В	Viscous friction coefficient of the load	[N.s/m]
B_e	Damping coefficient of the end-stroke head	[N.s/m]
Вi	Biot dimensionless number	[1]
b_{lin}	Linear coefficient	[1]
C	Sonic conductance	$[m^3/Pa.s]$
C_d	Discharge coefficient	[1]
C_{DN}	Sonic conductance according to De Negri's method	$[m^3/Pa.s]$
C_{DV}	Sonic conductance of the directional valve	$[m^3/Pa.s]$
C_{eq}	Equivalent sonic conductance	$[m^3/Pa.s]$
$CG_{x,y}$	x- and y -distances coordinates of the center of gravity	[m]
C_h	Sonic conductance of the hose	$[m^3/Pa.s]$
C_{PFR}	Sonic conductance according to PFR method	$[m^3/Pa.s]$
C_{TV}	Sonic conductance of the throttle valve	$[m^3/Pa.s]$
C_V	Flow coefficient	[US gal/min]
c_{Al}	Specific heat capacity of the aluminum	[J/kg.K]
c_p	Constant pressure specific heat	[J/kg.K]
c_v	Constant volume specific heat	[J/kg.K]
DF114	Diagnostic features	[1]
d_c	Piston diameter	[m]
d_h	Hose diameter	[m]
d_r	Rod diameter	[m]
E	Energy	[J]
E_{fr}	Friction energy	[J]
E_H	Hydraulic energy	[J]
E_{kn}	Kinetic energy	[J]
E_P	Pneumatic energy	[J]

e	Specific energy	[J/kg]
F	Force	[N]
F_{Bv}	Viscous load force	[N]
F_C	Coulomb friction force	[N]
F_{ext}	External force	[N]
F_{fr}	Friction force	[N]
F_G	Generic force	[N]
F_{imp}	Impact force	[N]
F_{Kx}	Spring load force	[N]
F_L	Load force	[N]
F_{LC}	Load cell force	[N]
F_{Ma}	Inertial load force	[N]
F_{pn}	Pneumatic force	[N]
F_r	Reaction force	[N]
F_S	Static friction force	[N]
Gr	Grashof dimensionless number	[1]
g	Gravity acceleration	$[m/s^2]$
h	Specific enthalpy	[J/kg]
I	Moment of inertia	$[kg.m^2]$
K	Spring stiffness	[N/m]
K_d	Corrective factors for damper-based application	[1]
K_m	Adjustment factor of the PFR method	[1]
K_p	Pressure-dependent coefficient of the ISO6358 model	[1/Pa]
K_{s}	Corrective factors for spring-based application	[1]
k_{18}	Coefficients of the friction model	[1]
k_c	Thermal conductivity of the fluid	[W/m.K]
k_e	Spring stiffness of the stroke-end head	[N/m]
k_{fk}	Corrective factor for forced convection	[1]
k_{nk}	Corrective factor for natural convection	[1]
k_w	Cylinder wall thermal conductivity	[W/m.K]
L	Cylinder stroke	[m]
L_0	Initial lengths of the test rig structure	[m]
$L_{AT},L_{SP},L_{\Phi},L_{\Psi}$	Lengths of the test rig structure	[m]
L_c	Characteristic length	[m]
L_h	Hose length	[m]
L_{w}	Cylinder wall thickness	[m]

M	Mass	[kg]
M_p	Mass of cylinder piston	[kg]
M_{st}	Mass of the rotating structure	[kg]
m	Mass of air	[kg]
m_A	Mass of air in chamber A of the cylinder	[kg]
m_B	Mass of air in chamber B of the cylinder	[kg]
m_0	Initial air mass	[kg]
Nu	Nusselt dimensionless number	[1]
Nu_F	Nusselt number for forced convection	[1]
Nu_N	Nusselt number for natural convection	[1]
n	Coefficient of the forced convection Nusselt number	[1]
P	Probability	[1]
P_H	Hydraulic power	[W]
P_P	Pneumatic power	[W]
ppr_R	Reference pair of pressure ratio	[1]
Pr	Prandtl dimensionless number	[1]
p	Absolute pressure	[Pa]
p_0	Atmospheric pressure	[Pa]
$p_{\mathrm{A}},p_{\mathit{B}}$	Chambers A and B pressures	[Pa]
p_s	Supply pressure	[Pa]
Q	Heat	[J]
Q_{inn}	Inner heat exchange	[J]
Q_n	Nominal volumetric flow	$[Nm^3/s]$
Q_{out}	Heat exchanged with the external environment	[J]
Q_{st}	Heat stored in the cylinder wall	[J]
Q_r	Required nominal flow rate	$[Nm^3/s]$
q	Subsonic index of the ISO6358 model	[1]
q_{mA},q_{mB}	Mass flow rate of air in chambers A and B	[kg/s]
q_V	Volumetric flow rate	$[m^3/s]$
R	Specific gas constant	[J/kg.K]
Ra	Rayleigh dimensionless number	[1]
R_C	Robustness	[1]
Re	Reynolds dimensionless number	[1]
r	Rolling radius	[m]
r_{A}	Cylinder area ratio B to A	[1]
r_{C}	Sonic conductance ratio of flow paths B to A	[1]

T	Temperature	[K]
T_W	Wall temperature	[K]
T_0	Temperature at the reference conditions	[K]
T_{CS}	Temperature at the control surface	[K]
t	Time	[s]
t_a	Actual displacement time	[s]
t_d	Displacement time	[s]
t_e	Emptying time	[s]
t_f	Final time of the piston displacement	[s]
t_{s}	Start time of the piston displacement	[s]
t_{ss}	Steady-state time	[s]
t_{ts}	Transient-state time	[s]
u	Specific internal energy	[J/kg]
U	thermal transmittance	$[W/m^2.K]$
V	Volume	$[m^3]$
$V_{ m A},V_{ m B}$	Chambers A and B volumes	$[m^3]$
v	Velocity	[m/s]
v_e, v_r	Extending, retracting velocities	[m/s]
v_m	Mean velocity	[m/s]
v_{end}	End-stroke velocity	[m/s]
v_{s}	Stribeck velocity	[m/s]
W_e	Work exchanged with the environment	[J]
W_P	Pneumatic work	[J]
W_t	Task work	[J]
X_f	Exergy of the fluid	[J]
\boldsymbol{x}	Piston position	[m]
x_e	Postion of the extending cylinder of the test rig	[m]
x_{pre}	Spring pre-load	[m]
x_r	Postion of the retracting cylinder of the test rig	[m]
x_s	Deformation of the traction spring of the test rig	[m]
y	Vertical position	[m]
Z	Dynamic friction model coefficients	[1]

SUMMARY

ACHN	OWLEDGEMENTS	6
ABSTE	RACT	7
RESUN	МО	8
RESUN	MO EXPANDIDO	9
FIGUR	ES LIST	15
TABLI	ES LIST	18
LIST C	OF ABBREVIATIONS	19
LIST C	OF SYMBOLS	20
GREE	K ALPHABET	20
SYMB	OL LIST	21
SUBSC	RIPTS LIST	21
LATIN	ALPHABET	22
SUMM	ARY	26
1	INTRODUCTION	16
1.1	OBJECTIVES	19
1.2	JUSTIFICATIVE AND CONTRIBUTIONS	20
1.3	THESIS STRUCTURE	21
2	LITERATURE REVIEW	22
2.1	PNEUMATIC ACTUATION SYSTEMS	22
2.1.1	Discrete actuation systems	23
2.1.2	Continuous actuation systems	24
2.2	OPTMIZATION OF PNEUMATIC ACTUATION SYSTEMS	26
2.2.1	Energy-saving pneumatic circuits	27
2.2.2	Online optimization of pneumatic systems	30
2.2.3	Optimization of system parameters and components	32
2.3	SIZING OF PNEUMATIC ACTUATION SYSTEMS	33
2.3.1	Empirical methods	33
2.3.2	Method based on natural frequency	37
2.3.3	Exergy based method	39
2.3.4	Methods based in numeric optimization	40
2.4	POWER, ENERGY AND EXERGY OF PNEUMATIC SYSTEMS	41
2.5	FINAL CONSIDERATIONS ABOUT CHAPTER 2	47
3	SYSTEM MODELING	48

3.1	PNEUMATIC VALVES AND RESTRICTIVE ELEMENTS	48
3.2	CYLINDERS	51
3.2.1	Pressure dynamics	51
3.2.2	Temperature dynamics	53
3.2.3	Heat transfer dynamics	55
3.2.4	Motion dynamics	62
3.2.5	Pneumatic friction modeling	63
3.3	DYNAMIC MODEL VALIDATION AND ANALYSIS	67
3.4	FINAL CONSIDERATIONS ABOUT CHAPTER 3	73
4	SIZING OF PNEUMATIC ACTUATORS	74
4.1	THE STEADY-STATE ANALYSIS	74
4.1.1	The operating curve	75
4.1.2	The loading curve	77
4.1.3	The optimal operating condition	80
4.1.4	The velocity/C curve	85
4.2	EXPERIMENTAL ANALYSIS OF THE FRICTION COEFFICIENT	91
4.3	CLASSIFICATION OF DISCRETE PNEUMATIC APPLICATIONS	106
4.3.1	Static applications	106
4.3.2	Dynamic applications	107
4.4	SIZING METHOD OF PNEUMATIC ACTUATORS	120
4.5	FINAL CONSIDERATIONS ABOUT CHAPTER 4	127
5	SIZING OF PNEUMATIC VALVES	128
5.1	CHARACTERISTIC BEHAVIOR OF THE VELOCITY PROFILE	128
5.1.1	The emptying time	131
5.1.2	The transient-state time	133
5.1.3	The equivalent sonic conductance	136
5.2	PNEUMATIC THROTTLE AND DIRECTIONAL VALVES	137
5.2.1	Equivalent sonic conductance for meter-out configurations	139
5.2.2	Equivalent sonic conductance of meter-in configurations	140
5.3	SIZING METHOD OF PNEUMATIC VALVES	142
5.4	FINAL CONSIDERATIONS ABOUT CHAPTER 5	143
6	SETUP OF PNEUMATIC ACTUATION SYSTEMS	144
6.1	THROTTLING IN PNEUMATIC ACTUATION SYSTEMS	144
6.2	ONLINE PARAMETER OPTIMIZATION	152

6.2.1	The reference operating condition	153
6.2.2	Sensitivity analysis	157
6.2.3	The Hybrid Machine Learning Model (HML)	158
6.2.4	The model training	161
6.3	OVERVIEW OF THE DESIGN AND SETUP FRAMEWORK	165
6.4	FINAL CONSIDERATIONS ABOUT CHAPTER 6	167
7	SIMULATION AND EXPERIMENTAL RESULTS	168
7.1	EVALUATION OF SIZING METHODS FOR PNEUMATIC ACTUAT	ΓΙΟΝ
SYSTEMS		
7.1.1	Simulation-based assessment of the sizing methods	170
7.1.2	Experimental assessment of the sizing methods	179
7.2	EVALUATION OF THE HML MODEL FOR ONLINE PNEUMATIC SYS	TEM
OPTIMIZATION197		
7.2.1	Test rig for evaluating the HML model	197
7.2.2	Experimental evaluation of the tested architectures	199
7.3	FINAL CONSIDERATIONS ABOUT CHAPTER 8	204
8	CONCLUSIONS	205
8.1	FUTURE WORKS	207
REFERI	ENCES	209
APPENI	DIX A – IDENTIFICATION OF FRICTION PARAMETERS	224
APPENDIX B – LINEARIZATION OF THE MASS FLOW RATE EQUATION229		
APPENDIX C – AIR TEMPERATURE BEHAVIOR IN PNEUMATIC THROTTLE		
VALVES	S	231
APPENDIX D - DERIVATION OF THE MASS FLOW RATE MODEL FOR		
COMPRESSIBLE FLOW		
APPENDIX E – THE YBITÚ TEST RIG239		

1 INTRODUCTION

The growing demand from society for the development of sustainable and less aggressive technologies for the environment, as well as the expansion of renewable energy sources, are among the main strategies for the reduction of greenhouses gas emission and the addressing of climate changes. In recent decades, these aspects are becoming prominent in the public policies of highly industrialized countries and in the agendas of non-governmental organizations. Notable examples include the Kyoto Protocol in 1997, the European Climate Change plan in 2009, United Nations' 17 Sustainable Development Goals in 2015, the Paris Agreement in 2016. Additionally, the Conference of the Parties (COP), held annually since 1995, will host its 30th session in Brazil in 2025.

However, global energy consumption has been increasing year after year, rising from 8,588.9 million tons of oil equivalent in 1995 to 13,147.3 million in 2015 (Dong; Dong; Jiang, 2020). At the same time, the ecological footprint, which measures the environmental impact of human activities, is closely linked to energy consumption (Destek; Sinha, 2020). In view of the growing energy demand and the need to reduce environmental impacts, Ahmad and Zhang (2020) emphasize that energy performance is one of the key pillars for achieving the so-desired sustainable development.

The industry sector, responsible for about 37% of world energy consumption (IEA, 2022), frequently utilizes three main types of actuation technologies in its productive processes: electromechanical, hydraulic and pneumatic drives. Regarding pneumatic drives, studies show that in countries such as Australia, Germany and the United States, compressed air systems accounts for approximately 7% to 16% of total industrial energy consumption, highlighting the significance of this technology for the productive sector (Climate Managers, 2009; Love; Lanke; Alles, 2012; Radermacher *et al.*, 2021; Unger; Radgen, 2017; Xenergy, 2001).

Characteristics such as agility, versatility, reliability, robustness, high power density, and low acquisition and maintenance costs make pneumatic technology an effective solution for sectors with a high degree of automation. Moreover, air does not produce sparks, poses no risk to human health, and can be easily stored, making it applicable in explosive environments like the chemical industry (Beater, 2007).

However, the energy efficiency of compressed air systems has become a growing field of interest in recent years. Some authors argue that throughout the cycle of production, distribution, and usage of compressed air, only 2% to 20% of the consumed energy is effectively transformed into useful work (Shi *et al.*, 2019). Consequently, the energy cost can represent

more than 75% of the total cost of ownership when the costs associated with maintenance, storage, acquisition, and operation throughout the equipment lifecycle are considered (Mousavi; Kara; Kornfeld, 2014; Rakova; Hepke; Weber, 2016). This scenario significantly contrasts with electromechanical actuators (EMAs), whose energy efficiencies are around 85% and have become more popular in recent years (Zhu *et al.*, 2018).

Despite having lower energy efficiency, pneumatic drives possess characteristics that make them difficult to replace with electromechanical drives, especially their capacity to produce maximum force for unlimited periods without heating and with minimal continuous energy consumption (Harris; O'Donnell; Whelan, 2012). In contrast to linear electromechanical actuators, pneumatic drives do not have the electrical motor mechanically attached to the actuator, making them more flexible, compact, and resistant to harsh environments. Furthermore, the produced power can be easily controlled with variable restrictions, such as throttle valves, and translational movement can be easily achieved using a circular piston and sleeve (Beater, 2007).

This way, a considerable effort by the scientific community has been made to improve the energy efficiency of pneumatic systems. Strategies focused on reducing consumption, preventing losses and reusing compressed air result in significative enhancements of energy efficiency. Some examples of research in this field include the use of cross flow valves to interconnect the cylinder chambers for a period of time (Doll; Neumann; Sawodny, 2011; Endler; De Negri; Castelan, 2015; Merkelbach; Murrenhoff, 2015; Shen; Goldfarb, 2007), the independent control of each cylinder chamber (Boyko; Weber, 2024b; Gryboś; Leszczyński, 2024; Padovani; Barth, 2018; Raisch; Sawodny, 2019b; Reese; Reinertz; Schmitz, 2024), the use of distinct supply pressures for each chamber (Harris; Nolan; O'Donnell, 2014; Šešlija; Dudić; Milenković, 2017), the reuse of exhausted air for low-pressure applications (Du *et al.*, 2022; Farias, 2020; Leszczynski; Grybos, 2019; Markowski *et al.*, 2023; Šešlija; Šulc; Reljić, 2013; Šešlija *et al.*, 2021), and the optimization of the system's parameters (Doll; Neumann; Sawodny, 2015; Hepke; Weber, 2013; Raisch; Sawodny, 2019a).

In some cases, the improvement in energy efficiency can be in the range of 20 to 50% compared to conventional solutions (Saidur; Rahim; Hasanuzzaman, 2010). However, Merkelbach and Murrenhoff (2015) argue that the application of energy-saving strategies in industrial environments is not common, a scenario that is still commonly observed at the present. This aspect can be explained by the high degree of complexity associated with energy-saving solutions, which increases the likelihood of production line stoppages and reduces the attractiveness of potential gains from energy savings.

This scenario demonstrates that the applicability of an optimized solution depends not only on the energy efficiency gains. Instead, it depends on the combination of potential reductions in energy consumption, along with the assurance of an equipment that is robust, reliable, and capable of adapting itself to the numerous uncertainties that may occur during operation.

Therefore, it is believed that the proper sizing of the cylinder-valve set plays a relevant role in improving the energy efficiency and the robustness of pneumatic systems. This hypothesis is based on the discussions presented in Doll; Neumann and Sawodny (2015), Rakova; Hepke and Weber (2016), and Vigolo (2018), which demonstrates the positive impacts of a well dimensioned drive.

Optimization algorithms have been developed to optimize the parameters of pneumatic systems. Some examples include genetic algorithms (Harris; Nolan; O'Donnell, 2014), pattern search algorithms (Hepke; Weber, 2013), and gradient based algorithms (Raisch; Sawodny, 2019a), all of which aim to minimize air consumption while meeting the requirements of the applications. However, these approaches require theoretical knowledge and computational tools that are often not easily accessible to application engineers. Moreover, aspects related to robustness are not considered by the algorithms, which can potentially lead to actuators operating close to their maximum force capacity, compromising the functionality of the system during eventual oscillations of the load force.

In general, pneumatic system components are commonly dimensioned based on designer experience or empirical methods, often leading to oversized systems (Boyko *et al.*, 2024; Doll; Neumann; Gauchel, 2024; Doll; Neumann; Sawodny, 2015; Raisch; Sawodny, 2019a). Another common approach is using software and technical guidelines from manufacturers like Festo (2024a), Metal Work S.p.A (2024), SMC (2024b), and Camozzi (2019a). In this case, the sizing task is delegated to a 'black box,' leaving designers with little understanding of the assumptions and methods used, as well as the impact of design decisions on the system's behavior.

Among the available sizing procedures in the literature, a common challenge is the need to precisely know the application's load force. However, uncertainties inherent in many design processes often make accurate load force prediction difficult. As a result, conservative estimates are frequently used, potentially leading to pneumatic drives with excessive energy consumption or low robustness. Therefore, a proper cylinder sizing method is necessary, but not enough, to have an efficient operation.

In view of these challenges, this PhD thesis aims to balance energy efficiency and robustness in pneumatic drives. A novel metric is proposed to assess cylinder robustness, based on the sensitivity of piston displacement time to variations in load force. An optimal operating condition is established by deriving a set of steady-state equations from the system's governing equations. Consequently, a new sizing method and monitoring system were developed to design and set up pneumatic actuation systems to operate at this optimal condition, ensuring robustness and efficiency even under uncertain operating conditions.

1.1 OBJECTIVES

The main objective of this thesis is to develop a comprehensive design and setup framework for discrete pneumatic actuation systems, comprising a sizing method for cylinder and valves, along with assembly guidelines and a monitoring and setup approach to enhance the operation of pneumatic drives. This framework aims to ensure robust and efficient operation, addressing the inherent uncertainties in operating conditions while optimizing energy consumption and robustness.

In order to achieve the main objective, the following specific objectives have been defined:

- Develop a sizing method for selecting pneumatic cylinders, throttle valves, and directional valves capable of balancing air consumption and robustness;
- Analyze the effects of applications with distinct load components, such as high inertial loads, springs, and dampers, and their impact on drive sizing;
- Determine correlations between cylinder friction forces and factors such as cylinder diameter, piston velocity, and chamber pressures;
- Propose guidelines for proper throttling method based on application characteristics;
- Develop an online optimization strategy to aid in setting up pneumatic actuation systems, including supply pressure optimization and throttle valve adjustment.
- Validate the effectiveness of the design and setup framework through experiments in test rigs;
- Compare the proposed solutions with alternative solutions available in the literature and on the market.

1.2 JUSTIFICATIVE AND CONTRIBUTIONS

The constant demand from society for sustainable economic development, the need to address climate change, and the rising energy costs are among the primary reasons for developing technologies aimed at increasing the energy efficiency of industrial processes. Pneumatic systems, in turn, have an important role in economic development, as they enable the development of more robust and productive equipment.

Even though this technology is known for its low energy efficiency, several strategies can enhance it. However, these strategies usually involve the use of additional components and/or complex control strategies, which increase acquisition costs and reduce system reliability and robustness, making market entry more challenging for these technologies.

Nonetheless, it is believed that with proper sizing of the actuation system, it is possible to optimize both robustness and energy efficiency without impacting acquisition costs or control strategies. It is still common, however, for simplistic rules of thumb to be applied in the sizing of these equipment, where actuators are sized based on the mass being moved, with a yield coefficient used to account for friction, pressure fluctuations, and dynamic effects such as acceleration.

Research on optimizing the sizing of pneumatic drives has attracted significant interest from researchers and institutes, particularly in Germany. Notable examples include the work at Dresden University of Technology (Hepke; Weber, 2013; Rakova; Weber, 2016), and the University of Stuttgart (Doll; Neumann; Gauchel, 2024; Doll; Neumann; Sawodny, 2015; Raisch; Sawodny, 2019a). In Brazil, the Laboratory of Hydraulic and Pneumatic Systems (LASHIP) made the first step toward developing a novel sizing method in 2009 (Oliveira, 2009). Since then, the research group has published several papers and master's theses. However, a comprehensive design and setup framework has yet to be published.

The main contributions of this thesis are:

- Development of a novel design method for pneumatic actuation systems that reduces uncertainties during the design process and provides designers with a well-founded model, offering a clear understanding of the assumptions made and the consequences of design choices;
- Development of quantitative metrics for robustness assessment of pneumatic drives, enabling the evaluation of their capacity to maintain performance under varying working conditions;

- Enhanced understanding of friction forces in pneumatic drives, along with predictive tools that enable estimation of these forces during the early stages of the design process;
- Improved understanding of the effects of multiple load components (inertia, springs, dampers) on pneumatic drives and their impact on system design and performance;
- Development of setup guidelines for selecting the most suitable throttling method, along with an online optimization strategy to improve the energy efficiency of pneumatic drives.

1.3 THESIS STRUCTURE

This thesis is organized into eight chapters. In this first Chapter, a contextualization of the problem is presented, along with the general and specific objectives, justification, and contributions of the doctoral research.

Chapter 2 provides a literature review on pneumatic actuation systems, including the main strategies for optimizing these systems, current monitoring approaches, methods for measuring energy efficiency, and existing sizing methods for pneumatic drives.

Aspects related to system modeling are presented in Chapter 3, including the modeling of pneumatic valves, cylinders and the evaluation of different heat exchange models;

Chapter 4 defines an optimal operating condition and derives analytical equations for sizing of pneumatic cylinders. It includes a study of friction for a wide range of operating conditions and the impact of distinct load force components on the actuator selection.

In Chapter 5 it is presented the characterization of the system displacement time, which serves as the basis for deriving analytical equations for sizing pneumatic throttle and directional valves.

Chapter 6 presents an analysis of different setup strategies, as well as the development of an online optimization system for the setup of pneumatic drives.

Simulation and experimental results are shown in Chapter 7, demonstrating the effectiveness of the proposed design and setup framework. Finally, Chapter 8 presents the conclusions of this thesis.

2 LITERATURE REVIEW

Before presenting the development of the framework proposed in this thesis, some concepts related to pneumatic actuation systems need to be reviewed.

2.1 PNEUMATIC ACTUATION SYSTEMS

Pneumatic systems are employed as a means of energy transformation, enabling mechanical energy provided by rotating machines, such as electric motors or combustion engines, to be converted into pneumatic energy, making it easier to transmit, store, and control. The use of pneumatic energy is accomplished by pneumatic actuators, which perform mechanical work through linear or rotational displacement (Rabie, 2009).

In this process of energy transformation, Hepke and Weber (2012) highlights that an industrial pneumatic system is composed of four subsystems: the production, distribution, control, and usage of compressed air.

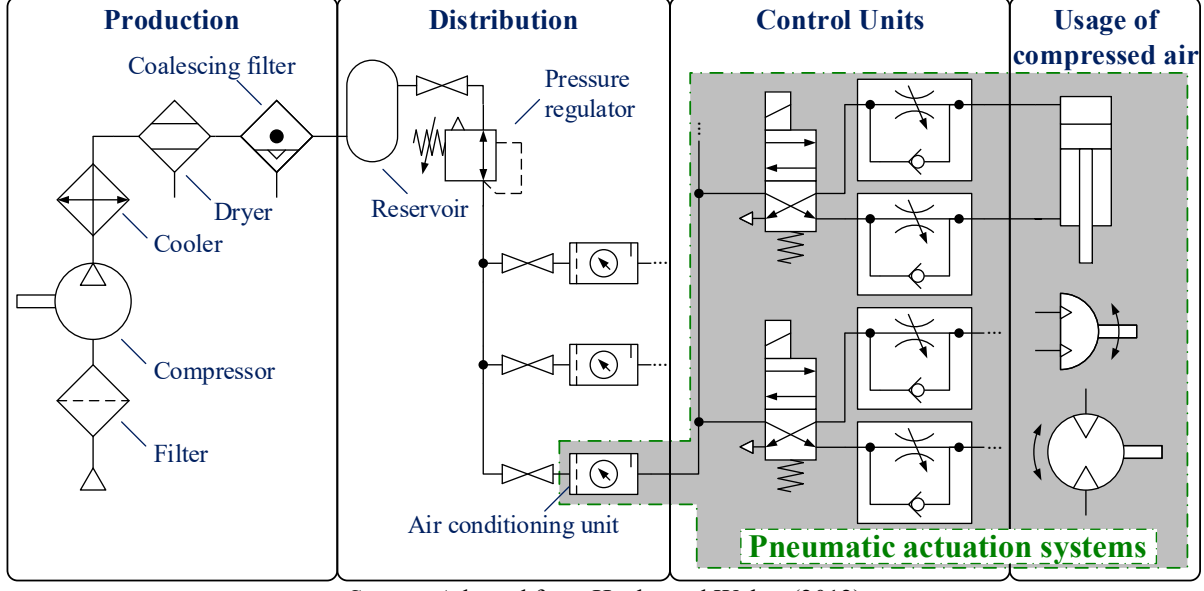


Figure 2.1 – Structure of an industrial pneumatic system

Source: Adapted from Hepke and Weber (2012).

The classical structure of a pneumatic actuation system is highlighted in the shaded area of Figure 2.1. Fundamentally, De Negri (2001) explains that a generic pneumatic actuation system must receive pneumatic energy from a constant pressure source and convert it into mechanical energy through a control signal. According to classical literature on pneumatic

systems, such as Andersen (1967), Bollmann (1997), Beater (2007), Krivts and Krejnin (2006), and Rabie (2009), pneumatic actuation systems may include components such as directional valves, throttle valves, quick exhaust valves, proportional valves, limit switch sensors, position transducers, and actuators.

According to Bollmann (1997), pneumatic actuators can be categorized into two major groups: linear and rotary actuators. Linear actuators include single or double-acting cylinders, with or without rod, and can be symmetric or differential. In the group of rotary actuators, there are the pneumatic motors and rotary cylinders, also known as oscillators. In addition to linear and rotary actuators, various other concepts can be found on the market, such as grippers, suction cups, and pneumatic muscles (FESTO, 2024b).

A widely accepted classification divides systems into two categories: discrete systems (often referred to as discrete-state systems or automation systems) and continuous systems (commonly known as continuous-state systems or control systems). This classification is adopted in this thesis to characterize pneumatic actuation systems, as presented in the following subsections.

2.1.1 Discrete actuation systems

Discrete actuation systems are widely used in simple on/off tasks where only two stable states are possible, such as extended or retracted linear cylinders, open or closed grippers, activated or deactivated suction cups, and clockwise or counterclockwise rotation of pneumatic motors, among others. Limit switches or vacuum sensors are commonly used to detect the current state of the system, while throttle valves control the transition speed between states. (Krivts; Krejnin, 2006).

Figure 2.2 presents two examples of discrete actuation systems. In the first example (Figure 2.2-a), velocity control is achieved by throttling the air entering the actuator's chamber, a method known as 'meter-in' throttling. Figure 2.2-b shows a setup where velocity control is managed by throttling the air exhausting from the cylinder's chamber, known as 'meter-out' control.

Several authors, such as Bollmann (1997), Barber (1997), Prudente (2000), Fialho (2004), and Beater (2007), do not recommend using meter-in control in pneumatic systems. The reason is the pressure decrease in the chamber that is performing the movement, which is caused by the increase of its volume due to the piston displacement. This phenomenon leads to erratic and intermittent piston movement, particularly when the load force is variable or at low

speeds, where stick-slip is more likely compared to a meter-out setup (Sagara; Hosono; Yang, 1999). Moreover, meter-in throttling offers no velocity control when the load is applied in the same direction as the movement, leading to potentially dangerous operation of the system. Section 6.1 provides a thorough analysis of meter-in and meter-out setups, supported by experimental results, to identify the conditions under which each throttling method can be recommended.

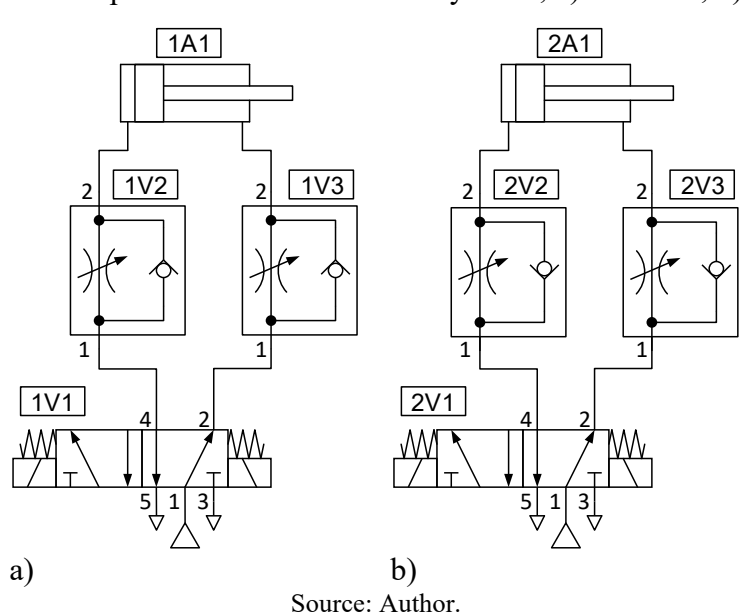


Figure 2.2 – Examples of discrete actuation systems; a) Meter-in, b) Meter-out

The setups for a discrete actuation system are not limited to those presented in Figure 2.2. Several other configurations are possible depending on the application's requirements, including the use of single-acting cylinders, quick exhaust valves, and logic valves such as AND and OR. Examples of such setups can be found in Bollmann (1997) and Prudente (2000).

2.1.2 Continuous actuation systems

The main characteristic of a continuous actuation system is the ability to position the rod at any point within the actuator stroke. These systems typically use closed-loop controllers, where the variable to be controlled (such as position or force) is continuously measured and compared with a reference signal. If a difference exists between these two variables, the controller adjusts the valve's opening or closing as needed until the difference becomes negligible, equaling the controlled signal with the desired one, thus characterizing a closed-loop system (Krivts; Krejnin, 2006).

In pneumatics, the most commonly used continuous actuation systems are pneumatic positioners (or servopositioners). These are used in applications where it is necessary to maintain the piston at an intermediate position within the cylinder stroke. Examples of applications for pneumatic positioners include food product packaging (Wang; Pu; Moore, 1999), automation in magnetic resonance equipment (Fischer *et al.*, 2008), collaborative robotic manipulators (Festo, 2022), rehabilitation devices (Vigolo; Rodrigues; *et al.*, 2024), fatigue testing equipment for radioactive environments (Pohja *et al.*, 2013), and speed governors for hydraulic turbines (Mendonza; De Negri; Soares, 2014; Vigolo *et al.*, 2020).

The working principle and main components of a pneumatic positioner are shown in Figure 2.3. To position the mass M, the proportional directional control valve (1V1) regulates the inflow and outflow of air in the chambers of cylinder 1A1. The position transducer (1S1) measures the cylinder rod position in real time and compares it with the reference signal U_C . The resulting difference is converted into a control signal, which adjusts the valve's flow paths as necessary. Unlike discrete actuation systems, pneumatic positioners do not use throttle valves, as flow control to achieve the desired speed is handled by the proportional directional control valve.

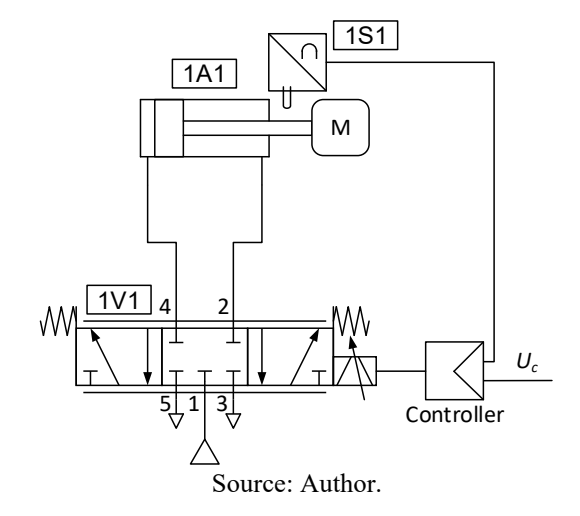


Figure 2.3 – Example of a pneumatic positioner

Similar to discrete pneumatic actuation systems, there are several possible configurations for pneumatic positioners, such as using two proportional directional valves (Carneiro; de Almeida, 2014; Righettini; Giberti, 2002), proportional pressure regulator valves (Conterato *et al.*, 2019; Muzy; Caporali, 2018; Šitum, 2013), as well as fast-switching on-off valves with PWM control (Locateli, 2011; Messina; Giannoccaro; Gentile, 2005; Najafi;

Hejrati, 2009). Regarding the types of actuators that can be applied, options include linear cylinders (with or without rods) and rotary cylinders, such as motors and oscillators.

2.2 OPTMIZATION OF PNEUMATIC ACTUATION SYSTEMS

Pneumatic systems use one of the most expensive energy sources in industrial applications. However, their low acquisition costs, robustness, agility, and flexibility make them widely used in automation of equipment (Hepke; Weber, 2012; Mousavi; Kara; Kornfeld, 2014). Consequently, the energy consumption of pneumatic systems represents a significant portion of the total energy used by the industrial sector. In Germany, for instance, energy consumption from pneumatic systems accounts for up to 17% of the total energy consumption in certain sectors, such as rubber, plastic, glass, and ceramics (Unger; Radgen, 2017).

Pneumatic systems are widely known for their low energy efficiency. Some authors, such as Saidur; Rahim and Hasanuzzaman (2010) and Shi *et al.* (2019), argue that only 2 to 20% of the energy consumed in producing compressed air is effectively converted into work. Among the main sources of inefficiency are the generation of compressed air, where the typical efficiency of industrial compressors ranges from 40 to 60%, and the use of compressed air, where approximately 50% of the energy supplied to the actuator is released into the atmosphere during chamber depressurization.

This scenario is supported by data presented by Rakova and Weber (2016), which shows that, throughout the life cycle of pneumatic systems, approximately 75% of the total cost of ownership (including acquisition, maintenance, and operation) is due to energy consumption, whereas for other technologies, such as electromechanical actuators, this cost represents only around 2%. This highlights the need for energy optimization in pneumatic technology to make it competitive with other technologies and meet industrial demands.

Optimization possibilities range from complex and costly actions, such as the reuse of exhaust air, to simpler actions, such as leak detection. Based on the work of Hepke and Weber (2013), Harris; O'Donnell and Whelan (2012), Unger and Radgen (2017), Harris; Nolan and O'Donnell (2014) and, Boyko *et al.* (2024), optimization strategies for pneumatic systems can be organized into three categories, as presented in Figure 2.4.

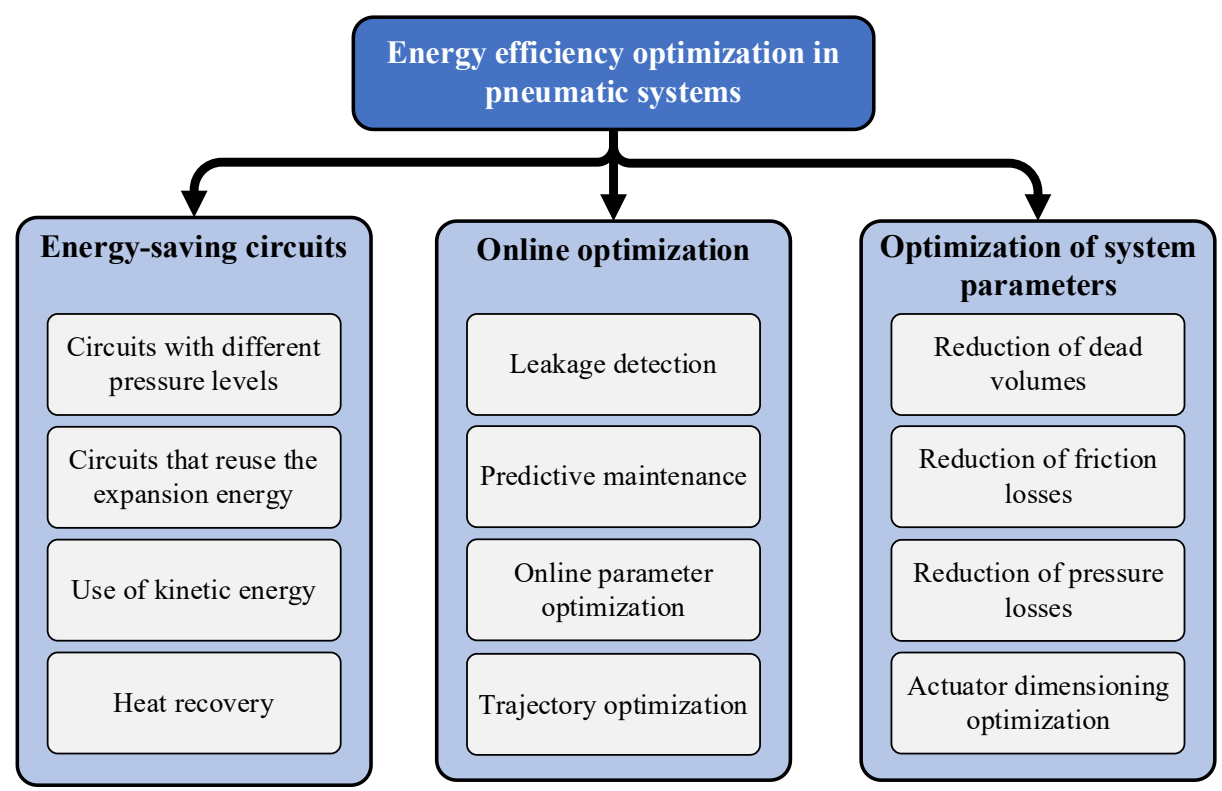


Figure 2.4 – Optimization Strategies of Pneumatic Systems

Source: Based on work published by Hepke and Weber (2013), Harris; O'Donnell and Whelan (2012), Unger and Radgen (2017), Harris; Nolan and O'Donnell (2014), and Boyko *et al.* (2024).

A literature review of the main advances in each optimization category will be provided in sections 2.2.1, 2.2.2, and 2.2.3.

2.2.1 Energy-saving pneumatic circuits

According to Hepke and Weber (2013), although several strategies exist to improve the energy efficiency of pneumatic drives, only a few are economically viable due to the costs associated with the need for additional components. The authors developed an exhaust air recovery system to reuse the expansion air during the retraction movement (Figure 2.5-a), achieving an increase in energy efficiency of 56% and a payback time of less than two years.

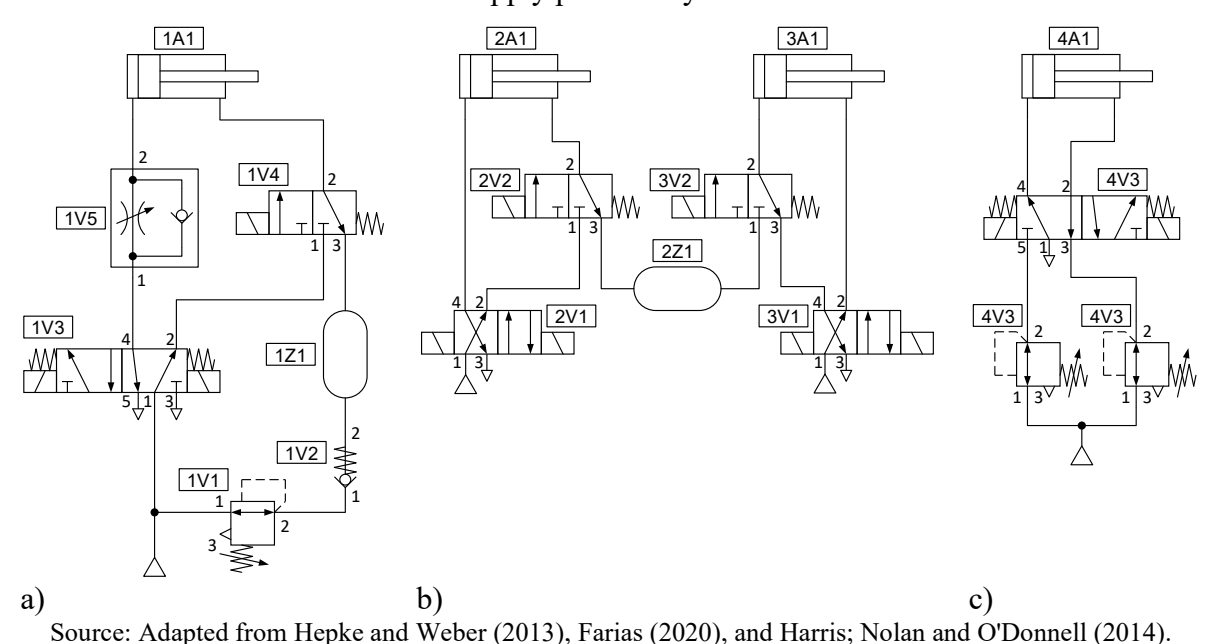
The reuse of compressed air is also applied to subsystems that operate at lower pressures. For instance, Farias (2020) utilized two 3/2 valves and a reservoir to store the pneumatic energy of the extending chamber of a high-pressure actuator (Figure 2.5-b). This energy will later be used for the retracting movement of a subsystem operating at lower pressure, achieving savings of approximately 34% in compressed air consumption. In the approach presented by Šešlija; Šulc and Reljić (2013), the recovered air is stored in an auxiliary

reservoir, which includes pressure monitoring to maintain a minimum operating pressure of 2.8 bar_{abs}. Thus, improving energy availability and reducing air consumption by 31%.

The strategies for compressed air recovery and storing it in an auxiliary reservoir can achieve significant savings in pneumatic systems. However, one of the main side effects is the spring effect created by the reservoir's counterpressure, which can potentially affect the movement dynamics of the high-pressure actuator. Novakovic *et al.* (2015) conducted a study to identify the pressure levels that could impact the actuator's dynamics and establish the recovery limit. According to the study, the extension velocity of the experiments was significantly impacted when the reservoir pressure reached half of the supply pressure. However, this conclusion cannot be generalized across all systems due to the variability in system behavior related to piston diameter, not being applicable, for instance, if the actuator is undersized.

Since in many applications the load force acts in only one direction of movement, the use of two supply pressure lines is widely discussed in the literature. Harris; Nolan and O'Donnell (2014), for instance, present a solution that utilizes two pressure regulating valves (Figure 2.5-c), enabling the individual setup of the supply pressure for each chamber of the cylinder and providing a reduction of up to 27% in compressed air consumption. A similar solution is presented by Beater (2007), Harris; O'Donnell and Whelan (2012), and Boyko and Weber (2020).

Figure 2.5 – Examples of energy-saving pneumatic circuits: a) Reusing expansion air during the retraction movement; b) Reusing expansion air for a lower pressure subsystem; c) Dual supply pressure system

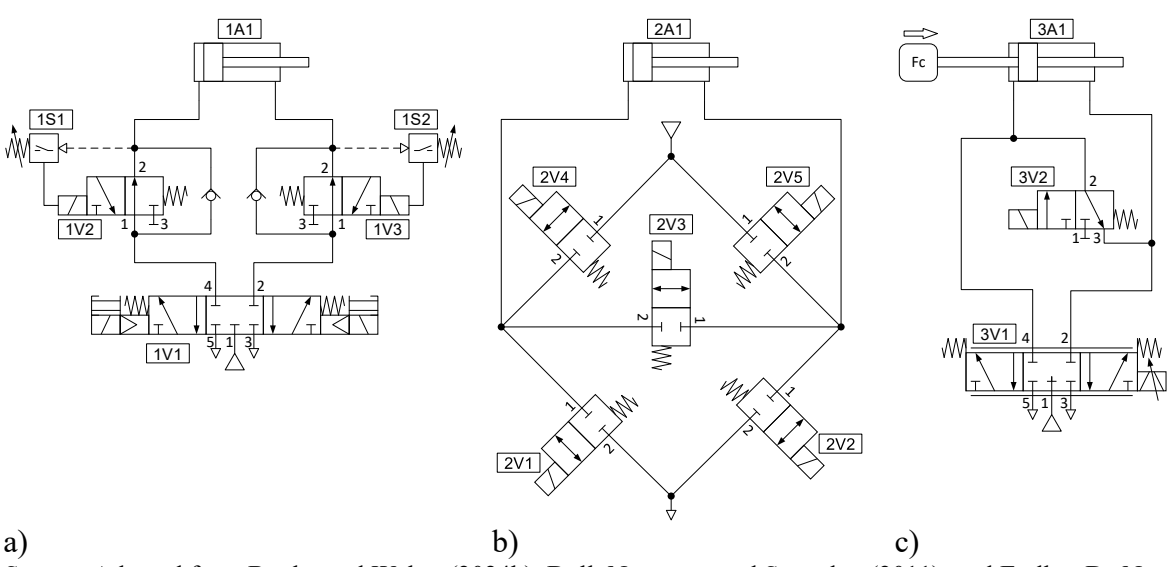


According to the data presented by Shi *et al.* (2019), around 50% of the supplied energy of an actuator is released into the atmosphere during the retraction movement. This characteristic is frequently highlighted as the main disadvantage of pneumatic drives and serves as motivation to optimize these systems (Harris; O'Donnell; Whelan, 2012; Hepke; Weber, 2013; Shi *et al.*, 2019). An additional factor that worsens this condition is the pressurization that occurs in the chamber after the movement has ended, as useful work has already been completed but the system is still consuming compressed air.

To reduce the impact of this effect, a technique called supply pressure cut-off has been developed. This technique involves shutting off the supply pressure line when the task is completed or just before it is finished. According to Boyko and Weber (2024b), there are three principles for implementing supply pressure cut-off: time-based, position-based, and pressure-based. The authors developed a pressure-based strategy (Figure 2.6-a), achieving a 71% reduction in air consumption when using an oversized cylinder. However, when well-sized cylinders were used, this technique resulted in impact vibrations during high-inertia tasks. Raisch and Sawodny (2019b) and Raisch; Hülsmann and Sawodny (2018) applied a circuit with two 3/3 valves and established optimal cut-off times to avoid exceeding the allowable impact energy of the actuator, achieving a 49.4% reduction without damaging the cylinder due to excessive impact energy. The app 'ECO Drive' from the Festo Motion Terminal is a commercially available solution that employs this principle by halting the inflow of compressed air upon task completion (Festo, 2017).

The interconnection of the cylinder chambers is a strategy aimed at reusing exhaust air. In this strategy, the pressurized chamber is briefly connected to the depressurized chamber, allowing for partial reuse of the compressed air that would otherwise be released into the atmosphere. This approach is described in Doll; Neumann and Sawodny (2011), where a pneumatic circuit in the form of a bridge, using five 2/2 valves, is employed (Figure 2.6-b). A similar solution is presented by Endler; De Negri and Castelan (2015), who uses a fast-switching 3/2 valve to interconnect both chambers of a symmetric actuator (Figure 2.6-c). The supply pressure is shut off when movement occurs in the same direction as the load, and velocity control is achieved through a PWM signal sent to the 3/2 valve, resulting in a 54% reduction in compressed air consumption.

Figure 2.6 – Examples of pneumatic circuits for air consumption reduction: a) Pressure-based supply cut-off; b) Bridge pneumatic circuit; c) Chamber interconnection with fast-switching 3/2 valve



Source: Adapted from Boyko and Weber (2024b), Doll; Neumann and Sawodny (2011), and Endler; De Negri and Castelan (2015).

Even with energy-saving potentials estimated at around 50%, the optimization strategies presented above have some drawbacks. For instance, they require additional components and complex control strategies to operate the actuation system. Moreover, in many cases, these systems become more susceptible to operational failures. As highlighted by Radgen e Blaustein (2001 apud HARRIS et al, 2012), in most industrial processes, the cost of production losses is often more significant than the potential gains in energy efficiency. Consequently, in many instances, the optimization strategies are not effectively employed, leading to a preference for the traditional architecture of actuation systems described in section 2.1.

2.2.2 Online optimization of pneumatic systems

This category of optimization strategies refers to real-time optimization processes that occur while the system is in operation. These strategies are characterized by being non-invasive, meaning they do not aim to change the architecture of the system already in operation. Within this category, one of the most discussed approaches in the literature is condition monitoring

Condition monitoring of pneumatic drives has become a growing field of interest. With the emergence of Industry 4.0, the Internet of Things (IoT), and big data analysis, researchers and companies are investing significant efforts in developing smart devices and platforms, such as FESTO's 'Automation Experience,' Camozzi's 'CoilVision,' and Emerson-Aventics' 'Smart Pneumatics Analyzer.' These systems have built-in capabilities to monitor their 'health' status and consumption trends.

Although research on condition monitoring of pneumatic systems has been conducted over the past 20 years, most approaches have focused on identifying wear and predicting faulty system operations. In Karpenko and Sepehri (2002), for instance, an Artificial Neural Network (ANN) was used to identify three different faults in a pneumatic process valve. The inputs for the ANN were obtained by 8 signals read from the valve's controller and the trained network was capable to identify which fault was occurring and also its magnitude with an error lower than 5%. A similar approach was used by Subbaraj and Kannapiran (2010), where an ANN was applied to detect 19 different faults in a pneumatic actuator of a process valve. By using sensor data from the valve, the ANN was capable of correctly detecting nearly 100% of the actuator faults.

Air leakage detection has also been a field of interest related to pneumatic monitoring. Sun *et al.* (2021) applied a Convolutional Neural Network to detect four different levels of leakages in a pneumatic actuator used to control the opening and closing of a train door. Metrics based on the distance and correlation between two volumetric flow rate time series are used in Kosturkov; Nachev and Titova (2021) to identify and classify leakages of a pneumatic circuit composed of directional valves, flow control valves, and a linear actuator.

In Nakutis and Kaškonas (2008), the authors developed linear and nonlinear metrics based on the pattern profile of the flowrate consumed by a linear pneumatic actuator. These metrics were used as inputs for machine learning techniques, such as Support Vector Machine (SVM) and ANN, to identify leakages on the actuation system. In addition to the commonly used pressure and flow rate data, Wang *et al.* (2023) utilized exergy data to detect faults in pneumatic systems using machine learning models such as ANN and SVM. They successfully identified failures, including internal and external leakages, with accuracies ranging from 83% to 100%.

Boyko and Weber (2024a) developed a strategy based solely on displacement time to detect abnormal operation in pneumatic drives. They created three decision trees, each applicable to meter-out and meter-in throttles as well as oversized cylinders. Using the time-based rules, it was possible to identify failures such as internal and external leakages and increased friction.

Focusing on reducing air consumption by monitoring the actual loading conditions, Dudić *et al.* (2021) developed a prototype of an automatic pressure regulator, adjusting the

supply pressure based on the ongoing task. A reference pressure was previously determined according to the weight of the workpieces, thus requiring its previous assessment and identification. The module PCC Blue from Mader (Mader, 2017) aims to identify the cylinder load and automatically adjust the supply pressure to reduce air consumption. However, it is applicable only for cylinder sizes Ø50 upwards, has limited functionality on vertical applications, and currently offers no control adjustment to the user.

Another approach to optimizing pneumatic actuation systems is trajectory optimization for pneumatic manipulators. The goal of such approaches is to develop energy-optimal tracking trajectories. For example, in Wang and Gordon (2012), a sine wave-shaped piston velocity profile demonstrated a 3-7% improvement in energy efficiency compared to trapezoidal velocity profiles.

2.2.3 Optimization of system parameters and components

Optimizing component design involves improving valve geometry to reduce pressure drops and enhancing the tribological properties of materials and surfaces to minimize cylinder friction. Studies on novel friction seals, such as those by Raparelli; Mazza and Trivella (2012) and Belforte; Conte and Mazza (2014), have aimed to reduce friction between the piston and cylinder sleeve while maintaining acceptable levels of air leakage and seal wear. Many manufacturers offer low-friction variants in their cylinder portfolios, including the 63L series from Camozzi, the DSBC_L series from FESTO, and the C96Y series from SMC.

Applications where directional valves are located far from the cylinder often involve significant dead volumes. These volumes must be filled and emptied during each stroke of the cylinder, resulting in wasted compressed air. To minimize dead volumes between the directional valve and the cylinder, the valve can be repositioned closer to the cylinder, using, for instance, integrated cylinder-valve modules (FESTO, 2024c; Norgren, 2024; SMC, 2024a), or the tube diameter can be reduced. However, excessively reducing the tube diameter may significantly increase flow resistance, negatively affecting system dynamics (Festo *et al.*, 2012).

Since compressed air consumption depends on pressure levels and the volume of the cylinder chambers, correctly sizing pneumatic drives is a key point for designing an efficient actuation system. In studies presented by Rakova and Weber (2016), Raisch and Sawodny (2019a), and Vigolo and De Negri (2021), the positive impacts of well-sized drives are highlighted, showing significant gains in energy efficiency and dynamic performance. Several approaches have been developed to improve the selection of pneumatic drives. Given its

importance to this thesis, the available pneumatic sizing methods will be presented in Section 2.3.

2.3 SIZING OF PNEUMATIC ACTUATION SYSTEMS

According to De Negri (2001), the main task in sizing an actuation system is the selection of the directional valve and the pneumatic actuator. Additionally, other components of the actuation system, such as throttle valves, hoses, and the supply pressure, must also be properly sized.

The sizing of pneumatic actuation systems is carried out to ensure that the system meets the application requirements, which typically involve performing displacements, holding, or moving objects. The main factors to consider when sizing an actuation system include load force, stroke, and displacement time (Doll; Neumann; Sawodny, 2011; 2015). Additionally, Fialho (2004) emphasizes the importance of characterizing the application, such as determining whether a load is present during displacement. While supply pressure is often assumed to be a fixed design parameter, Šešlija; Dudić and Milenković (2017) discusses optimizing pneumatic systems through proper adjustment of the supply pressure. Similarly, Hepke and Weber (2012; 2013) highlight the potential to reduce compressed air consumption by optimizing supply pressure. Therefore, supply pressure can also be considered an additional parameter to define during the sizing of a pneumatic actuation system.

Regarding the sizing process, the state of the art allows for classifying existing methods into four groups: empirical methods, a method based on natural frequency, an exergy-based method, and methods based on numerical optimization. Each method has distinct characteristics, advantages, and drawbacks. The following sections provide a detailed description of the sizing methods discussed in the literature.

2.3.1 Empirical methods

In the literature, several sizing methods are based on the tacit knowledge acquired by designers over the years and "thumb rules", which aim to manage the uncertainty of the sizing process using safety coefficients that ensure the properly operation of the system. The sizing of the cylinder diameter is traditionally conducted based on the force produced by the piston due to the pressure applied on the driving chamber. As an example of this approach, Fialho (2004) uses the following equation to determine the cylinder diameter (d_c)

$$d_c = 2\sqrt{\frac{F_L}{\pi(p_s - p_0)\eta}},$$
(2.1)

where F_L represents the load force, and the manometric pressure originally presented by the author has been transcribed in this work as the difference between the absolute supply pressure (p_s^{-1}) and ambient pressure (p_0) . A yield coefficient (η) , ranging from 0.67 to 0.8, is adopted by the author based on application characteristics, such as the presence or absence of a load during the movement and the displacement velocity. The author also suggests that the commercial diameter should be larger than the diameter calculated using Equation (2.1).

A similar approach is presented by Bimba (2011), where the author suggests a yield coefficient ranging from 0.5 to 0.8, depending on the desired velocity. Bollmann (1997) recommends adopting a yield coefficient between 0.8 and 0.9. Additionally, the author recommends using a lower pressure than the supply pressure to account for pressure drops at the directional valve, estimated at 0.5 bar (De Negri, 2001). Similar methods, based on yield and safety coefficients, are proposed by Meixner and Kobler (1977), Degem Systems (1990), SMC (1997), Barber (1997), Prudente (2000), Harvey (2009), Bimba (2011), and Camozzi (2019a). The infographic in Figure 2.7 summarizes the range of yield coefficients adopted by each author.

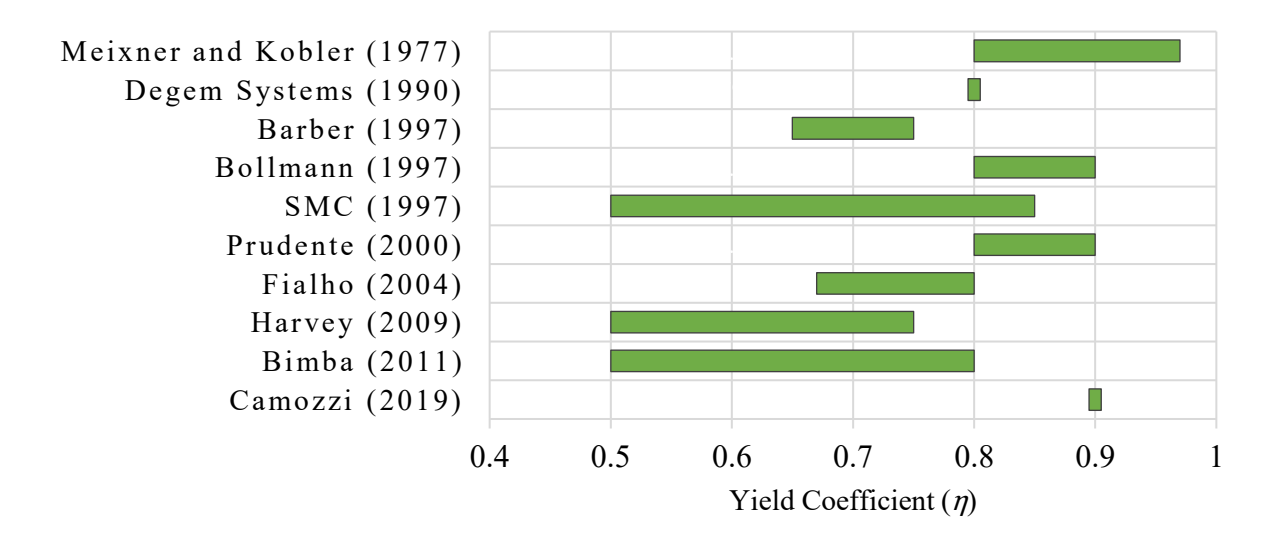


Figure 2.7 – Comparison of yield factor ranges by authors

Source: Compiled from data provided by the respective authors.

¹ All pressures and temperatures in this thesis are absolute unless stated otherwise.

The sizing of pneumatic cylinders using Equation (2.1) is practical, as the cylinder diameter can be determined through a simple and straightforward equation. However, Equation (2.1) is derived from the motion equation applied to the cylinder piston at steady state, with the yield coefficient accounting for uncertainties during motion, such as friction forces and pressure variations in the chambers, to ensure proper system operation. Nevertheless, as shown in Doll; Neumann and Sawodny (2011), Rakova and Weber (2016), and Rakova; Hepke and Weber (2016), the use of empirical methods often leads to oversized actuators, which directly increase the system's air consumption. This aspect will be further analyzed in Section 7.1, where the impact of different yield coefficients will be explored.

Regarding pneumatic valves, the main parameter to be dimensioned is their flow capacity, which must be enough to meet the displacement time and velocity requirements. The flow capacity of a pneumatic valve is typically defined according to ISO 6358-1 Standard (ISO, 2013), which characterizes the flow of compressed air through orifices using two parameters: the critical pressure ratio (b) and the sonic conductance (C). The model presented by this standard is further discussed in Section 3.1.

Commercial valves are also characterized by the VDI 3290 Standard (VDI, 1962), which, although no longer in effect, is still widely adopted by manufacturers. The parameter defined by this standard is the nominal flow rate (Q_n) , representing the amount of air, per unit of time, that flows through a pneumatic component under specific conditions: an upstream pressure of 7 bar_{abs}, a downstream pressure of 6 bar_{abs}, and a temperature of 20°C.

In North America, the characterization of pneumatic components is typically performed using a flow coefficient (C_V), as defined by the NFPA T3.21.3 Standard (NFPA, 2008). This coefficient represents the amount of water, in gallons per minute, that flows through an orifice with a pressure difference of 1 PSI (gauge) and a temperature of 68°F (20°C). De Negri (2001) and Beater (2007) provide correlations between the ISO 6358, VDI 3290, and NFPA T3.21.3 standards, enabling comparisons of components from different manufacturers.

Similarly to the sizing of pneumatic cylinders, the literature also presents several methods for the sizing of directional valves, usually based on simplistic rules, such as the estimative of the volumetric flow based on the chamber volumes and pressures, as well as the displacement time. For instance, in Camozzi (2019a), the required flow rate (Q_r) of the valve can be determined according to

$$Q_r = \frac{ALp_S}{t_d p_0},\tag{2.2}$$

where the total volume of compressed air consumed during a complete displacement is divided by the desired displacement time (t_d) to calculate the volumetric flow rate. This flow rate is approximated to NTP (Normal Temperature and Pressure) conditions by dividing the supply pressure (p_S) by the atmospheric pressure (p_0) , assuming an isothermal process. In Equation (2.2), A represents the cylinder area, and L represents the cylinder stroke.

As shown by Camozzi (2019a), the nominal flow rate (Q_n) of the selected valve must be greater than the required flow rate (Q_r) . However, no guidelines are provided on how much greater the nominal flow rate should be compared to the required flow rate. Therefore, it can be implied that $Q_n \ge Q_r$.

The C_V model adopted by the NFPA Standard is based on the non-compressible flow equation. Therefore, in addition to considering the volumetric flow, it also accounts for the pressure drop between the directional valve and the actuator. Various authors recommend different values for the pressure drop. For instance, SMC (1997) suggests a maximum pressure drop of 23% of the supply pressure. Beater (2007) describes a "good design practice," where the pressure drop should be around 10% of the upstream pressure. Similar recommendations can also be found in Sullivan (1989) and Bimba (2011). The equation presented by Sullivan (1989) for determining the C_V coefficient has been transcribed into this work with the appropriate SI unit conversions, resulting in the following equation

$$C_V = \frac{ALp_s \ 1.4799 \times 10^7}{t_d p_0 \sqrt{p_2 \Delta p}},\tag{2.3}$$

where p_2 stands for the valve downstream pressure.

The main drawback of equations (2.2) and (2.3) is the assumption of supply pressure at driving chamber, which is valid only moments after the piston reaches the stroke end. To address this limitation, De Negri (2001) employs Equation (2.4), derived from the ISO 6358 Standard (ISO, 2013). This equation calculates the sonic conductance (C) of the directional valve based on the mass flow rate determined from the upstream and downstream pressure differential across the valve. The author recommends a pressure drop of 0.5 bar, a critical pressure ratio (b) of 0.4, and assumes isothermal behavior.

$$C_{DN} = \frac{ALp_2}{t_d p_S p_0 \sqrt{1 - \left(\frac{p_2}{p_S} - b\right)^2}},$$
(2.4)

where the subscript DN refers to the author's name of the method.

In Vigolo; Valdiero and De Negri (2021), it was shown that during the displacement of a pneumatic cylinder, the velocity profile has a high degree of variability, being divided into three distinct phases, as will be shown in Section 5.1. Therefore, the assumption of constant velocity in equations (2.2), (2.3), and (2.4) may result in undersized components unless appropriate safety coefficients are applied. These aspects will be further explored in Section 7.1, where the effectiveness of equations (2.2), (2.3), and (2.4) will be discussed in detail.

2.3.2 Method based on natural frequency

Doll; Neumann and Sawodny (2015) present a novel approach based on the natural frequency to size pneumatic drives. The authors define a coefficient named the "Pneumatic Frequency Ratio - PFR" (Ω), which is calculated as the ratio of the pneumatic dynamics (ω_0) to the dynamics of the task (ω_f). The dynamics of a pneumatic cylinder are related to the compressibility of air, where the pneumatic cylinder is modeled as a spring-mass system, and its natural frequency is determined by

$$\omega_0 = \sqrt{\frac{K}{M}},\tag{2.5}$$

where M is the system mass, and K is the spring stiffness, which depends on the force exerted by the cylinder as a function of its displacement.

Assuming a symmetric cylinder with pressure p equal in both chambers and input and output ports blocked, the minimal spring stiffness, which occurs at half of the cylinder stroke, is given by

$$k = \frac{4\gamma Ap}{I},\tag{2.6}$$

where γ is the specific heat ratio, A is the actuation area, and L is the cylinder stroke (Yin, 2020).

The dynamics of the task are determined by the application-specific frequency, which is associated with the displacement velocity of the cylinder and is given by $\omega_f = 2\pi/t_d$. Therefore, the authors assumed isothermal behavior and that the pressure in the cylinder chambers is equal to the supply pressure, resulting in the following expression for the sizing of pneumatic actuators

$$d_c = \frac{2\Omega}{t_d} \sqrt{\frac{\pi ML}{p_S}}. (2.7)$$

As pointed out in Boyko; Hülsmann and Weber (2021), the main drawback of Equation (2.7) is the absence of an external load force. This implies that a task performing a horizontal displacement is treated the same as a task performing a vertical movement, without accounting, for instance, for the effect of gravity. Therefore, Doll; Neumann and Gauchel (2024) developed an extended version of his approach, expressing the omega parameter as a function of the applied load $\Omega_{ext} = \Omega f(F_L)$ which ranges from $f(F_L) = 1$ (when $F_L = 0$) to $f(F_L) = 0$ when $(F_L = A_A p_S)$. This leads to the following equation

$$d_c = \frac{\Omega_{ext} + \sqrt{\Omega_{ext}^2 + 4\left(\frac{t_d}{\pi}\right)^2 \frac{K_m F_L}{ML}}}{2t_d \sqrt{\frac{p_s}{4\pi ML}}},$$
(2.8)

with K_m being an adjustment factor, which is assumed to be equal to one.

Beyond Equation (2.8), the author also states that the load force (F_L) should not exceed 50% of the cylinder's maximum force, making this a second check to be performed during cylinder selection.

To size the directional valves, the authors estimate the total volume of compressed air consumed during a complete displacement, divided by the desired displacement time, similar to the approaches adopted in equations (2.2) to (2.4). This hypothesis was applied to the equation of the ISO 6358 Standard (ISO, 2013), where the cylinder area is defined by Equation (2.8), resulting in

$$C_{PFR} = \frac{1}{p_0 \, \psi(p_A, p_S, b)} \frac{A_A L}{t_d},\tag{2.9}$$

here, the subscript PFR is added as a reference to the method's name, and the flow function $\psi(p_A, p_S, b)$ is assumed to be invariant and approximately equal to 0.4 (Doll; Neumann; Sawodny, 2015).

It can be seen that Equation (2.8) depends on the pneumatic frequency ratio (Ω). To address this, the authors used dynamic simulation software to optimize more than 750 distinct systems and identify a range of Ω values for optimal sizing. They concluded that well-sized cylinders correspond to Ω between 1.1 and 1.7. Larger Ω values result in oversized cylinders, while smaller values lead to undersized cylinders (Doll; Neumann; Sawodny, 2015). In their

recent study, a value of $\Omega = 1.1$ was adopted as the reference value for sizing pneumatic drives (Doll; Neumann; Gauchel, 2024).

The main goal of the approach presented by Doll; Neumann and Sawodny (2015) and Doll; Neumann and Gauchel (2024) is to define the minimum cylinder area capable of absorbing the kinetic energy of the task. While the method proposed by the authors is original and coherent, it still has some drawbacks. The ability to absorb kinetic energy is a characteristic of each actuator and is not solely dependent on cylinder diameter and supply pressure. The total volume of the pneumatic end-position cushions is one of the key parameters defining the damping capacity of pneumatic cylinders (Nazarov; Weber, 2022b). Moreover, each manufacturer has its own cylinder designs. Even within the same manufacturer, different models may have different end-position cushioning capacities, such as adjustable cushioning, self-adjusting cushioning, and mechanical/elastic cushioning versions of the same cylinder series (see, for instance, the 63 Series from Camozzi and the DSBC Series from Festo). The simulations performed by Doll; Neumann and Sawodny (2015) were based on a software developed by Festo, which may suggest that the optimal range of Ω defined by the authors might only be suitable to Festo cylinders.

Moreover, some high-inertia applications may not have the moving mass attached to the piston rod or may use external cushioning. In such cases, the proposed methods may result in oversized cylinders, as the main constraint will no longer be the cylinder's end-cushion damping capacity. These aspects will be further explored in Section 7.1, where the PFR method is compared with other methods in the literature.

2.3.3 Exergy based method

The application of exergy as a mean to determine the useful energy provided to a given pneumatic actuation system is a widely used strategy for assessing the energy efficiency of these systems. In this context, Rakova and Weber (2016) present a sizing method for pneumatic actuators based on exergy analysis. For this purpose, the authors introduce a sizing factor (*SF*), which depends on the ratio between the exergy lost in the actuator and the energy required for the task. According to the authors, the lost exergy corresponds to friction and damping losses, while the task energy consists of potential and kinetic energy. The authors perform an exergy balance between chambers A and B of a pneumatic actuator, corrected by the sizing factor. Based on these considerations, they developed the following expressions to size pneumatic cylinders for horizontal and vertical tasks that are, respectively:

$$d_{c} = \frac{1}{t_{d}} \sqrt{\frac{2 M L SF}{\pi \gamma (p_{3} - p_{4}) ln(\frac{p_{3}}{p_{4}})'}}$$
(2.10)

and

$$d_{c} = \frac{1}{t_{d}} \sqrt{\frac{2M(L + 2gt_{d}^{2})SF}{\pi \gamma (p_{3} - p_{4})ln(\frac{p_{3}}{p_{4}})r_{A}'}}$$
(2.11)

where r_A is the ratio of area B to area A, and the subscripts 3 and 4 refer to the pressures in chambers A and B, respectively.

The sizing factor (*SF*) was determined using dynamic simulation across a wide range of configurations involving different extending velocities and loads. The authors identified the minimum supply pressure required to maintain the desired movement profile. In this way, the *SF* value can be obtained from charts based on the movement type (horizontal or vertical), the mass being moved, and the velocity. Rakova; Hepke and Weber (2016) and Rakova and Weber (2016) demonstrated that using this approach could reduce energy consumption by up to 50% compared to empirical methods, such as those presented in Section 2.3.1.

However, the method presented by the authors has drawbacks. For instance, it requires the designer to define the pressures in chambers A and B, which introduces a wide margin for error since these pressures are not easily determined. Additionally, the need to graphically determine the sizing factor poses a challenge, as it makes the process non-deterministic.

2.3.4 Methods based in numeric optimization

In an optimization strategy, the dynamic model of the pneumatic actuation system is iteratively applied to predict the system's dynamic behavior based on parameters defined by the optimization process. This process typically involves an objective function aimed at minimizing compressed air consumption during a predefined operation cycle, such as the extension and retraction of the piston. Constraints are applied based on design requirements, such as load force, displacement time, and impact velocity. The main parameters to be optimized include the supply pressure, the cylinder diameter, and the sonic conductance of the directional valve (Harris; Nolan; O'Donnell, 2014). Generally, an optimization algorithm seeks the set of parameters that minimizes the objective function. Assuming the model used by the optimization strategy accurately represents the system's behavior, it is possible to identify the set of

parameters that satisfies the design requirements while minimizing compressed air consumption.

Different optimization algorithms are used for the sizing of pneumatic actuation systems, including genetic algorithms (Harris; Nolan; O'Donnell, 2014) and pattern search algorithms (Hepke; Weber, 2013). Genetic algorithms are known for their ability to track the best results obtained during the optimization process, while pattern search algorithms are recommended for problems with fewer parameters. However, Raisch and Sawodny (2019a) argue that these methods require excessive evaluations of the objective function, leading to high computational time, especially for genetic algorithms. To address this issue, the authors propose a gradient-based algorithm with a set of discrete parameters, such as cylinder diameter, supply pressure, and sonic conductance. This approach significantly reduces computation time while maintaining results comparable to other strategies.

The main drawback of numerical optimization strategies is their dependence on theoretical knowledge and computational tools for implementation and use. This demands a highly skilled professional with expertise in programming, simulation, and pneumatic system design. Furthermore, these optimization strategies do not provide a deterministic perspective on design choices, making it challenging to understand the impact of specific design decisions on system behavior.

2.4 POWER, ENERGY AND EXERGY OF PNEUMATIC SYSTEMS

In each optimization strategy described in Section 2.2, the goal is to achieve an improvement compared to a conventional system, similar to those presented in Section 2.1. To quantify this improvement, some authors assess the reduction in compressed air consumption (Doll; Neumann; Sawodny, 2015; Raisch; Sawodny, 2019a; Shen; Goldfarb, 2007), while others present results in terms of the energy efficiency of the pneumatic actuation system (Harris; O'Donnell; Whelan, 2012; Merkelbach; Murrenhoff, 2015; Rakova; Weber, 2016; Wang *et al.*, 2016; Yang *et al.*, 2017). Determining energy efficiency requires calculating the energy supplied to the system during an operating cycle. Therefore, this section aims to clarify aspects related to the thermodynamics of compressible flow, describe the procedure used to calculate energy efficiency, and explain why it differs from the procedure commonly applied in hydraulic systems.

According to Shames (1973), the first law of thermodynamics, when applied to a generic control volume with fluid inflow and outflow, heat (Q) and shaft work (W_e) exchange with the environment, can be expressed as:

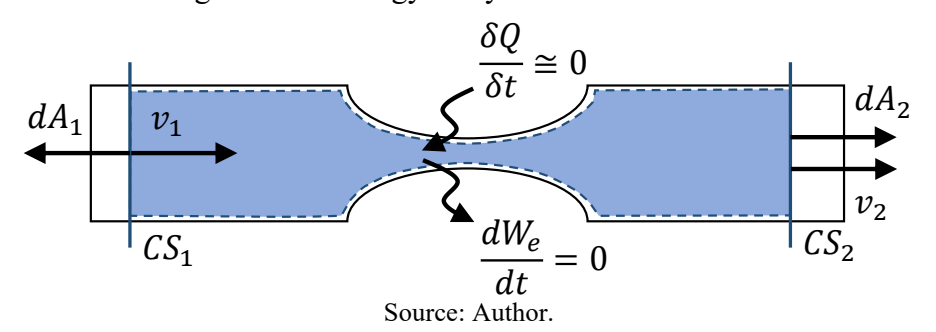
$$\frac{\delta Q}{\delta t} - \frac{dW_e}{dt} = \iint_{CS} \left(\frac{v^2}{2} + gy + u + pv \right) \left(\rho \vec{v} \cdot d\vec{A} \right) + \frac{\partial}{\partial t} \iiint_{CV} \left(\frac{v^2}{2} + gy + u \right) (\rho dV), \tag{2.12}$$

where ρ is the fluid density, u the specific internal energy, p the pressure, v the specific volume, v is the flow velocity, g the gravitational acceleration, and y the vertical height. The term pv represents the flow work per unit of mass. Furthermore, CS and CV indicate the control surface and control volume, respectively. $d\vec{A}$ is the outward-oriented area vector, \vec{v} the velocity vector, and V volume of the control volume.

Two aspects can be analyzed regarding the compressible flow in pneumatic systems: the temperature change across throttle valves and the pneumatic flow power.

To begin this analysis, Equation (2.12) is applied to the control volume of the throttle valve shown in Figure 2.8. In this case, the flow can be considered steady-state, since no energy is stored within the control volume and, consequently, no time variation of energy occurs.

Figure 2.8 – Energy analysis of a throttle valve



Assuming that the flow across a throttle valve does not have sufficient time or surface area for significant heat transfer to occur, the process can be assumed adiabatic. Also, no shaft work is produced by the throttle valve. Considering uniform flow at the control surfaces, Equation (2.12) simplifies to

$$0 = -\left(\frac{v_1^2}{2} + gy_1 + u_1 + p_1v_1\right)(\rho v_1 A_1) + \left(\frac{v_2^2}{2} + gy_2 + u_2 + p_2v_2\right)(\rho v_2 A_2)$$
(2.13)

The negative sign associated with the inlet control surface (CS_1) is due to the scalar product between the velocity vector and the outward-oriented area vector $(\vec{v} \cdot d\vec{A})$. The kinetic energy term $(v^2/2)$ and the potential energy term (gz) are often neglected, as they are typically

small compared to the internal energy (u) and the flow work (pv). By introducing the definition of enthalpy, h = pv + u, and considering the mass conservation principle, equation (2.13) can be rewritten as:

$$\Delta h = h_2 - h_1 = (u_2 + p_2 v_2) - (u_1 + p_1 v_1) = 0 \tag{2.14}$$

Therefore, the conservation of energy in a steady throttling process reduces to an isenthalpic process. For ideal gases, enthalpy depends only on temperature. Consequently, the temperature of an ideal gas remains constant across a throttle valve. However, for real gases, the fluid's temperature may either decrease or increase depending on the Joule-Thomson coefficient (Çengel; Boles, 2014). The validity of this assumption was experimentally investigated, and the results are presented in Appendix C.

Regarding the pneumatic flow power at the control surface, the first term on the right-hand side of Equation (2.12) represents the rate of energy transport by a flowing fluid. Under the aforementioned assumptions, this specific energy transport is equivalent to the enthalpy (h). For an ideal gas with constant specific heats, enthalpy is approximated by $h = C_pT$ (Çengel; Boles, 2014). Therefore, the equations for calculating the pneumatic power (P_p) and energy (E_p) are given, respectively, by

$$P_p = q_m C_p T, (2.15)$$

and

$$E_p = \int_0^t q_m C_p T dt. \tag{2.16}$$

Equation (2.15) represents the total energy rate of a flowing fluid. However, Cai; Kagawa and Kawashima (2002) and Gauchel; Hülsmann and Müller (2022) argue that enthalpy is not suitable for calculating pneumatic power because it does not capture the fluid's capacity to perform work in pressure-dominant systems. For example, in an ideal isothermal compressor, the enthalpy of the exiting fluid equals that of the entering fluid, as the heat generated during compression is dissipated to maintain constant temperature. However, the compressed air clearly has a greater capacity to do work than the ambient air at the inlet. This demonstrates that enthalpy is not suitable for describing the power of pneumatic systems.

In face of the limitations of Equation (2.15) in determining the power of pneumatic systems, Cai; Kagawa and Kawashima (2002) and Gauchel; Hülsmann and Müller (2022) present an analysis based on the isothermal change of state of compressed air and the work

transfer with the environment. The authors divide pneumatic work into two components: transmission work and expansion work.

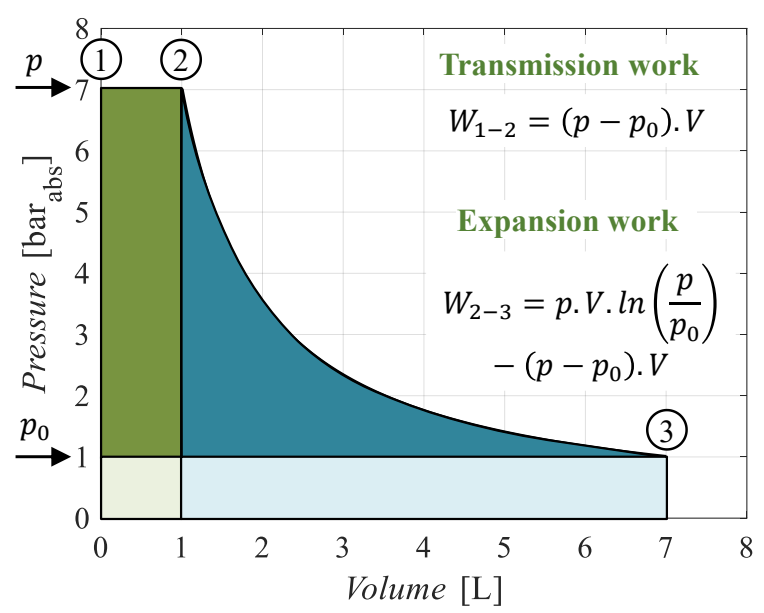


Figure 2.9 – Components of compressed air work

Source: Author's elaboration based on Cai; Kagawa and Kawashima (2002), and Gauchel; Hülsmann and Müller (2022).

The transmission work refers to the energy required to displace a portion of compressed air at constant pressure. On the other hand, the expansion work represents the fluid's ability to perform work during its expansion until it reaches atmospheric pressure. The dark green and blue areas in Figure 2.9 illustrate the useful parcels of transmission and expansion work, corresponding to pressures above atmospheric pressure (p_0) . Based on this analogy, the useful pneumatic work for an isothermal process is given by

$$W_p = W_{1-2} + W_{2-3} = pV ln\left(\frac{p}{p_0}\right). \tag{2.17}$$

Considering the analysis presented above, Cai; Kagawa and Kawashima (2002) argue that Equation (2.17) should represent the energy of pneumatic power. To generalize this conclusion, the authors utilize the concept of exergy to describe the capacity to extract useful work from the compressed air supplied to a pneumatic system. Exergy evaluates usable energy by considering both the total energy (enthalpy) and the energy irreversibly lost due to entropy generation during pneumatic processes, which cannot be converted into useful work.

In Vigolo (2018), the mathematical derivation of the exergy model for a flow stream is presented, based on the concepts introduced by Çengel and Boles (2014) to describe the

useful energy that can be extracted from closed and open systems. Neglecting kinetic and potential effects, the exergy of a fluid stream (X_f) is given by

$$X_f = \int_0^t q_m c_p (T - T_0) dt - \int_0^t q_m T_0 \left(C_p ln \left(\frac{T}{T_0} \right) - R ln \left(\frac{p}{p_0} \right) \right) dt, \tag{2.18}$$

where T is the temperature of the fluid, and R is the ideal gas constant. The subscript 0 denotes the equilibrium conditions with the environment, representing the state where no useful work can be extracted from the fluid.

From Equation (2.18), it can be observed that when the fluid is at ambient temperature, the resulting exergy rate (and consequently the pneumatic power) is

$$P_p = \dot{X}_f = pq_V ln\left(\frac{p}{p_0}\right), \tag{2.19}$$

where q_V is the volumetric flow rate, given at the fluid's stream pressure and ambient temperature.

As can be seen, Equation (2.19) resembles the total pneumatic work expressed in Equation (2.17) and is widely used to determine the air power of compressed air systems, rather than Equation (2.15) (Harris; Nolan; O'Donnell, 2014; Harris; O'Donnell; Whelan, 2012; Shi *et al.*, 2019; Yang *et al.*, 2017).

However, Equation (2.19) is a particular case of the exergy model provided by Equation (2.18). Equation (2.18) has been broadly applied in numerous studies to assess the efficiency of pneumatic systems (Boyko; Weber, 2020; Hepke; Weber, 2012; Merkelbach; Murrenhoff, 2015; Merkelbach *et al.*, 2016; Rakova; Hepke; Weber, 2016; Rakova; Weber, 2016; Wang *et al.*, 2016). Therefore, aiming for a consistent and general approach, this work employs Equation (2.18) to determine the useful energy supplied to pneumatic actuation systems.

To determine the energy efficiency, it is necessary to determine the required work to perform a given task (W_t) . This work can be calculated based on the kinetic and potential energies, and the forces acting on the system during the displacement, including friction forces (F_{fr}) and any generic external force (F_G) .

$$W_t = \int_0^x Madx + \int_0^y Mg \, dy + \int_0^x F_{fr} \, dx + \int_0^x F_G \, dx, \tag{2.20}$$

$$W_{t} = \int_{0}^{t} Mav(t)dt + \int_{0}^{t} Mgv_{y}(t)dt + \int_{0}^{t} F_{fr}v(t)dt + \int_{0}^{t} F_{G}v(t)dt,$$
 (2.21)

where dx is the differential of the piston position, M is the load mass, g is the gravitational acceleration, dy is the differential of the vertical position, v(t) is the instantaneous velocity of the piston, and $v_v(t)$ is the vertical component of the piston velocity.

Finally, the exergy efficiency of the system (η_{sis}) , henceforth referred to as energy efficiency for convenience, is defined as the ratio of the work required to perform the task to the exergy supplied to the system

$$\eta_{sis} = \frac{W_t}{X_f}. (2.22)$$

In fact, a similar energy analysis can be carried out for hydraulic systems where the fluid is nearly incompressible. Pritchard (2011) demonstrates that, for a steady, incompressible, and frictionless flow, the variation in internal energy from Equation (2.12) cancels with the heat transfer term in the energy balance. In other words, heat transfer only affects the fluid's internal energy (i.e., its temperature), not its mechanical energy ($v^2/2 + gy + pv$). Therefore, internal energy is conventionally excluded from the analysis of hydraulic power and energy consumption.

Considering that pressure energy (pv) is much greater than kinetic (gy) and potential $(v^2/2)$ terms, and applying the same rationale used to deduce Equation (2.15), the hydraulic power (P_H) and energy (E_H) can be expressed, respectively, by

$$P_H = q_V p, (2.23)$$

and

$$E_H = \int_0^t q_V p \ dt. {2.24}$$

These expressions highlight that, in hydraulic systems, the useful power and energy are effectively determined by the pressure and volumetric flow rate, whereas in pneumatic systems, the compressible nature of the fluid requires that its expansion capacity be considered to determine the useful power and energy.

2.5 FINAL CONSIDERATIONS ABOUT CHAPTER 2

As presented in Section 2.1, a pneumatic actuation system is a relatively simple system, typically composed of a set of valves and an actuator. Its robustness and low acquisition cost are also well known, which is why this technology is widely adopted for developing automated equipment. However, concerns related to energy efficiency drive the continuous improvement of pneumatic systems. In Section 2.2, a general overview of research on the optimization of these systems was presented, highlighting developments in energy-saving circuits, pneumatic system monitoring, and the optimization of system parameters.

Even though the optimization strategies presented in Section 2.2 present great potential for reducing energy consumption, it is notable that they require additional components and complex control algorithms, which reduces their attractiveness for industrial applications. As a result, conventional actuation systems are often preferred, without a proper assessment of their energy efficiency.

In this context, sizing optimization and operating condition optimization play a fundamental role in increasing the energy efficiency of pneumatic systems, since there is no need to invest in components and to change the classical control technique. However, the sizing procedure is often underestimated and carried out using simplistic models, such as those presented in Section 2.3.1, which rely on yield coefficients to ensure proper system operation. Additionally, the system is rarely assessed during operation to correct potential load estimation errors. As a result, pneumatic systems are often oversized, significantly reducing their energy efficiency.

As discussed in this chapter, several manufacturers provide computer programs for sizing pneumatic drives. However, in such cases, designers become dependent on these technologies and third-party expertise for the design of pneumatic systems. Moreover, they are susceptible to the unintentional use of the approaches presented in Section 2.3.1, as they have no insight into the procedures adopted by the software developers.

These aspects highlight the importance of the sizing process for pneumatic systems and reveal a gap in their design and setup. Effectively balancing air consumption with robust operation, without prior experimental assessment of the actuation system or its application, represents the primary challenge addressed in this doctoral research, which will be presented in detail in the following sections.

3 SYSTEM MODELING

This chapter presents the development, validation, and analysis of a dynamic simulation model for a pneumatic actuation system. This model has been widely used throughout the thesis to understand dynamic phenomena and perform statistical analyses of pneumatic drives. For readers familiar with the modeling of pneumatic drives, reading this chapter is optional, as the simulation model has been used mainly as a tool for developing the proposed design and setup framework, and is not an integral part of it.

In the field of fluid power, a common approach to simulating system components is based on the theory of lumped parameters, which assumes that pressure and temperature are evenly distributed within a control volume, with volumes connected by resistors (Oshtorjani; Mikkola; Jalali, 2018). According to this theory, the system is divided into two groups of components: volumes and resistances. In the pneumatic domain, the first group includes reservoirs, hoses, and actuators, while the second group encompasses pneumatic throttles, such as directional valves and flow control valves.

In this chapter, a lumped parameter simulation model is developed, focusing on a system comprising a double-acting cylinder, a set of throttle valves, and a directional valve. The derivation of the system's governing equations is presented, along with experimental validation. Additionally, the model explores key characteristics such as heat transfer, friction forces, and flow through pneumatic restrictions, providing insights into the trade-offs between model complexity and accuracy.

The results indicate that while modeling these phenomena in greater detail provides a deeper understanding of system dynamics, simpler models can achieve comparable accuracy with reduced modeling complexity and parameterization time, supporting the use of simplified models for efficient system analysis without significant loss of precision.

3.1 PNEUMATIC VALVES AND RESTRICTIVE ELEMENTS

The modeling of compressed air flow through an orifice can be approached in several ways. Pritchard (2011) and Andersen (1967), for instance, presents a mathematical derivation based on the mass conservation and momentum conservation equations, where the total pressure of the fluid is defined as the isentropic stagnation pressure (See Appendix D). Beater (2007) and Ohligschläger (1990) use the first law of thermodynamics. In both approaches, the authors assume isentropic flow through a well-rounded nozzle from a large reservoir with

constant pressure and negligible velocity. This results in an equation to determine the fluid velocity at each section of the nozzle, which is then applied to the continuity equation to calculate the mass flow rate through a given orifice, resulting in

$$q_{m} = A_{0} p_{1} \sqrt{\frac{2}{RT_{1}}} \sqrt{\frac{\gamma}{\gamma - 1}} \sqrt{\left(\frac{p_{2}}{p_{1}}\right)^{2/\gamma} - \left(\frac{p_{2}}{p_{1}}\right)^{(\gamma + 1)/\gamma}}$$
(3.1)

where A_0 is the orifice area, γ is the specific heat ratio and the subscripts 1 and 2 are the upstream and downstream pressures, respectively.

According to Beater (2007), the challenges in determining the parameters of Equation (3.1) motivated the search for approximations to describe the mass flow rate in pneumatic components. In Sanville (1971), a model based on the equation of an ellipse was proposed. This model, a generalization of Purdue's work (1969 apud Beater, 2007, p. 41), became a provisional CETOP standard recommendation in 1973 and was adopted as the ISO 6358 standard in 1989 (ISO, 1989).

The ISO 6358 standard characterizes the flow capacity of pneumatic orifices using two parameters: the sonic conductance (C), which defines the maximum flow capacity of the valve, and the critical pressure ratio (b), which defines the condition at which air velocity reaches sonic speed. The model also distinguishes between subsonic flow and sonic (choked) flow, as shown in Figure 3.1-a).

$$q_{m} = \begin{cases} 0 & \text{for } 1 - \frac{\Delta p_{c}}{p_{1}} < \frac{p_{2}}{p_{1}} \leq 1 \\ Cp_{1}\rho_{0}\sqrt{\frac{T_{0}}{T_{1}}} \left\{ 1 - \left(\frac{\frac{p_{2}}{p_{1}} - b}{1 - \frac{\Delta p_{c}}{p_{1}} - b}\right)^{2} \right\}^{q} & \text{for } b < \frac{p_{2}}{p_{1}} \leq 1 - \frac{\Delta p_{c}}{p_{1}} \\ Cp_{1}\rho_{0}\sqrt{\frac{T_{0}}{T_{1}}} & \text{for } \frac{p_{2}}{p_{1}} \leq b \end{cases}$$

$$(3.2)$$

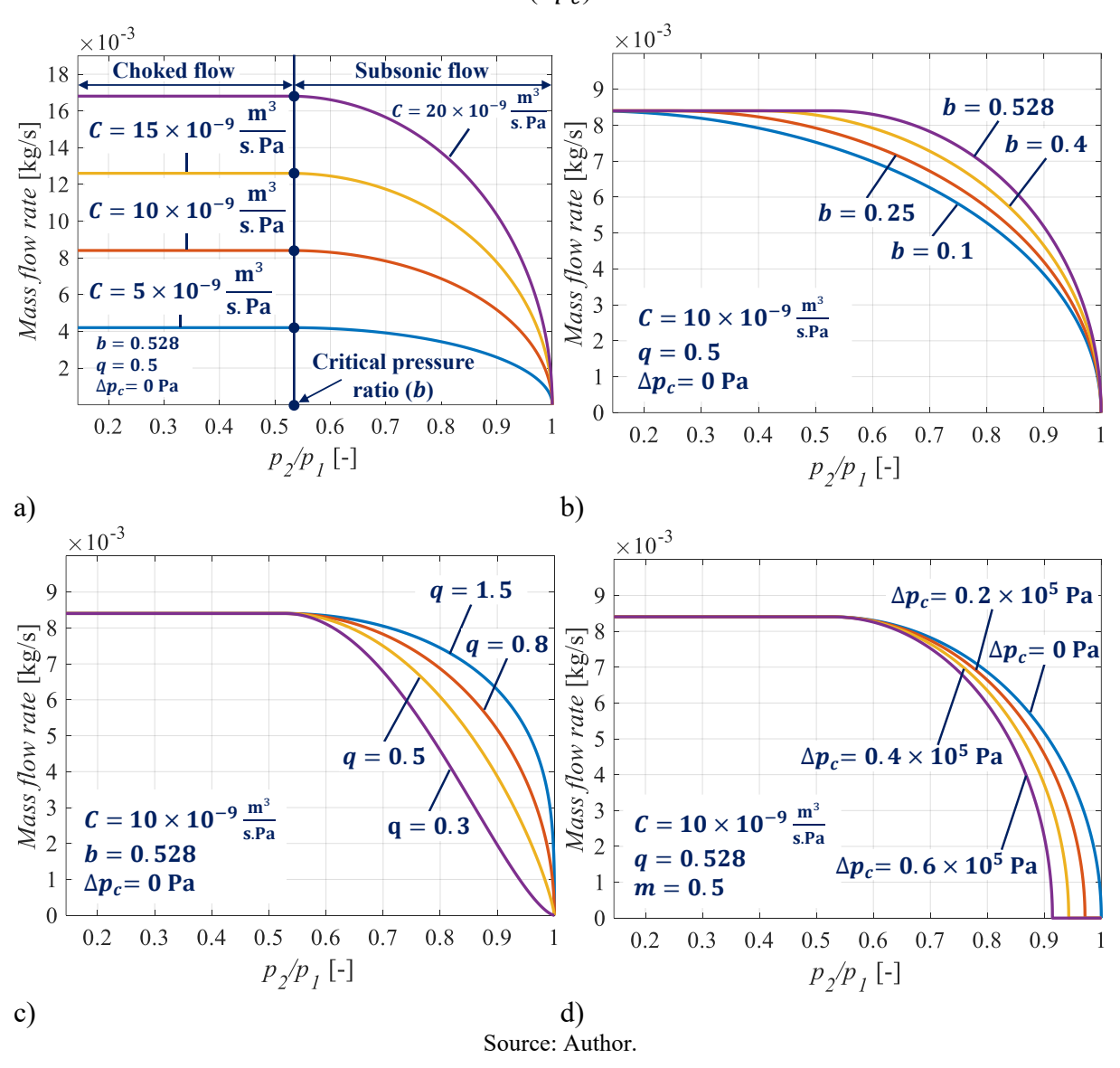
where the subscripts 1 and 2 represent the upstream and downstream pressures, respectively, while subscript 0 denotes the reference atmospheric conditions. q is defined as the subsonic index and Δp_c is the cracking pressure.

The subsonic index and the cracking pressure were introduced in the most recent update to the ISO 6358 standard (ISO, 2013). The subsonic index (q) is typically close to 0.5 for components with a fixed flow path but can be adjusted to better fit experimental data for

other components. The cracking pressure (Δp_c) represents the pressure differential required to start the flow process (e.g., in a check valve).

In Figure 3.1, the impact of the four parameters of the ISO 6358 mass flow rate model is exemplified.

Figure 3.1 – Impact of parameters on the ISO 6358 mass flow rate model: a) Sonic conductance (C), b) Critical pressure ratio (b), c) Subsonic index (q), d) Cracking pressure (Δp_c)



The mass flow rate, driven by the propagation of pressure waves, reaches the condition of choked flow when the flow velocity reaches the speed of sound, which occurs when the pressure ratio equals the critical pressure ratio. Under these conditions, further reducing the downstream pressure does not increase the mass flow rate, as pressure waves cannot propagate faster than the speed of sound. Therefore, during choked flow, the mass flow rate becomes

independent of the downstream pressure. It is important to note that in components with specific geometries, such as Laval nozzles, supersonic flow can occur. However, this is not the case for typical pneumatic components (Beater, 2007).

The critical pressure ratio for pneumatic components typically ranges between 0.2 and 0.528 (Hildebrandt *et al.*, 2005; Krichel; Sawodny; Hildebrandt, 2010). The parameters that characterize the mass flow rate of a pneumatic valve depend on the geometry of its internal components and the valve's operating mechanism. These parameters are determined following the procedures established by the ISO 6358 standard (ISO, 2013).

3.2 CYLINDERS

The behavior of a pneumatic cylinder involves modeling a gas chamber with variable boundaries and in/out mass flow rates. According to Sorli and Gastaldi (2009), the mathematical modeling of a pneumatic cylinder requires evaluating the displacement and velocity of the piston, the mass flow rate of air, and the pressures and temperatures in the cylinder chambers. Therefore, each variable requires a mathematical model for proper representation, which will be addressed in the following sections.

3.2.1 Pressure dynamics

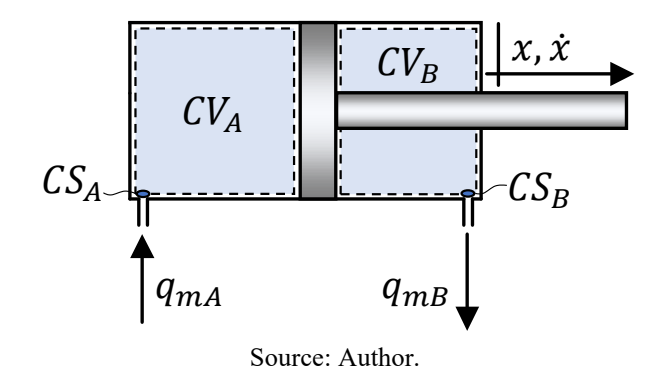
The pressure behavior of a pneumatic actuator is described by the continuity equation applied to a control volume, which states that the 'net flow of mass through a control surface is equal to the change of mass within the control volume' (Von Linsingen, 2016). For a generic control volume, the continuity equation is given by

$$\int_{CS} \rho \overrightarrow{v} \cdot d\overrightarrow{A} + \frac{\partial}{\partial t} \int_{CV} \rho dV = 0, \tag{3.3}$$

where *CS* stands for control surface, *CV* stands for control volume, ρ is the fluid specific mass, \vec{v} is the velocity vector, $d\vec{A}$ is the outward-oriented area vector, t is time, and V is the volume of the control volume.

Figure 3.2 illustrates the control volumes and control surfaces of chambers A and B of a differential pneumatic linear cylinder, which are used to apply the continuity equation and derive the pressure dynamics of the system.

Figure 3.2 – Control volumes of a pneumatic actuator



Applying Equation (3.3) to the control volumes in Figure 3.2 and assuming no internal or external leakages, with the specific mass evenly distributed throughout the control volume, leads to:

$$-q_{mA} + \frac{\partial}{\partial t}(\rho_A.V_A) = 0, \tag{3.4}$$

and

$$q_{mB} + \frac{\partial}{\partial t}(\rho_B.V_B) = 0. ag{3.5}$$

Taking the product derivative of equations (3.4) and (3.5) results in

$$-q_{mA} + \frac{d\rho_A}{dt}V_A + \frac{dV_A}{dt}\rho_A = 0, \tag{3.6}$$

and

$$q_{mB} + \frac{d\rho_B}{dt}V_B + \frac{dV_B}{dt}\rho_B = 0. ag{3.7}$$

The time derivative of the specific mass can be obtained by differentiating the ideal gas law (pV = mRT), leading to

$$\frac{d\rho}{dt} = \frac{dp}{dt}\frac{1}{RT} - \frac{p}{RT^2}\frac{dT}{dt}.$$
(3.8)

Combining Equation (3.8) with equations (3.6) and (3.7) results in the mathematical expressions used to model the pressure dynamics of chambers A and B of a pneumatic actuator, given, respectively, by

$$\frac{dp_A}{dt} = \frac{p_A}{T_A} \frac{dT_A}{dt} + \frac{1}{V_{A,0} + A_A x} \left(q_{mA} T_A R - p_A A_A \frac{dx}{dt} \right), \tag{3.9}$$

$$\frac{dp_B}{dt} = \frac{p_B}{T_B} \frac{dT_B}{dt} + \frac{1}{V_{B,0} + (L - x)A_B} \left(p_B A_B \frac{dx}{dt} - q_{mB} T_B R \right), \tag{3.10}$$

where V_{A_0} and V_{B_0} are the dead volumes of chambers A and B, respectively, L is the cylinder stroke, and x is the piston position. The temperature rate change terms (dT_A and dT_B) are obtained from equations (3.13) and (3.14), respectively, which are discussed in Section 3.2.2.

3.2.2 Temperature dynamics

A pneumatic chamber has the thermodynamic behavior of an accumulator. Various authors have analyzed its temperature behavior using different thermodynamic processes: polytropic (Doll; Neumann; Sawodny, 2011; Hildebrandt *et al.*, 2005; Jimenez; Reinertz; Schmitz, 2024; Raisch; Sawodny, 2019a), isothermal (Nouri *et al.*, 2000; Virvalo, 1993), or isentropic (Endler; De Negri; Castelan, 2015; Locateli, 2011; Mendonza, 2006; Oliveira, 2009). According to Nazarov and Weber (2022a), the complexity of the thermodynamic model depends on the application being simulated. The authors state that for simple air consumption calculations, an isothermal approach is sufficient. However, for energy-saving strategies, servo-pneumatic applications, or frequently operated drives, thermal processes should not be neglected.

A more accurate alternative for describing the thermal behavior of a pneumatic actuator involves using the energy equation introduced in Chapter 2. The energy equation applied to a generic control volume with inflow and outflow is given by Equation (2.12). Applying this model for a pneumatic cylinder enables modeling the heat exchange between the cylinder and the environment during the expansion and compression processes of the pneumatic chambers, resulting in the dynamic behavior of the air temperature.

Analyzing the control volume of chamber A in Figure 3.2 during an extending displacement, the following assumptions are made:

- a) Kinetic and potential energies are neglected due to their relatively small values compared to internal energy and enthalpy (Beater, 2007);
- b) The only shaft work is performed by the piston rod;
- c) The specific mass is uniformly distributed across the control surface and volume.

Based on these assumptions, Equation (2.12) can be written as:

$$\frac{\delta Q}{\delta t} - p_A A_A \frac{dx}{dt} = -h q_{mA} + \frac{du}{dt} m_A + \frac{dm_A}{dt} u, \tag{3.11}$$

where m_A represents the quantity of mass inside the control volume at a given instant.

Considering the correlation between enthalpy and temperature at the control surface, which can be approximated by $h = C_p T_{CS}$, and internal energy and temperature, approximated by $u = C_V T$, and assuming no internal or external leakages (such that $dm_A/dt = q_{mA}$), Equation (3.11) can be written as:

$$\frac{\delta Q}{\delta t} - p_A A_A \frac{dx}{dt} = -C_p T_{CS} q_{mA} + \frac{C_v dT_A}{dt} m_A + q_{mA} C_v T_A. \tag{3.12}$$

The rate of temperature change over time is, therefore,

$$\frac{dT_A}{dt} = \frac{\frac{\delta Q_{inn_A}}{\delta t} - p_A A_A \frac{dx}{dt} + C_p T_{CS} q_{mA} - C_v T_A q_{mA}}{C_v m_A}.$$
(3.13)

The subscript *inn* has been added to the heat exchange rate term, which refers to inner convective heat transfer, which is the heat transfer mode taking place at the compressed air inside the cylinder chamber. Further details about the heat transfer modes are given in section 3.2.3.

For chamber B, the modeling follows the same approach. However, it should be noted that during an extending movement, the mass flow rate exits chamber B, and the environment performs work on its control volume. Therefore

$$\frac{dT_B}{dt} = \frac{\delta Q_{inn_B}}{\delta t} + p_B A_B \frac{dx}{dt} - C_p T_{CS} q_{mB} + C_v T_B q_{mB}}{C_v m_B}.$$
(3.14)

In equations (3.13) and (3.14), the temperature at the control surface (T_{CS}) depends on the fluid flow direction. When the fluid exits the chamber, its temperature is equal to the internal chamber temperature. When the fluid enters the chamber, its temperature equals the temperature at the valve's output port connected to the chamber. However, since the throttling process of ideal gases does not change the fluid temperature (Çengel; Boles, 2014), the temperature of the fluid entering the chamber can be assumed equal to the temperature at the valve's input port. This assumption was experimentally investigated, and the results are presented in Appendix C.

The quantity of mass inside the control volumes $(m_A \text{ and } m_B)$ is defined by the initial mass in each chamber $(m_{A_0} \text{ and } m_{B_0})$ and the change in mass. Since internal and external leakages are neglected, it can be stated that

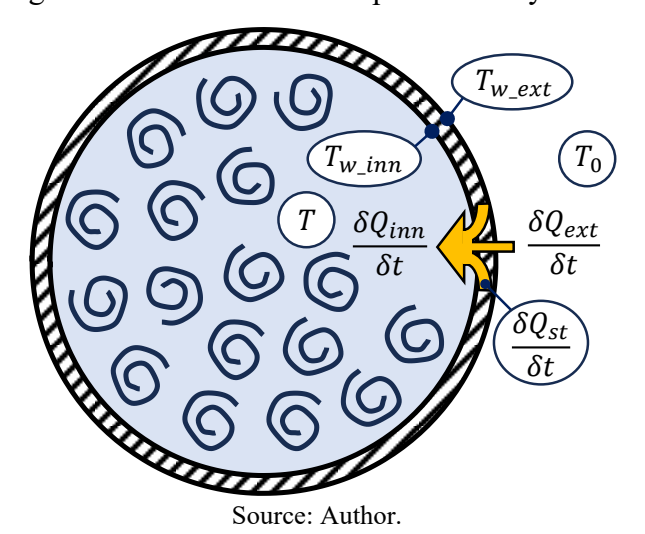
$$m_A(t) = \int q_{mA} dt + m_{A_0}, \tag{3.15}$$

$$m_B(t) = \int -q_{mB}dt + m_{B_0}. {3.16}$$

3.2.3 Heat transfer dynamics

Heat transfer between the environment and the compressed air inside the chambers occurs through three modes: 1) free convection between the external cylinder wall and the environment; 2) thermal conduction and storage within the cylinder walls; and 3) forced and free convection between the compressed air and the inner walls of the cylinder.

Figure 3.3 – Heat transfer in pneumatic cylinders



One approach to model the heat transfer is based on an overall heat transfer coefficient, also known as a thermal transmittance coefficient. In this approach, the Newton's law of cooling is used along with the thermal transmittance, accounting for all three modes of heat transfer, that is

$$\frac{\delta Q}{\delta t} = U A_s (T_0 - T),\tag{3.17}$$

where U is the thermal transmittance, A_s is the heat flow surface area, T_0 is external environment temperature, and T is the fluid temperature inside the chamber.

As can be seen, this approach considers the temperature difference between the external environment (T_0) and the temperature of the fluid inside the chamber (T), since the thermal transmittance encompasses all thermal resistances between the inner fluid and the external environment. It should be noted that when U = 0, the process becomes adiabatic, and when U tends to infinity, the process become isothermal.

Various strategies can be used to calculate the thermal transmittance. Hepke (2016) adopts a temperature-dependent coefficient U = f(T), in which U increases linearly as the fluid temperature deviates from the ambient temperature. Det; Scavarda and Richard (1989) proposed a pressure- and temperature-dependent model U = f(T,p), which is derived from models used for combustion engines (Eichelberg, apud Det et al., 1989). The same model is used by Carneiro and de Almeida (2007), who introduces an experimental method to calculate a reference thermal transmittance. Vigolo (2018) measured the thermal transmittance of a cylinder with a piston diameter of 125 mm, reporting a value of 163.96 W/m²·K. Pasieka (apud Beater, 2007) presents results from measurements of U in different phases of a working cycle, with values ranging from 5 to 460 W/m²·K. The following expression is presented in Hepke (2016) to calculate the thermal transmittance of the cylinder.

$$\frac{1}{UA_{s}} = \frac{1}{\lambda_{inn}A_{s}} + \frac{L_{w}}{k_{w}} + \frac{1}{\lambda_{ext}A_{s}},\tag{3.18}$$

with L_w being the cylinder wall thickness, k_w the cylinder wall thermal conductivity, and λ_{ext} and λ_{inn} are the external and inner convective heat transfer coefficient, respectively.

However, it should be noted that the Equation (3.18) applies only to steady-state heat flow and does not account for heat stored within the cylinder wall (Bergman *et al.*, 2011). As a result, the thermal transmittance is likely dominated by the external convective heat transfer coefficient, which has the highest thermal resistance among the three coefficients. In practice, however, the cylinder wall also acts as a thermal storage, absorbing part of the heat flow.

Another approach to modeling heat transfer in a pneumatic cylinder involves accounting for individual components of heat transfer, including inner and external convection, conduction, and heat storage in the cylinder wall. This approach, which is based on the work of de Giorgi; Bideaux and Sesmat (2006), Ohligschläger (1990), and Nazarov and Weber (2022a), is presented of the following subsections.

According to Newton's law of cooling, the inner convective heat flow is modeled by

$$\frac{\delta Q_{inn}}{\delta t} = \lambda_{inn} A_s (T_{w_inn} - T), \tag{3.19}$$

where T_{w_inn} is the inner wall temperature, T is the fluid temperature inside the chamber, and λ_{inn} is the inner convective heat transfer coefficient.

As it will be presented in Section 3.2.3.2, due to the small wall thickness, the wall temperature is assumed to be uniform, therefore, $T_{w_inn} = T_w$, and T_w is given by Equation (3.35).

The inner heat exchange of a pneumatic chamber with the cylinder wall occurs through two modes of convection: forced and free convection. Forced convection results from high fluid turbulence, such as that caused by compressed air filling and emptying the chambers, as well as the cylinder's displacement. Consequently, forced convection is expected to account for the majority of the inner heat transfer in a pneumatic cylinder. In contrast, free convection is driven by temperature gradients and occurs in low-turbulence flows, typically at low displacement velocities and during temperature stabilization after the chamber is emptied or filled.

Both the forced and free convective heat transfer coefficients can be determined with the Nusselt number, which provides a measure of the convective heat transfer occurring at a surface. It can be calculated for different fluids and geometries under various flow conditions, including free and forced convection (Bergman *et al.*, 2011). The Nusselt number is correlated with the convective heat transfer coefficient for a quasi-static process through the following relationship

$$Nu = \frac{\lambda L_c}{k_c},\tag{3.20}$$

where Nu is the Nusselt number, λ is the convective heat transfer coefficient, L_c is the characteristic length, and k_c is the thermal conductivity of the fluid.

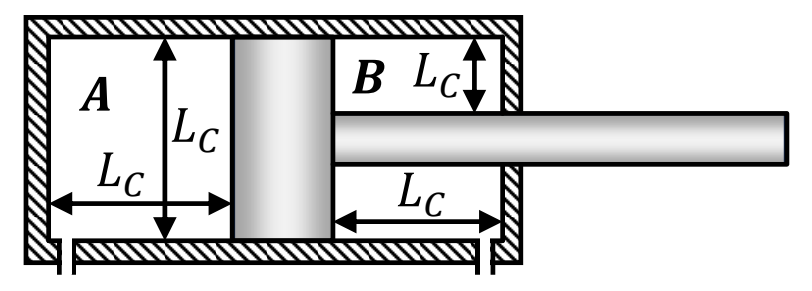
For forced convection, the Nusselt number depends on the flow regime, whether the flow is laminar or turbulent, which is determined by the Reynolds number

$$Re = \frac{\rho v L_c}{\mu},\tag{3.21}$$

here, μ represents the dynamic viscosity of the fluid.

For a pneumatic cylinder, the characteristic length can be determined from the cylinder's geometry. According to Ohligschläger (1990), its value depends on the piston's position and is equal to the smaller of two dimensions: the distance between the cylinder head and the piston, or the cylinder diameter, as shown in Figure 3.4.

Figure 3.4 – Characteristic length of a pneumatic cylinder



Source: Adapated from Ohligschläger (1990).

Determining the fluid velocity inside the cylinder chamber is challenging because the flow is non-uniform, and the control volume's geometry is not fixed. A rough estimation can be obtained using the continuity equation under steady-state conditions, which is the same approach commonly used to model the mass flow rate of compressible fluids through orifices. Thus, the fluid velocity can be expressed as:

$$v = \frac{q_m}{\rho A} \tag{3.22}$$

where A corresponds to the cross-sectional area of either cylinder chamber A or B, and q_m is the mass flow rate entering or exiting the respective chambers.

The thermal conductivity (k_c) and dynamic viscosity (μ) of air depend on the fluid's temperature (T). The following expressions, as used by Ohligschläger (1990), were adopted to determine these properties of air.

$$k_c = (26.5 + (T - 298)0.074) \times 10^{-3},$$
 (3.23)

$$\mu = (18.2 + (T - 298)0.044) \times 10^{-6}.$$
 (3.24)

The Prandtl number (Pr) is a dimensionless parameter required to for calculating the Nusselt number in both forced and free convection. According to Bergman *et al.* (2011), it is a fluid property that measures the relative effectiveness of momentum and energy transport within the thermal and velocity boundary layers. For compressed air at pressures of 1-8 bar and

temperatures of -50°C to 100°C, its value is approximately 0.7. Nonetheless, the Prandtl number can be calculated using the following expression:

$$Pr = \frac{\mu C_p}{k_c}. (3.25)$$

The approach to determine the Nusselt number for forced convection was based on the internal flow in circular tubes (Bergman *et al.*, 2011). For turbulent flow ($Re \ge 2000$), the Nusselt number is

$$Nu_F = k_{fk} 0.023 Re^{4/5} Pr^n, (3.26)$$

and for laminar flow (Re < 2000)

$$Nu_F = 3.66,$$
 (3.27)

where n is 0.4 for heating $(T_{w_inn} > T)$ or 0.3 for cooling $(T_{w_inn} < T)$, and k_{fk} is a corrective factor for forced convection, which was introduced to improve the fitting of the model with experimental results (see Section 3.3).

According to Bergman *et al.* (2011), Equation (3.27) is valid when the wall temperature is constant, which is a reasonable assumption for pneumatic cylinders. This is because the temperature of the cylinder walls remains mostly constant during a cylinder cycle, due to the high thermal capacitance of the materials used in the cylinder body.

For free convection, the Nusselt number depends on two other dimensionless numbers: the Grashof number (Gr) and the Rayleigh number. Bergman $et\ al.\ (2011)$ state that the Grashof number measures the ratio of buoyancy forces to viscous forces in the velocity boundary layer. It is the equivalent of the Reynolds number in forced convection.

$$Gr = \frac{g\alpha_V \rho^2 (|T - T_w|) L_C^3}{\mu^2},$$
(3.28)

here, g represents the gravity acceleration, and α_V is the volumetric thermal expansion coefficient. For an ideal gas, $\alpha_V = 1/T$ (Bergman *et al.*, 2011).

Bergman *et al.* (2011) explain that free convection is not limited to laminar flow, as hydrodynamic instabilities may occur, leading to disturbances in the flow. Therefore, the Rayleigh number (Ra), which is the product of the Grashof number and the Prandtl number, is used to distinguish between laminar and turbulent flows in free convection

$$Ra = Gr. Pr. (3.29)$$

The authors present empirical correlations to determine the Nusselt number for free convection in different geometries. For pneumatic cylinders, the considered geometry is an upper horizontal hot plate, similar to the expression adopted by Ohligschläger (1990), and de Giorgi; Bideaux and Sesmat (2006).

$$Nu_N = k_{nk} 0.54 Ra^{1/4}$$
 for $10^4 \le Ra < 10^7$, (3.30)

$$Nu_N = k_{nk} 0.15 Ra^{1/3}$$
 for $10^7 \le Ra \le 10^{11}$, (3.31)

here k_{nk} , is a corrective factor for natural convection, also introduced to improve the model's agreement with experimental results (see section 3.3).

Although equations (3.30) and (3.31) are valid only for Rayleigh numbers greater than 10^4 and smaller than 10^{11} , these ranges should encompass all common applications of pneumatic drives. For example, a Rayleigh number of 10^4 occurs for air at 1 bar (absolute), 10° C above ambient temperature, and a characteristic length of less than 18 mm. Any increase in pressure or characteristic length results in a higher Rayleigh number.

During operation, the convective heat transfer coefficient can be influenced by forced convection (at high flow velocities) or free convection (at low flow velocities). Bergman *et al.* (2011) present the following equation to combine both forced and free convection into a single Nusselt number.

$$Nu = \left(Nu_F^3 + Nu_N^3\right)^{1/3}. (3.32)$$

By applying Equation (3.32) to Equation (3.20), the inner convective heat transfer coefficient (λ_{inn}) of the air inside the pneumatic chambers can be determined. This coefficient is then used, along with Equation (3.19), to calculate the inner heat flow rate. However, Equation (3.19) depends on the inner wall temperature (T_{w_inn}), which requires modeling heat conduction through the cylinder wall, as discussed in the following subsection.

3.2.3.2 Heat conduction in the cylinder wall

For conduction in the cylinder wall, an energy balance must be performed, as part of the heat flow is absorbed by the wall (Figure 3.3). Assuming no thermal energy generation within the wall, the thermal energy balance can be expressed as follows

$$\frac{\delta Q_{st}}{\delta t} = \frac{\delta Q_{ext}}{\delta t} - \frac{\delta Q_{inn}}{\delta t},\tag{3.33}$$

here $\delta Q_{st}/\delta t$ represents the heat flow rate absorbed (stored) by the wall material as sensible heat. The input and output energies are determined by the convection of heat to and from the cylinder wall. Therefore, for a one-dimensional model:

$$\rho_{Al}c_{Al}A_{s}dx\frac{dT}{dt} = \frac{\delta Q_{ext}}{\delta t} - \frac{\delta Q_{inn}}{\delta t},\tag{3.34}$$

where ρ_{Al} and c_{Al} represent the density and specific heat capacity of the wall material, which is typically aluminum for pneumatic cylinders.

Equation (3.34) is known as a lumped capacitance model, where the temperature of the cylinder material is assumed to be spatially uniform (Bergman *et al.*, 2011). This assumption is valid for Biot numbers ($Bi = \lambda L_c/k_c$) smaller than 0.1, a condition that is easily satisfied for pneumatic cylinder.

As shown in Di Giorgi, Equation (3.34) can be discretized into a single element ($dx = L_w$) due to small thickness of the wall. Therefore, the inner and external wall temperature are assumed to be equal ($T_{w_inn} = T_{w_ext} = T_w$), and Equation (3.34) results in a dynamic model for the wall temperature

$$\frac{dT_w}{dt} = \left[\frac{\delta Q_{ext}}{\delta t} - \frac{\delta Q_{inn}}{\delta t}\right] \frac{1}{\rho c A_s L_w}.$$
(3.35)

As can be seen, the dynamic model of the wall temperature depends on the inner heat flow $(\delta Q_{inn}/\delta t)$, given by Equation (3.19), and the external heat flow $(\delta Q_{ext}/\delta t)$, which is discussed in the following subsection.

3.2.3.3 External convective heat flow

The external heat flow is also modeled according to the Newton's law of cooling

$$\frac{\delta Q_{ext}}{\delta t} = \lambda_{ext} A_s (T_{w_ext} - T_0), \tag{3.36}$$

where T_{w_ext} is the external wall temperature, T_0 is the external environment temperature, and λ_{ext} is the external convective heat transfer coefficient.

As discussed in Section 3.2.3.2, due to the small wall thickness, the wall temperature is assumed to be uniform, therefore, $T_{w_ext} = T_w$, and T_w is given by Equation (3.35).

The external convective heat transfer occurs through free convection. For this case, the following expression can be used to calculate the Nusselt number:

$$Nu_N = \left\{ 0.60 + \frac{0.387Ra^{1/6}}{[1 + (0.559/Pr)^{9/16}]^{8/27}} \right\}^2. \tag{3.37}$$

Equation (3.37) is valid for a wide range of the Rayleight number ($Ra < 10^{12}$) for free convection in long horizontal cylinders. It can be applied along with equations (3.20), (3.28), and (3.29) to determine the external convective heat transfer coefficient (λ_{ext}). However, it should be noted that the characteristic length, in this case, is equal to the external diameter of the cylinder, and the specific mass of the air is based on the external conditions of pressure and temperature.

By applying the set of equations presented in Section 3.2.3, it is possible to model the heat transfer between the cylinder and the environment, including the transient effects on the cylinder wall temperature, as well as the forced and free convection within the cylinder chambers. The results of this model will be experimentally validated in Section 3.3.

3.2.4 Motion dynamics

The piston motion dynamics are governed by Newton's second law applied to the cylinder's piston, where a balance of forces acting on the piston is considered. For a pneumatic cylinder, the equation of motion is given by:

$$M\frac{d^{2}x}{dt^{2}} = \begin{cases} p_{A}A_{A} - p_{B}A_{B} - p_{0}A_{r} - F_{fr} - F_{ext} - F_{imp} & \text{for } 0 > x > L \\ p_{A}A_{A} - p_{B}A_{B} - p_{0}A_{r} - F_{fr} - F_{ext} & \text{for } 0 \le x \le L \end{cases},$$
(3.38)

where M is the moving mass, F_{fr} is the cylinder friction force, F_{ext} is the external load force, and F_{imp} is the force due to impact at the stroke-end heads of the cylinder, occurring when the piston reaches either end of its stroke end.

To model the effects of the impact force at the stroke-end heads, Bacca; De Negri and Assaf (2010) adopted the theory of elastoplastic collision. In this model, the stroke-end heads are assumed to behave like a mass-spring-damper system, as shown in Figure 3.5. When the piston reaches either of the stroke-end heads, its resulting acceleration includes a significant

deceleration force, though not infinite, enabling a more realistic representation of the actual behavior.

Figure 3.5 – Stroke-End Heads of a Pneumatic Cylinder

The impact force of the stroke-end heads is given by

$$F_{imp} = \begin{cases} k_e x + B_e \dot{x} & \text{for } x < 0 \\ k_e (x - L) + B_e \dot{x} & \text{for } x > L \end{cases}$$
 (3.39)

here, the spring constant of the stroke-end head is denoted by k_e , and its damping coefficient is represented by B_e .

3.2.5 Pneumatic friction modeling

The study of friction in this work is divided into two sections. In the current section, a brief overview of friction modeling for simulating pneumatic actuators is provided, while Section 4.2 discusses an approach to estimate the expected friction force during pneumatic the actuator sizing. Although the goal of both sections is the same, determining the friction force in pneumatic cylinders, their approaches differ in terms of available data and the resulting precision. This section employs accurate models to represent friction forces in dynamic simulations, which require prior experimental assessment of the cylinder for model parameterization. In contrast, Section 4.2 proposes a less accurate model that requires only basic data available in the early stages of the design process.

In fluid power cylinders, friction force occurs mainly from the piston seals, which are pressed against the cylinder sleeve to prevent leakage between chambers, and from the rod seals, which prevent leakage to the external environment (Beater, 2007; Rao; Bone, 2008). Figure 3.6 shows the classical behavior of friction force in fluid power drives as a function of velocity in steady-state conditions. This behavior is characterized by static friction, Coulomb friction, viscous friction, and Stribeck friction.

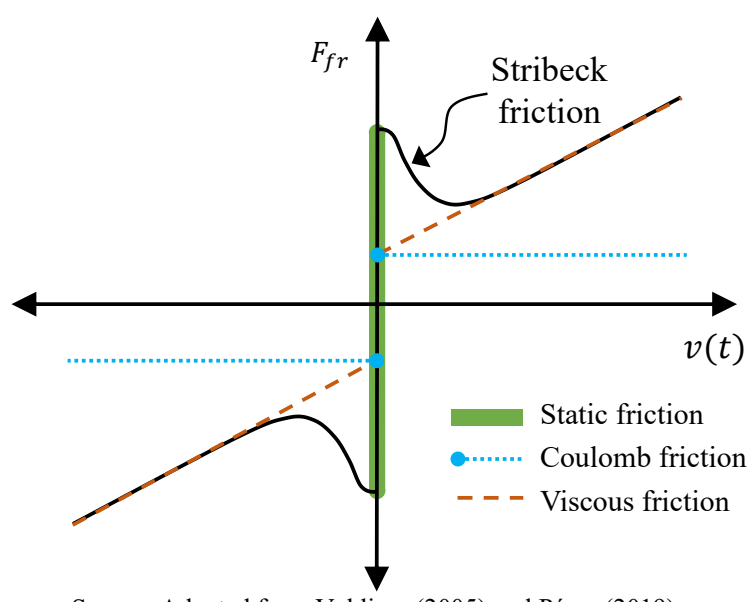


Figure 3.6 – Steady-state friction force characteristics

Source: Adapted from Valdiero (2005) and Pérez (2019).

Several models are available in the literature to describe friction phenomena in fluid power drives. The simplest are static models, which are static functions dependent only on the instantaneous velocity of the cylinder. Some examples of works that apply such static models include the Stribeck model (Hepke, 2016), tangent functions (Meng; Tao; Zhu, 2013), and switch-based polynomials (Endler; De Negri; Castelan, 2015).

More complex models can represent dynamic behaviors, such as hysteresis, variable static friction, and pre-sliding motion. Some of the most referenced models in the literature include the Dahl model (Dahl, 1968) and the LuGre model (Canudas-de-Wit *et al.*, 1995), which provide a good balance between accuracy and complexity. In Valdiero (2012), an analysis of dynamic characteristics of friction phenomena can be found. More advanced models, such as the Generalized Maxwell-Slip model (Al-Bender; Lampaert; Swevers, 2005), can also account for effects like rate-independent hysteresis with nonlocal memory. However, this model requires a large number of parameters and state variables, making it more time-consuming to parameterize and less suitable for control applications (Carneiro; de Almeida, 2015).

There are several variations of the classical friction models described above. In the field of fluid power, some authors have adapted these models to incorporate application-relevant parameters, such as chamber pressures (Nazarov; Weber, 2021; Teixeira, 2015; Zhan; Wang; Wang, 2014) and load force (Tran; Hafizah; Yanada, 2012), modifying the parameters of the Stribeck function. Beater (2007) provides a summary of several static models, most of which depend on piston velocity and chamber pressures.

As pointed out in Tran; Nguyen and Tran (2019), the LuGre model has been widely applied in fluid power systems, with numerous modifications to its original formulation. These include the Modified LuGre model (MLG) (Yanada; Sekikawa, 2008), the New Modified LuGre model (NMLG) (Tran; Hafizah; Yanada, 2012), and the Revised Lugre Model (RLG) (Tran; Dao; Tran, 2016). These modifications aim to capture specific phenomena not accounted for in the original model, such as the decrease of the maximum friction force after one cycle of velocity variation (MLG) and distinct hysteretic behaviors in hydraulic cylinders (NMLG) and pneumatic cylinders (RLG).

Most modifications of the LuGre model focus on the specific behavior of the presliding regime, which occurs before the cylinder effectively reaches its breakaway force, with displacements of less than 1 mm (Tran; Dao; Tran, 2016). In this section, an adaptation of the classical LuGre model is presented, where the static, Coulomb, and viscous coefficients are modified to be linearly dependent on the supply pressure. This approach is similar to the model proposed by Nazarov and Weber (2021) and Zhan; Wang and Wang (2014); however, this work incorporates a modified Stribeck function into the classical LuGre model, preserving its original dynamic characteristics.

The name 'LuGre' refers to the two universities of the authors who developed the model: Lund University (Sweden) and Grenoble University (France). In this model, the contact surfaces are represented as elastic bristles. When a tangential force is applied, these bristles deflect like springs, which characterizes the pre-sliding regime. Once the tangential force exceeds a certain threshold, the bristles yield, transitioning into the sliding regime (Canudas-de-Wit *et al.*, 1995).

Due to the random nature of irregular surface shapes, the bristle deflection is modeled as an average deflection (ξ), expressed as

$$\frac{d\xi}{dt} = v - \sigma_0 \frac{|v|}{g(v)} \xi,\tag{3.40}$$

where v is the relative velocity between the two contact surfaces, σ_0 is the stiffness coefficient of the bristles, and g(v) is a positive function that expresses the Stribeck effect, defined as

$$g(v) = F_C + (F_S - F_C)e^{-(v/v_S)^{\alpha_S}}, (3.41)$$

here, F_C is the Coulomb friction force, F_S is the static friction force, v_S is the Stribeck velocity, and α_S is an empirical parameter that defines the Stribeck region.

The LuGre friction force is given by

$$F_{fr} = \sigma_0 \xi + \sigma_1 \frac{d\xi}{dt} + \sigma_2 |v|^a, \tag{3.42}$$

the term σ_1 refers to the damping coefficient of the bristles, while σ_2 indicates the viscous friction coefficient. The parameter a, which is not included in the original LuGre model, has been incorporated into the friction models adopted by Hepke (2016) and Nazarov and Weber (2021) to provide an additional degree of freedom, improving the accuracy of the viscous friction force representation. Additionally, the modulus of the velocity is applied to prevent imaginary numbers when a is not integer.

At steady-state velocity, Equation (3.42) yields

$$F_{fr_ss} = F_C + (F_S - F_C)e^{-(v/v_S)^{\alpha_S}} + \sigma_2 |v|^a.$$
(3.43)

Based on the pressure dependence of friction force demonstrated by Nazarov and Weber (2021), the parameters for static, Coulomb, and viscous friction are linearized as $i_0 + p$. i_1 , where i corresponds to the friction parameter, and p represents the supply pressure.

$$F_C = F_{C \ 0} + p_s F_{C \ 1}, \tag{3.44}$$

$$F_S = F_{S_0} + p_S F_{S_1}, (3.45)$$

$$\sigma_2 = \sigma_{20} + p_s \sigma_{21}. \tag{3.46}$$

It should be noted that the parameters of equations (3.42) to (3.46) may take different values for positive and negative velocities due to the presence of the piston rod and the distinct loading conditions for extension and retraction. Therefore, for each direction of motion, the LuGre friction model presented in this chapter requires 9 static parameters (σ_{2_0} , σ_{2_1} , F_{S_0} , F_{S_1} , F_{C_0} , F_{C_1} , F_{C_1} , F_{C_2} , F_{C_3} , and 2 dynamic parameters (σ_{0} , σ_{1}). Appendix A provides a discussion on how to measure these parameters.

3.3 DYNAMIC MODEL VALIDATION AND ANALYSIS

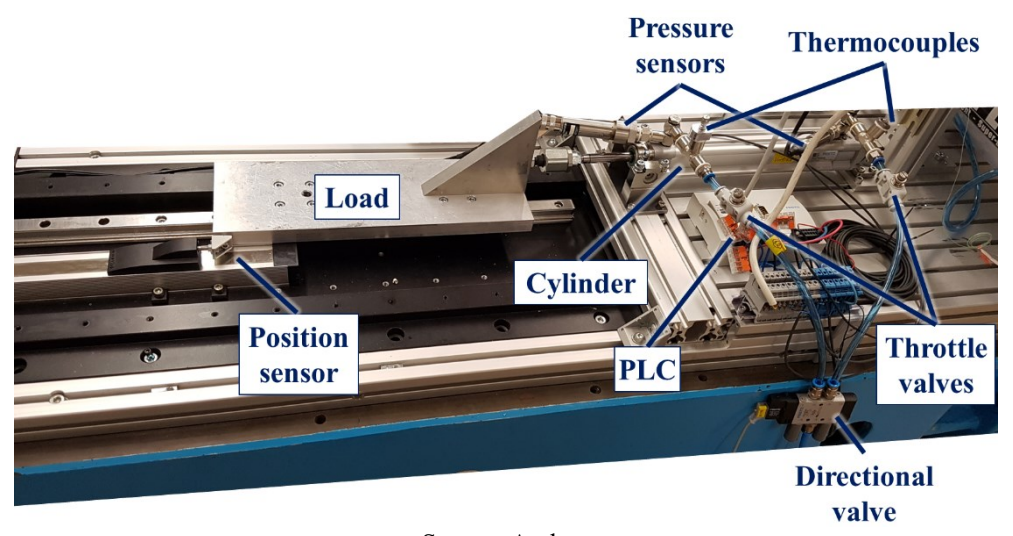
The equations presented in Sections 3.1 and 3.2 were adopted to model a pneumatic actuation system composed of a linear actuator, a set of two throttle valves, and a directional valve. These equations were implemented in MATLAB/Simulink for simulation purposes.

To verify the model's capability to predict the system's behavior, its results were compared with experimental data obtained from a test rig. The validation was conducted using the experimental test rig from the Fluidtronik Chair, Institut für Mechatronischen Maschinenbau, Technische Universität Dresden, Germany. The following components were used for the model validation: a linear cylinder (model DSBC-32-200-PPVA-N3 from Festo) with a piston diameter of 32 mm and a stroke length of 200 mm; two throttle valves (model QR1-DBS Ø8 from Aventics); and a directional valve (model CPE14-M1BH-5L-QS-8 from Festo). The throttle valves were assembled in a meter-out configuration, with approximately 1 turn of the regulating screw adjusted in each valve. The piping connecting the valves and the cylinder had an external diameter of 8 mm (5.5 mm internal diameter) and was approximately 300 mm long. The supply pressure was maintained at a constant 7.09 bar_{abs}.

The measuring equipment consisted of a position sensor (model MLO-POT-225-TLF) from Festo, pressure sensors (model PU5414) from IFM, and thermocouples (model 5TC-TT-KI-40-1M) from Omega. The thermocouples had thin wires with a 0.08 mm diameter, and their signal conditioning was performed using a TM1-2-3-0-100 C amplifier from LEG. Signal acquisition was conducted using a Yokogawa oscilloscope, model DL708E, with an acquisition rate of 1 kHz. Control signals were managed with a Festo PLC (CECC-D). The test rig setup is shown in Figure 3.7.

Prior to validation, an experimental assessment of the components was conducted to determine their parameters. This included ISO 6358 testing of the directional valve and throttle valves, as well as obtaining a friction map for the pneumatic cylinder. For the directional valve, one test was conducted for each flow path, while for the throttle valves, both flow paths were tested across the entire throttle control range. The cylinder's friction was evaluated at four different supply pressures, and the pressure-dependent parameters of the friction map were fitted accordingly, as shown in Appendix A. Table 3.1, Table 3.2 and Table 3.3 present the parameters of the model used for validation.

Figure 3.7 – Test rig utilized for the model validation



Source: Author.

Table 3.1 – General system parameters for the model validation

Parameter	Value	Unit	Parameter	Value	Unit
$p_{\mathcal{S}}$	7.091	bar _{abs}	М	8.442	kg
d_c	0.032	m	L_h	0.3	m
d_r	0.012	m	d_h	0.0055	m
L	0.200	m	k_e	98000000	N/m
$V_{A_{-}0}, V_{B_{-}0}$	1.7819×10^{-5}	m^3	B_e	50000	N.s/m

Source: Author.

Table 3.2-Valves parameters for the model validation

Parameter	Directional valve		Throttle vale	
Parameter	Value	Unit	Value	Unit
$C_{1 \rightarrow 2(A)}$	2.7822×10 ⁻⁸	m³/s.Pa	3.8877×10 ⁻⁹	m³/s.Pa
$C_{1 o 2(B)}$	2.8000×10^{-8}	m^3/s .Pa	3.8178×10^{-9}	m^3/s .Pa
$C_{2 o 1(A)}$	2.8842×10^{-8}	m^3/s .Pa	4.7033×10^{-10}	m^3/s .Pa
$\mathcal{C}_{2 o 1(B)}$	2.8654×10^{-8}	m^3/s .Pa	3.9888×10^{-10}	m^3/s .Pa
$b_{1 o 2(A)}$	0.4760	[1]	0.3394	[1]
$b_{1 o 2(B)}$	0.4642	[1]	0.3353	[1]
$b_{2 o 1(A)}$	0.4767	[1]	0.4508	[1]
$b_{2 o 1(B)}$	0.4899	[1]	0.5168	[1]
$q_{1 o 2(A)}$	0.5	[1]	0.8825	[1]
$q_{1 o 2(B)}$	0.5	[1]	0.9404	[1]
$q_{2 o 1(A)}$	0.5	[1]	0.5947	[1]
$q_{2\rightarrow 1(B)}$	0.5	[1]	0.6161	[1]

Source: Author.

Table 3.3 – Friction parameters for the model validation

Danamatan	Positive velocity		Negative velocity		
Parameter	Value	Unit	Value	Unit	
σ_0	2×10^{6}	N/m	2×10^{6}	N/m	
σ_1	12.02	N.s/m	12.02	N.s/m	
σ_{2_0}	34.751	N.s/m	-49.844	N.s/m	
$\sigma_{2_1}^{-}$	8.7342×10^{-5}	N.s/Pa.m	-9.7638×10^{-5}	N.s/Pa.m	
v_{s}^{-}	0.00223	m/s	-0.00401	m/s	
$F_{C_{-}0}$	-0.4450	N	-0.8141	N	
$F_{C_{-1}}$	4.8992×10^{-6}	N/Pa	-3.4369×10^{-6}	N/Pa	
$F_{S_{-}0}$	14.559	N	-8.2815	N	
$F_{S_{-1}}$	1.1917×10^{-5}	N/Pa	-1.7554×10^{-5}	N/Pa	
$lpha_{\scriptscriptstyle S}$	1	[1]	1	[1]	
a	0.4282	[1]	0.4536	[1]	

Source: Author.

In Table 3.2, the subscript $1 \to 2(A)$ denotes the flow path connecting the supply pressure to chamber A, whereas the subscript $2 \to 1(A)$ represents the flow path connecting chamber A to atmospheric pressure. The same notation is used for the flow paths of chamber B.

The model validation consisted of one complete extending and retracting stroke of the cylinder. The load consisted of a moving mass of approximately 8.15 kg, guided by a low-friction linear bearing. The results for position, velocity, chamber pressures, and temperatures are presented in Figure 3.8.

As can be seen, the simulation model accurately represents the pneumatic actuation system. For position and velocity, the experimental and simulation results show an almost perfect match. For the chamber pressures, small oscillations can be observed in chambers A and B, likely caused by fluctuations in the friction force, without significantly affecting the system's behavior.

Similar to the procedure adopted by Nazarov and Weber (2022a), the gain coefficients for natural and forced convection were adjusted according to the values shown in Table 3.4 to better align the simulated temperatures with the experimental results.

Table 3.4 – Correction coefficients for natural and forced convection

Parameter	Exte	nding	Retracting	
	Chamber A	Chamber B	Chamber A	Chamber B
$\overline{k_{nk}}$	20	5	5	3
k_{fk}	80	40	25	30

Source: Author.

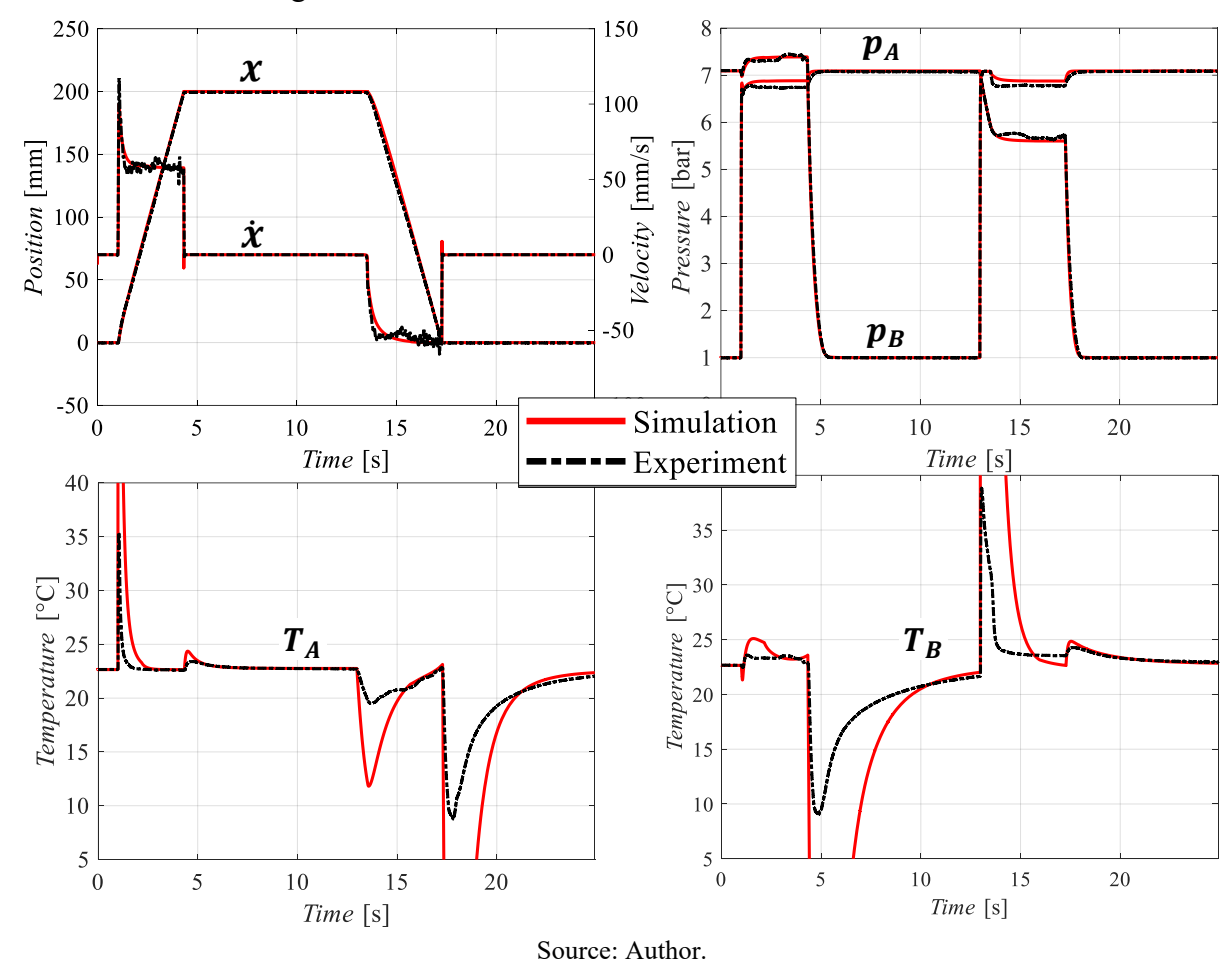


Figure 3.8 – Validation curves for the simulation model

Overall, the model accurately estimated the chamber temperature for most of the simulation. However, discrepancies between the model and the experiment were observed, particularly during the flow of compressed air at the beginning and end of the piston movement, where the piston remained stationary. These discrepancies can be attributed to challenges in modeling convective heat transfer during these periods, due to factors such as inhomogeneous flow and inaccuracies in estimating the Reynolds number. Similar deviations have also been

reported by Nazarov and Weber (2022a).

It should be noted that the Nusselt number equations presented in Section 3.2.3 are applicable to low-speed flows of compressed air with a Mach number below 0.3 (Bergman *et al.*, 2011), which may not be valid throughout the entire experiment. More detailed models for the Nusselt Number are available in literature, such as the study presented by Fagotti and Prata (1998), who propose a modified Nusselt number calculation, including the dependence on the derivative of volume. However, the coefficients of the equation require numerical or experimental determination, which are beyond the scope of this work.

The time constant of the thermocouples used was experimentally estimated by Nazarov and Weber (2022a) to be 92 ms, corresponding to a settling time of 460 ms. Consequently, temperature spikes may not have been accurately captured due to the thermocouples' response limitations. Nevertheless, for most of the experiment, the model successfully estimated the temperatures in the cylinder chambers, demonstrating its validity.

Even though the simulation model presented in this chapter provided high-fidelity results when compared to the experimental data, two drawbacks must be highlighted: 1) High parametrization time: The large number of parameters, including friction parameters, valve parameters, and heat flow parameters, makes it time-consuming to properly acquire and adjust the system's parameters; 2) Simulation time: The highly detailed simulation results in several discontinuities, often causing the simulation to stall due to the need for variable-step solvers.

Therefore, a simplified simulation model was also investigated. The goal of the model was to retain the main characteristics of the actuation system while providing a more straightforward model for parameterization and simulation. The motivation for this simplification was the batch simulations conducted in this work, which required thousands of simulations with various cylinder and valve configurations. In such cases, it is desirable to reduce non-essential state variables and parameters to speed up the analysis process. As a result, the following simplifications were applied to the model:

- The models of the of throttle and directional valves were replaced by the model of a nonsymmetric directional valve;
- The friction model parameters were averaged at an intermediate pressure;
- The heat transfer model was replaced with a constant thermal transmittance model.

The justification for assuming such simplifications is related to the characteristics of the simulations performed in this work, which include: 1) Short hose lengths, resulting in pressures between the directional valve and the throttle valve that are nearly equal to the supply or ambient pressures; 2) A focus on load force applications, where the small deviation in friction force caused by pressure is not significant; 3) Single-stroke simulations, which prevent significant differences between the cylinder wall temperature and the external environment.

To incorporate the characteristics of two valves in series (the directional and throttle valves) into a single restrictor, the Equation (5.18), presented in Beater (2007), was adopted to calculate the equivalent sonic conductance and critical pressure ratio. To estimate the thermal

transmittance, the thermal time constant method, as applied in Vigolo (2018), was used on the cylinder under analysis, yielding a value of 279.4 W/m².K.

In Figure 3.9, the results of the full model, which includes the throttle and directional valves, the complete heat transfer model, and the pressure-dependent friction model, are compared with the results of the simplified model that incorporates the aforementioned simplifications.

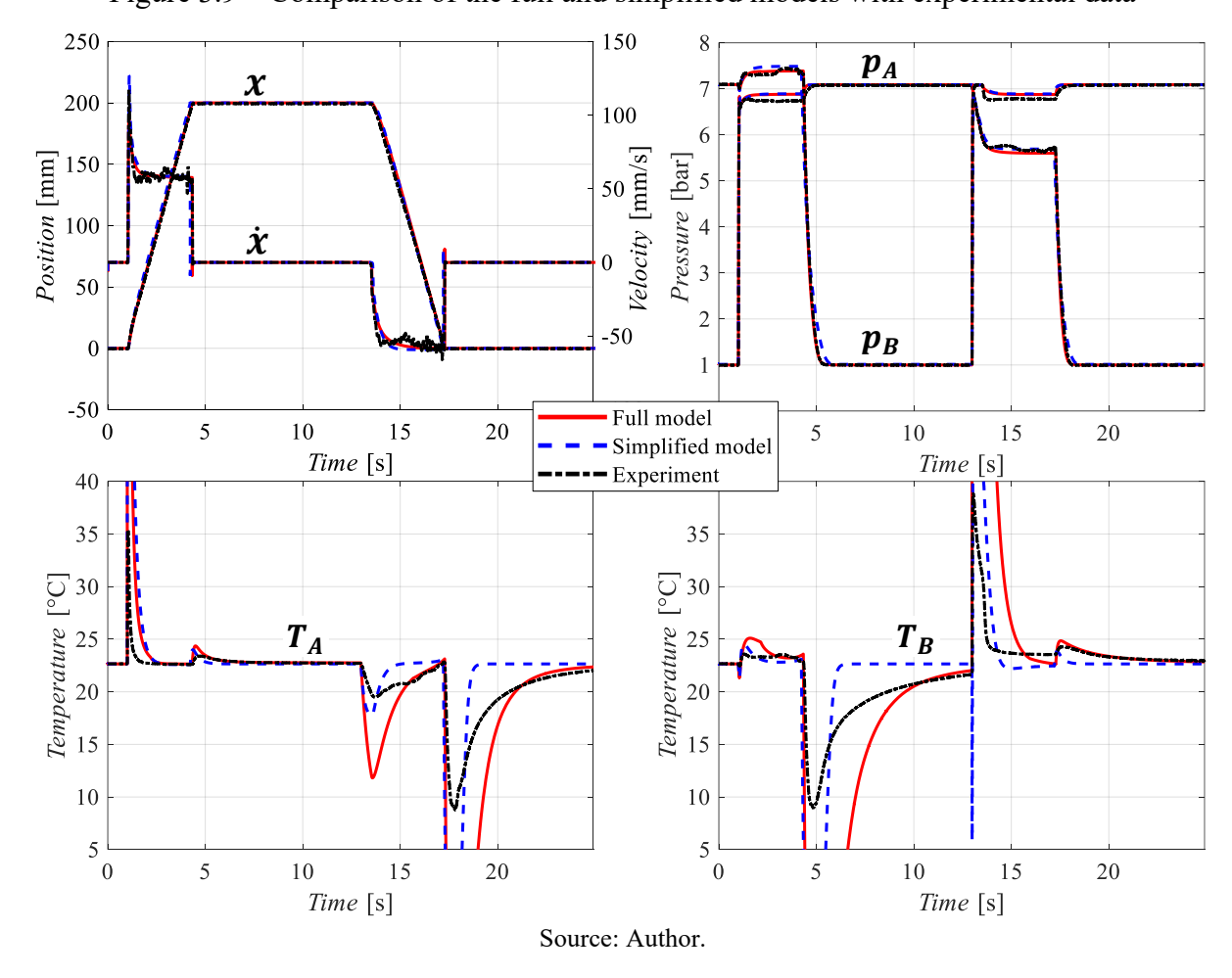


Figure 3.9 – Comparison of the full and simplified models with experimental data

As can be seen, the simplified and full models present nearly identical behavior. Differences in position and velocity profiles are almost nonexistent. For the chamber pressures, small differences of about 0.1 bar are observed during the displacement of the piston, likely due to the simplified friction model. Regarding temperature behavior, the simplified model showed smaller temperature spikes compared to the full model. However, during low-velocity flow phases, the simplified model reached the environment temperature much faster, highlighting its inability to accurately model temperature behavior in such cases. Nevertheless, according to

the full model, the total supplied exergy at the directional valve upstream port was 474.6 J, whereas the simplified model received a total exergy of 471.6 J.

Therefore, based on the observed results, it can be concluded that **the simplified model is capable of accurately predicting piston position and velocity behaviors**, with exergy and chamber pressure errors in the range of 0.5% to 1.5% compared to the full model. These aspects, combined with easier parametrization and faster simulation times, justify the adoption of the simplified model in the studies carried out in this thesis.

3.4 FINAL CONSIDERATIONS ABOUT CHAPTER 3

This chapter presented the fundamental equations applied to the dynamic simulation of pneumatic actuation systems, including the modeling of mass flow rate through restrictors, as well as the pressure and temperature dynamics of the cylinder chambers and piston motion. Additionally, a comprehensive model of the heat exchange phenomena was explored, along with the implementation of a LuGre friction model with pressure-dependent parameters for static, Coulomb, and viscous friction.

The developed model was experimentally validated, showing good agreement with the experimental results. Furthermore, a simplified model was investigated, which demonstrated behavior nearly identical to the full model. This simplified model presents a viable alternative for use in the following chapters of this thesis, particularly for the exploratory and batch-based analyses that will be performed.

4 SIZING OF PNEUMATIC ACTUATORS

This chapter presents the developed approach for the sizing of pneumatic actuators. It begins with a description of the operating point method, which serves as the basis for determining the optimal operating conditions of pneumatic actuators. Additionally, a metric is introduced to evaluate the robustness of pneumatic drives to load changes, providing an effective means to determine whether a cylinder is over- or undersized. Part of the content presented in this chapter has been published in the author's previous study, available in the papers Vigolo and De Negri (2021), Vigolo; Valdiero and De Negri (2025), and Vigolo; Boyko; et al. (2024).

This chapter also includes an approximate solution to the operating method, enabling its application without the need for numerical solvers. It presents a thorough analysis of the friction forces of several commercially available cylinders, highlighting the existence of friction force patterns that allow for their estimation based solely on design parameters. Additionally, it analyzes the impact of different load force components on the system's dynamic behavior, enabling the design of cylinders for more efficient operation without compromising robustness.

Based on the developed model and analyses, a comprehensive sizing method for pneumatic actuators is presented. It consists of five activities, covering everything from determining the sizing load force to optimizing the supply pressure.

4.1 THE STEADY-STATE ANALYSIS

As discussed in Chapter 3, predicting the chamber pressures in a pneumatic actuator is a complex task because it involves modeling physical phenomena using several non-linear differential equations with interdependent states, such as temperature, mass flow rate, piston position, and velocity. Therefore, describing the chamber pressures requires the use of numerical integration methods, such as Euler, Runge-Kutta, Dormand-Prince, among others (Liermann; Feller; Lindinger, 2021; Schulz *et al.*, 2007).

The concept of the operating point was introduced by Oliveira (2009), who derived a set of equations to determine the behavior of cylinder chamber pressures during piston displacement under steady-state conditions, that is, when there are no significant changes in chamber pressures. Oliveira's equations were further developed by Hené (2010) and Hené *et al.* (2010), where effects so far neglected were added to the equations, such as the use of non-symmetric valves and temperature effects. Vigolo (2018) and Vigolo and De Negri (2021)

applied the operating point method to describe the piston steady-state velocity, highlighting characteristics of the dynamic performance and energy efficiency of pneumatic drives. This enabled the definition of an optimal operating condition and demonstrated the method's applicability for optimizing the sizing of pneumatic actuators.

The following subsections provide a brief description of the mathematical derivation of the equations that compose the operating point method. However, it is recommended to consult the aforementioned references for a more comprehensive understanding of the derivation procedure.

4.1.1 The operating curve

The behavior of pressures in the cylinder chambers is described by equations (3.9) and (3.10). Assuming steady-state piston displacement, the terms related to the time derivatives of pressure and temperature can be neglected. In this way, it is possible to determine a mathematical correlation between the pressure in chamber A and the pressure in chamber B of a pneumatic cylinder. This correlation is possible due to the velocity term, which allows both equations to be merged, since the piston velocity is the same in both cylinder chambers, that is

$$\frac{dx}{dt} = \frac{q_{mA}}{\rho_A A_A} = \frac{q_{mB}}{\rho_B A_B}. (4.1)$$

The mass flow rate, described by Equation (3.2), characterizes the flow regime in both subsonic and choked flow conditions. To correlate the pressures in chambers A and B, Oliveira (2009) derived four equations for the extension movement and four for the retraction movement. These equations account for the possible flow regimes that can theoretically occur. The possible combinations are shown in Table 4.1, where the terms P-A and P-B denote the flow paths connecting the supply pressure to chambers A and B, respectively. Similarly, the terms B-T and A-T represent the flow paths connecting chambers B and A to atmospheric pressure, respectively.

Table 4.1 – Flow regimes at the valve

Ex	į	
P-A (Flow regime)	B-T (Flow regime)	Operating condition
Subsonic	Subsonic	Condition I
Subsonic	Choked	Condition II
Choked	Subsonic	Condition III
Choked	Choked	Condition IV

Ex		
P-B (Flow regime)	A-T (Flow regime)	Operating condition
Subsonic	Subsonic	Condition I
Subsonic	Choked	Condition II
Choked	Subsonic	Condition III
Choked	Choked	Condition IV

Source: Author.

Through numerical analyses, Oliveira (2009) identified that the only possible conditions are Conditions I and II. Conditions III and IV resulted in values that are impossible to occur during the cylinder's displacement. Therefore, by applying Equation (3.2) in (4.1) and considering the ideal gas law, uniform temperature throughout the system, a symmetrical valve, no cracking pressure, and a subsonic index (m) equal to its typical value (0.5), the equations that correlate the chamber pressures for Conditions I and II during the extending movement are, respectively:

$$\frac{p_0}{p_B} = b + \sqrt{b^2 - 2b + 1 + r_A^2 + (2br_A^2 - r_A^2) \left(\frac{p_A}{p_S}\right)^{-2} - 2br_A^2 \left(\frac{p_A}{p_S}\right)^{-1}},$$
(4.2)

$$\frac{p_A}{p_S} = \frac{\left(br_A + \sqrt{b^2 r_A^2 - 4b + 1 + 5b^2 - 2b^3 - 2br_A^2 + r_A^2}\right) r_A}{1 - 2b + b^2 + r_A^2}.$$
(4.3)

For the retracting movement, Conditions I and II are, respectively:

$$\frac{p_0}{p_A} = \frac{br_A + \sqrt{r_A^2(b^2 - 2b + 1) + 1 - 2b\left(\frac{p_B}{p_S}\right)^{-1} + \left(\frac{p_B}{p_S}\right)^{-2}(2b - 1)}}{r_A},\tag{4.4}$$

$$\frac{p_B}{p_S} = \frac{b + \sqrt{b^2 - 4br_A^2 + r_A^2 + 5b^2r_A^2 - 2b^3r_A^2 - 2b + 1}}{r_A^2 - 2br_A^2 + b^2r_A^2 + 1},$$
(4.5)

where b is the critical pressure ratio (assumed to be equal for all flow paths), r_A is the area B to area A ratio, p_A and p_B are the pressures in chambers A and B, respectively, and p_S and p_O denote the supply and ambient pressures, respectively.

Figure 4.1 shows the curves obtained for Conditions I and II during the extending and retracting movements of a pneumatic cylinder with a piston diameter of 125 mm, a rod diameter of 32 mm, operating at a pressure of 6 bar_{abs} and a valve with critical pressure ratio of 0.3.

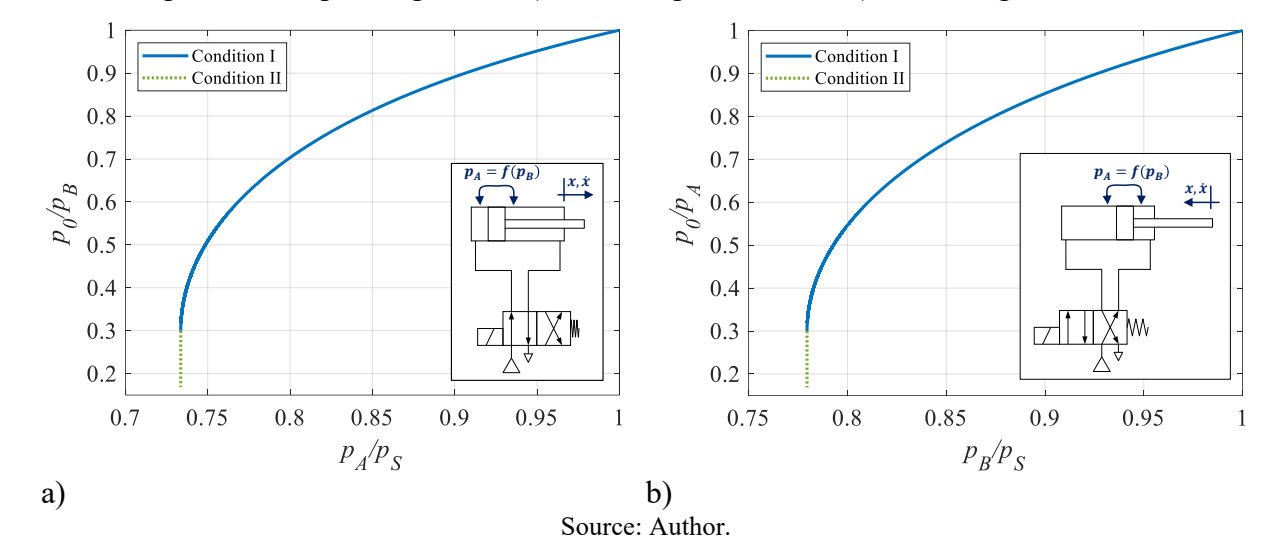


Figure 4.1 – Operating curve; a) Extending movement, b) Retracting movement

The curves presented in Figure 4.1 show the relationship between the pressures in chambers A and B of a pneumatic actuator when it is moving without significant changes in pressure, that is, at steady state. Each point on these curves represents an operating point of the system, and the definition of the operating point is inherently related to the cylinder's maximum actuation force and the applied load.

Vigolo (2018) observed that the operating points of Condition II result in a poor combination of load force and maximum cylinder force, meaning that only highly oversized systems can operate near Condition II. Therefore, in the following analysis of this thesis, Condition II will be neglected, as it does not contribute to the sizing of efficient pneumatic drives. Furthermore, the curve of Condition I will henceforth be referred to as the operating (Op) curve because it represents the possible operating points of a pneumatic actuation system.

4.1.2 The loading curve

The definition of a specific operating point, at which the system operates, depends on the relationship between the load force handled by the cylinder and the cylinder's maximum load capacity, which is the product of the supply pressure and the cylinder's actuation area. To quantify this relationship, the movement equation (Eq. (3.38)) is used, where the terms related to the external load force (F_{ext}) and inertial force ($M d^2 x/dt^2$) are combined into a single term called the load force (F_L), that is

$$F_L = F_{ext} + M \frac{d^2 x}{dt^2}. (4.6)$$

The cylinder friction force is correlated with its maximum actuation force using the model presented by Virvalo (1993), $F_{fr} = p_S A_A \mu_d$, with μ_d being the dynamic friction coefficient.

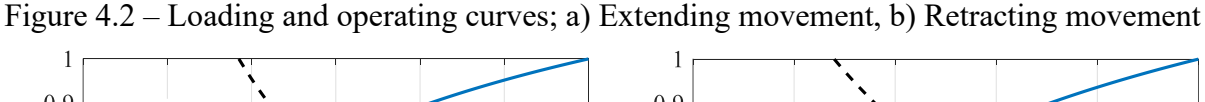
Under these assumptions, the motion equation can be algebraically manipulated to express its variables as pressure ratios, resulting in the loading (Ld) curve of the system for extending and retracting movements, given by Equations (4.7) and (4.8), respectively:

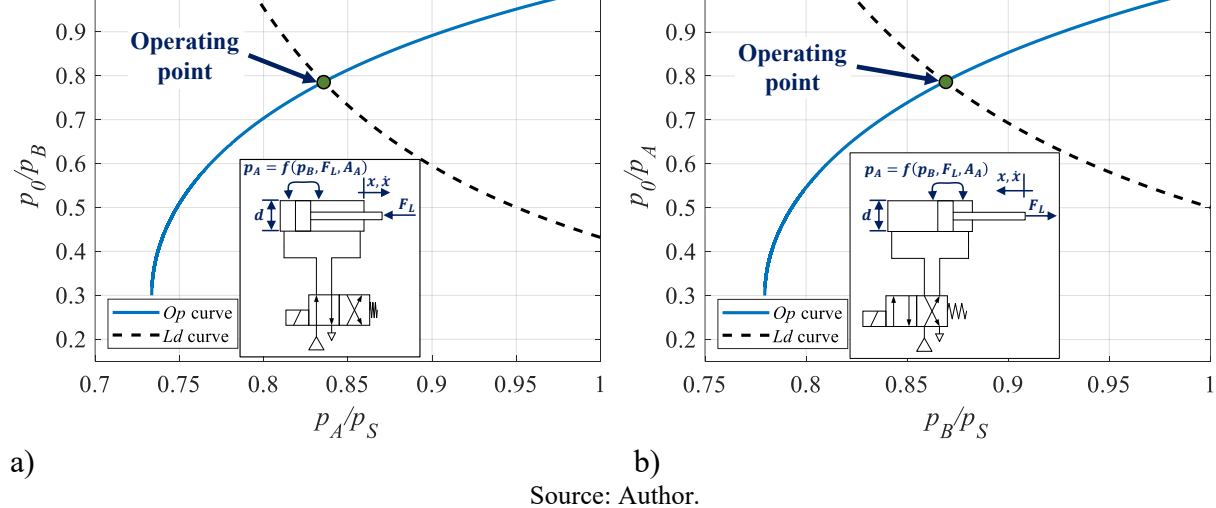
$$\frac{p_A}{p_S} = \frac{F_L}{p_S A_A} + r_A \left(\frac{p_0}{p_S}\right) \left(\frac{p_0}{p_R}\right)^{-1} + \frac{p_0}{p_S} (1 - r_A) + \mu_d,\tag{4.7}$$

$$\frac{p_B}{p_S} = \frac{F_L}{p_S A_B} + \frac{1}{r_A} \left(\frac{p_0}{p_S}\right) \left(\frac{p_0}{p_A}\right)^{-1} - \frac{p_0}{p_S} \frac{(1 - r_A)}{r_A} + \frac{\mu_d}{r_A}.$$
 (4.8)

Analyzing the loading curve equations, it can be observed that, to determine the cylinder area, a set of pressure ratios must be defined $(p_A/p_S \text{ and } p_0/p_B \text{ for extending, or } p_B/p_S \text{ and } p_0/p_A \text{ for retracting})$. Therefore, the main goal of the operating point method is to determine a set of optimal pressure ratios, which can then be used for sizing the cylinder area. This aspect will be further explored in Section 4.1.4.

The loading curve for an extending movement is graphically presented in Figure 4.2, which results from the same cylinder parameters utilized in Figure 4.1, with a load force of 5.5 kN and a dynamic friction coefficient of 0.1.

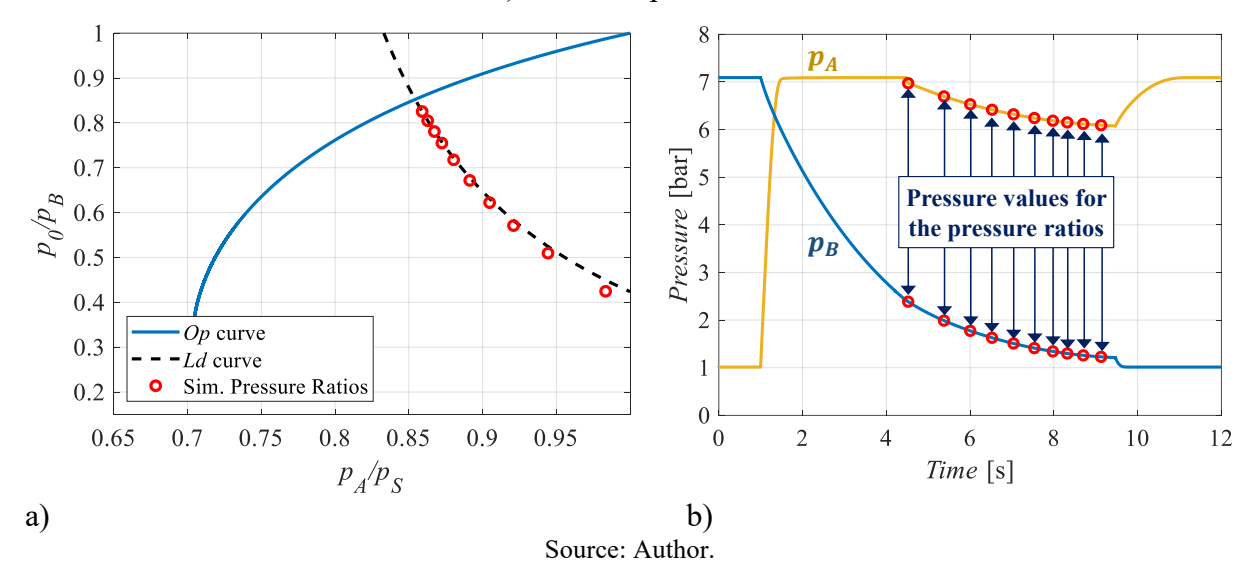




The operating point of a pneumatic system is defined as the pressure ratio at the intersection of the operating curve and the loading curve. At this point, the system reaches a steady state where the piston moves at constant velocity, chamber pressures stabilize, and acceleration approaches zero.

During dynamic displacement, the pressure ratios are usually located below the operating curve but are unlikely to be located above it, as shown by the results of a dynamic simulation in Figure 4.3-a). Moreover, the figure demonstrates that even under conditions of dynamic changes in pressure and velocity, the pressure ratios tend to remain close to the loading curve. This behavior is due to the correlation between the pressures in the cylinder chambers: a change in the pressure of one chamber automatically affects the pressure in the other, resulting in minimal variation in the pressure difference between the two chambers during displacement under a constant load force.

Figure 4.3 – Loading and operating curves with dynamic simulation data; a) Pressure ratios, b) Chamber pressures



As can be observed, the pressure behavior during displacement closely follows the loading (Ld) curve, even when there are changes in the chamber pressures. The small deviations that can be observed are due to variations in the friction force and acceleration force, as the loading curve assumes these forces to be constant and only accounts for a fixed value added to the load force (F_L) .

It can be emphasized that, for sizing purposes, any point on the loading curve can be used. Therefore, by selecting the intersection point with the operating (Op) curve, the loading curve of the system is automatically determined. In this way, the assumption of steady-state

conditions made during the development of the operating curve does not affect the sizing of the system, as the loading curve is valid for any operating condition.

4.1.3 The optimal operating condition

The main goal of the operating point method is to define an optimal point, which is a set of pressure ratios along the operating curve that result in an optimal operating condition. This set of pressure ratios can then be applied to the loading curve equations to size the actuation area, in such a way that the system operates under these optimal conditions.

Hené (2010) proposed that the optimal point corresponds to the condition where the choked flow rate begins at the flow path connecting the counterpressure chamber to the atmosphere. This point corresponds the transition from condition I to condition II, as described in Section 4.1.1. According to the author, designing the system to operate near this point minimizes pressure losses at the valve and, consequently, increases pneumatic force and displacement speed.

However, this analysis does not consider aspects related to the energy efficiency of the actuation system. Furthermore, for the system to operate close to condition II, a high counterpressure is required for the flow to become choked at the exhaust flow path. This results in a lower pneumatic force available at the cylinder rod, evidencing that this is not an optimal operating condition.

Vigolo (2018) conducted a sensitivity analysis to determine the optimal operating point, taking into account displacement time, end-stroke velocity, and energy efficiency. The analysis involved a series of dynamic simulations performed under identical operating conditions, such as load force, supply pressure, and the sonic conductance of the directional valve, with the exception of the cylinder diameter, which was the control variable used to evaluate its impact on system behavior.

With this analysis, Vigolo (2018) demonstrated the existence of a relationship between energy efficiency and the dynamic performance of the system, the latter represented by displacement time and end-stroke velocity. More specifically, it was shown that maximum energy efficiency always occurs with the minimum area required to move the applied load. However, under such conditions, displacement occurs at low velocities, increasing the displacement time and making it more challenging to control the piston speed, as the pressures in the cylinder chambers are already close to their limit conditions (supply and atmospheric pressures).

In addition to the lower dynamic performance, it was also observed that cylinders operating near their maximum energy efficiency become excessively sensitive to changes in the load force. Specifically, small variations in the load applied to the cylinder rod can significantly affect the cylinder's displacement time, potentially even causing a complete cylinder stall, which is undesirable for system operation. Therefore, the optimal operation of a pneumatic drive can be characterized by two key features:

- 1) Energy efficiency: It consumes the least amount of compressed air to perform a given task.
- 2) Robustness: It maintains its response characteristics under variable loading conditions.

Seeking to quantify the robustness of pneumatic actuators, two metrics are introduced in this thesis: Sensitivity (S_c) and Robustness (R_c) of the pneumatic cylinders. These metrics are defined by the following equations:

$$S_C = \frac{\Delta t_d / t_d}{\Delta F_L / F_L},\tag{4.9}$$

$$R_C = \frac{4e^{-S_C}}{(1 + e^{-S_C})^{2'}} \tag{4.10}$$

where Δt_d represents the change in displacement time and ΔF_L is the change in the load force.

The sensitivity (S_C) of a pneumatic actuator corresponds to the relative change in displacement time caused by the relative change in load force. For instance, if the load force increases from 100 N to 110 N ($\Delta F_L/F_L = 10\%$), this change will impact the displacement time of the cylinder. If the time to complete the task changes from 1 second (under a load force of 100 N) to 1.1 seconds (under a load force of 110 N), the relative change in displacement time ($\Delta t_d/t_d$) will also be 10%, resulting in a sensitivity (S_C) of 1. The impact on the displacement time depends on how sensitive the system is. An oversized actuator may have sensitivity values close to 0, whereas undersized actuators may have sensitivity values tending to infinity.

From the sensitivity, an expression for robustness can be defined such that high sensitivity corresponds to low robustness, while minimal sensitivity corresponds to maximum robustness of 1. This is achieved using the derivative of a standard logistic function, where large values of its argument (the sensitivity) yield values near zero, and small values of its argument lead to bounded values. A scaling factor of 4 is applied to the robustness (R_C) to ensure its values range from 0 to 1.

The sensitivity and robustness of a pneumatic actuator are determined by assessing the impact caused by changes in load force, with all other system parameters (e.g., supply pressure, throttle valve opening) remaining constant. This approach evaluates the effects of load force fluctuations, such as those arising from slightly varying load masses, friction changes on sliding surfaces, or degradation of actuator seals, on the system's displacement time.

In order to demonstrate the effects of systems with different values of robustness and sensitivity, Figure 4.4 shows the impact of changes in load force on displacement time. The continuous blue line represents the system's behavior with no change in load force, which reflects the expected condition during the setup of an actuation system, where displacement time is adjusted to meet the design requirement (in this case, 0.8 seconds). The dashed lines show the impact on displacement time due to a relative increase of +10% in load force. Each dashed line corresponds to the same pneumatic actuator with a different supply pressure, resulting in different sensitivity and robustness values. The dot-dashed lines represent the impact on displacement time caused by a 10% reduction in load force.

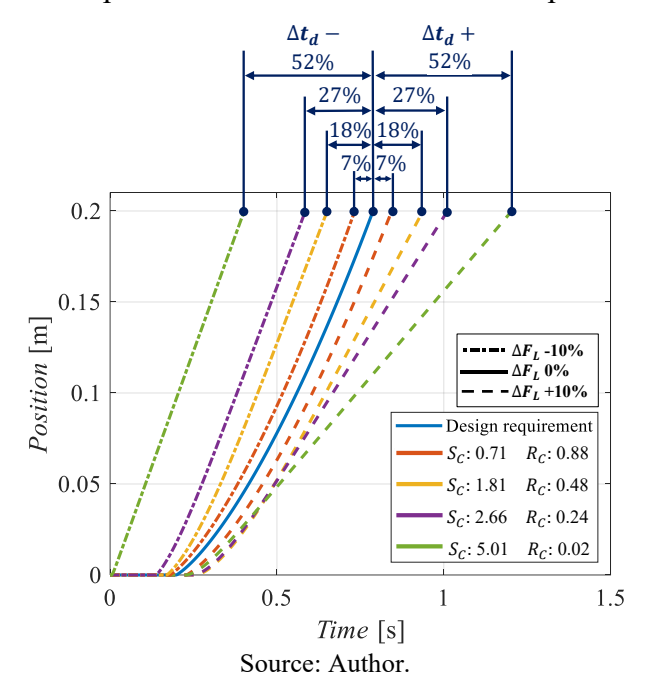


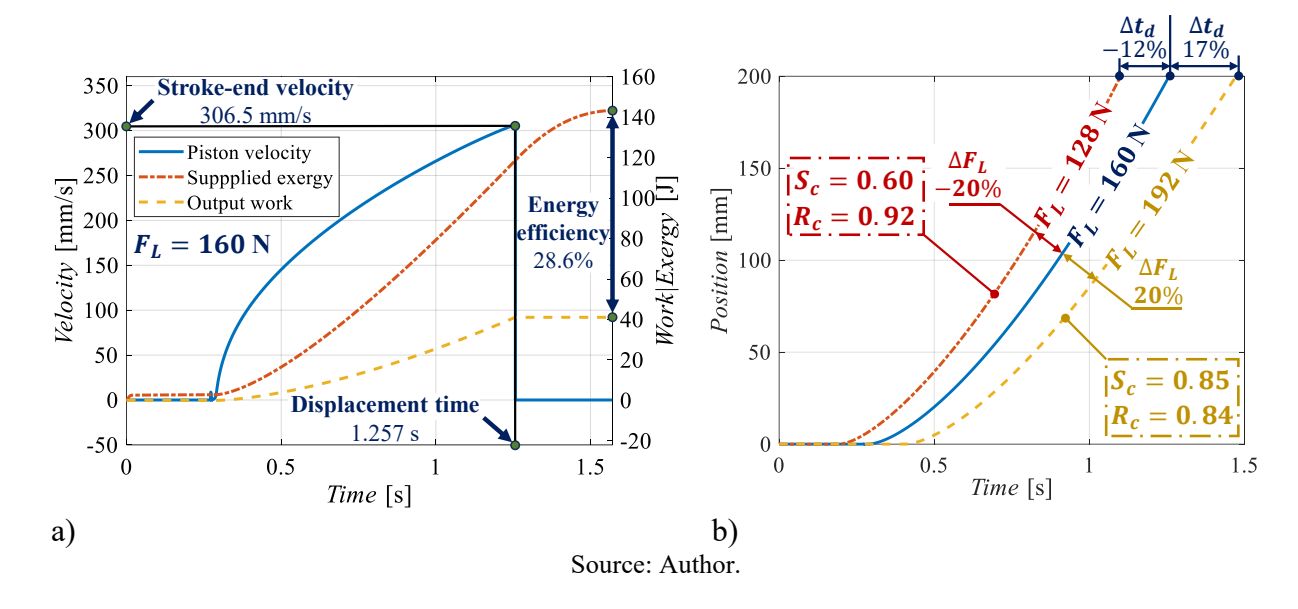
Figure 4.4 – Impact of load force variations on displacement time

As can be seen with the green lines, pneumatic actuators with low robustness present significant changes in displacement time due to both positive and negative oscillations in load force. This aspect negatively affects the development of automation equipment by compromising the repeatability of the automation process. In contrast, pneumatic actuators with high robustness, such as the red lines, show minimal changes in displacement time despite

variations in load force, making them a desirable choice when designing pneumatic actuation systems.

Although high robustness is a desirable characteristic, it is associated with larger actuation areas, leading to higher energy consumption and reduced energy efficiency. Therefore, a balance between robustness and energy efficiency must be achieved. To explore this balance, a sensitivity analysis was conducted to investigate the impact of cylinder diameter on energy efficiency, displacement time, end-stroke velocity, and the robustness of a pneumatic actuation system. Figure 4.5 shows the time-dependent results of one simulation, illustrating how the data of the sensitivity analysis were obtained.

Figure 4.5 – Time-dependent results for the Ø26 mm cylinder: a) Piston velocity, supplied exergy and task-consumed energy; b) Piston displacement position under different load forces



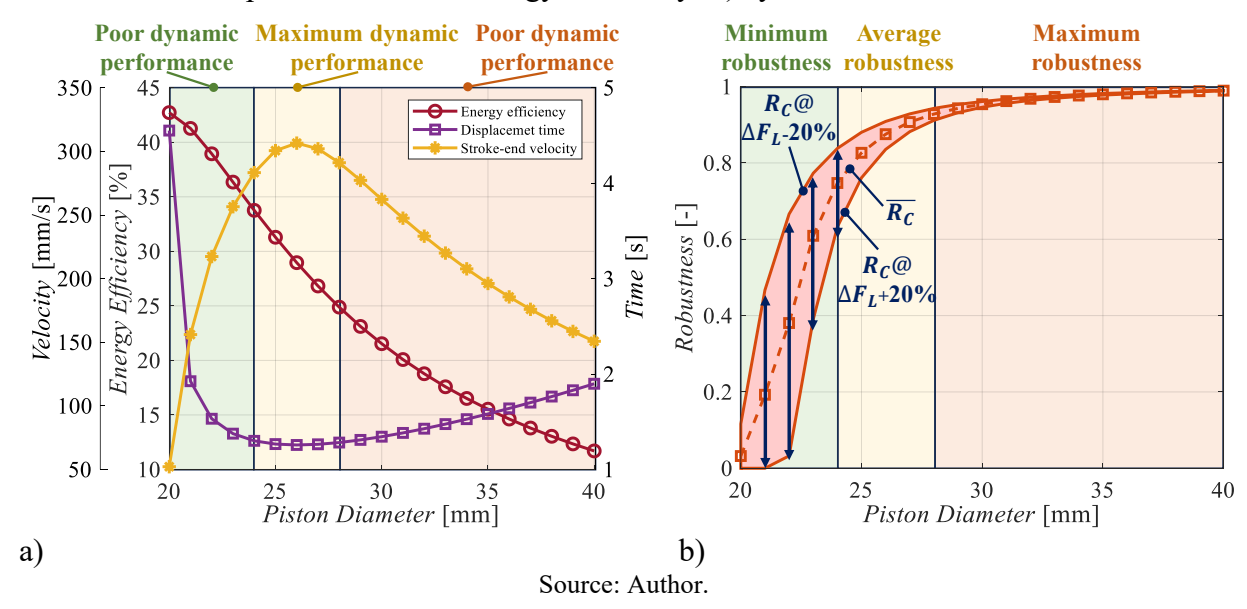
The energy efficiency, calculated using equation (2.22), is determined by the ratio of the total output work to the supplied exergy. The supplied exergy includes the energy used to fill the driving chamber after the task is completed, as shown in Figure 4.5-a). The robustness is determined through an additional simulation that increases or decreases the load force to evaluate its impact on displacement time compared to the original simulation, as shown in Figure 4.5-b).

It can also be seen that the effect of load force variations on robustness is asymmetric. In other words, a positive change in load force increases the displacement time by a different amount than the decrease in displacement time caused by a negative change in load force of the same magnitude. This asymmetric behavior is shown in Figure 4.5-b). The symmetric behavior presented in Figure 4.4 was intentionally induced to highlight the influence of different

robustness levels. This was achieved by slightly adjusting the system's supply pressure until the desired symmetry was observed. However, such symmetry is not typical of pneumatic drives.

The results of the sensitivity analysis, conducted with cylinder piston diameters ranging from 20 to 40 mm, a stroke of 200 mm, a load force of 160 N, and a supply pressure of 7 bar_{abs}, are shown in Figure 4.6.

Figure 4.6 – Sensitivity results showing the impact of cylinder diameter on: a) dynamic performance and energy efficiency; b) cylinder robustness.



Aspects related to dynamic performance are highlighted in Figure 4.6-a). Smaller diameters (green area) results in higher energy efficiency but higher displacement time and lower end-stroke velocity. In such cases, trying to address the lower dynamic performance by using higher flow capacity valves will not be effective, as the cylinder is already operating near its maximum force capacity. Similarly, larger cylinder diameters (orange area) also negatively impact dynamic performance. This is due to the larger volume of air required to flow through the valve to perform the task, which increases the time needed to complete it. The diameters corresponding to maximum dynamic performance (yellow area) are characterized by maximum end-stroke velocity, minimum displacement time, and average energy efficiency.

For the performed analysis, actuator robustness was evaluated under changes in the load force of [+20%, +10%, -10%, -20%] relative to the initial force applied to the system. This resulted in the robustness red area shown in Figure 4.6-b), with the dashed red line representing the mean robustness ($\overline{R_C}$) values for each cylinder diameter. The smaller diameters (green area) presented low robustness values, indicating the actuator's inability to maintain its original

displacement time when small changes in the load force were applied. Additionally, high variability in robustness was observed due to both positive and negative changes in the load force. This highlights that undersized actuators have a poor capacity to maintain consistent displacement time, even when the load decreases during operation. Such variability leads to either an increase or decrease in displacement time, affecting the repeatability of the automation process in which the drive is applied.

The largest cylinders in the orange area, in turn, demonstrated high robustness for both positive and negative changes in the load force. This means that, in such cases, the drive is capable of maintaining a steady response time regardless of increases or decreases in the load force. This is a desirable characteristic for time-based applications, where pneumatic drives are frequently used.

Based on the sensitivity analysis presented above, a clear trade-off between energy efficiency and robustness can be observed: a robust drive requires higher energy consumption, while lower energy consumption is achievable with a less robust actuator. However, robustness does not increase indefinitely, it eventually reaches a plateau where further increases in cylinder area have minimal impact on robustness, while the effect on energy efficiency remains nearly linear with cylinder diameter. Therefore, the cylinders highlighted in the yellow area, centered around the cylinder with maximum end-stroke velocity, present characteristics desirable for sizing purposes. These cylinders achieve maximum dynamic performance without significantly compromising energy efficiency and operate near the robustness plateau, ensuring robust and efficient operation and defining the optimal operating condition.

The results presented in Figure 4.6 demonstrate the robustness concept for pneumatic drives and its correlation with energy efficiency and dynamic performance, defining an optimal operating condition. The effectiveness of the optimal operating condition in balancing robustness and energy efficiency across a wide range of operating conditions will be further explored in Chapter 7.

4.1.4 The velocity/C curve

At the end of the piston displacement, the system tends to reach a steady-state behavior. Therefore, end-stroke velocity, which serves as a reference condition for defining the optimal operating condition, can be modeled using the operating point equations, as will be shown for the extending movement. According to Equation (4.1), the steady-state velocity (v_{e_ss}) is a function of mass flow rate, specific mass, and actuation area, that is

$$v_{e_SS} = \frac{q_{mA}}{\rho_A A_A}. (4.11)$$

As seen in Section 4.1.1, the mass flow rate entering chamber A during an extending movement will always be subsonic at steady-state. Assuming a uniform air temperature throughout the system, it can be stated that:

$$v_{e_ss} = \frac{p_s C p_0 \sqrt{1 - \left(\frac{p_A}{p_S} - b\right)^2}}{p_A A_A}.$$
(4.12)

In order to assess the piston velocity with the operating point, the actuator area has to be correlated with the pressure ratios of chambers A and B, which is achieved by the loading curve equation. Therefore, combining Equation (4.7) with (4.12) and diving both sides by the sonic conductance leads to:

$$\frac{p_S^2 p_0 \left(\frac{p_A}{p_S} - \left(\frac{p_B}{p_0}\right) \left(\frac{p_0}{p_S}\right) r_A - \frac{p_0}{p_S} (1 - r_A) - \mu_d\right) \sqrt{1 - \left(\frac{\frac{p_A}{p_S} - b}{1 - b}\right)^2}}{p_A F_L}.$$
(4.13)

As can be seen, the ratio of steady-state velocity to the sonic conductance becomes a function of the chamber pressure ratios (p_A/p_S) and p_0/p_B . As shown in Section 4.1.1, the chamber pressure ratios are mathematically correlated, as given by the operating curve equation. Therefore, applying Equation (4.2) to Equation (4.13) leads to the equation that describes the Velocity/C (vC) curve for an extending movement.

$$\frac{v_{e_ss}}{C} = \frac{p_S p_0}{\left(\frac{p_A}{p_S}\right) F_L} \sqrt{1 - \left(\frac{p_A}{1 - b}\right)^2 \left(\frac{p_A}{p_S} - \frac{p_0}{p_S} (1 - r_A) - \mu_d\right)} - \frac{\left(\frac{p_0}{p_S}\right)}{\frac{b}{r_A} + \sqrt{\frac{b^2 - 2b + 1}{r_A^2} + 1 + \left(\frac{p_A}{p_S}\right)^{-1} \left(-2b + \left(\frac{p_A}{p_S}\right)^{-1} (2b - 1)\right)}} \right).$$
(4.14)

Similarly, for the retracting movement:

$$\frac{v_{r_ss}}{C} = \frac{p_S p_0}{\left(\frac{p_B}{p_S}\right) F_L} \sqrt{1 - \left(\frac{\frac{p_B}{p_S} - b}{1 - b}\right)^2 \left(\frac{p_B}{p_S} + \frac{p_0}{p_S} \frac{(1 - r_A)}{r_A} - \frac{\mu_d}{r_A}\right)} - \frac{\left(\frac{p_0}{p_S}\right)}{br_A + \sqrt{r_A^2 (b^2 - 2b + 1) + 1 + \left(\frac{p_B}{p_S}\right)^{-1} \left(-2b + \left(\frac{p_B}{p_S}\right)^{-1} (2b - 1)\right)}} \right). \tag{4.15}$$

The vC equation becomes a function of on unique pressure ratio (p_A/p_S) for extending and p_B/p_S for retracting) and parameters that can be estimated during the initial design phase, such as supply pressure (p_S) , atmospheric pressure (p_0) , area ratio (r_A) , dynamic friction coefficient (μ_d) , critical pressure ratio (b), and load force (F_L) .

Figure 4.7 shows the operating curve along with the vC curve, energy efficiency, and robustness for the simulations presented in Figure 4.6. The three curves in each chart are correlated by the horizontal axis, as demonstrated by the vertical line placed at the point of maximum velocity.

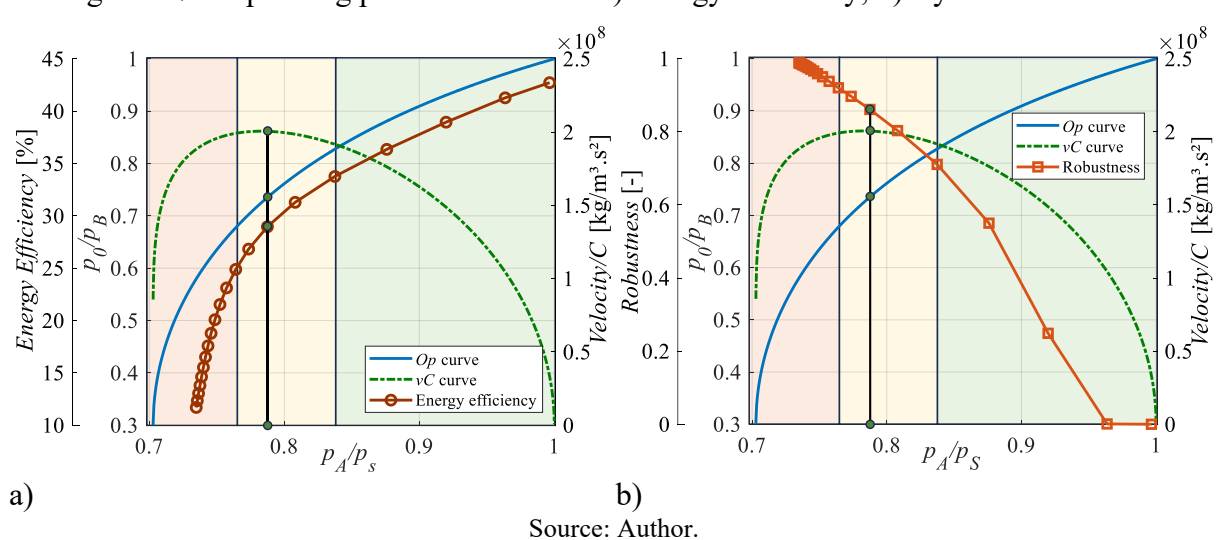


Figure 4.7 – Operating point curves with: a) Energy efficiency; b) Cylinder robustness

In Figure 4.7, the steady-state curves of the operating point method were analytically determined using equations (4.2) and (4.14). The data for energy efficiency and robustness were obtained through dynamic simulations, with each point corresponding to a simulation in the

sensitivity analysis shown in Figure 4.6. The green, yellow, and orange rectangles aim to facilitate the correlation between Figure 4.6 and Figure 4.7. As can be seen, the vC curve accurately describes the expected velocity behavior shown in Figure 4.6, with its maximum point coinciding with the cylinder that achieved the highest velocity in the sensitivity analysis.

The capacity of the vC curve to determine the maximum velocity area was thoroughly investigated during the development of this thesis and published in the Author's previous work (Vigolo, 2018; Vigolo; De Negri, 2021), including cases with larger cylinder diameters, higher load forces, and experimental results.

Therefore, the optimal operating condition, defined as the cylinder area that results in the maximum end-stroke velocity for a given application, is determined by a set of two pressure ratios. The first is the argument that maximizes the vC curve (p_A/p_S) for an extending movement and p_B/p_S for retracting), while the second corresponds to the counterpressure chamber pressure ratio (p_0/p_B) for an extending movement and p_0/p_A for retracting), as defined by Equations (4.2) and (4.4). This optimal set of pressure ratios is applied in Equations (4.7) or (4.8), which are valid for dynamic behavior and can be used to determine the optimal cylinder area.

However, due to the complexity of the vC curve equations, it is not possible to use their derivative to determine the pressure ratio corresponding to the maximum point, making the process dependent on numerical solutions. Nevertheless, certain characteristics of these equations enable the determination of an approximate function.

The first characteristic is the load force (F_L) , which appears only in the denominator of the vC equation and, consequently, does not affect the argument that maximizes the function. Moreover, the parameter related to sonic conductance (b) has a limited range of values between 0 and 0.528, with fixed values commonly adopted during the design phase. Beater (2007) suggests a value of 0.2 for commercial valves, while De Negri (2001) adopts a value of 0.4. Therefore, in this work, a fixed value of b = 0.3 will be assumed. Similarly, atmospheric pressure can also be considered constant due to its small variations with elevation relative to sea level. Thus, in this work, a value of $p_0 = 101,325$ Pa will be assumed for atmospheric pressure.

The remaining parameters that impact the argument that maximizes the vC equation are the supply pressure (p_S) , the area ratio (r_A) , and the dynamic friction coefficient μ_d . However, for most applications, these values are limited. For instance, the area ratio, according to the standardized dimensions in ISO 6432 (ISO, 2015) and ISO 15552 (ISO, 2004), has only

seven distinct values: [0.75, 0.84, 0.86, 0.90, 0.935, 0.96, 1.00]. The supply pressure is constrained by commercially available components, with values below 3 bar_{abs} or above 13 bar_{abs} rarely used. The dynamic friction coefficient of the cylinder typically ranges from 0.05 to 0.15, but high-speed tasks result in higher friction forces. Therefore, a friction coefficient ranging from 0.05 to 0.50 should cover most practical applications.

Considering that the argument that maximizes the vC equation depends solely on three parameters, which have limited values for most applications, it is possible to numerically calculate the argument that maximizes Equations (4.14) and (4.15) for all possible combinations of supply pressure, area ratio, and friction coefficient.

Figure 4.8 shows the graphical results for the argument that maximizes Equation (4.14), henceforth called $(p_A/p_S)_{Opt}$. The chart considers 11 discrete supply pressure values (3–13 bar_{abs}), 10 friction coefficient values (0.05–0.50), and the 7 area ratios from ISO 6432 and ISO 15552. It consists of 11 groups of vertical bars (supply pressure), each group containing 7 vertical bars (area ratios) subdivided into 10 color segments (friction coefficients). To use the chart, a group of supply pressure is selected on the horizontal axis, then a vertical bar is chosen based on the area ratio (see the r_A values legend), and a color segment corresponding to the friction coefficient (see the μ_d values legend) is selected. The $(p_A/p_S)_{Opt}$ value can be read from the vertical axis based on the selected color segment.

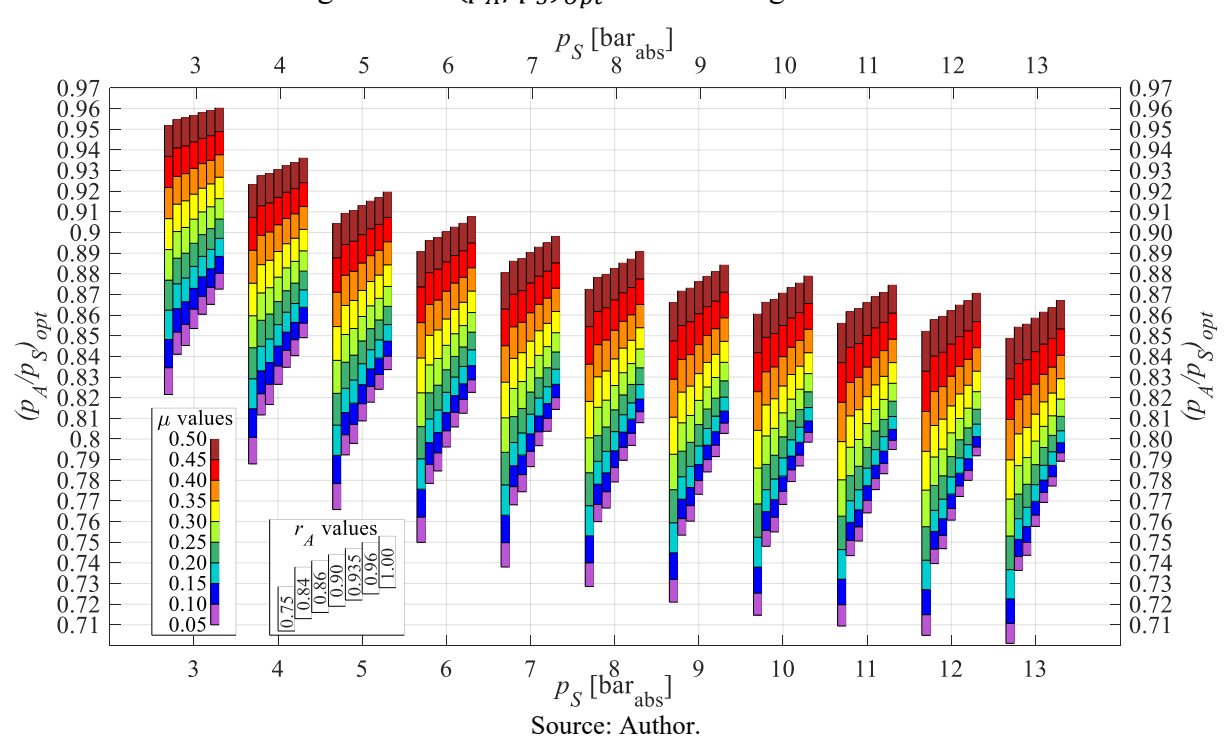


Figure $4.8 - (p_A/p_S)_{Opt}$ for extending movements

Similarly, for the retracting movement, the argument that maximizes Equation (4.15), referred to as $(p_B/p_S)_{Opt}$, is shown in Figure 4.9.

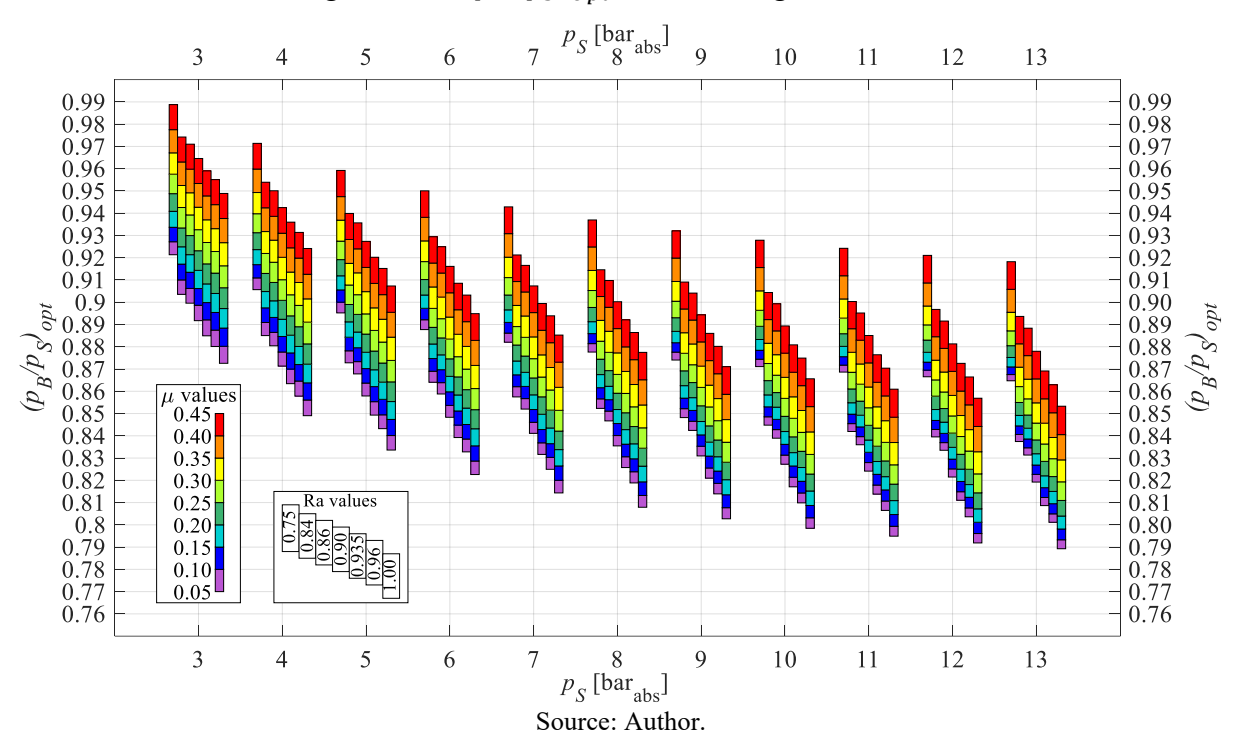


Figure $4.9 - (p_B/p_S)_{Opt}$ for retracting movements

As seen in Figure 4.8 and Figure 4.9, patterns can be identified to determine an approximate function. The $(p_A/p_S)_{Opt}$ and $(p_B/p_S)_{Opt}$ present an exponential decay with the supply pressure and show a linear correlation with the area ratio and friction coefficient. Therefore, based on these patterns, a nonlinear equation structure was proposed and a nonlinear regression was performed to determine its coefficients, resulting in approximate models for calculating $(p_A/p_S)_{Opt}$ and $(p_B/p_S)_{Opt}$, which are given by:

$$\left(\frac{p_A}{p_S}\right)_{opt} = 0.571 + 0.2326e^{\left(\frac{-0.2492p_S}{1\times10^5}\right)} + 0.1678r_A + 0.2483\mu_d, \tag{4.16}$$

and

$$\left(\frac{p_B}{p_S}\right)_{opt} = 1.013 + 0.1829e^{\left(\frac{-0.2438p_S}{1\times10^5}\right)} - 0.2420r_A + 0.1716\mu_d.$$
(4.17)

Figure 4.10 presents histograms of the errors obtained by comparing the numerical results from Figure 4.8 and Figure 4.9 with the results from Equations (4.16) and (4.17), respectively.

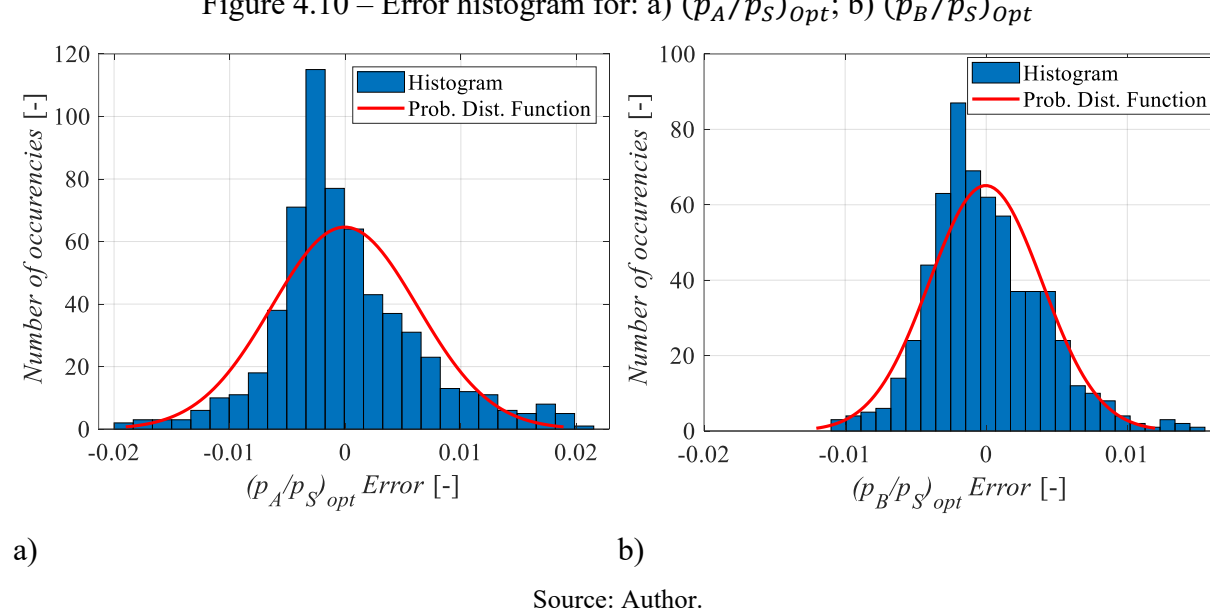


Figure 4.10 – Error histogram for: a) $(p_A/p_S)_{Opt}$; b) $(p_B/p_S)_{Opt}$

It can be concluded that 82% of the calculated values fall within a $\pm 1\%$ error margin. The maximum and minimum observed errors are 0.0208 and -0.0206, respectively, corresponding to percentage errors of 2.68% and -2.78% when compared to the numerical solution. This demonstrates that Equations (4.16) and (4.17) can satisfactorily determine the argument that maximizes the vC equation, thus making the operating point method independent of numerical solutions.

4.2 EXPERIMENTAL ANALYSIS OF THE FRICTION COEFFICIENT

Among the parameters required to apply the operating point method is the dynamic friction coefficient (μ_d), which is derived from a model proposed by Virvalo (1993). In this model, the cylinder friction is estimated based on the cylinder's maximum force capacity, that is

$$F_{fr} = \mu_d p_S A_A. \tag{4.18}$$

Even though the friction force is highly variable during piston displacement, with distinct characteristics such as static, Coulomb, and viscous friction that are not modeled by Equation (4.18), the model proposed by Virvalo (1993) has been adopted for the operating point equations due to its simplicity. Attempting to include a more detailed model, such as a viscous, velocity-dependent one, makes it unfeasible to derive the vC equation. Nonetheless, this friction coefficient model provides a rough estimation of the expected friction force in the application, which is sufficient for the early stages of the design process, where detailed data about cylinder friction is often unavailable.

Determining the correct value of the friction coefficient is a challenging task. Virvalo (1993) proposes a range for μ_d between 0.08 and 0.13, while in the tests performed by Vigolo and De Negri (2021), μ_d ranged from 0.17 to 0.33. As discussed in Section 2.3.1, some manufacturers suggest rules of thumb to estimate cylinder friction, often linked to cylinder efficiency ($\eta + \mu_d = 1$), where manometric pressure is commonly used instead of the absolute pressure assumed in this work. Overall, Figure 2.7 shows that the most common cylinder efficiency (η) is 0.8, which corresponds to a friction coefficient (μ_d) of 0.2, a widely used reference value during the design process.

Beyond the common challenges of modeling friction force in pneumatic cylinders described in Section 3.2.5, the designer has limited information about the system during the early stages of the design process. Typically, the only available information includes the expected load force, supply pressure, stroke, and displacement time.

In view of this, the literature currently lacks practical approaches for estimating friction forces during the design process. Fleischer (apud BEATER, 2007) proposes a rule of thumb in which the cylinder friction is correlated with the cylinder diameter ($F_{fr} = 400d_c$). Guido Belforte has published several papers on friction forces in pneumatic cylinders, focusing on correlations to determine friction force based on the physical characteristics of cylinders and seals (Belforte; Bertetto; Mazza, 2013; Belforte; D'Alfio; Raparelli, 1989; Belforte *et al.*, 2003; Mazza; Belforte, 2017), modeling contact pressure using experiments and Finite Element Methods (Belforte *et al.*, 2009; Belforte *et al.*, 2017; Belforte; Conte; Mazza, 2008), and proposing novel low-friction pneumatic seals (Belforte; Conte; Mazza, 2014). Similarly, Azzi *et al.* (2019) studied the impact of seal types, chamber pressure, piston diameter, and velocity on friction force.

Even though the aforementioned authors did not propose a model to predict friction force based solely on design parameters, they commonly reported the following observations:

1) Friction force increases almost linearly with air pressure; 2) The friction force increases with piston diameter, but not linearly, with a higher rate of increase for larger diameters; 3) The

friction force increases at a variable rate with increasing velocity, resulting convex, linear, or concave trends; 4) Lip seals results in higher friction forces compared to O-ring or lobed-type seals.

Therefore, a series of experiments were conducted in this thesis using a wide range of pneumatic cylinders to identify patterns in friction force and develop an approximate model based solely on three main parameters: piston velocity, piston diameter, and supply pressure. The tests involved 10 distinct pneumatic cylinders from Camozzi, as detailed in Table 4.2.

Table 4.2 – Specifications of the tested cylinders

Model	Piston diameter $d_{\mathcal{C}}$ [mm]	Rod diameter d _r [mm]	Stroke L [mm]	Seal type/ Material
16N2A08A100	8	4	100	Lip/Polyurethane
16N2A10A100	10	4	100	Lip/Polyurethane
16N2A12A100	12	6	100	Lip/Polyurethane
25N2A16A100	16	6	100	Lip/Polyurethane
25N2A20A100	20	8	100	Lip/Polyurethane
25N2A25A100	25	10	100	Lip/Polyurethane
63MT2C032A0100	32	12	100	Lip/Polyurethane
63MT2C040A0100	40	16	100	Lip/Polyurethane
63MT2C050A0100	50	20	100	Lip/Polyurethane
63MT2C063A0100	63	20	100	Lip/Polyurethane

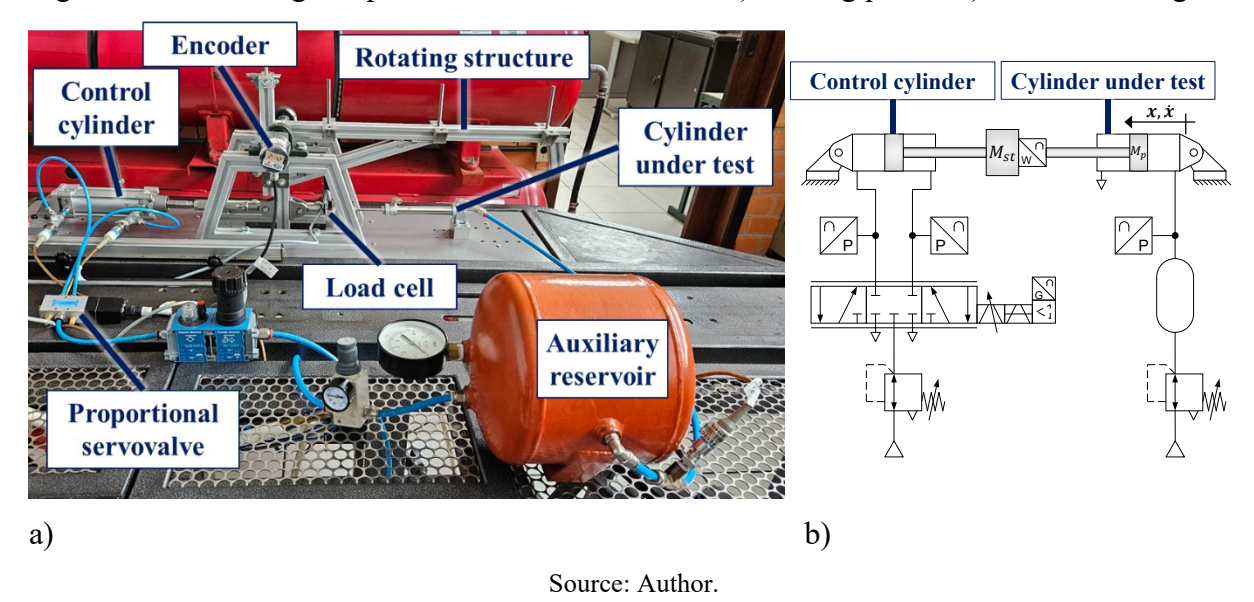
Source: Author.

Beyond the characteristics presented in Table 4.2, the cylinders used for the experiments were brand new, with barely any previous use. The compressed air supplied to the system met ISO 8573-1:2010 class 1.4.1 requirements, indicating very low particle and oil content and a moderate dew point (ISO, 2010). The ambient temperature during the tests was 23 ± 2 °C

The test rig used for the experiments is called Ybitú (Figure 4.11). It was set up so that one pneumatic chamber of the cylinder under test was maintained at a constant pressure, while the other chamber remained at atmospheric pressure. A small auxiliary reservoir was used to ensure a constant pressure for the cylinder under test. To control the piston velocity, an opposing cylinder was added to the test rig and controlled by a proportional servovalve, model MPYE5 1/4HF010B from FESTO. A load cell was attached to the rod of the cylinder under test, and the position was measured using an encoder that tracked the rotational displacement of the structure. Detailed information about the instrumentation and the test rig's mathematical

model is provided in Appendix E. Figure 4.11 shows the test rig setup with its main components.

Figure 4.11 – Test rig setup for friction measurement: a) Test rig photo; b) Pneumatic diagram



Tests were conducted measuring several full-stroke displacements of the cylinder. In each test, the piston velocity increased by a fraction. A force balance, according to Equation (4.19), was performed when the piston reached half of the total stroke.

$$M_p \frac{d^2 x}{dt^2} = p_A A_A - p_B A_B - p_0 A_r - F_{fr} - F_{L.C.}, \tag{4.19}$$

where M_p is the mass of the piston of the cylinder under test, F_{fr} is the friction force, and $F_{L.C.}$ is the load cell force.

Inertial effects caused by the moving structure's weight (M_{st}) were measured by the load cell. The inertial effects due to the piston assembly's weight (M_p) were minimal because of its relatively small mass. Nevertheless, an average acceleration was estimated by fitting a linear model to the velocity points obtained between 40% and 60% of the cylinder's stroke. For each cylinder, tests were conducted with three different pressure levels $(4, 6, \text{ and } 8 \text{ bar}_{abs})$ applied in chambers A (for extending displacement tests) and B (for retracting displacement tests). The results are shown in Figure 4.12.

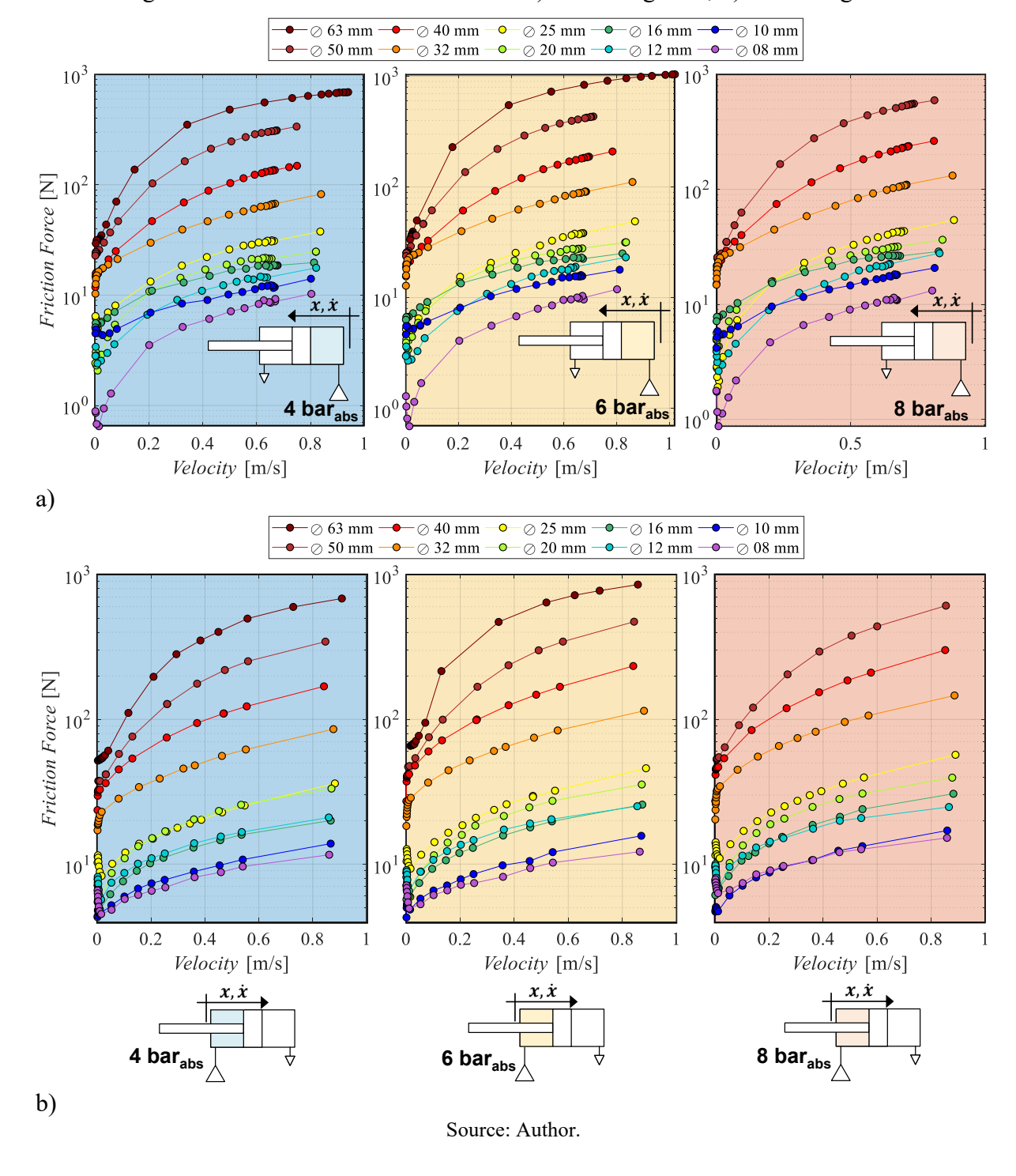


Figure 4.12 – Measured friction forces: a) Extending tests; b) Retracting tests

The reason for pressurizing only one chamber at a time is that, during operation, a pneumatic actuation system typically operates with one chamber at high pressure (the driving chamber), while the other remains close to atmospheric pressure (the counterpressure chamber). Therefore, the tests were conducted to assess friction under conditions closer to those expected during the operation of the drives.

It can be seen that the results align with the observations described by Belforte and Azzi, showing that friction force increases with supply pressure, cylinder diameter, and velocity. During extending tests at low velocities, cylinders with diameters of 10 mm and 16 mm presented out-of-trend behavior, with friction forces slightly higher than expected. Possible explanations for this behavior might include varying levels of lubrication and cylinder misalignment.

To identify patterns and derive approximate models, the friction force results obtained from the complete set of actuators were used to interpolate friction forces at uniform velocity intervals of 0.05 m/s, ranging from 0.05 to 0.7 m/s. The results for extending and retracting movements are presented in Figure 4.13. In this figure, the groups of vertical bars represent the three different pressure levels, as indicated in the legend. Cylinder diameters are distinguished by color and the interpolated experimental friction force values are represented with squares. Colored vertical arrows are used to indicate trend behaviors. Tests with the Ø63 mm cylinder at 8 bar_{abs} supply pressure could not be carried out, since only one cylinder of this diameter was available, and the Ø53 mm control cylinder was not capable of controlling the Ø63 mm piston at 8 bar.

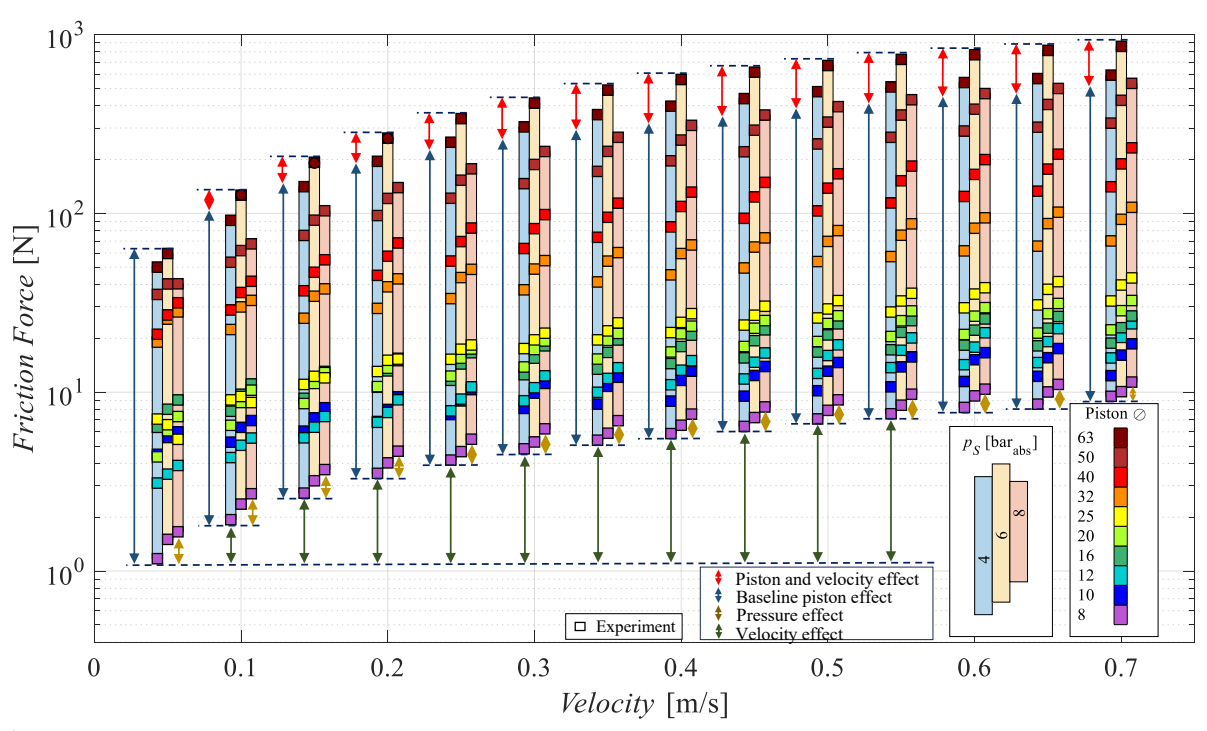
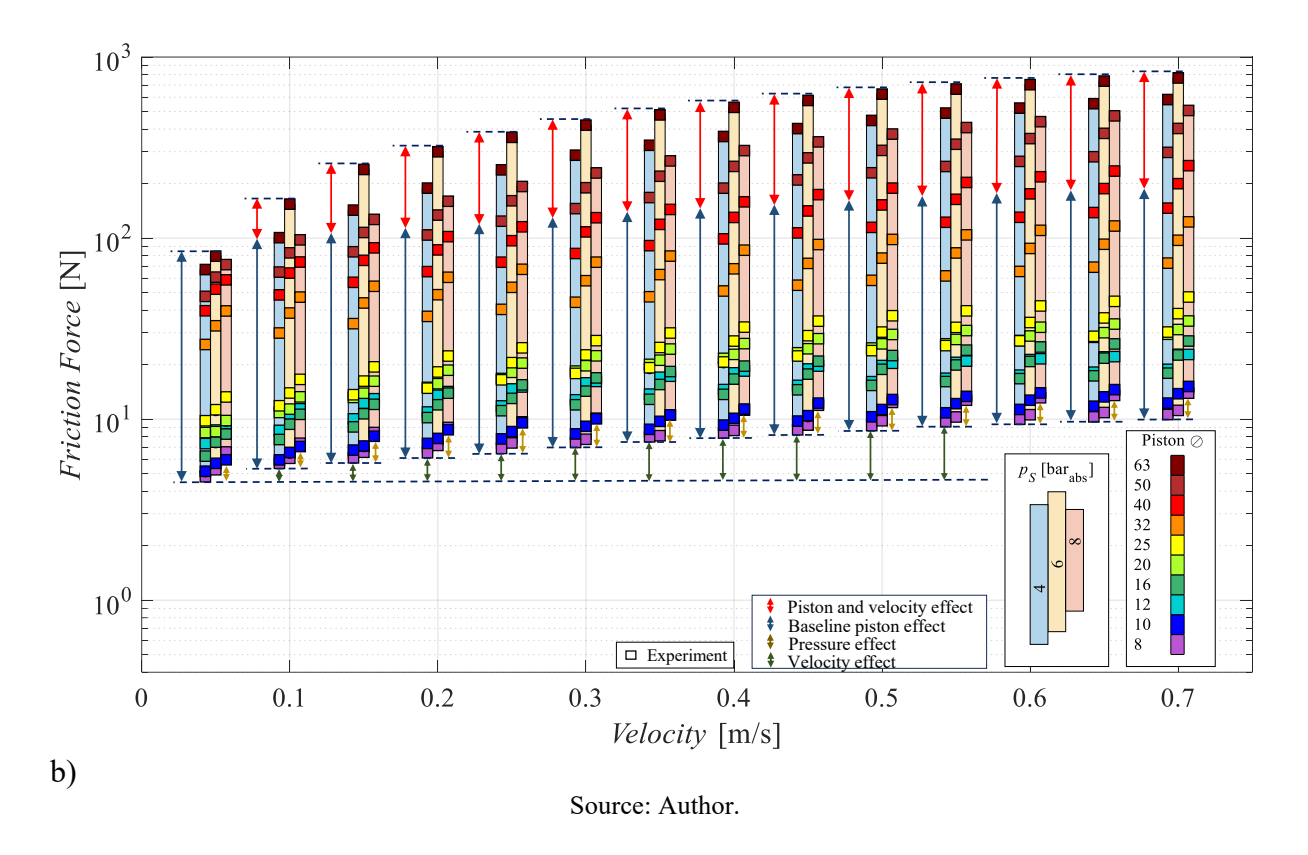


Figure 4.13 – Interpolated experimental results of friction force: a) Extending; b) Retracting

a)



In Figure 4.13, the blue arrows represent the baseline piston effect, with a fixed length equal to the friction force variation due to cylinder diameter at the smallest velocity. The red arrows are complementary to the blue arrows, showing the additional effect of piston diameter at higher velocities. The yellow arrows indicate the friction force variation due to chamber pressure changes at the same velocity, while the green arrows represent the variation caused by increasing velocity.

The results are consistent with commonly reported behavior in the literature, showing that friction force increases with supply pressure, cylinder diameter, and velocity (Azzi *et al.*, 2019; Beater, 2007; Belforte *et al.*, 2003). Moreover, for cylinders between Ø8 and Ø40 mm, the friction force during retraction is significantly higher than during extension. For the Ø50 mm and Ø63 mm cylinders, however, only minor differences are observed between extension and retraction. Consequently, the amplitude of friction force variation with cylinder piston diameter is greater during extension. A similar trend is also seen in the results presented by Azzi *et al.* (2019). A possible explanation for this behavior is that larger rod diameters often require a more robust rod seal design, which better resists pressure-induced deformation and reduces directional friction asymmetry.

In general, the results presented in Figure 4.13 evidence the existence of three main trends that affect the overall friction behavior of the ten tested cylinders, which are:

- 1) Friction force increases with velocity, but its rate of increase reduces at higher velocities (green arrows), resulting in a concave shape;
- 2) Piston and rod diameters exponentially affect the friction force (blue arrows), although their effect has a higher magnitude at higher velocities (red arrows);
- 3) Chamber pressures increase the friction force at a rate close to logarithmic (yellow arrows);

Based on the aforementioned patterns, the following nonlinear model was derived to represent the friction force (F_{fr}) as a function of piston velocity (v), chamber A and B pressures $(p_A \text{ and } p_B)$, and cylinder and rod diameters $(d_c \text{ and } d_h)$:

$$F_{fr} = e^{\underbrace{\left(\frac{-k_1}{|v|^{k_7} + (d_c + d_h)^{k_5} + k_6}\right)}_{\text{(1) Velocity-dependent term}} \cdot \underbrace{e^{k_2(d_c + d_h)} \cdot \left(k_3(d_c + d_h) + k_4ln\left(\frac{p_A + p_B}{1 \times 10^5} + k_8\right)\right)}_{\text{(3) Linear + Logarithmic pressure term}}, \tag{4.20}$$

In Equation (4.20), the first term describes the concave downward increase of friction force with piston velocity. The second term represents the exponential dependence on piston diameter, while the third term models the logarithmic influence of chamber pressures. The inclusion of piston and rod diameters in the first and third terms is intended to reflect the reduced influence of piston diameter on friction force at low velocities, as illustrated by the red arrows in Figure 4.13. It is important to note that, in Equation (4.20), the piston and rod diameters are given in millimeters. This differs from the rest of the equations presented in this thesis, which use SI units. The reason for this choice was to facilitate the convergence of results during the nonlinear regression.

Based on the proposed model and the experimental data obtained from the tested cylinders, the coefficients of Equation (4.20) were determined using nonlinear regression. The resulting coefficients for extending displacements are as follows:

$$k_1 = 0.5426, \qquad k_3 = -0.07416, \qquad k_5 = -0.02959, \qquad k_7 = 1.2198, \\ k_2 = 0.07196, \qquad k_4 = 4.9434, \qquad k_6 = -0.72996, \qquad k_8 = 1.4475.$$

Passivity is a desirable characteristic of friction models, as it ensures that the friction force always dissipates energy and never generates it (Mashayekhi *et al.*, 2014). As shown by Tadese *et al.* (2021), the energy dissipated due to friction (E_{fr}) can be calculated as the time integral of the friction force multiplied by velocity, that is:

$$E_{fr}(t) = \int_0^t F_{fr}(t). v(t) dt.$$
 (4.21)

To ensure the passivity of the model, it is required that $E_{fr}(t) \ge 0$ for all t. Since the exponential of a real number is always positive, the following conditions of Equation 4.20 must be satisfied to guarantee $F_{fr} \ge 0$:

$$k_8 > -\frac{p_A + p_B}{1 \times 10^{5'}} \tag{4.22}$$

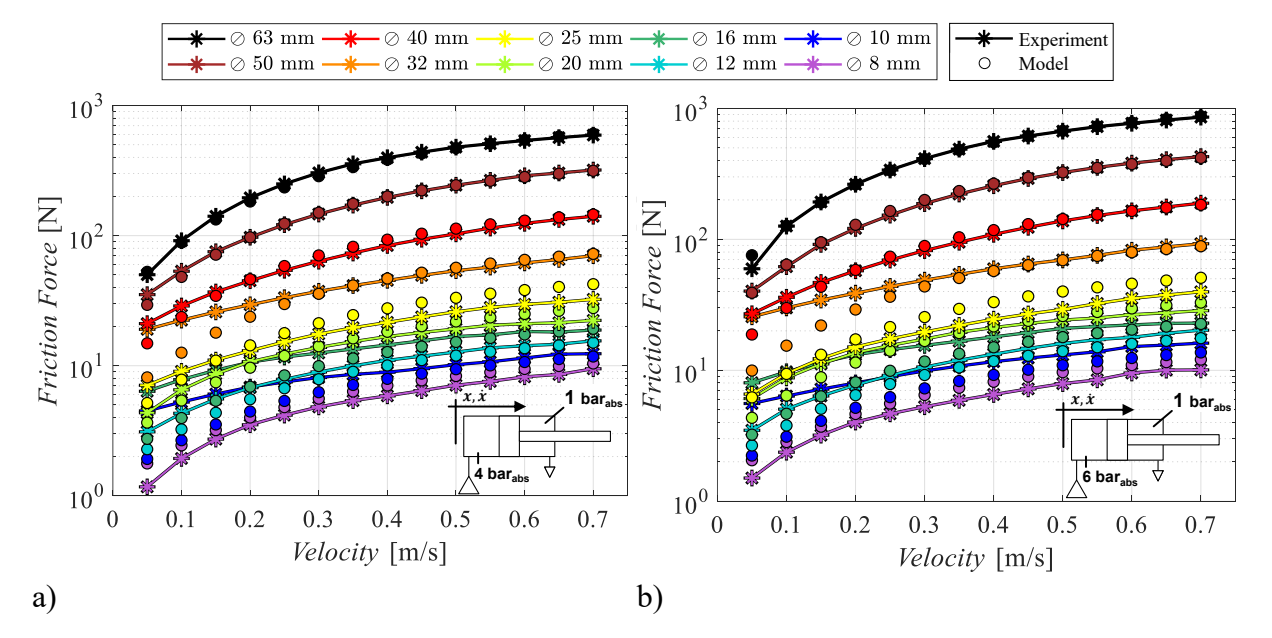
and

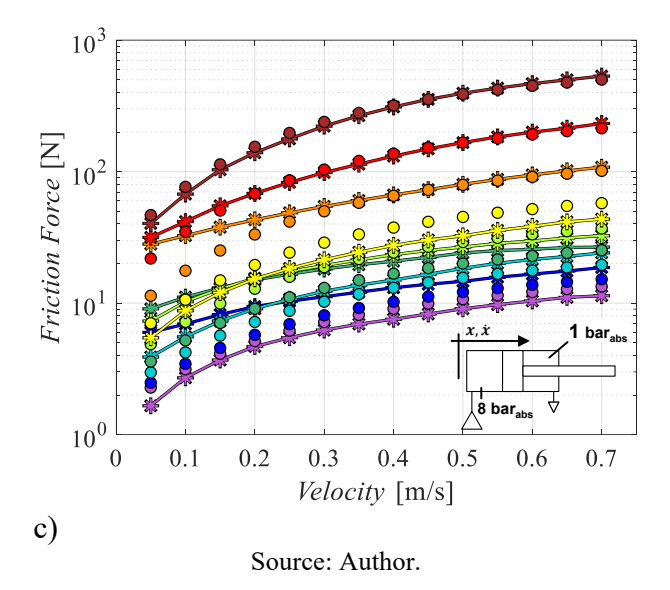
$$k_3 \ge -\frac{k_4 ln \left(\frac{p_A + p_B}{1 \times 10^5} + k_8\right)}{(d_c + d_h)}.$$
(4.23)

Based on the calculated coefficients, it can be concluded that Equation (4.20) ensures passivity for positive velocities when $p_A + p_B \ge 2.026 \times 10^5$ Pa, and $d_c + d_h \le 83$ mm, which are boundaries of the data over which the model was fitted. Therefore, the coefficients presented in this thesis are recommended for cylinders with a piston diameter (d_c) up to 63 mm.

The results of the proposed model are compared with the experimental results in Figure 4.14. In the figure, charts a), b), and c) correspond to experiments conducted at constant driving chamber pressures of 4, 6, and 8 bar_{abs}, respectively. In each chart, experimental results are represented by continuous lines with star markers, while the model predictions are shown as filled circles.

Figure 4.14 – Experimental and model results for friction in extending movement





As can be seen, the predicted values (filled circles) present a good agreement with the experimental values (continuous line with star markers), showing that the proposed model is capable of satisfactorily determining the friction force of the tested cylinders. As expected, it does not precisely determine the friction force for all evaluated points. However, it provides a good approximation of the expected cylinder friction. A quantitative assessment of the accuracy is provided by the histograms in Figure 4.16.

For negative velocities, the calculated coefficients of Equation (4.20) are:

$$k_1 = 0.4195, \qquad k_3 = -0.0661, \qquad k_5 = -0.1913, \qquad k_7 = 1.3323, \\ k_2 = 0.0730, \qquad k_4 = 4.0969, \qquad k_6 = -0.2770, \qquad k_8 = 1.3580.$$

For negative velocities, passivity is ensured when $p_A + p_B \ge 2.47 \times 10^5$ Pa, and $d_c + d_h \le 83$ mm. Moreover, due to the exponential terms, Equation (4.20) does not yield negative values for retracting movements, which requires a careful analysis of the reference coordinate system. Depending on the application scope, for instance, simulation or control purposes, a sign(v) function might be required in Equation (4.20) for consistency. However, for cylinder sizing, the sign(v) function is not necessary.

In Figure 4.15, the experimental results are compared with the model results for the retracting movement.

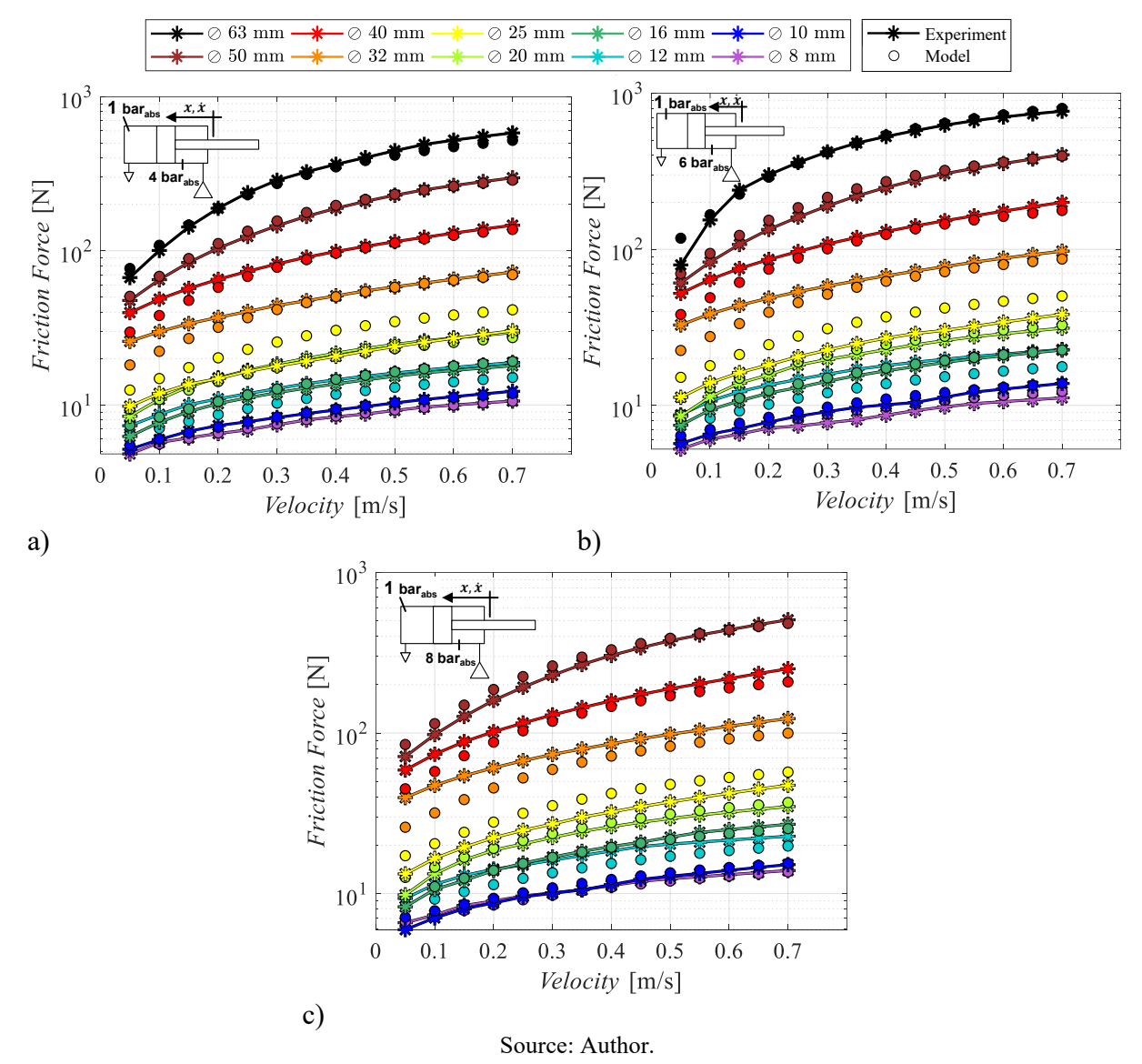


Figure 4.15 – Experimental and model results for friction in retracting movement

Once again, it can be seen that the predicted values (filled circles) present a good agreement with the experimental values (continuous line with star markers), demonstrating the model's satisfactory performance in determining friction force during both extension and retraction. Figure 4.16 provides a quantitative assessment, comparing the relative friction force error (F_{fr} error) of the proposed model against a baseline model. The baseline model corresponds to the most frequent yield value reported in Figure 2.7 ($\eta = 0.8$), which is equivalent to a friction coefficient μ_d of 0.2.

In Figure 4.16, the F_{fr} error is calculated as follows:

$$F_{fr} \text{ error} = 100. \frac{F_{fr_exp} - F_{fr_model}}{F_{fr_exp}}, \tag{4.24}$$

with F_{fr_exp} representing the experimental friction forces. For the proposed model, F_{fr_model} is calculated using Equation (4.20), while the baseline model, F_{fr_model} is calculated using Equation (4.18), assuming μ_d to be 0.2.

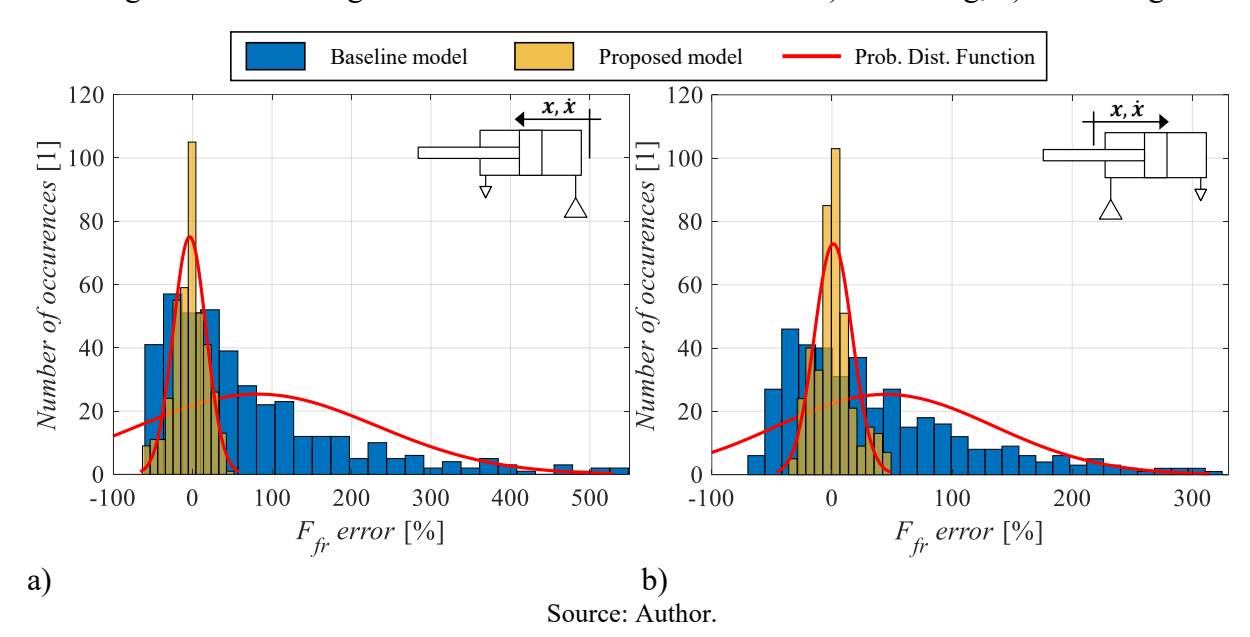


Figure 4.16 – Histogram of relative friction force error: a) Extending; b) Retracting

The histograms in Figure 4.16 demonstrate that the errors of the proposed model remained within a \pm -30% error margin for 88.9% of the data, and the maximum observed errors were -61.2% to 51.3%. This represents a significant improvement compared to the commonly assumed value of $\mu_d = 0.2$, which resulted in errors of more than 600%. As shown in Figure 4.14 and Figure 4.15, the largest prediction errors occur at low velocities, where the friction force is relatively small compared to the cylinder's maximum force. Therefore, the high local errors observed under these conditions are not significant for the design process of pneumatic drives.

However, to apply Equation (4.20) for estimating the friction coefficient, the cylinder diameter must be known. This introduces the need for an iterative process during the design phase, as the vC equation requires the friction coefficient to determine the cylinder area.

Therefore, for each combination of cylinder diameter, supply pressure, and piston velocity in Figure 4.13, an optimal load force was determined. This optimal load force is defined as the force that should be applied in a pneumatic actuation system operating with specific values of supply pressure, chamber area, and friction force, in order to operate near the

maximum velocity point of the vC curve shown in Figure 4.7, that is, near the optimal operating point.

To determine the optimal load force, friction force values were predicted using Equation (4.20) over a wide range of data, including supply pressure $p_s = [4, 6, 8]$ bar_{abs}, piston velocity v = [0.05, ..., 0.7] m/s, and piston diameter $d_c = [8, ..., 63]$ mm. The predicted friction values were converted into a calculated dynamic friction coefficient ($\mu_{d,calc}$) using Equation (4.18). The calculated dynamic friction coefficients, associated with the piston area and supply pressure, were then applied to Equations (4.16) and (4.2), respectively, resulting in the optimal pair of pressure ratios ($(p_A/p_A)_{opt}$, $(p_0/p_B)_{opt}$). This set of optimal pressure ratios, together with the cylinder area (A_A), dynamic friction coefficient (μ_d), and supply pressure (p_s), was subsequently applied in Equation (4.7) to calculate the resulting load force, representing an optimal loading condition.

The procedure described above was applied for the extending movements. For retracting movements, a similar approach was followed, but using Equations (4.18), (4.17), (4.4), and (4.8). This analysis enabled the correlation of the dynamic friction coefficient with piston velocity, supply pressure and load force, and the results are presented in Figure 4.17.

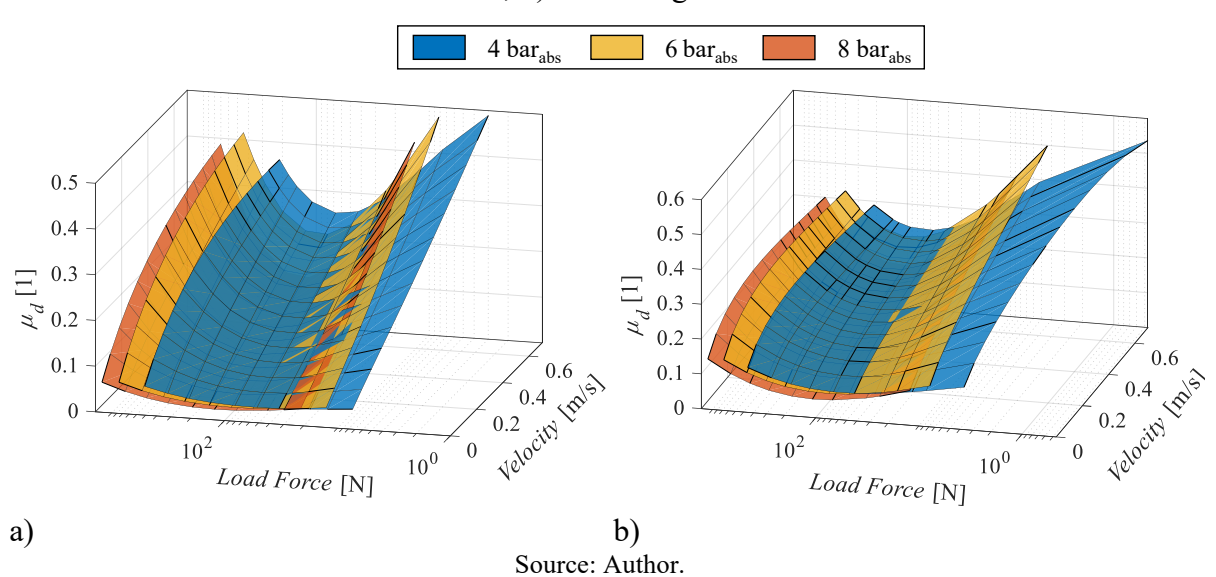


Figure 4.17 – Correlation of friction coefficient, piston velocity, and load force: a) Extending movement; b) Retracting movement

The reason for adopting a calculated dynamic friction coefficient (μ_{d_calc}) in this analysis, rather than directly using the experimental data to define (μ_d), is that μ_{d_calc} relies on the friction force determined by Equation (4.20). This formulation better represents the global

behavior of the tested cylinders and is therefore more suitable for generalizing the friction force behavior. Nonetheless, Figure 4.14 and Figure 4.15 show that Equation (4.20) is capable of closely representing the friction data obtained from the experiments.

The surfaces in Figure 4.17 indicate an inverse correlation between the friction coefficient and supply pressure. Specifically, increasing the supply pressure reduces the friction coefficient, even though the friction force increases with supply pressure. This can be explained by the fact that the friction force increases at a lower rate than the pneumatic force produced by the cylinder when the pressure is increased.

Another noteworthy characteristic is that the friction coefficient has a minimum value for load forces around 40-180 N, which corresponds to cylinders in the range of 16 to 32 mm. This characteristic may be the result of a combination of factors, including the tendency of smaller cylinders having higher friction coefficients due to ratio of cylinder circumference to the piston area and the fact that bigger cylinders require an increased seal area, increasing the friction force. Even though this is not the goal of the current work, the results of Figure 4.17 indicate that it is preferable to work with cylinders in the range of 16 to 32 due to its lower relative friction.

Based on the results shown in Figure 4.17, the following polynomial model has been derived to predict the friction coefficient as a function of load force, supply pressure, and piston velocity.

$$\mu_d = v^{z_7} \left(z_1 \left(ln(F_L) + \frac{z_4 p_s}{1 \times 10^5} \right) + z_2 \left(ln(F_L) + \frac{z_5 p_s}{1 \times 10^5} \right)^2 + z_3 \left(ln(F_L) + \frac{z_6 p_s}{1 \times 10^5} \right)^3 \right). \tag{4.25}$$

For extending displacements, the coefficients of Equation (4.25) are

$$z_1 = 0.2613, \qquad z_3 = 0.0149, \qquad z_5 = 0.2175, \qquad z_7 = 1.$$
 $z_2 = -0.1042, \qquad z_4 = 0.7581, \qquad z_6 = 0.0146,$

And for retracting movements, the z coefficients are

$$z_1 = 0.09827,$$
 $z_3 = 0.00644,$ $z_5 = 0.46136,$ $z_7 = 0.54676.$ $z_2 = -0.0428,$ $z_4 = 1.97957,$ $z_6 = 0.11524,$

The histograms in Figure 4.18 show the relative dynamic friction coefficient error, which is given by

$$\mu_d \text{ error} = 100. \frac{\mu_{d_calc} - \mu_{d_model}}{\mu_{d_calc}}, \tag{4.26}$$

where μ_{d_calc} corresponds to the calculated dynamic friction coefficients shown in Figure 4.17, and μ_{d_model} is given by Equation (4.25) for the proposed model. For the baseline model, μ_{d_model} is assumed to be 0.2, corresponding to the most frequent yield value ($\eta = 0.8$) reported in Figure 2.7.

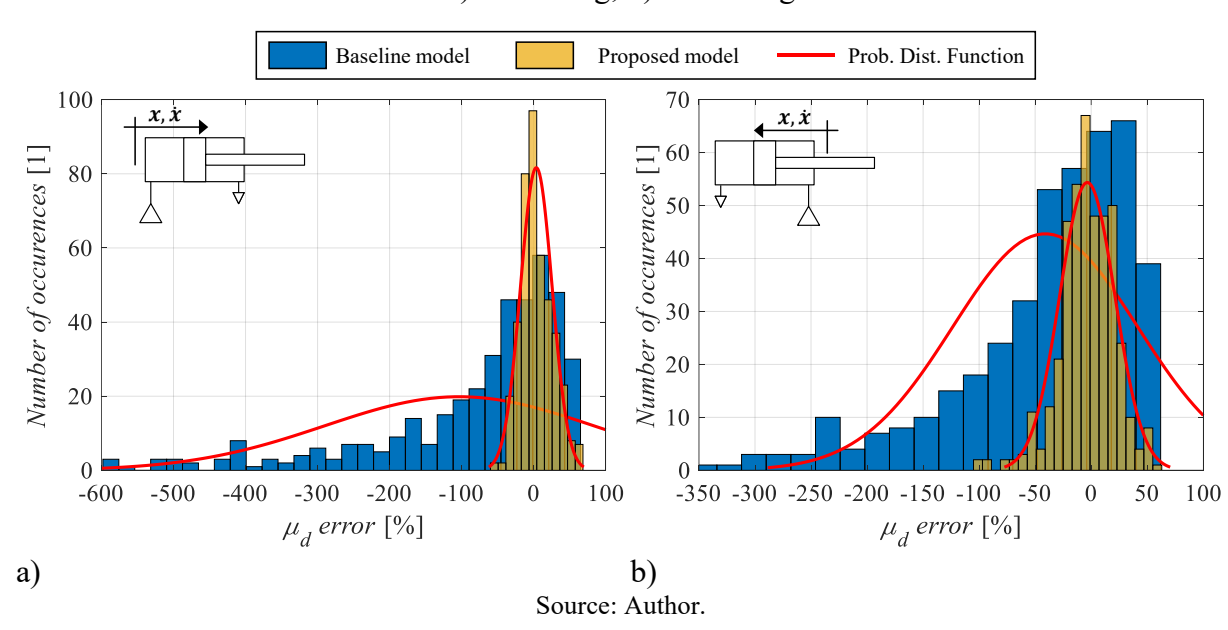


Figure 4.18 – Relative error histogram of the dynamic friction coefficient model: a) Extending; b) Retracting

Once again, the errors predicted by the proposed model were significantly smaller than those of the baseline model. Specifically, 83.2% of the data fell within a $\pm 30\%$ error margin, representing a significant improvement compared to the baseline model, where only 36.7% of the data remained within this margin. The main advantage of Equation (4.25) is that it provides an estimate of the expected dynamic friction coefficient using inputs commonly used as design requirements for the dimensioning of pneumatic drives, which are load force, supply pressure and piston velocity. This characteristic enables Equation (4.25) to be used along with the operating point equations, not requiring the use of an iterative process to determine the dynamic friction coefficient (μ_d), and avoiding the use of heuristic rules during the selection of pneumatic cylinders.

It should be noted that the results presented by Equations (4.20) and (4.25) are valid only under the conditions stated at the beginning of this section, which include, among others, the specific cylinder manufacturer, cylinders in brand-new condition, and unlubricated air. Using the presented equations beyond this scope is likely to result in significant errors. As Beater (2007) stated, 'a bit of lubrication can change everything.' Nonetheless, in the absence

of more precise system information, the equations presented in this section should provide a rough estimate of the expected friction force and dynamic friction coefficient for pneumatic actuators with cylinder diameters ranging from 8 to 63 mm.

4.3 CLASSIFICATION OF DISCRETE PNEUMATIC APPLICATIONS

Due to their robustness, agility, low acquisition cost, and power-to-weight ratio, pneumatic actuation systems have a wide range of applications, each with specific characteristics that must be considered during the sizing process. For example, Fialho (2004) adopts different safety coefficient values for applications with fast or slow displacement velocities and with or without the presence of a load during movement. Bimba (2011), on the other hand, considers only a coefficient related to displacement velocity, while Boyko; Hülsmann and Weber (2021) classify applications into press and movement tasks.

Based on the applications of pneumatic actuation systems described in Bollmann (1997), Prudente (2000) and Hesse (2001), and considering the aspects outlined in Fialho (2004) and Boyko; Hülsmann and Weber (2021), a classification of discrete pneumatic actuation systems into two categories is proposed: static and dynamic applications. Each category has distinct characteristics that define the requirements for cylinder sizing.

4.3.1 Static applications

It covers applications where the force produced by the actuator during piston displacement is either minimal or nonexistent. In such cases, the maximum force for which the cylinder is dimensioned occurs when the piston is stationary. The main characteristic of a static application is the constant chamber volume during the execution of the cylinder's main task, resulting in stable chamber pressures and, consequently, facilitating their determination.

A static application is not limited to scenarios without piston displacement. Instead, it involves the requirement of maximum force during moments of null or quasi-static displacement. Examples include tasks such as fixing parts, pressing, stamping, and forming. Load-generating equipment, such as tensile and compression testing machines, also falls into this category. Figure 4.19 presents a generic example of the main forces acting in a static application.

 x, \dot{x} F_{KS} $(p_s p_0)AA$ F_{KS} F_{KS}

Figure 4.19 – Generic example of a static pneumatic application

Source: Author.

Figure 4.19 shows an application of a single-acting cylinder. In this case, the forces acting on the piston are the force produced by the driving chamber $((p_S - p_0)A_A)$, the compressive force of the spring (F_{Kx}) , and the reaction force (F_r) , exerted by a rigid surface that holds the piston stationary. Therefore, for a static application, the sizing load is simply determined by

$$F_L = MgSin(\alpha) + K(x_{pre} + L) + F_r, \tag{4.27}$$

with $MgSin(\alpha)$ representing the gravitational forces, K the spring stiffness and x_{pre} the spring preload.

It can be highlighted that the forces presented in Figure 4.19 represent a generic example of a static application. In each specific case, additional forces may need to be considered, or some may need to be removed, depending on the application's characteristics. However, the fundamental characteristic of a static application is the constant volume of the chambers during the execution of the main task for which the actuator is being dimensioned. In such cases, the pressure in the driving chamber and the opposing chamber will be equal the supply pressure and atmospheric pressure, respectively.

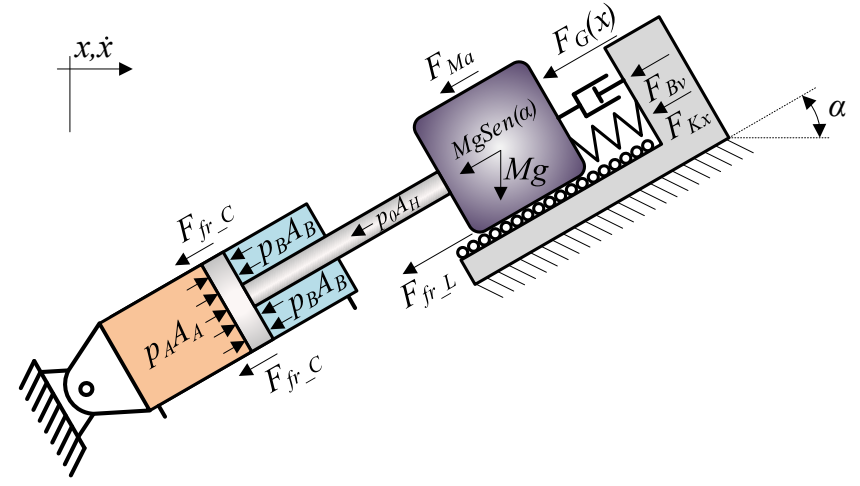
4.3.2 Dynamic applications

This category includes applications that require significant force during piston displacement, such as the movement and manipulation of objects, actuation of articulated mechanisms, assembly tasks, and various manufacturing processes, including folding, drilling,

cutting, and machining, among others. Figure 4.20 presents the main forces acting in a dynamic application, which can be classified into two groups: pneumatic forces and load forces.

The pneumatic forces include those that are independent of the load, that is, the forces produced by the pressures in chambers A $(p_A A_A)$ and B $(p_B A_B)$, the atmospheric pressure acting on the cylinder rod $(p_0 A_h)$, and the cylinder's friction force (F_{fr_C}) . The second group encompasses all forces produced by the load being moved, such as inertial forces (F_{Ma}) , gravitational forces $(MgSin(\alpha))$, friction between the mass and the surface (F_{fr_L}) , compressive forces from springs (F_{Kx}) and dampers (F_{Bv}) , and a generic force (F_G) that accounts for forces not covered by the aforementioned categories.

Figure 4.20 – Generic example of a dynamic pneumatic application



Source: Author.

In dynamic applications, the behavior of the pressures in both chambers is influenced by changes in their volumes. Since the application requires force during piston displacement, the sizing of the actuator must account for these pressure changes. This aspect justifies the use of operating point equations, whose main goal is to determine the pressures in the cylinder chambers for optimal operation.

Beyond the pressure changes in the cylinder chambers, the load force applied to the cylinder in dynamic applications usually presents some degree of variability throughout the piston stroke. This variability can be caused by factors such as friction forces on cylinder guides or loads, the presence of springs and dampers, nonconstant acceleration during displacement, or the actuation of mechanisms that result in Cartesian force decomposition.

The amplitude of variability depends on the specific application. Tasks involving the displacement of objects are generally assumed to have constant load forces, although inertial

forces and friction between the load and the moving surface may influence the load force to some extent. In general, linear bearings present negligible viscous forces, and the spring in single-acting cylinders rarely accounts for more than 10% of the maximum cylinder force. Applications involving the actuation of mechanical arms, mechanisms, or large masses are more likely to show a strong dependence of the load force on the cylinder stroke.

Therefore, to better understand how the load force behaves during piston displacement, a set of 12 experiments was performed to investigate the impact of different load components and their magnitudes on the load force profile. The effects of four load force components were investigated, which are:

- Gravity Force: The force generated by gravitational acceleration acting on the mass.
- **Spring Force:** A force proportional to the displacement caused by the compression or stretching of springs.
- Viscous Force: A force proportional to the piston velocity, resulting from the displacement of dampers or viscous materials.
- **Inertial Force:** The force generated due to the acceleration of a moving mass.

The experiments were divided into three groups (G) with the following characteristics:

G1: Gravity force is dominant over the other forces;

G2: All force components have similar magnitudes;

G3: The gravity force magnitude is minimal.

Within each group, the experiments are characterized by four different combinations of load components:

GX.1: Gravity and acceleration forces;

GX.2: Gravity, spring, and acceleration forces;

GX.3: Gravity, viscous, and acceleration forces;

GX.4: Gravity, spring, viscous, and acceleration forces.

The experiments were conducted on the Ybitú test rig, using cylinders with piston diameters of 25 mm and 50 mm, each with a 100 mm stroke performing an extending movement. The valve setup consisted of a directional valve and a set of two throttle valves configured in a meter-out setup. The different load components were reproduced by specific features of the test rig structure, which enables experiments with:

High inertia: Placing weights on the lower part of the vertical arm;

High gravity forces: Placing weights on the upper horizontal arm;

Spring forces: Traction springs attached to the vertical arm;

Viscous forces: Cylinder placed on the opposite side of the testing cylinder.

An overview of the test rig structure and its load force components is shown in Figure 4.21, and detailed information about the instrumentation and the test rig's mathematical model is provided in Appendix E.

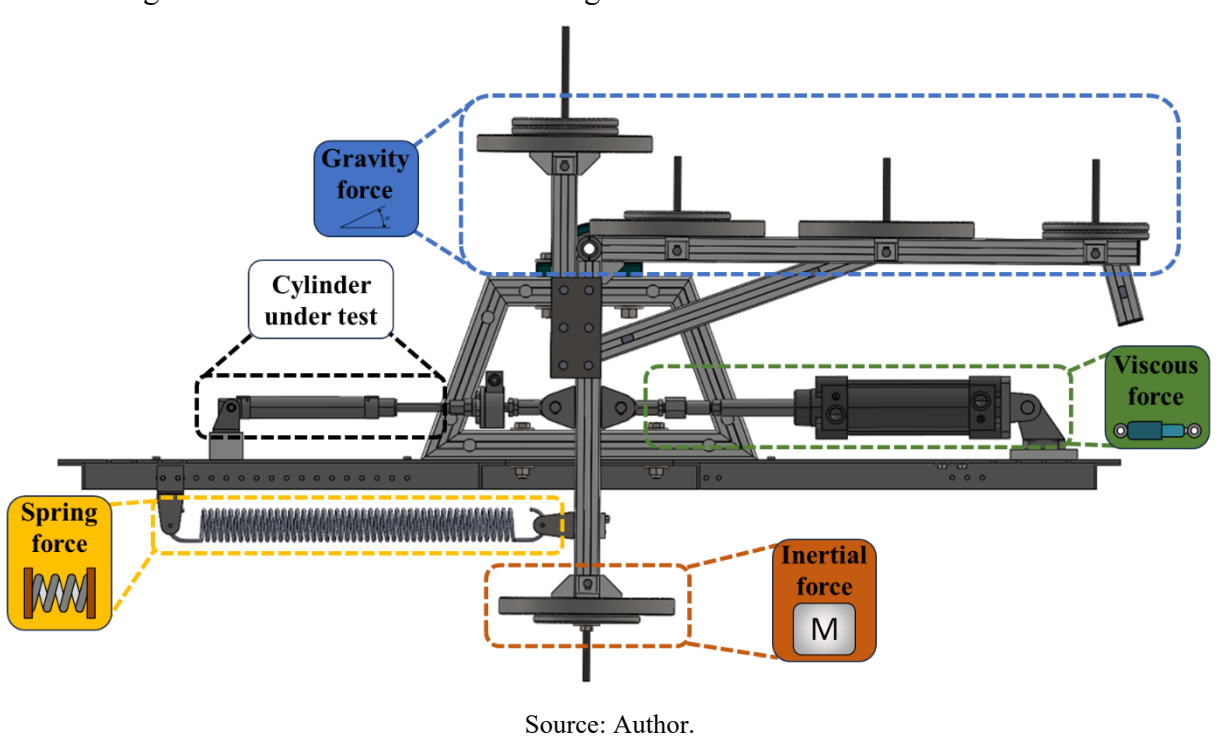


Figure 4.21 – Overview of the test rig structure and load force characteristics

The features of the test rig were selected to represent the desired characteristics of the experiment. This involved an iterative process among the kinematic model of the structure, its

3D model, and the dynamic simulation of the actuation system until the desired effect on the load force was achieved.

In Figure 4.22, the results of the load force as a function of relative displacement are presented for the experiments in Group 1, where gravitational force is dominant. The individual effects of each load force component are distinguished by different colors, derived from dynamic simulation. The force measured by the load cell on the test rig is represented by the purple line, which corresponds to the sum of the individual load force components. The supply pressure and the displacement time of each experiment are shown on the charts.

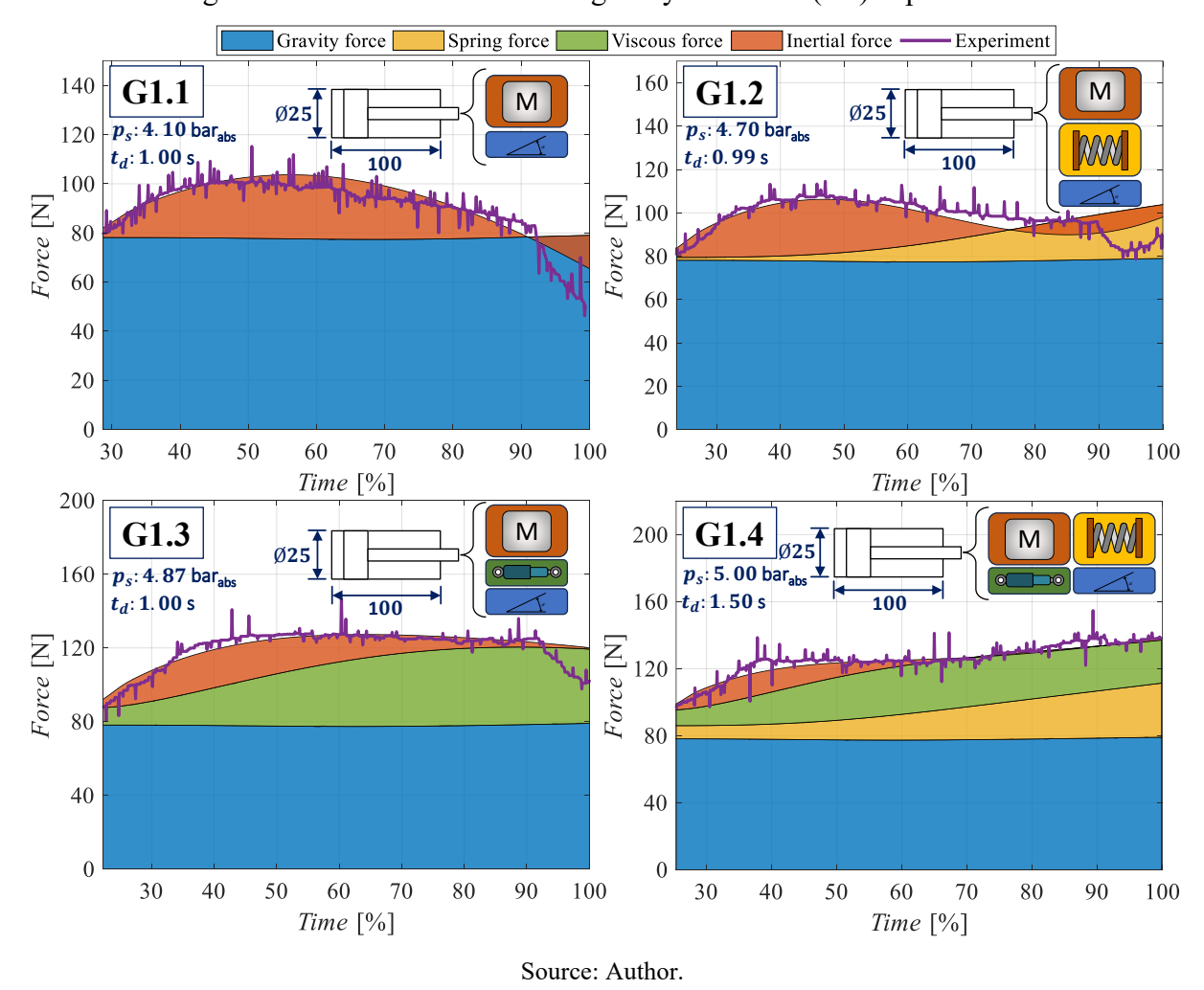


Figure 4.22 – Load forces for the gravity-dominant (G1) experiments

As can be seen, there is good agreement between the total load force from the simulations and the measured load force, demonstrating the coherence of the simulation model. For all four experiments, the load force remained nearly constant during piston displacement, with slightly lower values at the beginning due to smaller inertial forces. Additionally, the

inertial force tends to decrease near the end of the movement and, in some cases, becomes a positive force that pulls the cylinder rod, as observed in experiments G1.1 and G1.2. The start of movement, indicated by the appearance of inertial force on the left side of the charts, occurred at approximately 25-30% of the total displacement time. The measured force drop near the end of the movement is caused by the cylinder's end-stroke cushioning, which reduces the force acting on the load cell.

The experiments of Group 2, where all load force components have similar magnitudes, are shown in Figure 4.23.

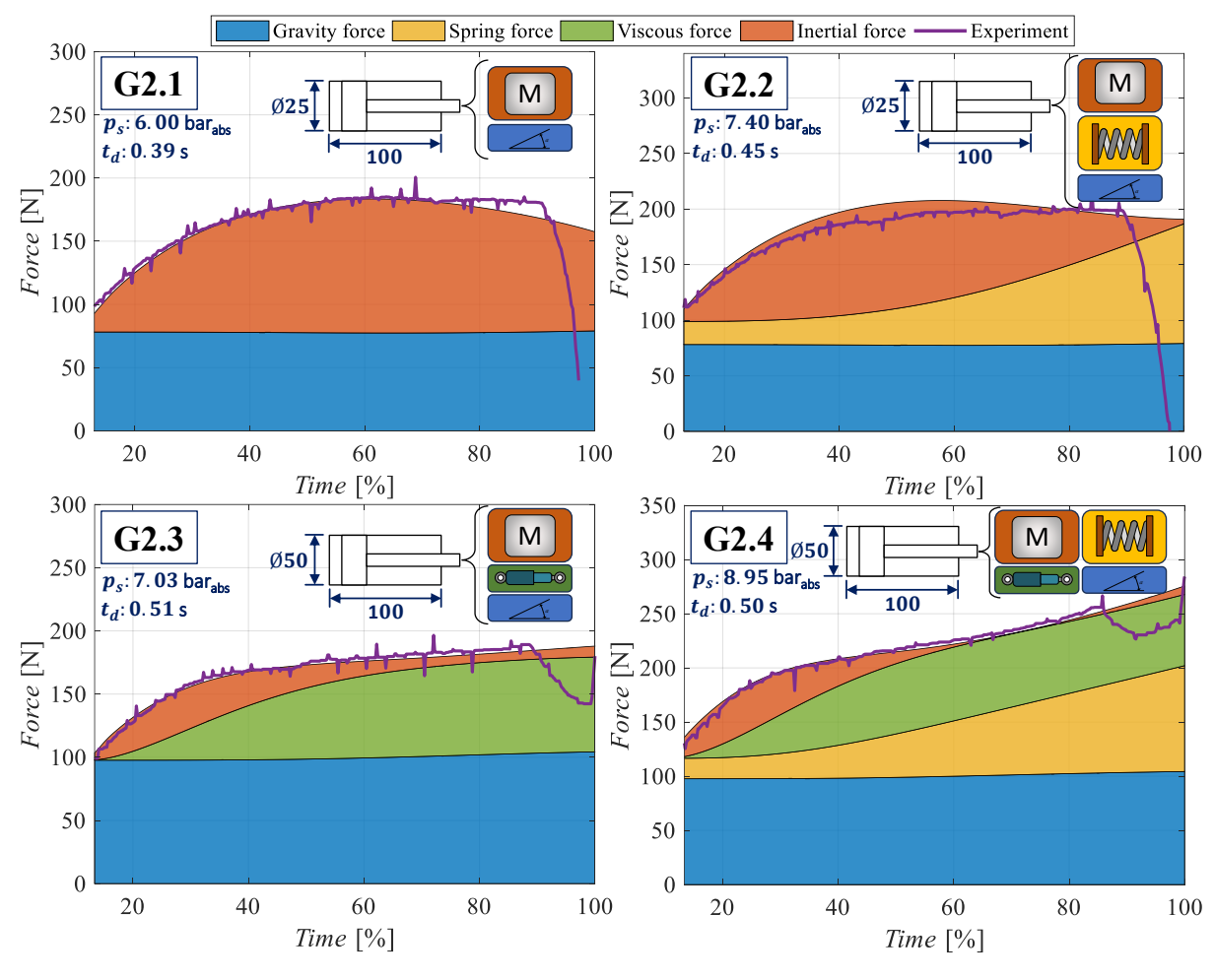


Figure 4.23 – Load forces for experiments with balanced force components (G2)

Source: Author.

For the second group of experiments, the simulation and experimental results also showed good agreement. A similar characteristic of smaller load force at the beginning of the movement, caused by smaller inertial forces, can be observed. Additionally, the inertial force tended to decrease at the end of the movement, particularly in experiments involving springs

(G2.2 and G2.4). The total load force presented an upward trend in experiments G2.3 and G2.4, while in experiments G2.1 and G2.2, it remained roughly constant after maximum acceleration. The start of the movement occurred around 10-15% of the total displacement time.

The experiments corresponding to the third group, in which the effects of gravity force are minimal, are shown in Figure 4.24.

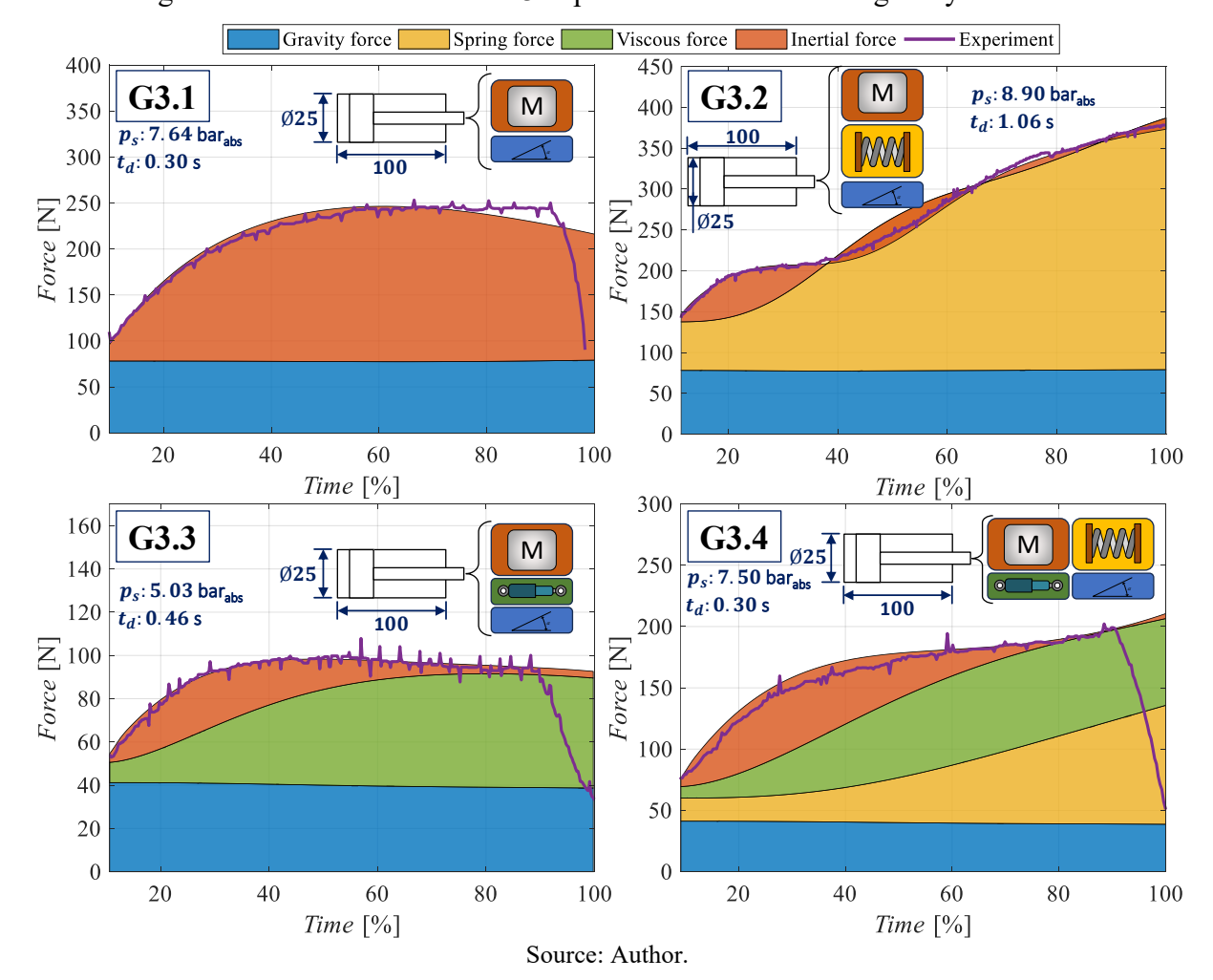


Figure 4.24 – Load forces for G3 experiments with minimal gravity influence

Once again, experimental and simulation results are closely correlated, as can be seen in the comparison between the experimental load force (purple line) and the total load force from the simulation. At the beginning of the movement, the total load force was smaller for all experiments, mainly due to the smaller inertial force. In experiments without a spring (G3.1 and G3.3), the load force remained nearly constant after reaching maximum acceleration, while an upward trend was observed in experiments with springs. With the exception of experiment G3.1, the inertial force approached zero at the end of the movement in the remaining

experiments. The beginning of the movement occurred at around 10% of the total displacement time.

Based on the analysis of these 12 experiments, the following conclusions can be drawn:

- 1) Applications involving springs and dampers tend to accelerate the mass quickly at the beginning of the movement. The subsequent increase in spring and viscous forces causes the inertial force to decrease to lower levels. Depending on the magnitude of the spring and damper forces, the inertial force may oscillate around zero, as observed in G2.4 and G3.2.
- 2) The inertial load reached its maximum within the first half of the displacement and showed a decreasing trend during the second half.
- 3) The magnitude of the gravitational force influenced the start of the movement. The greater the gravitational force magnitude, the longer the relative time required to start the movement.

In the context of cylinder sizing, the aforementioned observations raise the question of how to model the system dynamics to determine the sizing load force. Assuming a displacement entirely at constant velocity is clearly unfeasible, as acceleration forces were present throughout most of the displacement in all experiments. Several attempts have been made to develop more precise models to represent the system dynamics, including hypotheses of constant jerk displacement, second-order spring-mass-damper models, and heuristic formulations based on natural frequency. Unfortunately, none of these models were able to accurately represent the system behavior across all scenarios, discouraging further development of more detailed models.

For applications where inertial forces are significant, such as experiment G3.1, the model of a Uniformly Accelerated System (UAS) is capable of satisfactorily predicting the average inertial forces, as shown in Figure 4.25. The average inertial force is the main required input for the early stages of the design process.

In applications with low inertia, such as experiment G1.4, the deviation between the actual average inertial force and the value estimated by the UAS model may be more significant. However, in such cases, the magnitude of inertial forces is not relevant and should not impact the final design. Therefore, despite the variable nature of acceleration throughout the movement

seen in the conducted experiments, the hypothesis of a constant acceleration has shown to be the most effective to determine the inertial forces for the design of the pneumatic drives.

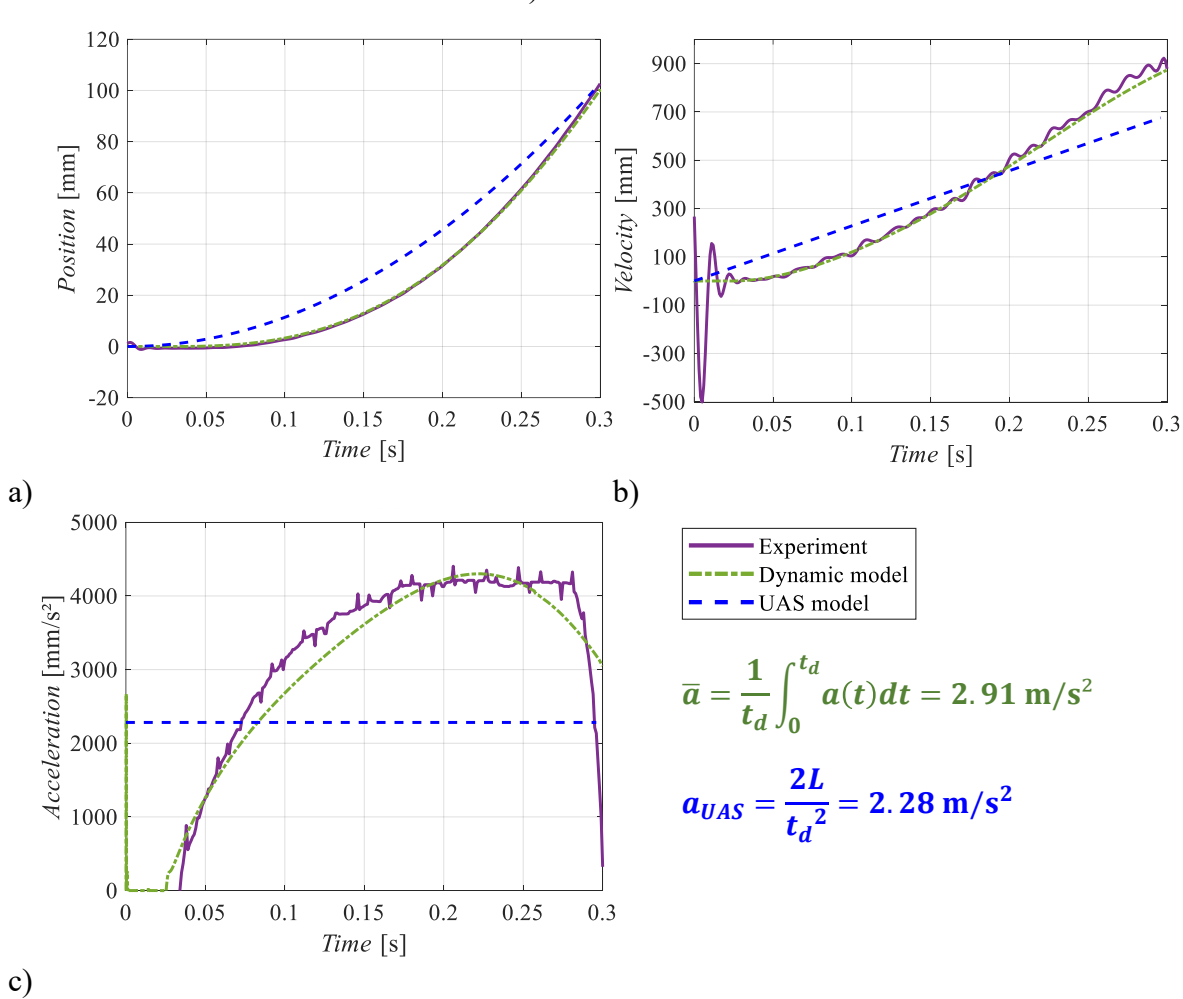


Figure 4.25 – Comparison of UAS model with the experiment G3.1: a) Position; b) Velocity; c) Acceleration

Another characteristic that impacts cylinder sizing is the upward trend in force profiles observed in some experiments, such as G2.4 and G3.2. A conventional engineering approach involves analyzing the most critical scenarios, typically the condition of maximum load force, which occurs at the end of the movement when springs and dampers are present. However, the operating point approach focuses on balancing energy efficiency and robustness when the cylinder moves with a constant load force throughout its entire stroke. Consequently, assuming the maximum load force for applications where this condition occurs only in a small portion of

Source: Author.

Therefore, based on the characteristics observed during the experiments, the unfeasibility of developing more representative models to determine the application load force,

the cylinder stroke may be overly conservative.

and the need to establish a reference load force for sizing pneumatic drives in variable load force applications, the following hypotheses have been assumed:

- 1) Pneumatic drives behave as Uniformly Accelerated Systems (UAS);
- 2) In applications involving only gravity and inertial forces, the inertial force can be estimated using the displacement time, cylinder stroke, and UAS equations;
- 3) In applications involving springs and dampers, the inertial force is estimated using UAS equations, while the spring and viscous forces are adjusted using a corrective factor.

Considering these hypotheses, the equation to determine the application load force for the generic example shown in Figure 4.20 is:

$$F_{L} = MgSin(\alpha) + \frac{2BL\sqrt{K_d}}{t_d} + K(x_{pre} + K_sL) + \frac{2ML}{t_d^2} + F_{fr_L} + F_G,$$
(4.28)

Gravity
force
force
M

where B is a viscous coefficient, K is the spring stiffness, x_{pre} is the spring pre load, and K_s and K_d are the corrective factors for springs and dampers, respectively.

The corrective factors represent the relative piston position at which the force should be determined for the sizing of the actuator. For instance, when K_d and K_s are equal to 1, Equation (4.28) yields the maximum load force of a constant acceleration system, where the viscous and spring forces are at their maximum at the end of the movement. Lower values of K_d and K_s correspond to the spring and damping forces expected in a constant acceleration system before reaching the end of the movement. For example, in Figure 4.26, the load force of a constant acceleration system at 60% of its stroke ($K_d = K_s = 0.6$) is highlighted.

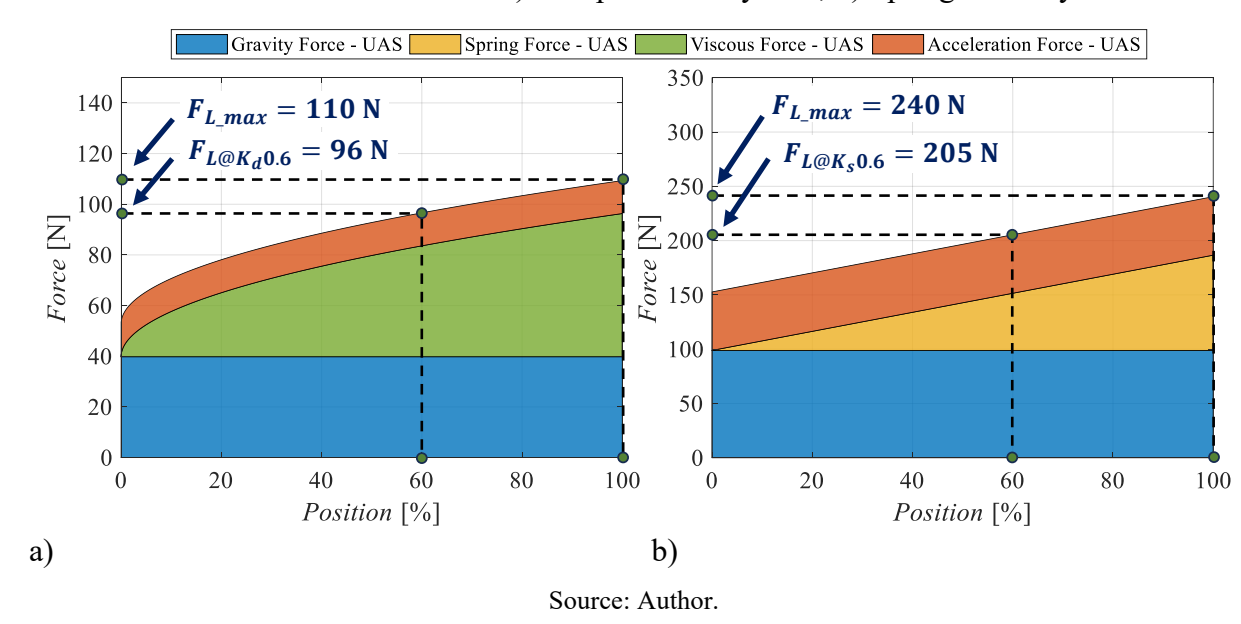


Figure 4.26 – Load forces of Uniformly Accelerated Systems highlighting the corrective factors at 60% of the stroke: a) Damper-based system; b) Spring-based system

In this way, if an application has a high inertial component, this force is accounted for by the fourth term of Equation (4.28). For spring and damper applications, the variability of the load force is addressed by the corrective factors. Therefore, this approach prevents the use of the maximum load force for sizing the actuator in variable load force applications.

In order to determine the proper corrective factors, Monte Carlo analyses were performed for spring- and damper-based applications. The Monte Carlo analyses allow for the assessment of the system under various working conditions, and the results can be used to perform a statistical analysis of the system's behavior. The question to be answered by the Monte Carlo analyses is: Assuming a constant acceleration displacement to model the load force of spring- and damper-based pneumatic actuation systems, which relative piston position $(K_d \text{ and } K_s)$ can be used to determine the sizing load force without significantly impacting the system's robustness?

In each Monte Carlo analysis, a set of 1,000 distinct design requirements was randomly generated using a uniform distribution within the range presented in Table 4.3, which covers most commonly used pneumatic applications. For each design requirement, the operating point equations were used to select a commercially available cylinder diameter. The supply pressure was adjusted in cases where the desired cylinder diameter did not match a commercially available option. Dynamic simulations were performed in MATLAB/Simulink using the simplified model described in Section 3.3.

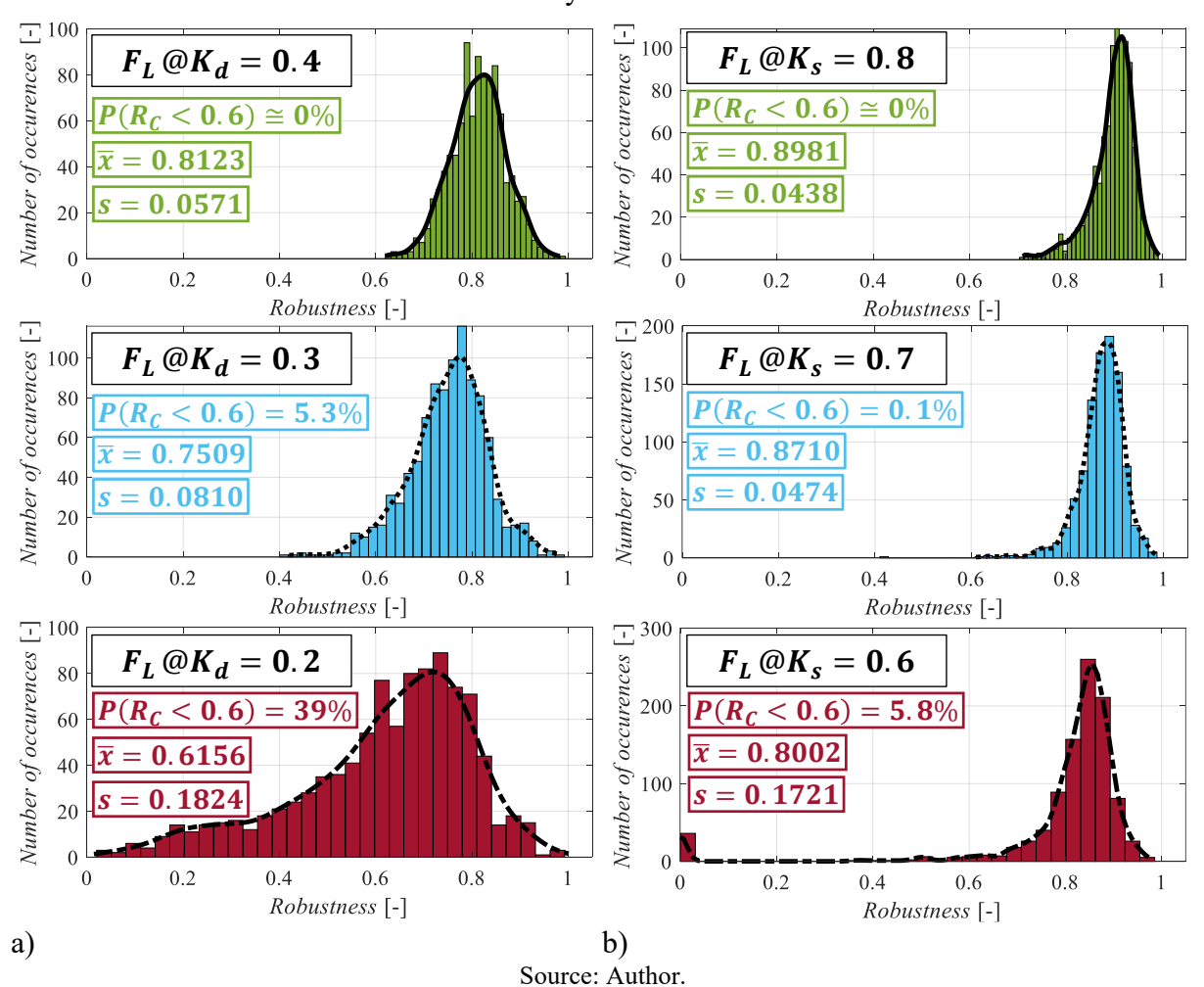
Table 4.3 – Range of design requirements for the Monte Carlo Analyses

Parameter	Range
Supply pressure (p_S) [4 - 9] bar _{abs}
Displacement time (t	(0.3 - 2] s
Stroke (L)	[0.05 - 0.5] m
(Viscous coefficient (B) [0.04 - 4,000] N.s/m
Spring stiffness (K)	[0.07 - 4,000] N/m
F_L Moving mass (M)	[0.01 - 800] kg
Working angle (α)	[0 - 90]°
C A1	

Source: Author.

In Figure 4.27, the robustness histograms and probability density functions of the Monte Carlo analysis performed with three different values of K_d and K_s are shown, demonstrating the transition from high-robust to low-robust operation. In the figure, \bar{x} represents the mean robustness among the 1,000 simulated systems, and s represents the sample standard deviation.

Figure 4.27 – Monte Carlo robustness analysis: a) Damper-based systems; b) Spring-based systems



As can be seen, the robustness histograms presented a skewed shape with a non-symmetric distribution of results. Therefore, the probability density functions (black lines) were computed using a Kernel Density Function, which is more suitable for irregular distributions than using a normal distribution (Drapala, 2023).

Based on the probability density functions, the probability (P) of a system having robustness smaller than 0.6 is shown in Figure 4.27 for each Monte Carlo analysis. As seen in Section 4.1.3, systems with robustness smaller than 0.6 present high uncertainty in their displacement time due to load changes. Therefore, the threshold of $R_c = 0.6$ has been adopted to distinguish between robust and non-robust operation.

The green histograms ($K_d = 0.4$ and $K_s = 0.8$) show results where most systems operated with high robustness, with a probability of R_c smaller than 0.6 being nearly 0%. Although high robustness is desirable, the analyses presented in Section 4.1.3 showed that excessive robustness is also associated with increased air consumption, thereby reducing the system's energy efficiency.

On the other hand, the red histograms ($K_d = 0.2$ and $K_s = 0.6$) show results where robustness starts to significantly decrease, with probabilities of operating with R_c lower than 0.6 at 39% and 5.8% for damper- and spring-based systems, respectively. Therefore, systems designed with these corrective factors have a significant probability of not being robust enough to withstand small changes in the load force, which is characteristic of undersized actuators.

The zero-robustness bar than can be seen in the spring-based systems histogram with $K_s = 0.6$ is due to the imposing aspect of the spring force, where the force continues to increase independently of the piston speed, causing the drive to stall if the cylinder is undersized. This aspect is not present in damper-based systems, where the task can still be completed, just at a lower velocity, which explains the better distribution of the damper-based systems' histograms in Figure 4.27.

Based on the results shown in Figure 4.27, it can be concluded that the corrective factors $K_d = 0.3$ and $K_s = 0.7$ correspond to a transitioning condition between excessively robust and non-robust operation, where there is only a small probability, ranging from 0.1% to 5%, of the system operating with robustness smaller than 0.6. As seen in Section 4.1.3, systems operating near this transitioning condition present a good balance between energy consumption and robustness.

Therefore, $K_d = 0.3$ and $K_s = 0.7$ are the recommended corrective factors to be used with Equation (4.28) to determine the sizing load force for the operating point method when

sizing pneumatic actuation systems for applications involving springs and/or dampers. The effectiveness of this design choice will be further investigated through simulation and experimental results in Chapter 7.

4.4 SIZING METHOD OF PNEUMATIC ACTUATORS

The sizing of pneumatic actuators involves defining a set of parameters for selecting a commercially available component. Among these, there are parameters that depend on the spatial arrangement of the actuator's working environment, such as cylinder stroke, and attachment devices. Other parameters are determined by the functional characteristics of the equipment, such as whether a single- or double-acting cylinder is used, symmetric or asymmetric cylinders, with or without end-stroke cushioning, and the type of actuator, such as linear, rotary, with or without a rod, among other characteristics.

The aforementioned parameters are intrinsically related to the application for which the drive is being selected. Therefore, the designer has little or no flexibility in choosing one characteristic over another, in other words, the parameters are defined by the application. However, the main parameters that offer a wider range of selection and significantly impact the system's dynamic and energy performance are the supply pressure and the actuation area.

The sizing process of pneumatic actuators proposed in this thesis consists of five activities, which encompass the tasks necessary to determine the actuation area and the system's supply pressure. A brief description of each activity is provided below, along with references to the equations derived in this chapter. This section concludes with a flowchart of the complete sizing process, designed to intuitively guide the designer through its activities.

Activity 1 - Definition of the Load Force: This activity aims to determine the load force value, in Newton, required for selecting the pneumatic actuator. The process differs for static and dynamic applications due to the distinct characteristics of each, as described in Section 4.3. For static applications, Equation (4.27) is used, whereas Equation (4.28) is applied to determine the load force for dynamic applications.

The friction between the mass and the surface $(F_{fr_{-}L})$ depends on the characteristics of the application. For tasks involving sliding objects over a surface, the friction force can be estimated using the following equation

$$F_{fr_{\perp}L} = MgCos(\alpha)\mu_{sli}, \tag{4.29}$$

where μ_{sli} is the sliding friction coefficient.

For tasks where the object slides by rolling over a surface, the friction force can be estimated by

$$F_{fr_L} = MgCos(\alpha) \frac{\mu_{rol}}{r}.$$
 (4.30)

where r is the rolling radius and μ_{rol} is the rolling friction coefficient, both expressed in meters.

Reference values for the sliding and rolling friction coefficients can be found in Oberg *et al.* (2016), Avallone; Baumeister III and Sadegh (2007), Gieck and Gieck (1997), and Davis (1997). Moreover, bearing manufacturers usually provide methods to determine the rolling friction force, as described in NSK (2013) and SKF (2015).

The generic force (F_G) represents forces that cannot be modeled by Equation (4.28), such as machining forces, flow forces, aerodynamic forces, Cartesian decomposition forces, etc. In such cases, the study presented in Vigolo; Valdiero and De Negri (2025) recommends using the 90th percentile of the load force profile, discretized along the cylinder stroke, which avoids using the maximum load force while still maintaining robust operation of the system.

Activity 2 – Chamber Pressures: In this activity, the pressures acting on the chambers are determined. This task involves distinguishing between compression and traction forces at the rod. Compression forces are commonly associated with extending movements, while traction forces are typically linked to retracting movements. However, it is also possible to have retracting tasks with compression forces at the rod or extending movements with traction forces. These scenarios are characterized by assistive loads, meaning the load moves in the same direction as the cylinder's movement.

For compression tasks of a static application, the pressure in chamber A equals the supply pressure, while the pressure in chamber B equals atmospheric pressure. For traction tasks, the pressures in chambers A and B are equal to atmospheric pressure and supply pressure, respectively.

For dynamic applications, defining the pressures acting on the cylinder chambers begins with specifying a few parameters for the operating point equations. Initially, the cylinder area ratio (r_A) must be defined. If the cylinder is symmetric, $r_A = 1$. For an asymmetric cylinder, r_A can be assumed to be 0.84, which is an average value for standardized cylinders (Boyko; Hülsmann; Weber, 2021). Additionally, an average critical pressure ratio of b = 0.3 is assumed for the valves in the actuation system.

The next required parameter is the friction coefficient (μ_d), which can be calculated using equation (4.25). Traditionally, a reference supply pressure (p_s) of 7 bar_{abs} can be used to begin the sizing process (Fialho, 2004). However, its value depends on the characteristics of the compressed air network. The velocity required to estimate the friction coefficient can be determined using the mean velocity achieved by the piston, which is

$$v_m = \frac{L}{t_d}. (4.31)$$

The chamber pressures for dynamic applications are represented by the optimal pressure ratios for chambers A and B. For compression tasks, Equations (4.16) and (4.2) are used to determine the optimal pressure ratios in chambers A and B, respectively. Similarly, for traction tasks, equations (4.17) and (4.4) are applied to calculate the optimal pressure ratios in chambers B and A, respectively.

Activity 3 – Cylinder Area: In this activity, the previously calculated information for load force and chamber pressures is used to determine the actuation area of the pneumatic actuator. In both static and dynamic applications, this is accomplished by performing a force balance based on the motion equation.

For static applications, since there is no movement during the execution of the main task, the motion equation for compression tasks can be simplified to

$$A_{A} = \frac{F_{L}}{p_{S} - p_{0}},\tag{4.32}$$

and for traction tasks, the motion equation yields

$$A_B = \frac{F_L}{p_S - p_0}. ag{4.33}$$

For dynamic applications, the actuation area is defined using the loading curve equation (Section 4.1.2), which is based on the motion equation expressed in terms of pressure ratios. Therefore, for compression tasks, the cylinder area of chamber A is given by

$$A_{A} = \frac{F_{L}}{p_{S} \left(\left(\frac{p_{A}}{p_{S}} \right)_{opt} - r_{A} \left(\frac{p_{0}}{p_{S}} \right) \left(\frac{p_{0}}{p_{B}} \right)_{opt}^{-1} - \frac{p_{0}}{p_{S}} (1 - r_{A}) - \mu_{d} \right)}.$$
(4.34)

For traction tasks, the cylinder area B is determined according to

$$A_{B} = \frac{F_{L}}{p_{S} \left(\left(\frac{p_{B}}{p_{S}} \right)_{ont} - \frac{1}{r_{A}} \left(\frac{p_{0}}{p_{S}} \right) \left(\frac{p_{0}}{p_{A}} \right)_{ont}^{-1} + \frac{p_{0}}{p_{S}} \frac{(1 - r_{A})}{r_{A}} - \frac{\mu_{d}}{r_{A}} \right)}.$$
(4.35)

The areas calculated using equations (4.32) to (4.35) are used to select a commercially available cylinder. As a guideline, the catalogue area must be greater than or equal to the calculated values. The selected actuator is considered a candidate solution, as further verification must be performed to ensure the selected actuator can withstand the application's kinetic energy.

Activity 4 – Kinetic Energy: This activity aims to verify if the pre-selected actuator is capable of absorbing the kinetic energy produced during the piston displacement. The first task involves determining the expected end-stroke velocity, which can be estimated by assuming the displacement follows a Uniformly Accelerated System (UAS). Therefore, the end-stroke velocity is

$$v_{end} \approx \frac{2L}{t_d}$$
 (4.36)

Some manufacturers, such as Camozzi (2019a), Parker (2020) and SMC (s.d.-a), provide information about the kinetic energy absorption capacity of their cylinders in the form of velocity and mass charts, as exemplified in Figure 4.28.

In the example shown in Figure 4.28, the intersection point of the stroke-end velocity and moving mass must be located below the curve of the pre-selected cylinder. Otherwise, it is recommended to use an external shock absorber, such as CAMOZZI (2019c) and Festo (s.d.), or to select a larger cylinder to prevent excessive wear due to high kinetic energy impacts at the end of the movement.

Instead of velocity and mass charts, some manufacturers provide information on the maximum absorbable kinetic energy, as seen in SMC (s.d.-b), EMERSON (2020), and Festo (2023). In such cases, the impact kinetic energy $(E_{kn\ d})$ of the application can be calculated by

$$E_{kn_{-}d} = \frac{Mv_{end}^2}{2}. (4.37)$$

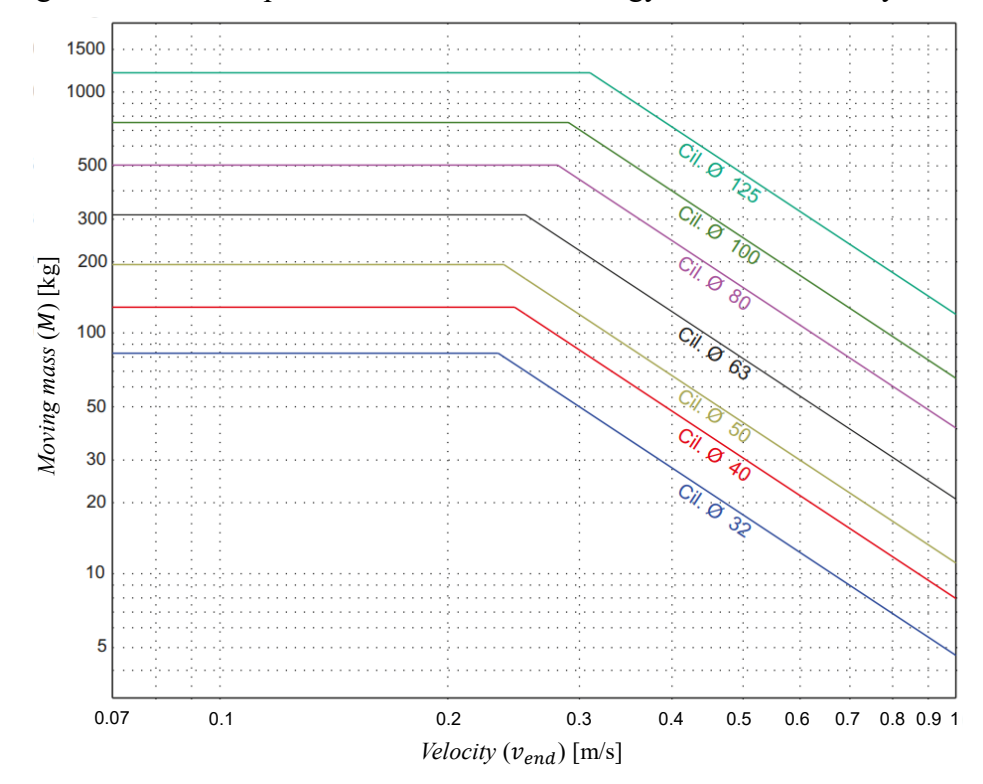


Figure 4.28 – Example of allowable kinetic energy for CAMOZZI cylinders

Source: Adapted from Camozzi (2019a).

If the calculated kinetic energy exceeds the absorbable kinetic energy of the preselected pneumatic actuator, an external shock absorber or a larger commercially available cylinder is recommended to properly absorb the application's kinetic energy.

Activity 5 – Supply Pressure Optimization: Due to the common mismatch between the commercially available actuator and the dimensioned actuator from Activity 3, as well as the potential need to increase the cylinder actuation area due to higher kinetic energy requirements, it is desirable to adjust the supply pressure to lower levels in order to avoid unnecessary air consumption. Even though this is not a mandatory activity, it provides an effective alternative to improve the system's energy efficiency.

To determine the optimized supply pressure levels, the movement equations from Activity 3 can be applied. Therefore, for static applications, the supply pressure for compression tasks is

$$p_S = \frac{F_L}{A_A} + p_0. (4.38)$$

For traction tasks, the supply pressure is

$$p_S = \frac{F_L}{A_B} + p_0, (4.39)$$

On the other hand, the optimized supply pressure for dynamic applications with compression tasks can be estimated using

$$p_{S} \approx \frac{F_{L} + A_{A} \left(r_{A} p_{0} \left(\frac{p_{0}}{p_{B}} \right)_{opt}^{-1} + p_{0} (1 - r_{A}) \right)}{A_{A} \left(\left(\frac{p_{A}}{p_{S}} \right)_{opt} - \mu_{d} \right)}$$

$$(4.40)$$

For traction tasks, the optimized supply pressure is,

$$p_{S} \approx \frac{F_{L} + A_{B} \left(\frac{p_{0}}{r_{A}} \left(\frac{p_{0}}{p_{A}}\right)_{opt}^{-1} - \frac{p_{0}}{r_{A}} (1 - r_{A})\right)}{A_{B} \left(\left(\frac{p_{B}}{p_{S}}\right)_{opt} - \frac{\mu_{d}}{r_{A}}\right)}.$$

$$(4.41)$$

In Equations (4.40) and (4.41), the supply pressure is only an estimate, since the dynamic friction coefficient and the optimal operating point determined in Activity 2 depend on the supply pressure. Therefore, the precise determination of the optimal supply pressure requires an iterative process. However, the initial approximation provided by Equations (4.40) and (4.41) should not differ significantly from the actual optimal value.

Most pneumatic valves operate with a combination of electropneumatic actuation, in which a small solenoid is used to activate an internal pneumatic pilot that actuates the valve's spool. Therefore, if the recalculated supply pressure is lower than 3 bar_{abs}, the supply pressure should be maintained at this level. Otherwise, the valves in the actuation system may not have the necessary pressure to operate properly.

After selecting the commercially available actuator and defining the supply pressure for the application, the sizing process of the pneumatic actuator is complete. Figure 4.29 presents a flow chart summarizing the five activities and equations employed in the application of the operating point method for pneumatic actuator sizing.

Supply pressure (p_S)
Cylinder stroke (L)
Displacement time (t_d) START Force during the $F_L = Mg|Sin(\alpha)| + \frac{2BL\sqrt{0.3}}{t_d} + K(x_{pre} + 0.7L) + \frac{2ML}{t_d^2} + F_{fr_L} + F_G$ $F_L = K(x_{pre} + L) + F_r$ b = 0.3 **∢** $\mu_d = \left(\frac{L}{t_d}\right)^{z_7} \left(z_1 \left(ln(F_L) + \frac{z_4 p_s}{1 \times 10^5}\right) + z_2 \left(ln(F_L) + \frac{z_5 p_s}{1 \times 10^5}\right)^2 + z_3 \left(ln(F_L) + \frac{z_6 p_s}{1 \times 10^5}\right)^3\right) + z_3 \left(ln(F_L) + \frac{z_6 p_s}{1 \times 10^5}\right)^3$ START Compression Load at $z_1 = 0.0983$ $z_3 = 0.0064$ $z_5 = 0.4614$ $z_2 = -0.0428$ $z_4 = 1.9796$ $z_6 = 0.1152$ $z_3 = 0.0149$ $z_5 = 0.2175$ $z_4 = 0.7581$ $z_6 = 0.0146$ $\left(\frac{p_B}{p_S}\right)_{ant} = 1.0103 + 0.1829e^{\left(\frac{-0.2438p_S}{1\times10^5}\right)} - 0.242r_A + 0.1716\mu_d$ Load Force $= 0.571 + 0.2326e^{\left(\frac{-0.2492p_4}{1\times10^5}\right)} + 0.1678r_A + 0.2483\mu_d$ $r_A^2(b^2-2b+1)+1-2b\left(\frac{p_B}{p_S}\right)^{-1}_{-ab}+\left(\frac{p_B}{p_S}\right)^{-2}_{-ab}(2b-1)$ $\left(\frac{p_0}{p_B}\right)_{out} = \bar{b} + \sqrt{\bar{b}^2 - 2\bar{b} + 1 + r_A^2 + r_A^2(2\bar{b} - 1)\left(\frac{p_A}{p_S}\right)^{-2} - 2\bar{b}r_A^2\left(\frac{p_A}{p_S}\right)}$ p_A, p_B Chamber pressures $p_S\left(\left(\frac{p_B}{p_S}\right)_{opt} - \frac{1}{r_A}\left(\frac{p_0}{p_S}\right)\left(\frac{p_0}{p_A}\right)_{opt}^{-1} + \frac{p_0}{p_S}\frac{(1-r_A)}{r_A} - \frac{\mu_d}{r_A}\right)$ $p_S \left(\left(\frac{p_A}{p_S} \right)_{opt} - r_A \left(\frac{p_0}{p_S} \right) \left(\frac{p_0}{p_B} \right)_{opt}^{-1} - \frac{p_0}{p_S} (1 - r_A) - \mu_d$ Cylinder Area Cylinder Catalogue $|A_{B_Cat} \ge A_B |$ $A_{A_Cat} \ge A_A$ $A_{B_Cat} \ge A_B$ Kinetic Energy Increase the cylinder diameter by one size p_S Cylinder Catalogue Supply Pressure Optimization E_{kn_d} > External shock END E_{kn_Cat} No Yes Optimize p_S Results in Yes $p_S = \frac{F_L}{A_A} + p_0$ $p_S = \frac{F_L}{A_B} + p_0$ $F_L + A_A \left(r_A p_0 \left(\frac{p_0}{p_B} \right)_{opt}^{-1} + p_0 (1 - r_A) \right)$ $F_L + A_B \left(\frac{p_0}{r_A} \left(\frac{p_0}{p_A} \right)_{opt}^{-1} - \frac{p_0}{r_A} (1 - r_A) \right)$ $A_A \left(\left(\frac{p_A}{p_S} \right)_{opt} - \mu_d \right)$ $A_B \left(\left(\frac{p_B}{p_S} \right)_{opt} - \frac{\mu_d}{r_A} \right)$ $p_S = 3 \text{ bar}_{abs}$ $p_S = 3 \text{ bar}_{abs}$ ≥ 3 bar_{ab} Yes Yes Supply defined! END

Source: Author.

Figure 4.29 – Pneumatic actuator sizing flow chart for discrete applications

4.5 FINAL CONSIDERATIONS ABOUT CHAPTER 4

This chapter presented a novel sizing method for pneumatic actuators called the operating point method. It described the fundamentals for developing the proposed method and introduced a new metric to assess the robustness of pneumatic drives. The results demonstrated that the operating point method effectively designs pneumatic cylinders to balance energy efficiency and robustness.

The friction force in pneumatic cylinders was experimentally investigated, revealing patterns dependent on supply pressure, load force, and piston velocity. These patterns enable friction force estimation early in the design process. Through experimental and simulation analyses, the effects of four distinct load force components were examined, highlighting patterns in inertial forces and spring- and damper-based systems. Monte Carlo analyses determined corrective factors for calculating the sizing load force in spring- and damper-based systems, preventing overestimation of load forces and contributing to more efficient operation without compromising system robustness.

Overall, the method developed in this chapter not only contributes to the efficient sizing of pneumatic actuators but also enhances the understanding of the dynamic behaviors and performance metrics crucial for achieving optimal system operation.

5 SIZING OF PNEUMATIC VALVES

This chapter describes the procedure adopted for the sizing of pneumatic valves. It presents the characteristic velocity profile of pneumatic cylinders, which consists of two main phases: the emptying time and the transient-state time. Analytical expressions are derived to describe the duration time of these phases as functions of system parameters and the equivalent sonic conductance of the actuation system's valve. Part of the content presented here has been published in the author's previous study, available in the paper Vigolo; Valdiero and De Negri (2021).

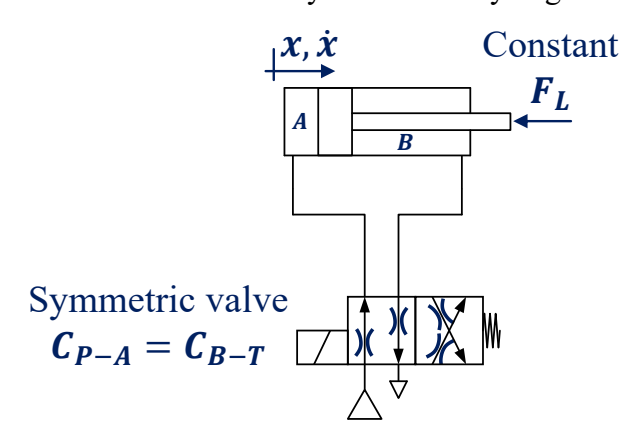
This chapter also introduces a practical approach for determining the sonic conductance of directional and throttle valves based on their equivalent sonic conductance. This method facilitates the selection of commercially available components that meet the design requirements of the application.

5.1 CHARACTERISTIC BEHAVIOR OF THE VELOCITY PROFILE

A pneumatic actuation system must fulfill two main requirements. The first is the ability to move or hold a given load, which depends on the drive's actuation area and the supply pressure, as discussed in Chapter 4. The second requirement is the time needed to complete the task, where the sonic conductance of the directional valve, the supply pressure, and the cylinder volume are the most significant parameters. Consequently, the sizing of the actuation system's valves must be performed after selecting the pneumatic actuator, when the supply pressure and cylinder diameter are already defined.

For the sizing of the system's valve, an approach based on the piston velocity profile is proposed. This profile presents a characteristic behavior that allows the development of simplified equations for sizing purposes. To analyze the characteristic behavior of the velocity profile, a standardized operating condition is assumed. This condition consists of a constant load force applied to the cylinder rod and operation with symmetric valve, where the sonic conductance of flow path P-A is equal to that of flow path B-T during an extending movement, as shown in Figure 5.1.

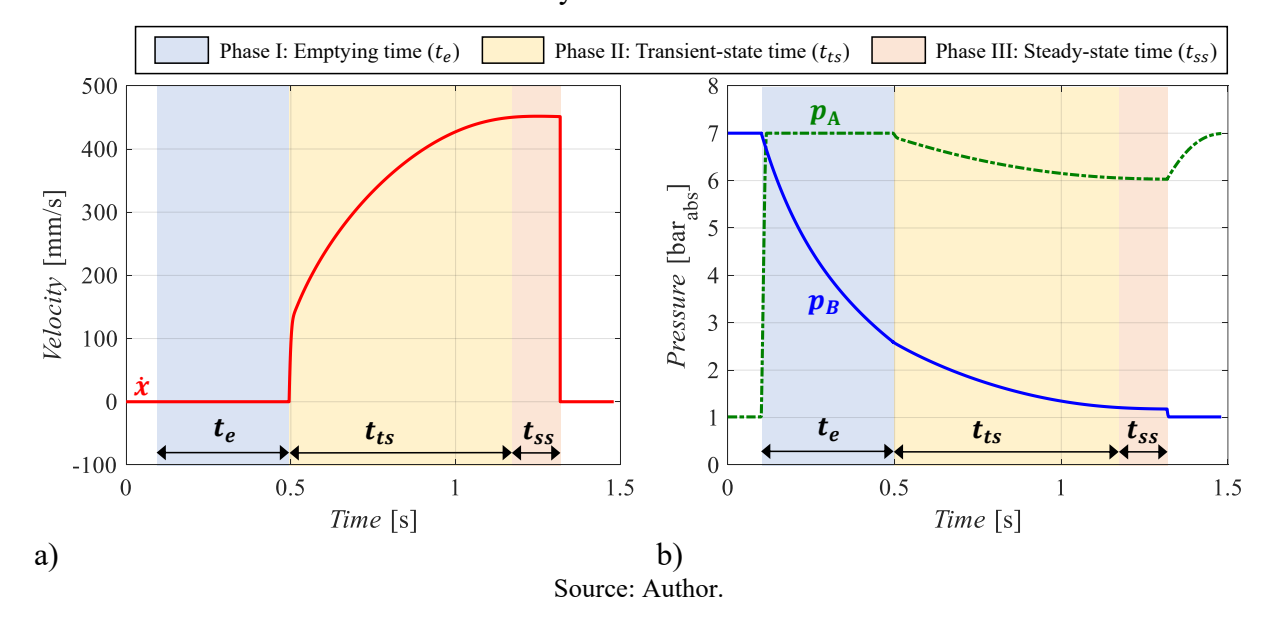
Figure 5.1 – Standardized actuation system for analyzing the velocity profile



Source: Author.

Under these hypotheses, the characteristic piston velocity profile can be divided into three phases: the emptying time (t_e) , the transient-state time (t_{ts}) , and the steady-state time (t_{ss}) , as exemplified in Figure 5.2 for an extending movement.

Figure 5.2 – Characteristic behavior of the velocity profile: a) Piston velocity; b) Pressure in the cylinder chambers



Each phase of the velocity profile is defined by the interaction between the chamber pressures and the load force. As shown in Figure 5.2-b), during Phase I, the time required to reduce the pressure in chamber B (the counterpressure chamber) is significantly longer than the time needed to increase the pressure in chamber A (the driving chamber). This behavior is explained by the fact that the counterpressure chamber volume is always bigger than the driving chamber volume at the beginning of the movement. Consequently, the emptying time is mainly

determined by the time needed to depressurize the counterpressure chamber until the force in the driving chamber is capable to overcome the forces opposing the movement.

When the piston displacement begins, the friction force decreases due to the Stribeck effect, causing a step response in the velocity profile. At the same time, the pressure in the driving chamber starts to decrease as its volume increases. During Phase II, the available pneumatic force exceeds the load force, resulting in piston acceleration. As the velocity increases, the viscous friction force also increases, and eventually, the pneumatic and load forces reach equilibrium. This defines the beginning of Phase III, where there is no change in chamber pressures, and the velocity becomes constant.

However, the study presented in Vigolo and De Negri (2021) demonstrates that the steady-state displacement is correlated with the actuation area of the cylinder. In general, for the same load force, as the actuation area increases, the piston displacement no longer reaches steady-state behavior. This is due to the increase in available pneumatic force, which is converted into acceleration throughout the entire displacement. This behavior is illustrated in Figure 5.3, where four different actuation areas were simulated for the same load force (160 N).

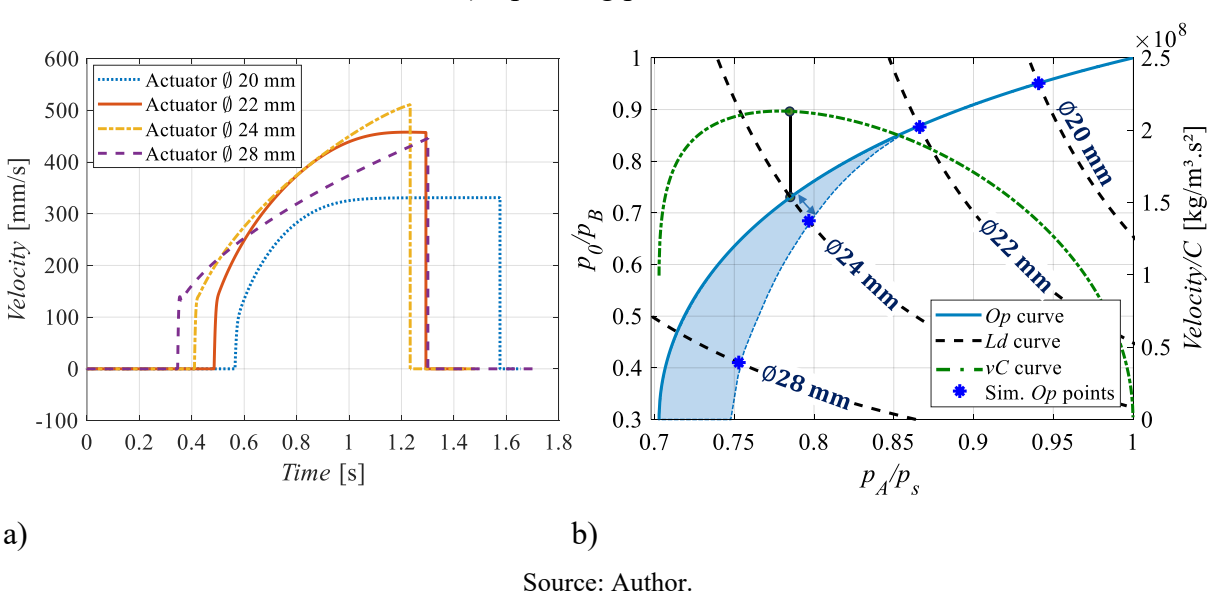


Figure 5.3 – Analysis of the velocity profile: a) Piston velocity for different actuators; b) Operating point chart

As shown in Figure 5.3-a), the steady-state phase is clearly observed in the smaller cylinders (20 and 22 mm), while the larger cylinders (24 and 28 mm) do not achieve a constant velocity displacement. The steady-state time decreases significantly as the actuation area increases, eventually becoming inexistent.

The operating points of the simulated systems in Figure 5.3-a) are shown in Figure 5.3-b). These points were determined using the pressure ratios of the cylinder chambers at the moment just before the piston hits the end-stroke head, which is the most likely instant for the system to reach steady-state behavior.

As shown in Figure 5.3-b), the smaller cylinders resulted in operating points located exactly on the Op curve, which is a steady-state curve. However, as the actuation area increases, the operating points deviate from the Op curve, indicating that these systems did not achieve steady-state behavior. This aspect is highlighted in the figure by the blue area, where its width represents the degree of deviation from steady-state behavior.

Based on the results in Figure 5.3, it can be observed that when the pneumatic cylinder is properly dimensioned, that is, operating near the maximum point of the vC curve, the steady-state time becomes negligible or nonexistent. This occurs because the system is on the eminence of reaching steady-state behavior without spending a significant amount of time moving at a constant speed. Therefore, for the sizing of the system's valves, only the emptying time and transient-state time are considered, as will be discussed in the following sections.

5.1.1 The emptying time

Due to the large volume of the counterpressure chamber, there is a delay (t_e) at the beginning of the piston displacement. This delay is defined as the time required for the counterpressure chamber to reduce its pressure until the driving chamber can overcome the load force, friction force, and counterpressure force. As discussed in Section 5.1, during the emptying phase, the driving chamber quickly reaches the supply pressure and maintains a constant pressure throughout the first phase of the movement. Therefore, the emptying time is governed by the pressure dynamics of the counterpressure chamber, which has a constant volume and predominantly choked flow due to the high-pressure differential.

Considering an extending movement and an isothermal process in the cylinder chamber, the continuity equation (Equation (3.3)) applied to chamber B of a linear actuator during the emptying time is

$$\frac{dp_B}{dt} = \frac{-q_{mB}T_BR}{V_{B\ 0} + LA_B}. ag{5.1}$$

Assuming a choked flow rate, Equation (3.2) is applied in Equation (5.1), which can be integrated from an initial condition ($p_i = p_S$ and $t_i = 0$) to a generic condition, resulting in

an equation that models the pressure in chamber B during the emptying time of an extending displacement

$$p_B = p_S e^{-\frac{tp_0 C}{V_{B_0} + LA_B}}. (5.2)$$

Since there is no movement during this phase and the pressure in chamber A is constant, the only variable in the motion equation is the pressure in chamber B, which is defined by Equation (5.2) and is a function of time. Therefore, the motion equation (Equation (3.38)) can be written as

$$p_{S}A_{A} - A_{B}p_{S}e^{\frac{-tp_{0}C}{V_{B_{-0}} + LA_{B}}} - p_{0}A_{r} - F_{fr,S} - F_{ext} = 0,$$
(5.3)

where F_{fr_s} is the static friction force of the cylinder.

Therefore, the emptying time is the time required to reach a balance between the driving chamber force and the forces opposing the movement, that is,

$$t_{e_{-}e} = \frac{V_{B_{-}0} + LA_{B}}{p_{0}C} \left[ln(p_{S}) - ln \left(\frac{p_{S} - p_{0}(1 - Ra)}{Ra} - \frac{F_{fr_{-}S} + F_{ext}}{A_{B}} \right) \right].$$
 (5.4)

Similarly, for the retracting movement, the emptying time is characterized by the pressure dynamics in chamber A. Therefore, it can be estimated using the following equation

$$t_{e_r} = \frac{V_{A_0} + LA_A}{p_0 C} \left[ln(p_s) - ln \left(p_s Ra + p_0 (1 - Ra) - \frac{F_{fr_s} + F_{ext}}{A_A} \right) \right]. \tag{5.5}$$

In equations (5.4) and (5.5), the static friction force can be estimated using the simplified model proposed by Virvalo (1993), which models the static friction force as a percentage of the maximum force produced by the actuator, similar to the dynamic friction model presented in Section 4.2. If the static friction coefficient is unknown, it can be estimated using values in the range of 0.05 to 0.15.

In Figure 5.4, Equation (5.2) is compared with the results of a dynamic simulation of a cylinder with a piston diameter of 24 mm and a rod diameter of 10 mm, a stroke of 300 mm, moving a load of 160 N, with a supply pressure of 7 bar_{abs} and a dead volume of 3.77×10^{-6} m³. The directional valve has a sonic conductance of 2.4×10^{-9} m³/Pa·s and a critical pressure ratio of 0.3.

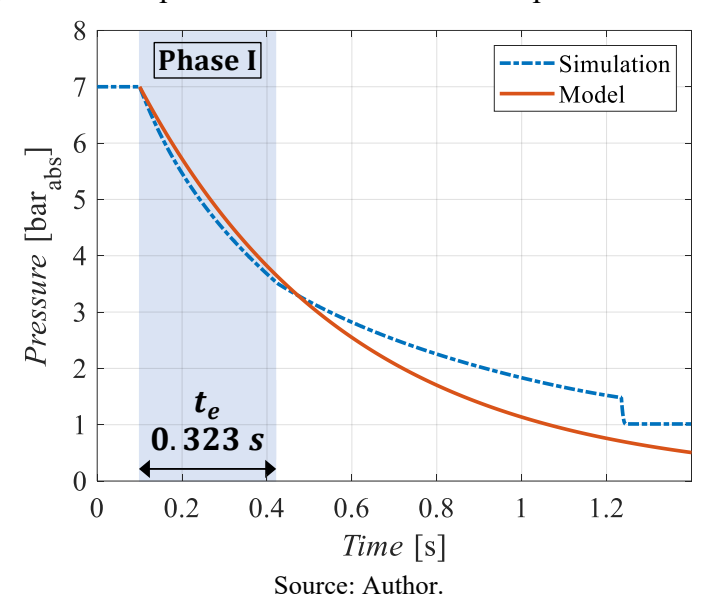


Figure 5.4 – Depressurization of the counter pressure chamber

As can be seen, Equation (5.2) presents good agreement with the simulation in modeling the pressure behavior during Phase I, which occurred between 0.1 and 0.423 seconds. Furthermore, applying Equation (5.4) to calculate the emptying time and assuming a friction coefficient of 0.05 yields a value of 0.342 seconds, while the actual emptying time is 0.323 seconds, highlighting the accuracy of the proposed model.

5.1.2 The transient-state time

When the driving chamber is capable to overcome the forces opposing the movement, the piston begins to move with high acceleration due to the slight reduction in friction force caused by the Stribeck effect. Following this, there is a progressive increase in friction force, which reduces the resulting force and eventually halts the acceleration. This interaction of forces results in the velocity profile shown in Figure 5.2-a), which resembles the characteristic behavior of a first-order system.

To derive a characteristic equation describing the dynamic behavior during the transient-state time (Phase II), the mass flow rate, continuity equation, and motion equation must be linearized and coupled using Laplace transformation.

During Phase II, the mass flow rate is predominantly subsonic. Consequently, the mass flow rate equation proposed by the ISO 6358 Standard (Equation (3.2)) can be linearized, such that the maximum mass flow rate occurs at the critical pressure ratio, as shown in Appendix B. In the S-domain, the linearized mass flow rates for the P-A and B-T flow paths during an extending movement are, respectively,

$$q_{mA}(s) = C\rho_0 \sqrt{\frac{T_0}{T_1}} \frac{1}{(1-b)} (p_S(s) - p_A(s)), \tag{5.6}$$

and

$$q_{mB}(s) = C\rho_0 \sqrt{\frac{T_0}{T_1}} \frac{1}{(1-b)} (p_B(s) - p_0(s)). \tag{5.7}$$

The pressures in the cylinder chambers are described by the continuity equation (Equation (3.3)). Assuming an isothermal process, the pressure dynamics in chambers A and B, in the S-domain, are, respectively

$$p_A(s) = \left(q_{mA}(s) - A_A \rho_A v(s)\right) \frac{RT_A}{V_A s'},\tag{5.8}$$

and

$$p_B(s) = \left(-q_{mB}(s) + A_B \rho_B v(s)\right) \frac{RT_B}{V_B s'},\tag{5.9}$$

where the specific masses, temperatures, and chamber volumes are assumed to be constant to obtain a linear model.

Combining Equations (5.8) and (5.6), (5.9) and (5.7), and assuming $T_1 = T_0$, yields the equations describing the pressure dynamics in the actuator chambers connected to the directional valve, which are

$$p_A(s) = \frac{p_S(s) - \frac{A_A \rho_A (1 - b) v(s)}{C \rho_0}}{\frac{(1 - b) V_A}{C \rho_0 R T_A} s + 1},$$
(5.10)

and

$$p_B(s) = \frac{p_0(s) + \frac{A_B \rho_B (1 - b) v(s)}{C \rho_0}}{\frac{(1 - b) V_B}{C \rho_0 R T_B} s + 1}.$$
(5.11)

The piston displacement dynamics is defined by the equation of motion, where the terms related to acceleration and viscous force are neglected to derive a first-order system. Therefore,

$$A_A p_A(s) - A_B p_B(s) - A_r p_0(s) = F_{ext}(s). (5.12)$$

In Equation (5.12), the external load force and atmospheric pressure are assumed to be constants (inputs) of the system. In this way, the system dynamics are characterized by the force balance of the pressures in the cylinder chambers. Applying Equations (5.10) and (5.11) in (5.12) results in the characteristic equation for the piston velocity of the cylinder and valve set.

$$\frac{\left(\frac{A_A^2 \rho_A V_B}{R T_B} + \frac{A_B^2 \rho_B V_A}{R T_A}\right) (1 - b)}{A_A^2 \rho_A C \rho_0 + A_B^2 \rho_B C \rho_0} s + 1 = 0.$$
(5.13)

Assuming an isothermal process, average volumes in the cylinder chambers and equal specific mass in both chambers, the system's time constant is given by:

$$\tau = \frac{\left(A_A^2 V_B + A_B^2 V_A\right) (1 - b)}{2C p_0 \left(A_A^2 + A_B^2\right)}.$$
 (5.14)

The transient-state time (t_{ts}) is the time required for the system to reach the steady-state condition. Assuming a criterion of 99.3%, the transient-state time is 5τ .

Applying the same derivation procedure for a retracting movement yields the same time constant, revealing that Equation (5.14) is invariant to the direction of motion, that is, it is valid for both extending and retracting movements.

In Figure 5.5, the piston velocity from the simulation described in Section 5.1.1 is compared with the response of a first-order system, where the time constant was determined according to Equation (5.14), and the step response was multiplied by 514 mm/s, which is the end-stroke velocity obtained in the simulation.

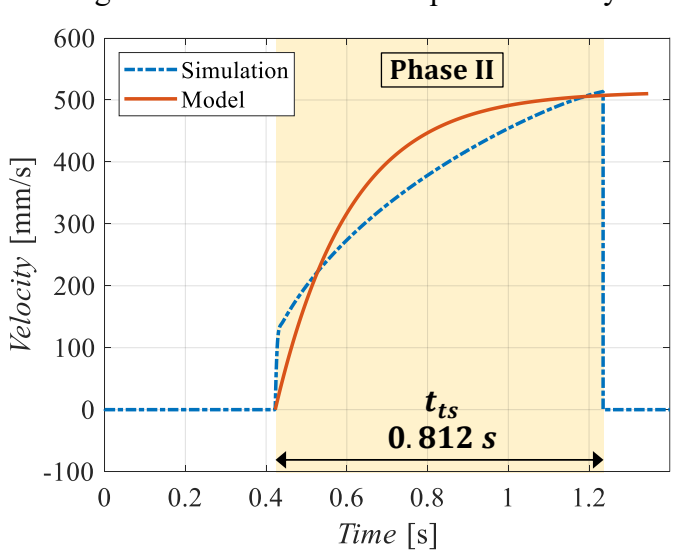


Figure 5.5 – Transient-state piston velocity

Source: Author.

As can be seen, the dynamics of the first-order system are similar to the velocity profile of the simulated system. Moreover, the transient-state time of the simulation was 0.812 seconds, whereas the value of 5τ yields 0.924 seconds, demonstrating the coherence of the results obtained by the proposed approach.

5.1.3 The equivalent sonic conductance

As described in Section 5.1, when the actuation area and supply pressure are properly dimensioned for the applied load, the displacement time (t_d) will consist of the emptying time and the transient-state time $(t_d = t_e + 5\tau)$. Therefore, the displacement time can be determined using Equations (5.4) and (5.14). Since the displacement time is a design requirement, Equations (5.4) and (5.14) are combined and used to determine the sonic conductance of the system's valves based on the displacement time, that is

$$C_{eq_{L}e} = \frac{1}{t_{d}p_{0}} \left\{ V_{B} \left[ln(p_{S}) - ln \left(\frac{p_{S}(1 - \mu_{S}) - p_{0}(1 - r_{A})}{r_{A}} - \frac{F_{L}}{A_{B}} \right) \right] + \frac{5(A_{A}^{2}V_{B} + A_{B}^{2}V_{A})(1 - b)}{2(A_{A}^{2} + A_{B}^{2})} \right\}.$$
(5.15)

where the subscript eq is added to indicate the equivalent sonic conductance of all the system's valves in series, while the subscript e stands for the extending movement

For simplicity, the external load force (F_{ext}) , which does not account for inertial forces, is replaced by the load force (F_L) , which incorporates the inertial forces for dynamic applications, as discussed in Section 4.1.2. This approximation is made because the impact of this assumption on the calculated value is small, and it simplifies the design process by eliminating the need to calculate two distinct forces.

Equation (5.15) was derived to calculate the equivalent sonic conductance (C_{eq_e}) for an extending movement. Applying the same approach to a retracting movement results in

$$C_{eq_r} = \frac{1}{t_d p_0} \left\{ V_A \left[ln(p_S) - ln \left(p_S(r_A - \mu_S) + p_0(1 - r_A) - \frac{F_L}{A_A} \right) \right] + \frac{5(A_A^2 V_B + A_B^2 V_A)(1 - b)}{2(A_A^2 + A_B^2)} \right\}.$$
 (5.16)

Therefore, analytical equations for calculating the equivalent sonic conductance are obtained using parameters available during the design phase of a pneumatic actuation system,

such as the desired displacement time, actuator volume, supply pressure, and load force. The correlation of the equivalent sonic conductance with the main valves of a standard actuation system, such as directional and throttle valves, is presented in Section 5.2.

5.2 PNEUMATIC THROTTLE AND DIRECTIONAL VALVES

Pneumatic actuation systems commonly use two types of valves in their architecture: directional valves and throttle valves. Directional valves are responsible for selecting the flow paths that connect the cylinder chambers to the supply and atmospheric pressure, while throttle valves are employed to control the displacement speed.

Even though different configurations are possible, such as the use of a single proportional directional valve for closed-loop systems, the inclusion of quick exhaust valves, or the addition of pressure regulator valves, the analysis of this sizing process will focus on the most common pneumatic actuation system, as described in Section 2.1.1. This system employs directional valves and throttle valves in either a meter-in or meter-out configuration.

In Section 5.1.3, an approach to determine the equivalent sonic conductance (C_{eq}) required for the application was presented. As for the next step, it is necessary to determine the flow capacities of the directional valve (C_{DV}) and the throttle valve (C_{TV}) to achieve the desired equivalent sonic conductance.

In the literature, there are thumb rules employed to determine the equivalent sonic conductance of series pneumatic restrictors. For instance, SMC (1997) and Camozzi (2019a) present two similar, though not identical, approaches. These approaches are based on the reciprocal of the square and cubic roots of the individual flow capacities, raised to the power of two and three, respectively. In ISO 6358-3 (ISO, 2014), a precise approach is presented to determine the equivalent sonic conductance of a series connection of restrictors. This model involves numerically iterating the pressure drops across the restrictors until a mass flow rate is achieved that does not result in vacuum pressure at the exhaust port of the last component.

Another alternative is presented in Gidlund and Eckersten apud Beater (2007), where the ISO 6358 model is applied to two restrictors in series, with the downstream pressure of the first restrictor becoming the upstream pressure of the second restrictor. The derivation procedure is based on a distinct analysis of the flow conditions in each restrictor, resulting in two different equations depending on which restrictor achieves choked flow first.

The model derived by Gidlund and Eckersten requires the calculation of an auxiliary variable called α_f

$$\alpha_f = \frac{C_1}{b_1 C_2},\tag{5.17}$$

where the subscripts 1 and 2 indicate the first (upstream) and second (downstream) components, respectively.

The value of α_f determines whether the flow becomes choked first in the upstream component ($\alpha_f < 1$), or in both components at the same time ($\alpha_f = 1$), or in the downstream component ($\alpha_f > 1$).

Based on the value of α_f , the equivalent sonic conductance of the series connection is given by:

$$C_{eq} = \begin{cases} C_1 & \text{for } \alpha_f \le 1 \\ \alpha_f b_1 + (1 - b_1) \sqrt{\alpha_f^2 + \left(\frac{1 - b_1}{b_1}\right)^2 - 1} & \text{for } \alpha_f \ge 1 \end{cases}$$

$$\alpha_f^2 + \left(\frac{1 - b_1}{b_1}\right)^2 \qquad \text{for } \alpha_f \ge 1$$
(5.18)

In a pneumatic restrictor, choked flow is achieved when there is a significant pressure differential across the restrictor. In other words, for choked flow to occur in a pneumatic valve, it must provide high flow restriction, otherwise there will not be enough pressure differential for the flow to become choked.

In a pneumatic actuation system, the valve responsible for providing flow restriction is the throttle valve, while the directional valve is mainly responsible for controlling the flow direction. Therefore, the flow is expected to become choked first at the throttle valve.

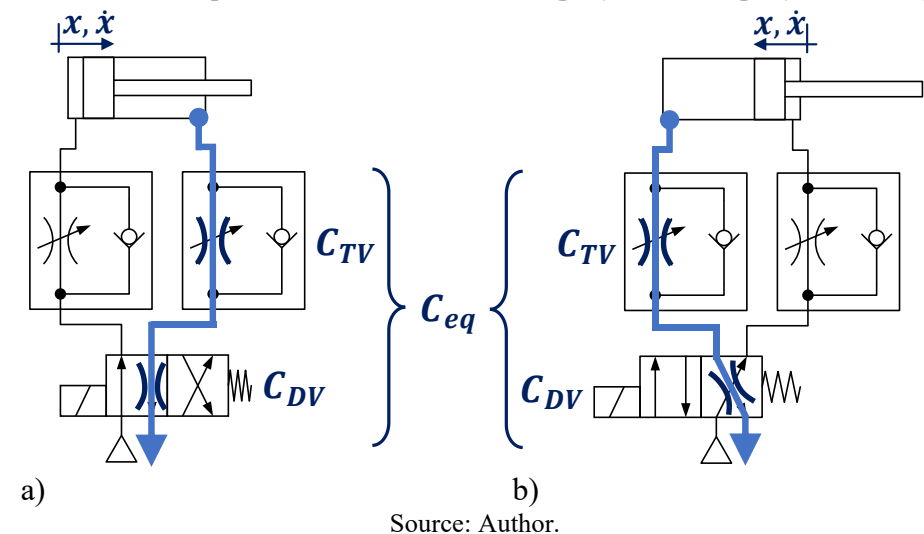
Since Equation (5.18) depends on the component that reaches choked flow first, the determination of the correlation between the equivalent sonic conductance and the sonic conductance of the directional and throttle valves are different for meter-in and meter-out applications. Because of this, each metering approach is analyzed separately.

5.2.1 Equivalent sonic conductance for meter-out configurations

A pneumatic throttle valve usually has different flow capacities for each flow direction. The throttle side has a higher flow resistance and, when completely closed, prevents air from flowing from one port to the other. However, on the bypass side, the flow restriction is much smaller, since the air has a bypass flow path, which allows flow through the valve even when the throttle needle is completely closed. Therefore, for the sizing of a throttle valve, the minimum flow capacity of the throttle side must be determined, as it has the highest resistance.

Consequently, the sizing of throttle and directional valves is performed for the B-T flow path during extending movements and the A-T flow path during retracting movements, as these are the flow paths with the highest flow restriction.

Figure 5.6 – Exhaust flow path for meter-out throttling: a) Extending, b) Retracting



Since the flow is expected to become choked first at the throttle valve due to its higher flow restriction, the α_f value in Equation (5.17) for meter-out throttling is smaller than 1, as it is the first restriction of the flow path. Therefore, according to Equation (5.18), the sonic conductance of the throttle valve (C_{TV}) is

$$C_{eq} = C_1 = C_{TV}. (5.19)$$

Since α_f is less than one, it can be stated that

$$\frac{C_{eq}}{b_1 C_{DV}} < 1. \tag{5.20}$$

Thus, assuming that $b_1 \cong 0.33$, to satisfy Equation (5.20), the sonic conductance of the directional valve has to be

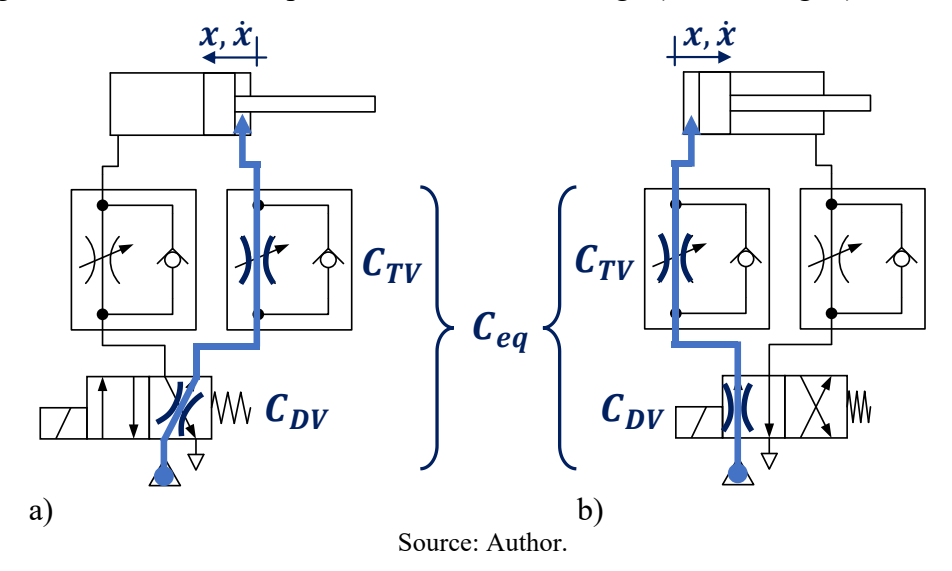
$$C_{DV} > 3C_{eq}. \tag{5.21}$$

This means that, for the flow rate not to be impacted by the restriction of the directional valve, its sonic conductance must be at least three times greater than the equivalent sonic conductance calculated using Equations (5.15) and (5.16). Similarly, the sonic conductance of the throttling path of the throttle valve must be greater than or equal to the sonic conductance calculated using Equations (5.15) and (5.16) in order to achieve the desired displacement time.

5.2.2 Equivalent sonic conductance of meter-in configurations

In a meter-in configuration, the determination of the flow capacities must also consider the flow path with the highest flow resistance. In this configuration, the highest resistance occurs for the flow path P-A during extending tasks and P-B during retracting tasks, as shown in Figure 5.7.

Figure 5.7 – Intake flow path for meter-in throttling: a) Retracting, b) Extending



As discussed in Section 5.2, the flow is expected to become choked first at the throttle valve due to its higher flow restriction. Therefore, for meter-in throttling, the α_f value in Equation (5.17) is greater than 1.

In Figure 5.8, the correlation of the sonic conductances of the throttle valve and directional valve as a function of α_f is presented for $b_1 = 0.33$. The vertical axis in the figure

represents how many times each individual sonic conductance needs to be greater than the equivalent sonic conductance (C_{eq}) for their series combination to equal C_{eq} .

3.5 $C_{DV} = 3C_{eq}$ $C_{DV} = 3C_{eq}$ $C_{TV} = 1.04C_{eq}$ $C_{TV} = 1.04C_{eq}$ $C_{TV} = 1.04C_{eq}$

Figure 5.8 – Correlation of the flow restrictors' sonic conductance with α_f

Source: Author.

Analyzing the results presented in Figure 5.8, it can be seen that if the sonic conductance of the directional valve is equal to C_{eq} , the sonic conductance of the throttle valve must be three times greater $(3C_{eq})$ for their series combination be equal to C_{eq} . Such a configuration does not make sense for a meter-in system, where the directional valve usually has the highest flow capacity. However, this scenario changes as α_f increases, with C_{TV} approaching $1C_{eq}$ as C_{VD} increases. That is, if C_{VD} is large enough, the flow restriction will be governed solely by C_{TV} .

When α_f is equal to 8.66, C_{DV} must be three times greater than C_{eq} , and C_{TV} must be 1.04 times greater than C_{eq} for their series combination to equal C_{eq} . Therefore, for simplicity and to be in accordance with the meter-out rules defined in Section 5.2.1, it can be stated that

$$C_{TV} = C_{eq}, (5.22)$$

and

$$C_{DV} > 3C_{eq}. ag{5.23}$$

In this way, equations (5.22) and (5.23) provide simple guidelines to determine the flow capacity of directional and throttle valves for meter-in throttling. For this purpose, equations (5.15) and (5.16) are used to determine the required equivalent sonic conductance for the system to achieve the displacement time for the application.

5.3 SIZING METHOD OF PNEUMATIC VALVES

According to the equations and analyses presented in this chapter, a flow chart can be defined for the sizing of the system's valves. The main input information includes the supply pressure, cylinder characteristics, load force, and displacement time.

The sizing method consists of a single activity, which involves identifying the direction of movement that requires the shortest displacement time. Following, the Equation (5.15) or (5.16) is used to determine the equivalent sonic conductance for extending or retracting tasks, respectively. The flow capacity of the throttle valve must be greater than or equal to the equivalent sonic conductance, while the flow capacity of the directional valve must be at least three times greater.

To convert the sonic conductance (C) of the valves into the nominal flow rate (Q_n) , commonly used by manufacturers to characterize the flow capacity of pneumatic valves, the following correlation can be applied.

$$Q_n[NL/min] = 2.5427 \times 10^{10} C[m^3/s. Pa].$$
 (5.24)

Equation (5.24) is derived from the analysis of the ISO 6358 model under the reference conditions established by the VDI 3290 Standard (7 bar_{abs} upstream pressure, 6 bar_{abs} downstream pressure) and a critical pressure ratio of 0.3.

The nominal flow rate can also be correlated with the flow coefficient (C_V), which is commonly used by North American manufacturers to characterize pneumatic valves (Beater, 2007):

$$Q_n[NL/min] = 984 C_V[US gal/min].$$
(5.25)

Some manufacturers present the unit of sonic conductance in L/(min.bar), a more practical unit for datasheets. The conversion to the SI unit of sonic conductance in $m^3/(s.Pa)$ is given by

$$C[L/\min. bar] = 6 \times 10^9 C[m^3/s. Pa].$$
 (5.26)

In Figure 5.9, the flow chart for the sizing of pneumatic valves is presented.

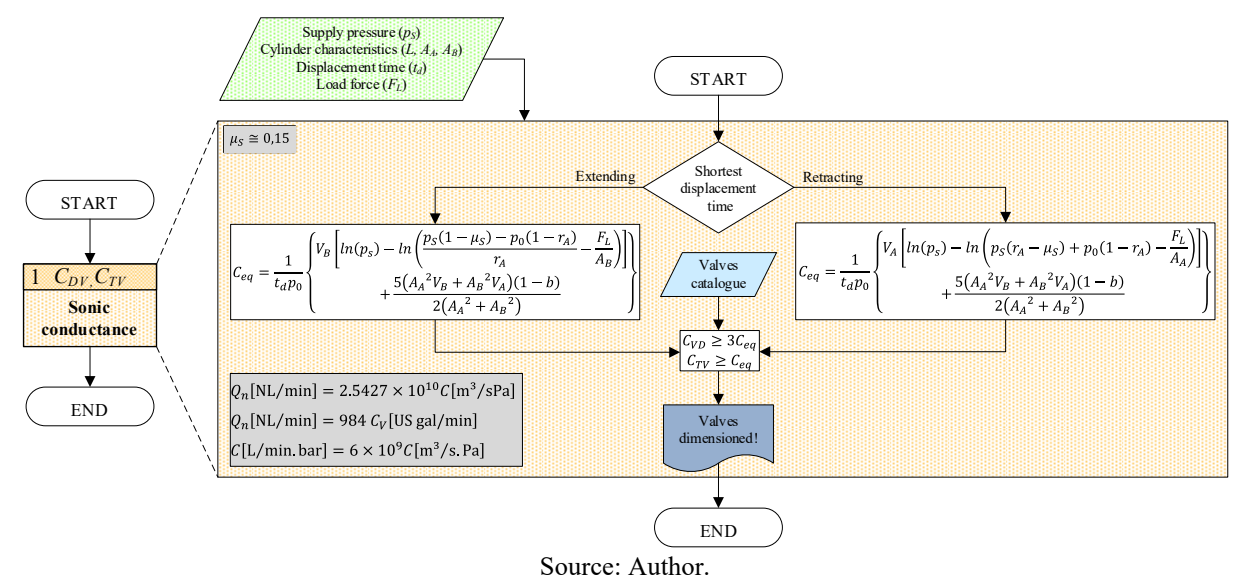


Figure 5.9 – Pneumatic valves sizing flow chart

5.4 FINAL CONSIDERATIONS ABOUT CHAPTER 5

This chapter presented an analysis of the characteristic velocity profile of standard pneumatic actuation systems, which is composed of three distinct phases: the emptying time, transient time, and steady-state time. According to the characteristics of each phase, simplified models were derived to correlate the flow capacity of an equivalent restrictor with the time length of each phase, thus enabling the derivation of an expression to determine the equivalent sonic conductance of the system as a function of the displacement time.

The equivalent flow restrictor analysis was extended to a series connection of pneumatic restrictors, which allowed for the determination of the minimum sonic conductance requirements for throttle valves and directional valve in both meter-in and meter-out applications.

The approach presented in this chapter is further analyzed in Chapter 7, where batch simulations and experimental testing are performed to evaluate the effectiveness of the proposed approach across a wide variety of working conditions, thus ensuring its robustness and applicability in practical applications.

6 SETUP OF PNEUMATIC ACTUATION SYSTEMS

In this chapter, the characteristics of the chamber pressures are analyzed based on the possible throttling configurations of the actuation system, the meter-out and meter-in throttling modes. This analysis provides a better understanding of the system's dynamic behavior and is confirmed through experimental testing, thus helping to define guidelines for selecting the most suitable configuration based on application characteristics.

This chapter also presents the development of a novel monitoring approach to optimize pneumatic drives during the setup of the actuation system. A model called Hybrid Machine Learning (HML) assesses, in real-time, the actual load being applied to the pneumatic drive and provides optimization actions to the user. These optimization actions enable the system to operate at its optimal condition by adjusting the supply pressure and throttle valve openings, serving as a practical setup assistive tool that requires no additional components during equipment operation. The development of this monitoring approach has been published in the author's papers, available at Vigolo *et al.* (2023) and Vigolo; Boyko; *et al.* (2024).

The strategies presented in this chapter allow for improved dynamic operation of the system and compensate for uncertainties frequently encountered during the design of pneumatic drives, which are among the main causes of oversized operation.

6.1 THROTTLING IN PNEUMATIC ACTUATION SYSTEMS

The displacement velocity of pneumatic drives is controlled by throttle valves placed between the directional valve and the cylinder chambers. A common approach is to use throttle valves with a built-in bypass, which allows for different flow capacities in each flow direction. Consequently, there are two possible configurations for assembling the valves: throttling the air entering the cylinder, known as meter-in, or throttling the air exhausting from the cylinder, known as meter-out.

In meter-out throttling, the air inflow to the driving chamber has lower restriction, allowing the driving chamber pressure to remain mostly constant throughout the piston displacement. The outflow from the counterpressure chamber, however, has a higher flow restriction, which is used as the controllable variable to achieve the desired piston velocity and displacement time. As a result, meter-out throttling leads to higher pressure levels in the cylinder chambers. In meter-in throttling, on the other hand, the flow restriction is higher for

the air inflow to the driving chamber, while the outflow restriction on the counterpressure chamber is lower, keeping its pressure close to atmospheric pressure.

The most recommended throttling approach for pneumatic drives is meter-out throttling (Barber, 1997; Beater, 2007; Bollmann, 1997; Fialho, 2004; Hepke, 2016; Prudente, 2000). There are several advantages of using meter-out over meter-in throttling, such as:

Increased safety of operation: Meter-out works with both resistive (load against the movement) and assistive (load in the same direction as the movement) loads, while meter-in controls velocity only for resistive loads.

Higher stiffness: The higher pressure levels in the cylinder chambers increase the stiffness of the drive, making it more robust to load oscillations and less susceptible to stickslip.

Higher end-stroke damping capacity: The increased pressure in the counterpressure chamber improves the kinetic energy absorption capacity of the end-stroke cushioning.

Meter-in throttling is typically recommended for single-acting cylinders or for very short cylinder strokes, where it is not possible to build up enough pressure to operate properly in a meter-out configuration (Beater, 2007). However, the following advantages of meter-in throttling can also be highlighted:

Lower emptying time: Connecting the counterpressure chamber, which has a larger volume at the beginning of the movement, to the less restrictive flow path reduces the time required to start the movement.

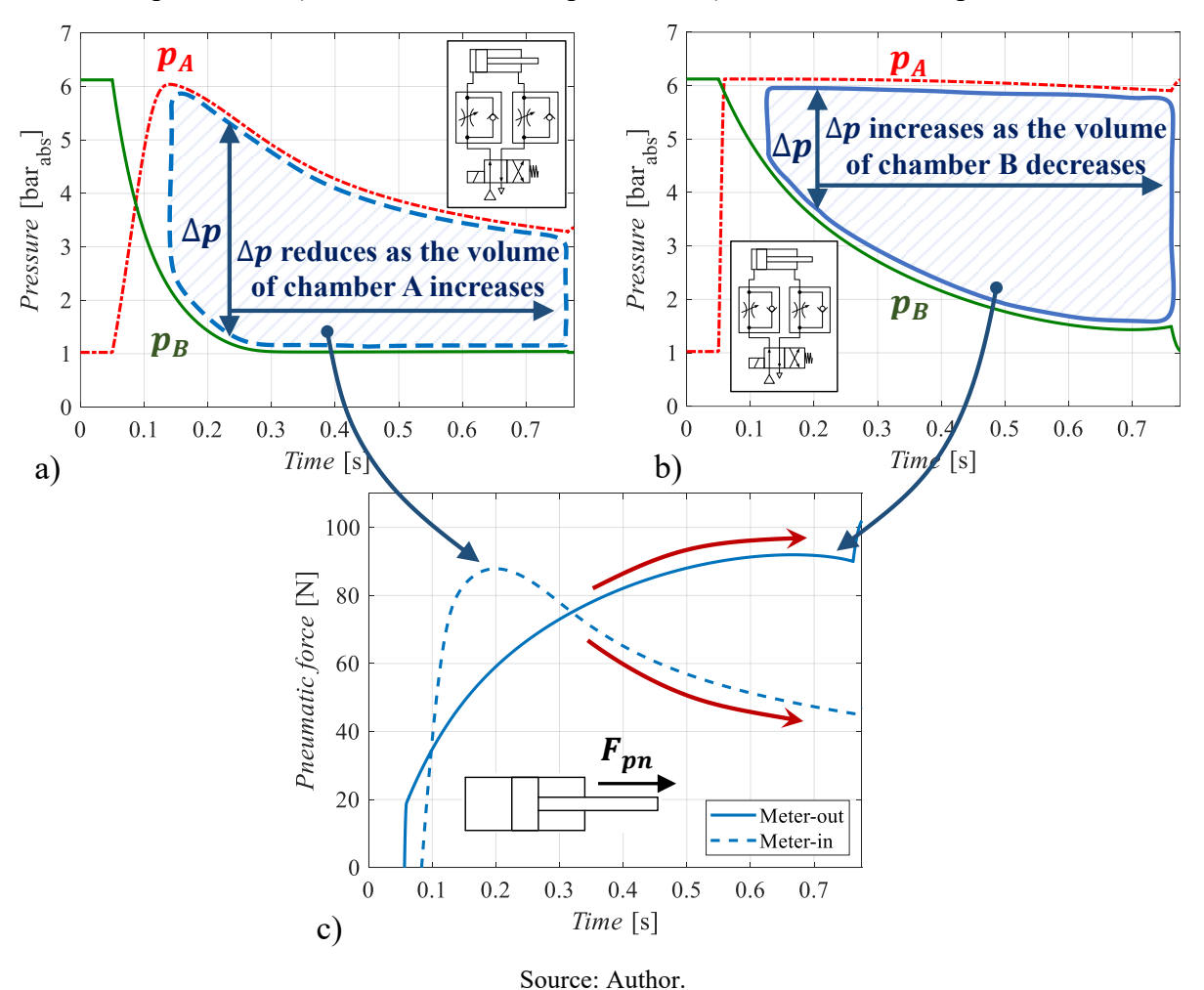
Lower jump-start: Increasing the driving chamber volume reduces the pneumatic force at the beginning of the movement, preventing a sudden jump of the piston (Sagara; Hosono; Yang, 1999).

Energy-saving capability: Since the counterpressure chamber operates at a lower pressure, meter-in throttling consumes less compressed air during the movement. Halting the air inflow after the task is completed has shown great potential for energy savings in pneumatic drives (Terashima *et al.*, 2000).

Properly understanding the characteristics, advantages, and disadvantages of each throttling approach is an important step in setting up a pneumatic actuation system. While the key aspects highlighted above provide a good overview of the characteristics of each throttling

approach, analyzing the chamber pressures offers additional insight into the system's behavior. Therefore, Figure 6.1 presents the pressure profiles of the cylinder chambers and the resulting pneumatic force ($F_{pn} = p_A A_A - p_B A_B - p_0 A_r$) for both the meter-in and meter-out approaches.

Figure 6.1 – Analysis of pneumatic actuation system throttling modes: a) Meter-in chamber pressures; b) Meter-out chamber pressures; c) Pneumatic forces profiles

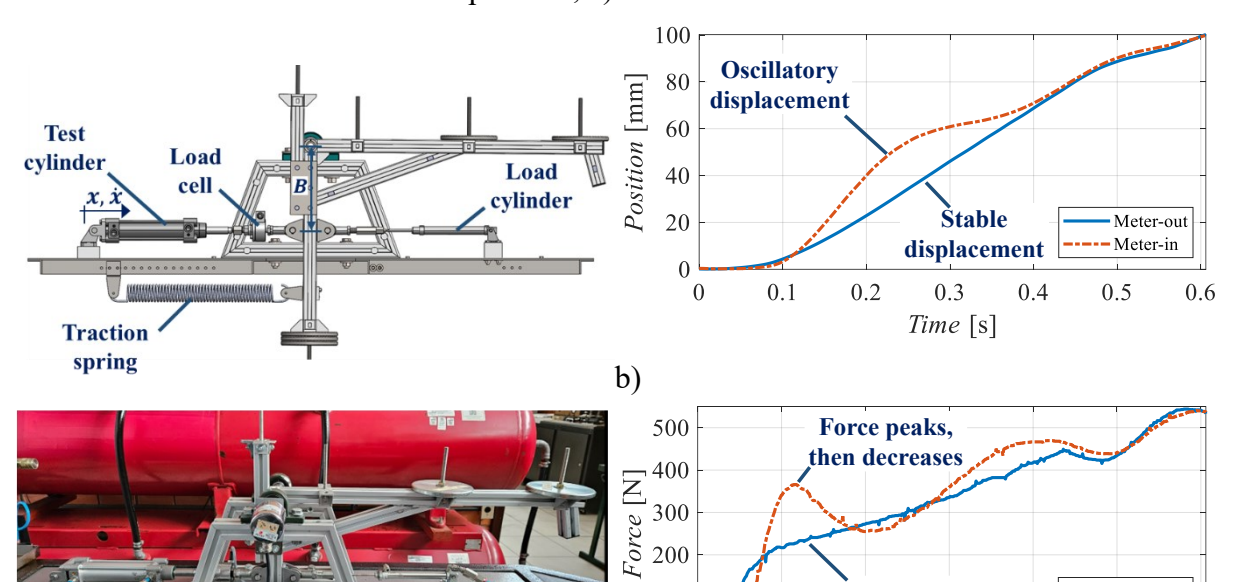


In a meter-in configuration, throttling of the driving chamber, combined with its volume increase during displacement, leads to a decreasing trend in pneumatic force. The pneumatic force reaches its maximum at the beginning of the movement and decreases as the piston moves. In contrast, for a meter-out assembly, the chamber being throttled is the same one being compressed during movement, resulting in an increasing pneumatic force throughout the piston displacement.

Based on these aspects, certain applications benefit from each throttling approach. Spring-based systems, for instance, tend to perform better with meter-out throttling, as the available pneumatic force increases during piston displacement, similar to the behavior of the

spring force. High-inertia applications, on the other hand, may benefit from meter-in throttling, since the available pneumatic force is higher at the beginning of the movement and decreases during displacement, aligning with the inertial force behavior discussed in Section 4.3.2, which is higher at the start and decreases toward the end of the movement.

Figure 6.2 presents the results of two experiments comparing the response of meter-in and meter-out throttling in an application where spring force is dominant. The experiments were conducted on the Ybitú test rig using a Camozzi cylinder model 63MT2C040A0100, with a piston diameter of 40 mm and a stroke length of 100 mm. Camozzi directional and throttle valves, models EN531-33 and RFU 483-1/8, respectively, were used. The spring stiffness was 1,220 N/m, and a constant load force of 170 N was applied using weights and a constant pressure of 7 bar_{abs} in chamber A of a load cylinder with a 16 mm piston diameter, positioned on the opposite side of the testing cylinder. The rotating arm had a moment of inertia of 0.84074 kg.m², which is approximately equivalent to a 22.3 kg mass in linear displacement, based on the rotation radius (B = 0.194 m) where the piston rod is connected. Further details about the test rig's mathematical modeling and instrumentation are provided in Appendix E.



100

c) Source: Author.

a)

0

0.1

Force increases

uniformly

0.2

0.3

Time [s]

0.4

Meter-out

Meter-in

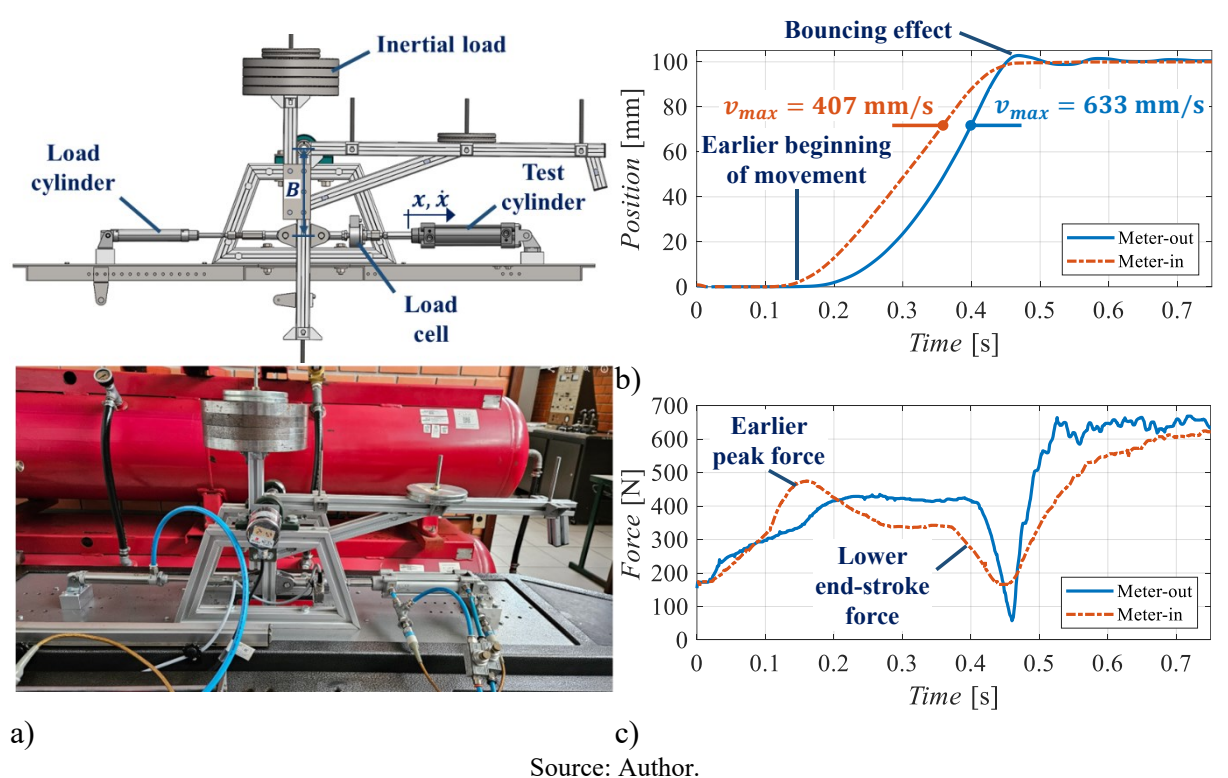
0.5

Figure 6.2 – Spring-based experiment with meter-in/out throttling: a) Test rig; b) Piston position; c) Load force

As can be seen, the displacement with meter-out throttling is more stable and uniform compared to meter-in throttling. The main reason for the oscillatory displacement in meter-in throttling is the reduction in pneumatic force, as shown in Figure 6.2-c). This reduction is caused by a drop in driving chamber pressure, which requires additional time to build up pressure and overcome the increasing spring force. Therefore, the increasing trend of pneumatic force in meter-out throttling is a favorable characteristic for spring-based applications.

In Figure 6.3, a comparison between meter-in and meter-out throttling is presented for applications with high inertial forces. The experiments were conducted on the Ybitú test rig using the same Ø40 mm Camozzi cylinder (model 63MT2C040A0100). Two throttle valves (model GRA-1/4-B from Festo) and a directional valve (model E551-16-15 from Camozzi) were utilized during the experiment. A constant load force of 335 N was applied using a combination of weights and a constant pressure of 7 bar_{abs} in chamber B of a Ø25 mm load cylinder, positioned on the opposite side of the testing cylinder. The rotating arm had a moment of inertia of 1.2222 kg.m², approximately equivalent to the linear displacement of a 32.5 kg mass, based on the rotation radius (0.194 m) where the piston rod is connected. Higher inertial forces were achieved with a shorter displacement time of 0.45 s. Further details about the test rig are provided in Appendix E.

Figure 6.3 – Inertial-based experiment with meter-in/out throttling: a) Test rig; b) Piston position; c) Load force



As can be observed, with meter-out throttling, the piston presented a bouncing effect at the end of its movement. This effect was mainly caused by two factors: 1) The increasing pneumatic force throughout the displacement caused continuous acceleration, resulting in the piston reaching the end-stroke at a higher velocity; and 2) The longer emptying time of the meter-out throttling reduced the time available to complete the task within the specified duration, requiring a higher displacement velocity. During the experiments, various end-stroke cushion settings were tested, however, tightening the cushion's needle further increased the bouncing effect.

For meter-in throttling, it was possible to achieve the same displacement time with a soft stop of the piston at the end of its movement. This behavior is explained by the peak pneumatic force at the beginning of the movement, as shown in Figure 6.3-c), which enables faster acceleration of the system's mass. Following this, the decreasing trend of pneumatic force helps in decelerating the mass before it reaches the end-stroke head. Additionally, the shorter emptying time of the meter-in throttling requires a lower piston velocity to achieve the same displacement time.

Some researchers argue that meter-out throttling is a better option for high-inertia applications because the high counterpressure increases the stroke-end cushion's capacity to absorb kinetic energy (Boyko; Weber, 2024b; Jimenez; Reinertz; Schmitz, 2024; Nazarov; Weber, 2022b). However, as shown in Figure 6.3-b), a 37.7% reduction in the maximum achieved velocity is observed with meter-in throttling. Since kinetic energy is proportional to the square of velocity, the resulting kinetic energy is 58.7% lower with meter-in throttling. Therefore, despite the lower kinetic energy absorption capacity of meter-in throttling, this configuration generates less kinetic energy compared to meter-out throttling, which appears to be a beneficial trade-off, explaining the better performance observed in Figure 6.3-b) with meter-in throttling.

Based on the characteristics of each throttling approach, the four-quadrant diagram in Figure 6.4 provides an overview of the typical applications where each configuration is most suitable.

As a general rule, pure resistive load forces are better suited for meter-in throttling, whereas assistive loads should always use meter-out throttling. However, applications with variable loads throughout the cylinder stroke are likely to perform better with meter-out throttling, even if the load is resistive, as demonstrated by the spring example shown in Figure 6.2. This is due to the higher stiffness of meter-out throttling, which results in more stable piston displacement.

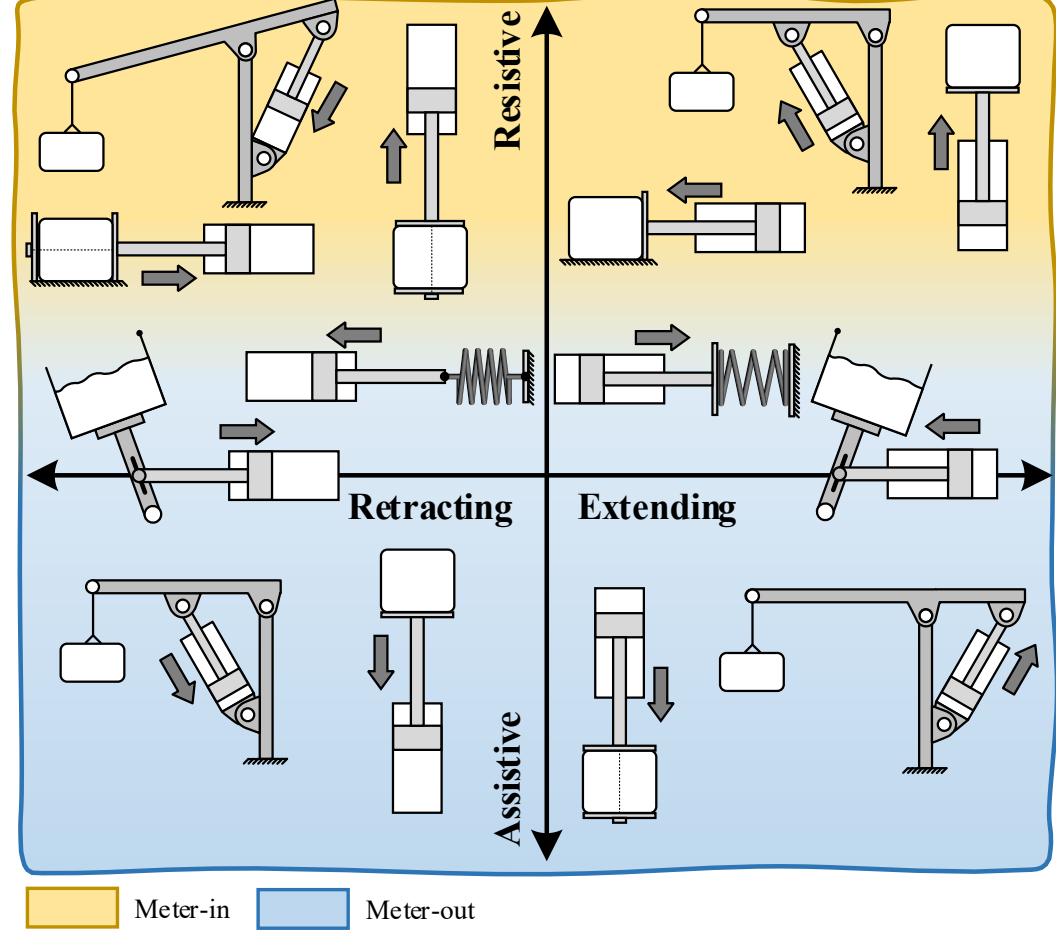


Figure 6.4 – Pneumatic throttling motion-load quadrants

Source: Author.

In Figure 6.4, the examples lying on the resistive/assistive edge represent applications where both load force characteristics are present during the displacement, such as the classic example of a dumping container. In this case, the force acts against the movement during a fraction of the cylinder stroke, and then the force becomes assistive, pulling the cylinder rod. For such cases, meter-out throttling should be used, as meter-in throttling does not provide velocity control for assistive loads, which can lead to dangerous system operation.

It should also be noted that in some applications, the load may be resistive in one direction and assistive in the opposite direction, such as when lifting and lowering a mass with the same actuator. In such cases, either meter-out throttling is recommended or a meter-in-out configuration (Figure 6.5), which applies meter-in throttling during resistive loads and meter-out throttling during assistive load forces.

a) b) c)

Figure 6.5 – Alternative throttling configurations: a) Meter-in-out at chamber A; b) Meter-in-out at chamber B; c) Meter-in-out with pressure reducer

For a meter-in-out configuration, a compact pressure reducer can also be included in the flow path connecting the directional valve directly to the cylinder chamber, as shown in Figure 6.5-c). This configuration prevents rapid pressurization of the driving chamber when displacement occurs in the same direction as the load, which can cause abrupt piston movement when the valve is switched. The pressure reducer valves can be adjusted to maintain a low pressure in the driving chamber, preventing such an effect.

Source: Author.

Based on the possible combinations of throttling methods and the overview diagram presented in Figure 6.4, Figure 6.6 presents a flowchart with guidelines to assist in selecting the best throttling approach. The key questions to be answered are: 1) Does the load during a specific movement consists of assistive loads pulling the cylinder rod, or is the load expected to vary significantly throughout the cylinder stroke? 2) Is the load purely resistive and mostly constant throughout the cylinder stroke, or is the movement performed without an external load? By analyzing both extending and retracting movements of the application and answering the questions above, the flowchart in Figure 6.6 guides the designer on the selection of the best throttling method.

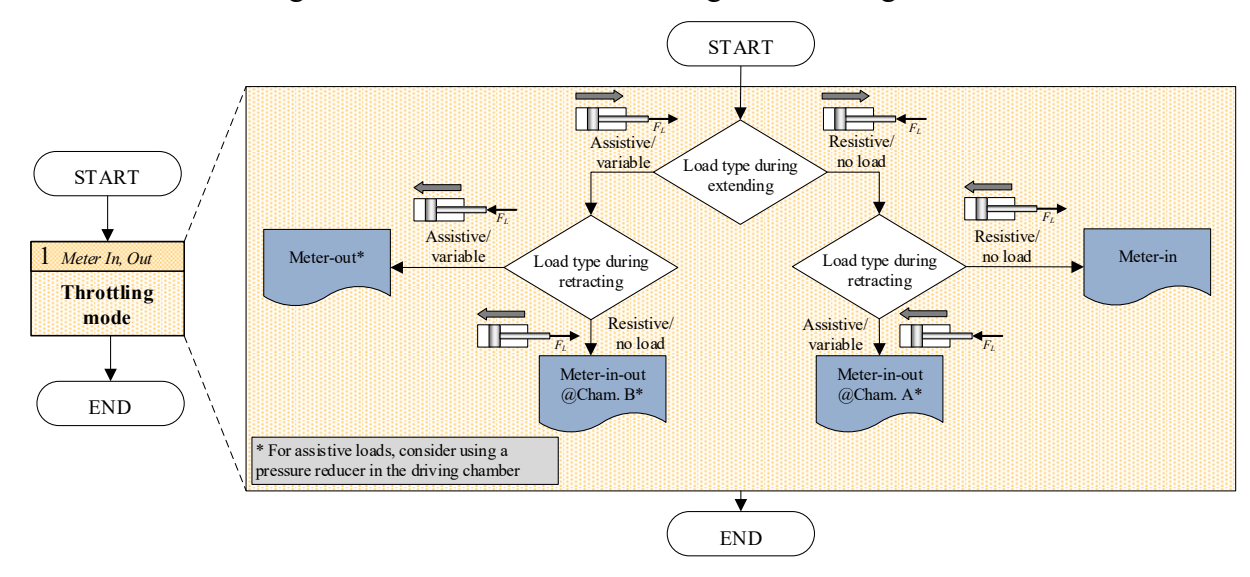


Figure 6.6 – Flowchart for selecting the throttling method

Source: Author.

6.2 ONLINE PARAMETER OPTIMIZATION

The sizing method of pneumatic actuators presented in Chapter 4 is a fundamental step toward developing a robust and efficient pneumatic actuation system. However, while the sizing method is a necessary condition, it is not sufficient for ensuring the system's optimal operation. The determination of the load force is a fundamental input in actuator sizing and must be accurately defined.

But the determination of application load forces presents a significant challenge. As discussed in Section 4.3.2, even in controlled environments where the tests with different loads were analyzed, deriving models capable of accurately predicting application load forces is challenging. Many applications require modeling complex phenomena that are highly dependent on the application. These phenomena include material properties, contact mechanics, thermal effects, fluid dynamics, tribology, and the system's kinematics and dynamics, among others, which can introduce significant uncertainties in load force prediction. Such uncertainties can lead to pneumatic systems operating with excessive energy consumption or poor dynamic performance, characteristics that are often not monitored during equipment operation.

The most logical approach to address these uncertainties involves a prior assessment of the load forces. This approach is particularly suitable for existing systems that operate with a steady load force throughout their life cycle, limiting its applicability to specific retrofit applications. Another approach relies on online monitoring and assessment of the drive

operation using real-time measured data, aiming to identify the actual loading conditions and adjust the system's properties to optimize its performance.

However, as presented in Section 2.2.2, most studies on monitoring pneumatic drives are mainly focused on detecting leakages, condition-based maintenance, and predicting component failures. Therefore, the goal of this section is to present the development of a monitoring strategy for pneumatic actuation systems designed to optimize their operating conditions based on the actual load applied to the piston rod.

The strategy involves the online assessment of the system's loading condition using pressure sensors in the cylinder chambers. Based on this assessment, the supply pressure and throttle valves are adjusted to ensure the system operates near its optimal condition, balancing air consumption and robustness. The goal is to minimize the supply pressure according to the applied load while meeting displacement time requirements, and resulting in a robust operation. Unlike existing approaches, the proposed strategy serves as a one-time assistive setup tool, eliminating the need for permanent integration of the monitoring device during equipment operation.

6.2.1 The reference operating condition

The main task of a monitoring system is to compare the actual working condition of a system with a reference condition. When a significant deviation is detected, a warning and/or corrective action should be taken. To define the reference condition, the optimal operating condition described in Section 4.1.3 is used.

As discussed in Section 4.1 and demonstrated in Figure 6.7, the optimal operating condition is determined by the maximum point of the vC curve, which corresponds to a point on the Op curve and defines the set of pressure ratios for the optimal operating point. This, in turn, is used to derive the Ld curve, which correlates the piston area with the system load. Due to the possible combinations of load force and piston area, there are infinite Ld curves. However, the Ld curve corresponding to the optimal operating point represents the system area that achieves an optimal balance of air consumption and robustness. Therefore, it is referred as the Ld_{opt} curve, as shown in Figure 6.7, and serves as the reference condition for the monitoring system.

The optimal operating point was used in Chapter 4 for piston area sizing. However, during system setup, the actuation area and supply pressure have already been defined.

Therefore, to define the optimal loading curve, the operating point equations can be applied to determine the optimal load force $(F_{L\ opt})$ that the system should handle.

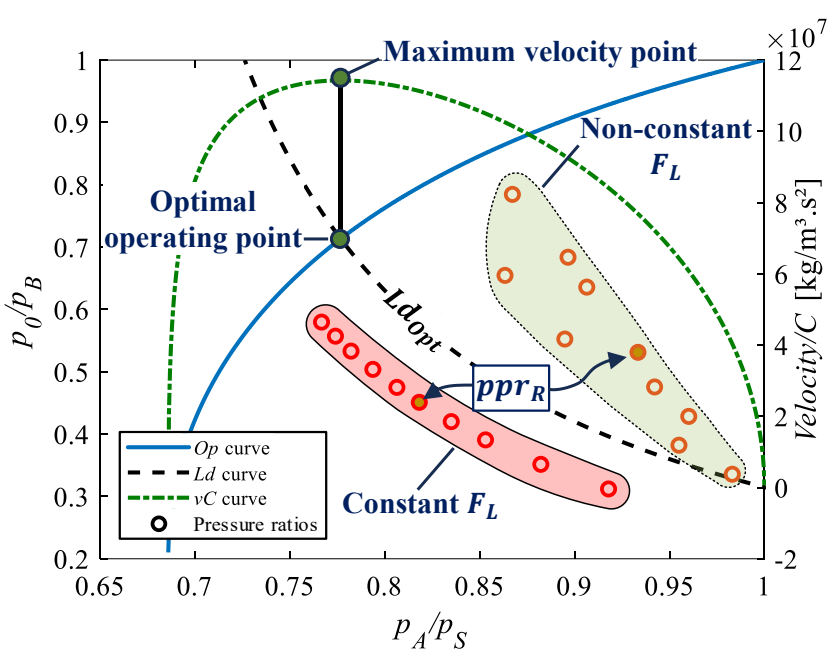


Figure 6.7 – Optimal operating point and the Ld_{opt} curve

Source: Author.

The procedure to define the F_{L_opt} for an extending movement begins by determining the argument (p_A/p_S) that maximizes the vC curve (Equation (4.14)). This can be done either by using Equation (4.16) for an approximate result or through a numerical approach. Given its low computational cost, the numerical method has been adopted in this thesis. To do so, the F_L value in Equation (4.14) is set to unity, and the vC equation is solved over a range of p_A/p_S from $(p_A/p_S)_{min}$ (Equation (4.3)) to 1. The MATLAB function [x,y] = max(f) retrieves the index y, which corresponds to the argument that maximizes the function. This value is then applied in Equation (4.2) to determine the corresponding p_0/p_B pressure ratio, defining the optimal operating point. This optimal operating point is subsequently used in Equation (4.7) to calculate the optimal load force, considering the optimal operating point, supply pressure, and piston area. Therefore, taking in account the parameters of the operating point equations, it can be stated that

$$F_{L \ opt} = f(p_S, b, r_A, \mu_d, A_A). \tag{6.1}$$

A pneumatic actuation system operating under optimal conditions should, during cylinder displacement, maintain pressure ratios as close as possible to the Ld_{opt} curve. Pressure ratios above the Ld_{opt} curve indicate that the system is overloaded, resulting in reduced robustness and velocity. On the other hand, pressure ratios below the Ld_{opt} curve indicate an underloaded condition, leading to lower energy efficiency and excessive air consumption.

Applications with a constant load force (e.g., vertically lifting a mass) will maintain a nearly constant pressure difference between the cylinder chambers, resulting in pressure ratios that follow the trend of the Ld_{opt} curve, as shown by the red circles in Figure 6.7. This allows for fitting all pressure ratios with the Ld_{opt} curve. However, for non-constant load forces (e.g., spring-based systems), the pressure ratios will deviate from the Ld_{opt} curve. For example, Figure 6.8 shows the impact of a hypothetical oscillatory and increasing load force on chamber pressures, with the corresponding pressure ratios represented by the orange circles in Figure 6.7.

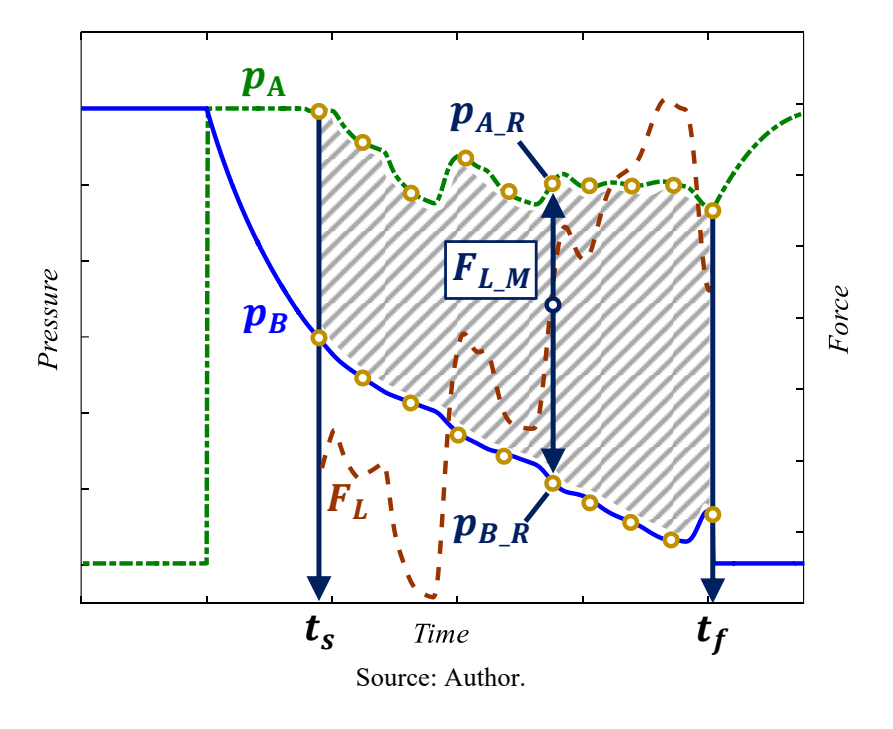


Figure 6.8 – Definition of the reference pair of pressure ratios

In such cases, it is impossible to perfectly match all the pressure ratios with the Ld_{opt} curve. Therefore, a reference pair of pressure ratios, $ppr_R = [p_{A_R}/p_S, p_0/p_{B_R}]$, is adopted, where p_{A_R} and p_{B_R} are the reference pressures for chambers A and B, respectively. These reference pressures result from the analysis of the load force throughout the entire cylinder displacement and are defined at the instant of the mean load force (F_{L_M}) , which is given by

$$F_{L_{-M}} = \frac{1}{t_e - t_f} \int_{t_s}^{t_f} (p_A(t)A_A - p_B(t)A_B - p_0A_h)dt, \tag{6.2}$$

where t_s and t_f are start and final time of the piston displacement, respectively.

For optimal operation, the reference pair of pressure ratios must be approximated from the Ld_{opt} curve. Since Equations (4.2), (4.7), and (4.14) are dependent on supply pressure, a parameter that can be continuously adjusted, the actuation system can be optimized by regulating the supply pressure. Increasing or decreasing the supply pressure will impact the total displacement time of the cylinder, which can also be adjusted using the system's throttle valves. For an extending movement, this can be formulated as the following optimization problem

Minimize
$$DF14 \qquad min \left(\frac{\left(\left(p_{A_R}/p_S \right) - \left(p_A/p_S \right)_{Ld_{opt}} \right)^2 + \left(\left(p_0/p_{B_R} \right) - \left(p_0/p_B \right)_{Ld_{opt}} \right)^2}{\left(\left(p_0/p_{B_R} \right) - \left(p_0/p_B \right)_{Ld_{opt}} \right)^2} \right)$$
 Subject to
$$0.9t_d \leq t_a \leq t_d$$

$$p_{S_min} \leq p_S \leq p_{S_max}$$

$$C_{TV_min} \leq C_{TV} \leq C_{TV_max}$$

where DF14 stands for Diagnostic Feature #14 (see Table 6.2), and represents the minimum Euclidean distance between the reference pair of pressure ratios (ppr_R) and the Ld_{opt} curve vectors $(p_A/p_S)_{Ld_{opt}}$, $(p_0/p_B)_{Ld_{opt}}$. The constraint t_d is the desired displacement time, while t_a is the actual displacement time. Both the supply pressure (p_S) and the sonic conductance of the throttle valve (C_{TV}) are constrained by minimum and maximum values, which are defined during the system's design.

Rather than using a cost function to determine what is a robust and efficient operation, Equation (6.3) is applied to determine how to achieve such an operation. The main advantage of this approach lies in the enhanced comprehensiveness of the results, which are fundamentally guided by the physical laws used to describe the system's behavior and served as the basis for deriving the operating point equations.

6.2.2 Sensitivity analysis

The operating point equations depend on six different parameters $[p_S, b, r_A, \mu_D, A_A, F_L]$. Due to their physical meaning, it is reasonable to assume that, in an online application, these parameters will have some degree of uncertainty associated with them. This uncertainty may have either a significant or not significant impact on the obtained results. To properly address this issue, a sensitivity analysis is conducted in this section to assess the overall impact of the operating point parameters.

The sensitivity analysis was performed using Sobol's indices, a variance-based method that evaluates the impact of each parameter or combination of parameters on the total variance of the model output (Saltelli *et al.*, 2008). Sobol's indices include first-order and total-effect indices. First-order indices measure the individual impact of each parameter on the variance of the results, while total-effect indices account for the contribution of a parameter, including all its interactions with other parameters.

The procedure described in Section 6.2.1 for determining the optimal load force (F_{L_opt}) was used to develop a custom function to calculate the Sobol's indices using the SAFE toolbox for MATLAB (Pianosi, 2022). Sobol's indices for Equation (6.1) were computed using a random matrix with 5000 instances of each parameter. The parameters were uniformly distributed within the ranges specified in Table 6.1, encompassing all commercially available pneumatic actuation systems.

Table 6.1 – Parameters range for Sobol's indices

Parameter	Range
Supply pressure (p_S)	[4 - 11] bar _{abs}
Critical pressure ratio (b)	[0.1 - 0.528]
Area ratio (r_A)	[0.75 - 1]
Dynamic friction coefficient (μ_d)	[0.02 - 0.5]
Piston diameter (d_c)	[8 - 320] mm

Source: Author.

The results of the sensitivity analysis are shown in Figure 6.9, where indices near zero indicate that the parameter has no significant impact on the model output, while higher values denote the most relevant parameters.

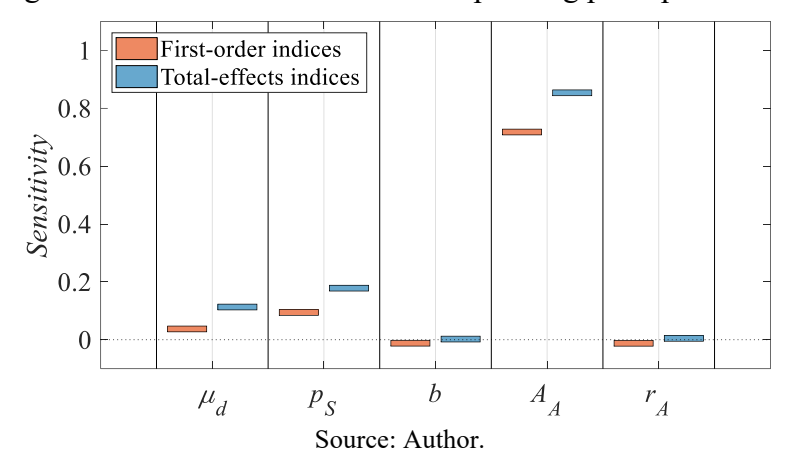


Figure 6.9 – Sobol's indices for the operating point parameters

As can be seen, the most relevant parameters in the operating point equations are the cylinder area (A_A) , supply pressure (p_S) , and the dynamic friction coefficient (μ_d) . In contrast, the critical pressure ratio (b) and the area ratio (r_A) have a negligible impact.

Therefore, based on the Sobol's sensitivity indices, it can be concluded that assuming a constant value of b=0.3 has no significant impact on the determination of F_{L_opt} . The supply pressure can be determined using sensor data, while A_A , and r_A are input values provided by the user. The dynamic friction coefficient (μ_d) is determined online using a Neural Network model, as shown in Section 6.2.3.

Beyond the five operating point parameters analyzed in this section, the author's papers Vigolo *et al.* (2023) and Vigolo; Boyko; *et al.* (2024) also address an additional parameter, r_C , which represents the ratio of the sonic conductance of flow path B to flow path A. However, since the sensitivity analysis presented Vigolo; Boyko; *et al.* (2024) showed that this parameter is not relevant for system optimization, it has been excluded from the analysis in this section to avoid having to rewrite the operating point equations, potentially leading to misunderstandings with the equations presented in Chapter 4.

6.2.3 The Hybrid Machine Learning Model (HML)

Although Equation (6.3) can correctly determine the system parameters for an optimal operating condition, applying this approach in an online system is not feasible due to the iterative nature of optimization solvers, such as gradient descent, which may result in prolonged setup times and potential operational risks.

As an alternative to using Equation (6.3) for online applications, machine learning models can process input data from sensors and predict corrective actions to achieve the system's optimal operating condition. Due to the discrete nature of the expected output

corrective actions, multi-class classification models, such as Support Vector Classifiers (SVC), Decision Trees, and K-Nearest Neighbors (KNN), among others, must be employed for this task.

However, to apply the operating point equations as an assessment tool for online applications, it is necessary to determine the cylinder's dynamic friction coefficient (μ_d). One possible solution would be to use Equation (4.25) to calculate the friction coefficient based on the supply pressure, mean velocity, and load force. However, as explained in Section 4.2, this equation was derived from a system operating under optimal conditions. Therefore, its application to oversized or undersized systems, which are the focus of the proposed monitoring approach, is likely to result in significant errors.

A different approach to using Equation (4.25) is the use of the available sensor data to estimate their value through machine learning models. In this case, the expected output is a continuous value, requiring the use of regression models such as Linear and Non-Linear Regression, Support Vector Machines (SVM), Regression Trees, and Artificial Neural Networks.

Combining machine learning models into a pipeline, where the output from one model becomes the input to the next, results in a hybrid model that aims to address the limitations of individual models. This approach has already been applied in various fields, such as heart disease prediction (Kavitha *et al.*, 2021), electricity peak load forecasting (Lee; Cho, 2022), and credit rating (Tsai; Chen, 2010).

For a machine learning model to interpret the data read from sensors and correctly provide the desired output, the data must be transformed into diagnostic features (DF), that is, converting the sensor data into meaningful values that are correlated with the desired output. For the model developed in thesis, 14 diagnostic features were used, as shown in Table 6.2.

Table 6.2 – Diagnostic features for an extending displacement

DF#	Description	DF#	Description
1	Relative displacement time error	8	$p_A/p_S \otimes F_{L_M}$
2	1 - $(p_A/p_S @ \text{last pressure ratio})$	9	$p_0/p_B \otimes F_{L_M}$
3	1 - $(p_0/p_B @ \text{last pressure ratio})$	10	$max(p_A/p_S)$
4	Supply pressure	11	$max\left(p_{0}/p_{B}\right)$
5	Mean velocity	12	$min(p_A/p_S)$
6	Cylinder stroke	13	$min(p_0/p_B)$
7	Cylinder diameter	14	$min_{dist}(ppr_r, \boldsymbol{Ld_{opt}})$

Source: Author.

The relative displacement time error is defined as the ratio of the displacement time error $(t_a - t_d)$, where t_a is the actual displacement time, to the desired displacement time (t_d) .

The diagnostic features are based on sensor data, user input, and features derived from the operating point equations, as shown in Figure 6.10, which graphically presents diagnostic features #2–3 and #8–14.

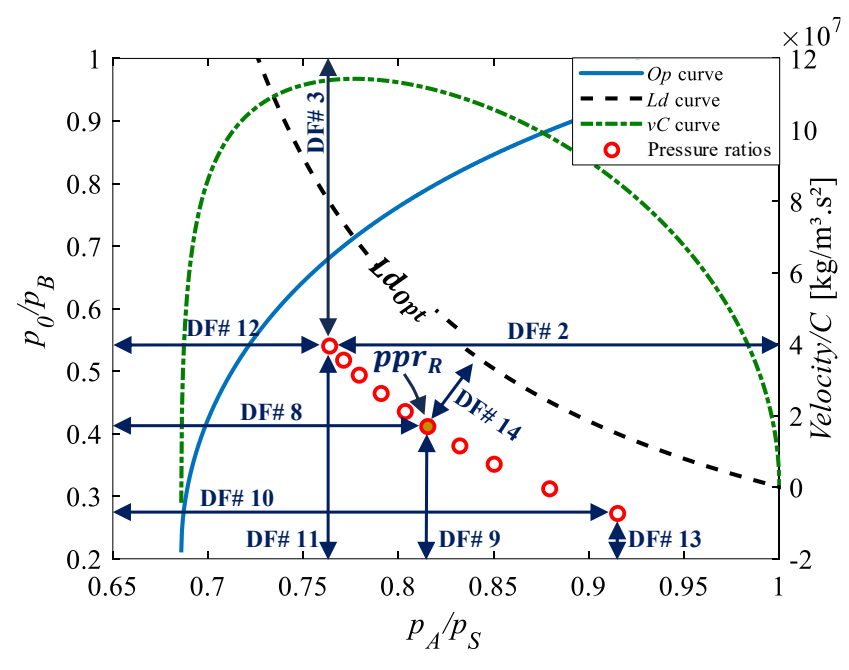


Figure 6.10 – Diagnostic features derived from the operating point

Source: Author.

As can be seen, the x- and y-axes in Figure 6.10 are not on the same scale. Therefore, to calculate the values of diagnostic features #2–3 and #8–14, the x- and y-data were scaled between 0 and 1 using the minimum and maximum values of the *Op* curve for each axis.

Since diagnostic feature #14 depends on the Ld_{opt} curve described in Section 6.2.1, the value of μ_d must be determined prior to calculating DF#14. Therefore, the regression model used to estimate μ_d is based solely on the first 13 diagnostic features, while the classification model for determining the corrective action utilizes all 14 diagnostic features. The resulting structure of the developed Hybrid Machine Learning (HML) model is shown in Figure 6.11, where LS(t) represents information from the limit switches, X_N denotes the diagnostic features, and \in_{Opt} refers to the output optimization action.

 $p_A(t)$, $p_B(t)$, LS(t)Feature Feature Multi-class Regression Extraction extraction classification model d_c , d_r , L, t_d $X_N[1-13]$ ϵ_{Opt} μ_D $X_N [1-14]$ 2nd Stage 1st Stage model

Figure 6.11 – Architecture of the Hybrid Machine Learning (HML) model

Source: Author.

In Figure 6.11, feature extraction stages 1 and 2 are responsible for feature engineering, where tasks such as subsetting the sensor data and performing the necessary calculations to determine the diagnostic features are carried out. The definition of the machine learning models used for regression and multi-class classification is discussed in Section 6.2.4.

As can be seen, the only sensor data required are the chamber pressures and the displacement time from the limit switches, facilitating practical applications. The monitoring system outputs will be either an action to adjust the supply pressure (increase or decrease) or an action to adjust the throttle valves (open or close). If no adjustment is needed, the output will be 'None'.

6.2.4 The model training

Machine learning models require a large quantity of data for training. This data can be obtained either from actual sensors, as in Karpenko and Sepehri (2002), Subbaraj and Kannapiran (2010), and Nakutis and Kaskonas (2007), or from a validated simulation model, as in Raduenz *et al.* (2020). Using a simulation model offers the advantage of generating data under various operating conditions, such as load forces, supply pressure, and system components, resulting in a robust model capable of performing effectively in different scenarios.

Therefore, this work has used the simplified dynamic simulation model described in Section 3.3 to generate training data. The working conditions for the simulations were randomly produced using a uniform distribution within the range presented in Table 6.3.

In total, 500 different design requirements were created. For each, an actuator with a standardized diameter was selected based on the sizing process described in Chapter 4. The minimum sonic conductance of each flow path was determined using the approach presented in Chapter 5. Throttle valves from the RFU series by Camozzi were then selected (CAMOZZI, 2019b), and a variable sonic conductance was modeled based on the number of screw turns of the throttle valves.

Parameter Range [4 - 11] bar_{abs} Supply pressure (p_s) Displacement time (t_d) [0.5 - 1.5] s Stroke (L)[0.05 - 0.5] m Uncertainty factor [0.5 - 1.5]Viscous coefficient (B) [0.07 - 4,500] N.s/m Spring stiffness (K)[0.04 - 3,500] N/m Moving mass (M)[0.04 - 1,500] kg Working angle (α) [0 - 90]°

Table 6.3 – Design requirement ranges for machine learning dataset generation

Source: Author.

After selecting a set of pneumatic cylinders and throttle valves, an uncertainty factor was applied to the load force components to account for scenarios where the required application force is not fully known. This approach allowed for the consideration of both oversized and undersized operating conditions.

To generate the dataset for predicting the friction coefficient, simulations were conducted for each of the 500 working conditions using 100 distinct combinations of throttle valve intermediate openings. This resulted in a dataset containing 50,000 lines of data, with diagnostic features #1-13 used to train the regression machine learning model for friction coefficient prediction.

Regression models available in MATLAB were evaluated to assess their predictive performance for this problem. The dataset was split into two parts: 90% for training the models and 10% for testing. The accuracy of the trained models was measured using the RMSE value obtained from the test data, as shown in Table 6.4.

Table 6.4 – RMSE performance of tested regression models

Regression model	RMSE
Linear regression	0.0512
Regression Tree	0.0404
Bagged Tree	0.0347
SVM	0.1138
ANN	0.0161

Source: Author.

The best results were obtained with an artificial neural network (ANN). In this work, a feedforward neural network was used, with a hyperbolic tangent sigmoid activation function for the hidden layer and a linear activation function for the output layer. The network

architecture was determined heuristically, starting with a small, shallow network and progressively expanding it. Excessively increasing the number of neurons or hidden layers negatively impacted performance. Thus, the network was configured with six neurons in a single hidden layer.

For training the classification model to predict corrective actions, the following approach was adopted. A new set of 500 design requirements was generated using the range described in Table 6.3. For each design requirement, the optimization strategy outlined in Section 6.2.1 was applied to determine the ideal parameters for the throttle valve (C_{TV_opt}) and the supply pressure (p_{S_opt}) . Equation (6.3) was used to develop a cost function, which was minimized using the MATLAB optimization function *fmincon*. Three simulations were performed for each optimized system to collect data for future predictions. In the first simulation, the supply pressure was set to its initial design value (p_{S_ol}) , and the throttle valve was set to its central opening position $(\overline{C_{TV}})$, simulating the likely first operating condition when the setup process begins.

From the first simulation, the values of diagnostic features #1-14 were recorded, and a corrective action was defined based on the following rule.

```
\begin{array}{ccc} \text{if} & p_{S\_opt} \neq p_{S\_d} \\ & \text{if} & p_{S\_opt} > p_{S\_d} \\ & & \text{Action = Increase} \, p_S \\ & & \text{else} \\ & & & \text{Action = Reduce} \, p_S \\ & & \text{end} \\ \end{array}
```

In the second simulation, the value of p_S was set equal to p_{S_opt} , and the values of diagnostic features #1–14 were recorded. This represents the response of the system after the correction of the supply pressure, but without optimizing the throttle valve opening. Therefore, the following rule was applied to adjust the throttle valve opening.

```
\begin{array}{l} \text{if } C_{TV\_opt} \neq \overline{C_{TV}} \\ \\ \text{if } C_{TV\_opt} > \overline{C_{TV}} \\ \\ \text{Action = Open } C_{TV} \\ \\ \text{else} \\ \\ \text{Action = Close } C_{TV} \\ \\ \text{end} \\ \end{array}
```

A third simulation was performed with both p_S and C_{TV} set to their optimal values. At this point, the 14 diagnostic features were recorded along with the 'None' corrective action, representing the system operating under optimal conditions.

Using this approach, a dataset with 1,500 lines of data was obtained, and the available classification models in MATLAB were used to assess the classification accuracy. The dataset was then split into two parts: 90% of the data was used for training the models, and the remaining 10% was used for testing. Table 6.5 presents the accuracy, which is the ratio of correct predictions to the total number of predictions, for the evaluated models.

Table 6.5 – Accuracy of tested classification models

Classification model	Accuracy
Decision Tree	87.4%
Bagged Tree	89.6%
SVC	89.0%
KNN	66.5%
ANN	62.4%

Source: Author.

The best results for corrective action prediction were obtained using the Bagged Tree model, an ensemble technique where multiple decision trees are trained on different subsets of the original dataset. The final prediction is made by aggregating the outputs of the individual trees, which reduces the variance of the results (Chelliah, 2021).

For the implementation of the classification models, 14 predictor variables (diagnostic features #1–14) and one target variable were used. The target variable was a categorical variable with five possible classes (Increase p_S , Reduce p_S , Open C_{TV} , Close C_{TV} , None), representing the possible corrective actions. The selected Bagged Decision Tree model was built using 100 individual decision trees, with a minimum leaf size of 1 and a maximum of 20 splits. The remaining parameters were set to the default values of MATLAB's *TreeBagger* function.

Figure 6.12 presents the confusion matrix for the test data of the Bagged Tree model. In the matrix, each column represents the target class (the class that the model is trying to predict), and each row represents the output class (the actual class predicted by the model). The cells along the diagonal show correct predictions (true positives), while the off-diagonal cells represent misclassifications, where the model predicted the wrong class.

0 0 0 78.6% 3 Close C_{TV} 0.0% 6.0% 1.6% 0.0% 0.0% 21.4% 15 0 0 100% Increase p_S 0.0% 8.2% 0.0% 0.0% 0.0% 0.0% Output Class 1 61 2 95.3% None 0.5% 33.5% 0.0% 1.1% 4.7% 0 3 40 3 87.0% 0.0% 1.6% 0.0% 22.0% 1.6% 13.0% 2 0 2 36 83.7% Reduce p_S 1.6% 1.1% 0.0% 1.1% 19.8% 16.3% 62.5% 100% 89.6% 78.6% 95.2% 87.8% 21.4% 37.5% 0.0% 4.8% 12.2% 10.4% Reduce PS **Target Class** Source: Author.

Figure 6.12 – Confusion matrix for predicting corrective actions on test data

The overall accuracy of the model demonstrates its capacity to predict corrective actions for unseen data. Moreover, the predicted class 'None' achieved an accuracy of 95.3%, indicating that for almost all cases, the classification model will iteratively adjust the system parameters until an optimal condition is reached.

As can be seen, the HML is adopted as an alternative to the cost function defined in Equation (6.3) to optimize the system parameters. However, the data used to train the machine learning models were generated based on the optimization performed using Equation (6.3), which relies on the operating point equations to establish an optimal operating condition. Therefore, the machine learning models do not determine what is the optimal operating condition but instead provide guidance on how to achieve it, as the optimal operating condition is fundamentally defined by the system's governing equations, from which the operating point equations were derived.

The effectiveness of the Hybrid Machine Learning (HML) model in reducing air consumption while maintaining robust operation for under- and oversized actuators is evaluated in Section 7.2, which presents the results of an experimental implementation of the HML.

6.3 OVERVIEW OF THE DESIGN AND SETUP FRAMEWORK

The design and setup framework presented in this thesis includes a sizing method for the pneumatic cylinder, throttle valves, and directional valve; guidelines for selecting the most appropriate throttling method; and an assistive setup tool to optimize supply pressure and throttle valves opening based on the application's requirements and the load handled by the pneumatic drive.

Throughout Chapters 4, 5, and 6, the fundamentals for developing the framework have been thoroughly presented. At the end of each chapter, a flowchart summarizes the key activities involved in each step of the design process. Figure 6.13 provides an overview of the four main steps of the developed framework. In the figure, ellipses represent results (e.g., data, documents, or the system itself), while rectangles indicate the steps performed during the design and setup process.

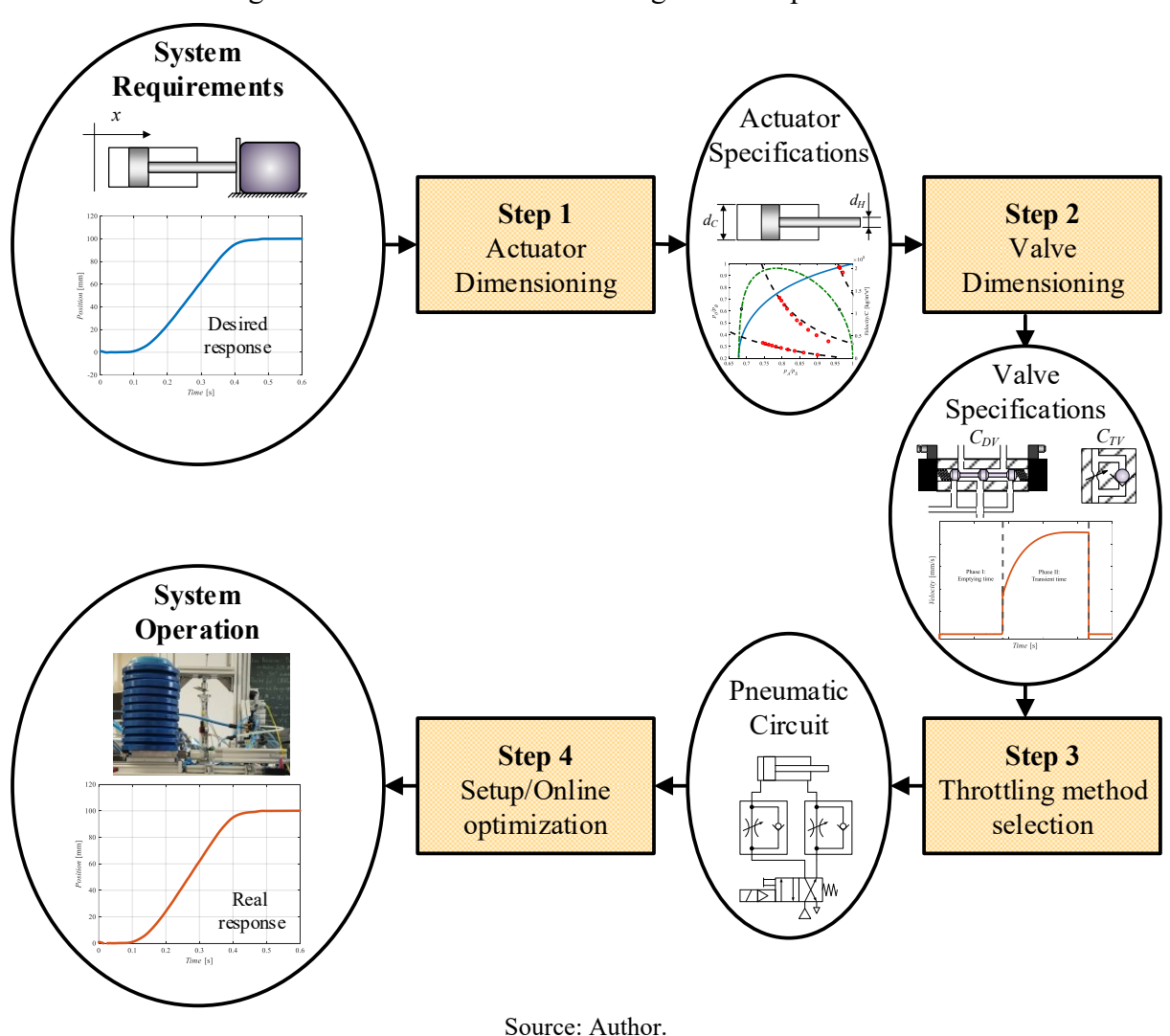


Figure 6.13 – Overview of the design and setup framework

The design and setup framework comprises four main steps. Step 1: Actuator Sizing includes five activities, as outlined in Figure 4.29 of Chapter 4. Step 2: Valves Sizing involves

a single activity, described in Figure 5.9 of Chapter 5. Step 3: Throttling Method Selection also consists of one activity, detailed in Figure 6.6 of Chapter 6. Finally, Step 4: System setup focuses on assembly and commissioning the designed system, during which online optimization of the supply pressure and throttle valve opening can be performed using the HML introduced in Section 6.2 of Chapter 6.

6.4 FINAL CONSIDERATIONS ABOUT CHAPTER 6

This chapter highlighted two characteristics relevant for pneumatic actuation systems during equipment setup. The first is related to the selection of the throttling mode, where the designer can opt for meter-in throttling, meter-out throttling, or a combination of both. Through an analysis of the pressure behavior in the cylinder chambers, it was demonstrated that meter-out throttling results in an upward trend in available pneumatic force, while meter-in throttling leads to a downward trend. These characteristics make each throttling method suitable for specific tasks: meter-out throttling is recommended for assistive load forces, while meter-in throttling is more appropriate for resistive load forces.

Another challenge faced during the system setup is determining whether it is operating under optimal conditions. Uncertainties in determining load forces during the design of the actuation system are likely to result in poor performance during operation. Furthermore, such conditions are often difficult to detect if the system is performing its tasks as expected. To address this, a monitoring system called HML has been developed to assess, in real-time, the actual working condition of the system based on measured pressure data from the cylinder chambers. The HML provides guidelines to the user for improving operating conditions, enabling the reduction of supply pressure while meeting displacement time requirements and ensuring robust performance. Its main application is as an assistive setup tool, used during the commissioning of the pneumatic actuation system. After setup, the HML can be removed without disrupting equipment operation, ensuring minimal cost impact on the system.

Therefore, in addition to having a sizing method derived from the governing equations of the system, focused on balancing air consumption with robustness, the tools provided in this chapter contribute to an enhanced operation through the correct throttling method and help overcome possible uncertainties faced during the sizing of the pneumatic drive.

7 SIMULATION AND EXPERIMENTAL RESULTS

In this chapter, the developed sizing method for pneumatic actuators and valves is compared with analytical sizing methods available in the literature. The initial analyses are performed in a simulated environment, where batch simulations are conducted under various working conditions. Subsequently, test rig experiments are carried out to highlight the strengths and weaknesses of each sizing method and to validate the results obtained from the simulations.

The Hybrid Machine Learning (HML) model is also evaluated in this chapter. It was embedded in a multi-purpose hardware platform and applied to optimize the working conditions of various actuation systems operating in diverse configurations, including over- and undersized applications. The results were compared with a traditional system setup approach and a commercially available energy-saving solution, demonstrating the effectiveness of the HML in optimizing the performance of pneumatic drives.

The results presented in this chapter provide a basis for confirming the hypotheses discussed in Chapters 4–6, demonstrating the balance between air consumption and the robustness of pneumatic actuation systems. They also highlight the capability of the developed methods to design systems that operate at this optimal balance.

7.1 EVALUATION OF SIZING METHODS FOR PNEUMATIC ACTUATION SYSTEMS

To compare the operating point method with analytical methods available in the literature, two approaches were selected. The first is the empirical method described in Section 2.3.1, which uses Equation (2.1) to size the cylinder area. Given the wide range of yield coefficients (η) used by different authors, this approach was further divided into three subapproaches, each considering a different yield coefficient: a lower value of $\eta = 50\%$, an intermediate value of $\eta = 70\%$, and a higher value of $\eta = 90\%$.

For each yield coefficient, a specific sizing approach for pneumatic valves was selected: the required flow rate method (Q_r) using Equation (2.2), the flow coefficient (C_V) method using Equation (2.3), and the method proposed by De Negri (2001), which employs the ISO 6358 model to calculate the sonic conductance (C_{DN}) using Equation (2.4).

To combine the empirical sizing methods for the cylinder and the valve, literature guidelines were followed. For example, Camozzi (2019a) suggests adopting the required flow rate method (Q_r) for the valve design, along with a yield coefficient of 90% to size the cylinder

actuation area. In contrast, SMC (1997) recommends the flow coefficient method (C_V) for the valve and a yield coefficient ranging from 50% to 85% for the cylinder; therefore, the flow coefficient model was combined with a yield coefficient of 50%. Meanwhile, the approach proposed by De Negri (2001) suggests a yield coefficient of 80% and a pressure drop of 0.5 bar for sizing of the cylinder and the sonic conductance of the valve. Therefore, to simplify comparisons and establish an intermediate evaluation point, the De Negri's approach (for directional valve sizing - C_{DN}) was combined with a yield coefficient of 70% and no pressure drop for the cylinder sizing.

The second approach considered in the analysis is the Pneumatic Frequency Ratio (PFR) method described in Section 2.3.2, which uses Equation (2.8) to size the piston diameter and Equation (2.9) to determine the flow capacity of the valves (C_{PFR}) .

The exergy-based method described in Section 2.3.3 was not considered in this analysis, as there are no clear guidelines for determining the chamber pressures to use in equations (2.10) and (2.11), and there are limitations in defining the SF factor for the applications analyzed in this thesis.

Table 7.1 summarizes the methods evaluated in this chapter, along with the references for the equations used.

Description Cylinder sizing Valve sizing **Abbreviation Operating Point** Op. Point Figure 4.29 Empirical method with $\eta = 90\%$ Equation (2.1)Equation (2.2) $\eta @ 0.9 \& Q_r$ Empirical method with $\eta = 70\%$ Equation (2.1)Equation (2.4) $\eta @ 0.7 \& C_{DN}$ Empirical method with $\eta = 50\%$ $\eta @ 0.5 \& C_V$ Equation (2.1)Equation (2.3)Pneumatic Frequency Ratio Equation (2.8)Equation (2.9) PFR

Table 7.1 – Sizing methods used for the comparative analyses

Source: Author.

For the empirical methods and the pneumatic frequency ratio method, no guidelines are provided for selecting the force to use when dealing with variable load forces. Therefore, the classical engineering approach was adopted, focusing on the most critical scenario, which involves the maximum expected load force. For the operating point method, the load force component analysis presented in Section 4.3.2 was considered.

7.1.1 Simulation-based assessment of the sizing methods

The initial analyses of the sizing methods were conducted using the simplified simulation model described in Section 3.3. The simulations were performed according to the design requirement ranges presented in Table 7.2, covering most pneumatic applications.

Four groups of 50 distinct applications were randomly generated based on the parameter ranges defined in Table 7.2, covering most standard pneumatic applications with piston diameters ranging from 8 to 63 mm. Each application represents a unique set of design requirements. The first group (G1) consisted of applications with only gravitational and inertial forces; the second group (G2) included gravitational, inertial, and spring forces; the third group (G3) was composed of gravitational, inertial, and viscous forces; and the fourth group (G4) encompassed all four load force components.

Table 7.2 – Design requirement ranges for evaluating the sizing methods

Parameter	Range
Supply pressure (p_S)	[4 - 9] bar _{abs}
Displacement time (t_d)	[0.3 - 2.0] s
Stroke (L)	[0.05 - 0.5] m
Viscous coefficient (B)	[0.4 - 840] N.s/m
Spring stiffness (K)	[10 - 1,900] N/m
F_L Moving mass (M)	[0.15 - 450] kg
Working angle (α)	[0 - 90] °

Source: Author.

For each of the 50 configurations, a commercially available cylinder was selected for each sizing method presented in Table 7.1. After selecting the cylinder, the supply pressure was adjusted to ensure an exact match between the application load and the selected piston diameter. As an example of the sizing results for group G1, Table 7.3 presents the results of all five sizing methods applied to one of its applications. It consists of a system with a moving mass of 56.21 kg, a working angle of 13.55°, a cylinder stroke of 125 mm, and a displacement time of 1.068 seconds.

The sizing load force of the *PFR* method differs from the remaining methods because it does not account for the inertial forces, as this component is addressed through the pneumatic eigenfrequency and pneumatic frequency ratio. To enable direct comparison, the results of all

valve sizing methods were standardized to the same unit using equations (5.24), (5.25), and (5.26).

		•		•		
Parameters	Unit	Op. Point	η @0.9 & Q_r	η @ 0 .7 & C_{DN}	η @0.5 & C_V	PFR
Sizing Load Force (F_L)	N	141.5	141.5	141.5	141.5	129.2
Piston Diameter (d_c)	mm	20	20	20	25	20
Supply pressure (p_S)	bar_{abs}	8.19	6.02	7.45	6.78	9.23
Hose length (L_h) / diameter (d_h)	m / m		(0.5 / 0.004	4	
Design sonic conductance (C_{eq})	L/min.bar	6.45	3.58	5.51	7.16	6.31

Table 7.3 – Sizing results for a Group #1 application example

Source: Author.

To avoid any potential interference from valve design in determining cylinder robustness, the sizing of the pneumatic valves was not considered in this initial analysis. This means that, in each application, the sonic conductance of the valves was increased as needed to achieve the displacement time specified by the design requirement. Therefore, the results shown in Figure 7.1 to Figure 7.4 do not consider the sizing of the valve, only the sizing of the cylinder. The combination of the cylinder and valves is analyzed in the results shown in Figure 7.5.

The robustness of the pneumatic drives was determined using equations (4.9) and (4.10), with the impact on displacement time resulting from an approximately 10% increase in load forces after the system was adjusted to meet the required displacement time, as explained in Section 4.1.3. To accurately determine the change in the load force, a position-averaged force was calculated using the following expression

$$\Delta F_{L} = \frac{1}{L} \int_{0}^{L} \left(F_{L_rob}(x) - F_{L_d} \right) dx, \tag{7.1}$$

where F_{L_rob} represents the load force applied during the robustness test, where each component of the load force was increased by 10%, while F_{L_d} refers to the load force used during the sizing of the actuator.

In addition to robustness, the simulations also assessed the impact on air consumption. For this purpose, the air consumption of the operating point method was used as a reference, measuring how much more or less compressed air each method consumed compared to the operating point method. The analysis considered the consumed compressed air after the task is completed, where the driving chamber reaches the supply pressure, as this is a common behavior in standard pneumatic applications.

The simulation results for robustness and relative air consumption for Group #1, which consisted of only gravity and inertial forces, are shown in Figure 7.1 as a box plots.

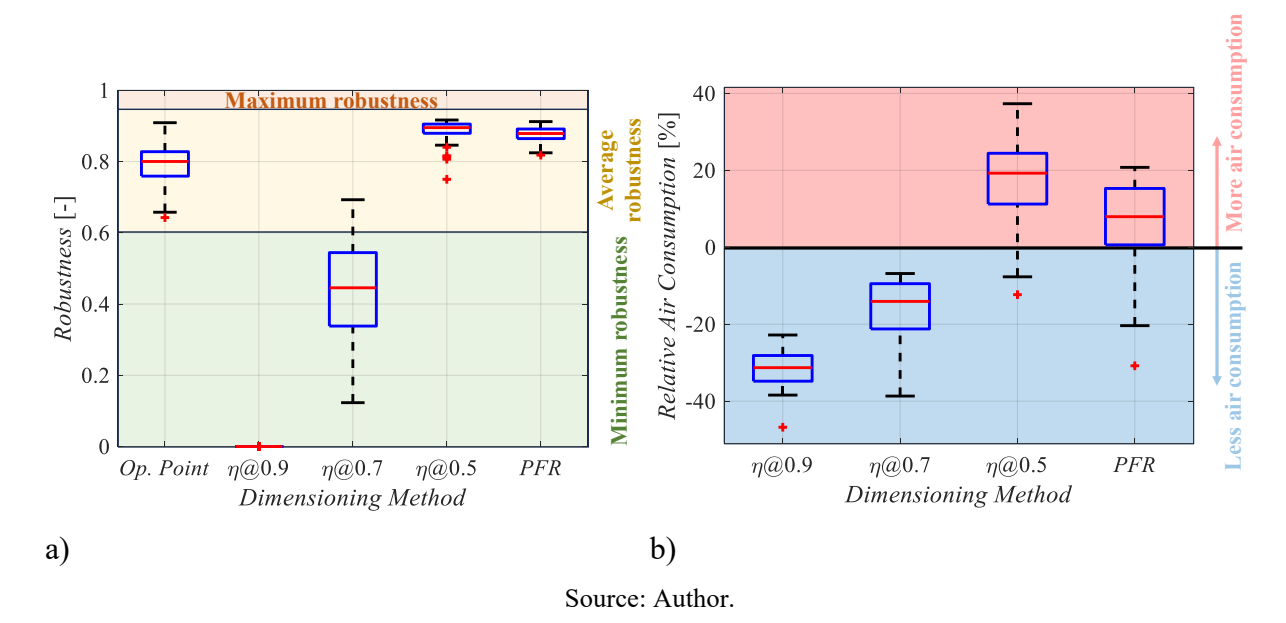


Figure 7.1 – Box plot results for gravity and inertial force applications: a) Robustness; b) Relative air consumption

As can be seen, the empirical method with $\eta=90\%$ resulted in zero robustness. This means that even if the drive is capable of meeting the design requirements, a slight change in the load force can cause the drive to move at a much lower speed or even stall. Increasing the yield coefficient (η) to 70% improved the robustness of the drive. However, 50% of the simulated systems had robustness values between 0.12 and 0.44, which is not an ideal range due to the higher sensitivity of the cylinders to load changes. The yield coefficient of 50% and the *PFR* methods, on the other hand, resulted in significantly higher robustness for all simulated systems, but this indicates excessive air consumption.

The operating point method, in turn, focuses on sizing cylinders with robustness between 0.6 and 0.95, as presented in section 4.1.3. In this range, aspects of dynamic performance are maximized, maintaining good robustness without excessive air consumption. As seen in the box plot in Figure 7.1, this range of robustness was achieved in the performed simulations.

In terms of air consumption, it can be observed that the methods with a yield coefficient (η) of 70% and 90% consumed less air than the operating point method, with an average reduction of 15% and 33%, respectively. However, this is also linked to poor dynamic performance and robustness, which makes it unsuitable for practical applications. For $\eta = 50\%$

and the *PFR*, where robustness is ensured, there was an average increase of 18% and 6%, respectively, in air consumption compared to the operating point method.

Following the range of design requirements presented in Table 7.2, another set of 50 applications was randomly generated. For this second group (G2), a spring force component was added to the inertial and gravitational force components. As an example of the sizing process results for G2 systems, Table 7.4 presents the design requirements and the results from the sizing process for one of its applications. It consists of a system with a moving mass of 11.74 kg, a working angle of 5.49°, a spring stiffness of 370.77 N/m, a cylinder stroke of 0.4 m, and an extending time of 0.99 seconds.

Table 7.4 – Sizing results for a Group #2 application example

Parameters	Unit	Op. Point	η @0.9 & Q_r	η@0.7 & C _{DN}	η @0.5 & C_V	PFR
Sizing Load Force (F_L)	N	124.4	168.9	168.9	168.9	159.3
Piston Diameter (d_c)	mm	32	32	32	40	32
Supply pressure (p_S)	bar_{abs}	4.04	3.35	4.01	3.71	4.98
Hose length (L_h) / diameter (d_h)	m / m		(0.5 / 0.004	4	
Design sonic conductance (C_{eq})	L/min.bar	43.29	15.52	30.20	58.19	49.12

Source: Author.

The differences observed in the sizing load forces are due to the different assumptions made in each approach. The operating point method uses a corrective factor for spring and damper applications, avoiding the use of the maximum load force, which is the typical assumption in empirical methods. Moreover, the load force in the *PFR* method differs from that in empirical methods because it accounts only for gravity and spring forces, excluding the inertial force component. According to the *PFR* method, the sizing load force should not exceed 50% of the cylinder's maximum force. Therefore, whenever necessary, the supply pressure was increased to keep it below this threshold.

The simulation results for robustness and relative air consumption for the second group (G2) of 50 applications are shown in Figure 7.2.

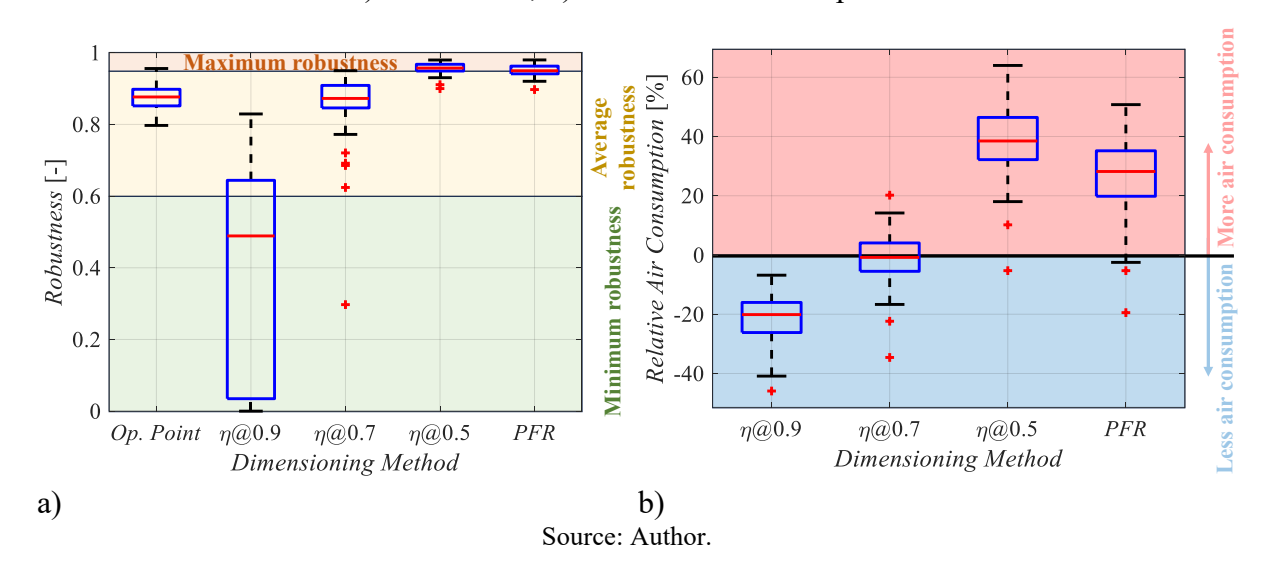


Figure 7.2 – Box plot results for gravity, inertial, and spring force applications: a) Robustness; b) Relative air consumption

The main difference observed between the results of the simulations performed without spring force is that the robustness for all three yield factors (η) of the empirical method and the *PFR* method was higher. For $\eta = 90\%$, which presented zero robustness without spring force, robustness values greater than 0.5 were achieved in nearly 50% of the performed simulations. The relative air consumption, in turn, also showed higher values compared to the cases without spring force, with the yield factor $\eta = 50\%$ and the *PFR* methods consuming more compressed air than the operating point method in nearly 100% of the cases.

Another characteristic that can be observed is the number of outliers (indicated by the red plus signs). These outliers are associated with configurations where the cylinder's friction force is relatively high, requiring greater pneumatic force to complete the task, which results in lower robustness values.

For the operating point method, robustness in the range of 0.79 to 0.95 were achieved, which is similar to the results of pure inertial and gravity force applications. The main reason for this is the corrective factor K_S , presented in Section 4.3.2, which prevents the oversizing of the actuator for spring-based applications.

For the third group of applications, the spring force was replaced by a viscous force component, and another set of 50 applications was created using the range shown in Table 7.2. Table 7.5 presents an example of the sizing results for this group. The example consists of a system with a moving mass of 16.73 kg, a working angle of 31.81°, a viscous coefficient of 116.91 N.s/m, a cylinder stroke of 0.16 m, and an extension time of 0.95 seconds.

Parameters	Unit	Op. Point	η @0.9 & Q_r	η@0.7 & C _{DN}	η@0.5 & C _V	PFR
Sizing Load Force (F_L)	N	114.1	131.9	131.9	131.9	126.0
Piston Diameter (d_c)	mm	20	20	20	25	20
Supply pressure (p_S)	bar_{abs}	6.93	5.68	7.01	6.39	9.03
Hose length (L_h) / diameter (d_h)	m / m		(0.5 / 0.004	4	
Design sonic conductance (C_{eq})	L/min.bar	8.75	4.73	7.46	10.11	8.83

Table 7.5 – Sizing results for a Group #3 application example

Source: Author.

The differences in the sizing of load forces are also related to the different assumptions made for each design requirement, similar to the application shown in Table 7.4. For the *PFR* method, the sizing load force once again exceeded 50% of the cylinder's maximum force, requiring an increase in supply pressure to keep it below this threshold, as recommended by Doll; Neumann and Gauchel (2024).

The results for robustness and relative air consumption from the simulations with the third group (G3) of 50 applications are shown in Figure 7.3.

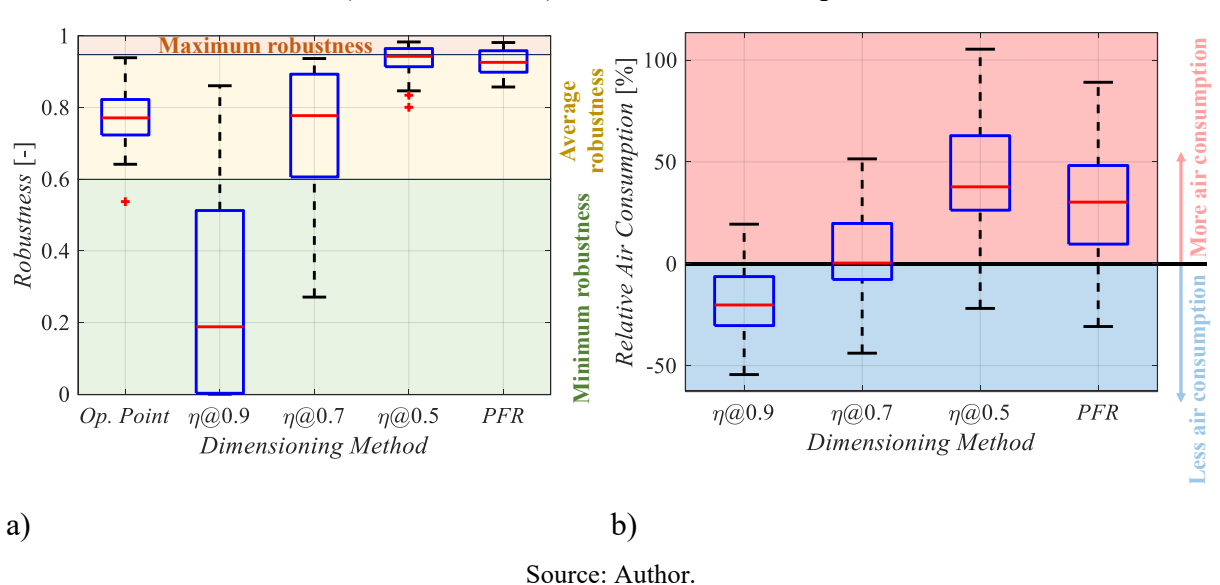


Figure 7.3 – Box plot results for the gravity, inertial, and viscous force (G3) applications: a) Robustness; b) Relative air consumption

The replacement of a spring component with a viscous component did not significantly impact the robustness and relative air consumption trends. In general, the robustness box plot results showed a slight downward shift for all sizing methods, which can be explained by the higher total load force during the displacement of viscous components. On the other hand,

spring-based forces have a maximum force closer to the stroke end, as presented in Figure 4.24 with experiments G3.2 and G3.3. This characteristic may result in slightly higher robustness for spring-based systems.

In the fourth group (G4) of applications, all four load force components were combined, resulting in a set of 50 distinct systems. Table 7.6 presents an example of the sizing results for one of the G4 application. This example involves a task with a moving mass of 56.15 kg, a working angle of 9.59°, a spring stiffness of 254.78 N/m, a viscous coefficient of 139.42 N.s/m, a cylinder stroke of 0.16 m, and a displacement time of 1.09 seconds.

Table 7.6 – Sizing results for a Group #4 application example

Parameters	Unit	Op. Point	η @0.9 & Q_r	η @0.7 & C_{DN}	η @0.5 & C_V	PFR
Sizing Load Force (F_L)	N	157.6	188.3	188.3	188.3	173.3
Piston Diameter (d_c)	mm	25	25	25	32	32
Supply pressure (p_S)	bar_{abs}	6.27	5.27	6.49	5.70	5.32
Hose length (L_h) / diameter (d_h)	m / m		(0.5 / 0.004	4	
Design sonic conductance (C_{eq})	L/min.bar	11.20	5.71	9.29	13.94	18.26

Source: Author.

In this application, the sizing load force of the *PFR* method also exceeded 50% of the cylinder's maximum force, requiring an increase in supply pressure to keep it within this threshold. Once again, the differences in sizing load forces across the methods are due to the distinct assumptions used in each, similar to the configurations shown in Tables 7.3 to 7.5.

The results for robustness and relative air consumption from the simulations with the fourth group (G4) of 50 configurations are shown in Figure 7.4.

The main characteristic observed with all four load force components is the increased robustness of the sizing methods. The empirical method with a yield coefficient of 90% achieved robustness values greater than 0.5 for 75% of the simulated systems. A yield coefficient of 50% and the *PFR* methods resulted in a narrow box plot with nearly 80% of the simulated systems with robustness higher than 0.95. Consequently, relative air consumption also increased, with around 60% of all simulated systems consuming more compressed air than the operating point method.

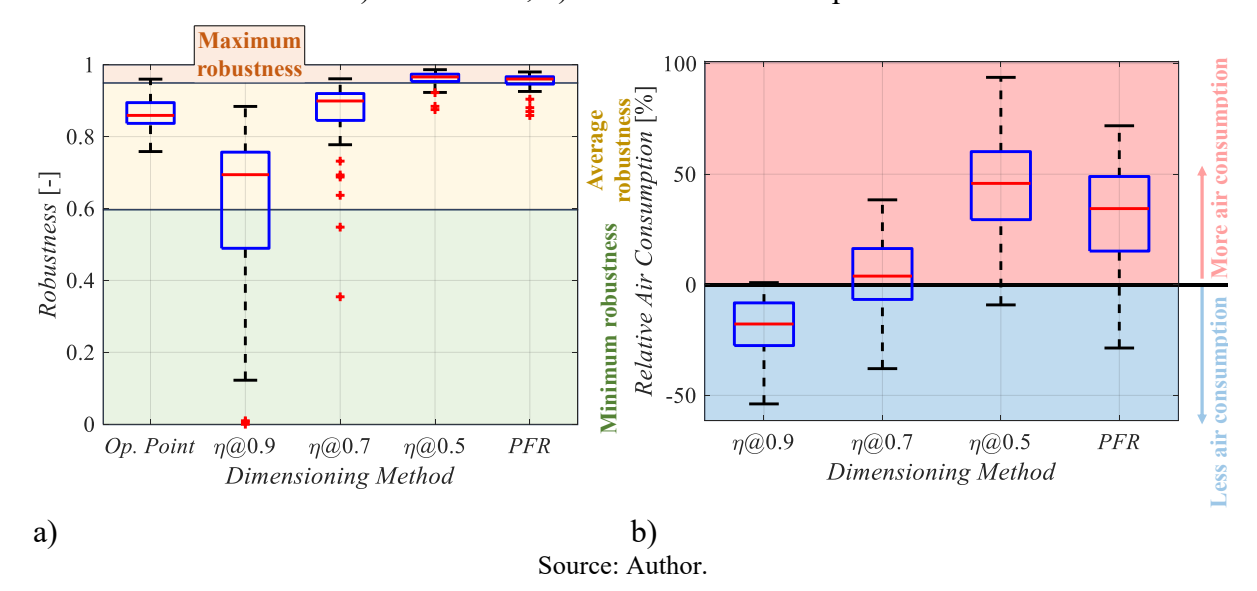


Figure 7.4 – Box plot results for gravity, inertial, spring, and viscous force (G4) applications: a) Robustness; b) Relative air consumption

Once again, the cylinders dimensioned using the operating point method achieved robustness values in the range of 0.76 to 0.96, demonstrating its effectiveness in balancing air consumption and robustness.

The results presented in Figures 8.1–8.4 help explain the wide range of yield coefficients reported in the literature. While a yield coefficient of 90% performs reasonably well for applications with various load force components, it performs poorly in cases involving the vertical displacement of heavy masses. This, combined with the common uncertainty in determining the actual load force of the application, often leads designers to establish their own sizing rules based on past experiences of 'what worked' and 'what didn't'.

After analyzing the sizing methods without constraints on the flow capacity of the valves, a second round of simulations was performed to evaluate the effectiveness of the valve sizing methods. This time, the goal was not to analyze cylinder robustness or air consumption but rather the system's ability to achieve the displacement time specified by the design requirements.

For this analysis, the same four groups of applications with different load force components were considered. The valves and cylinders were dimensioned using the methods presented in Table 7.1. Simulations were performed for both meter-in and meter-out throttling, with the calculated sonic conductance from each sizing method applied to the more restrictive flow path, while the other flow path was set to a sonic conductance up to three times bigger.

Figure 7.5 presents the box plot results for the relative displacement time of each sizing method, which is the ratio of the time required to complete the task to the time specified by the design requirement.

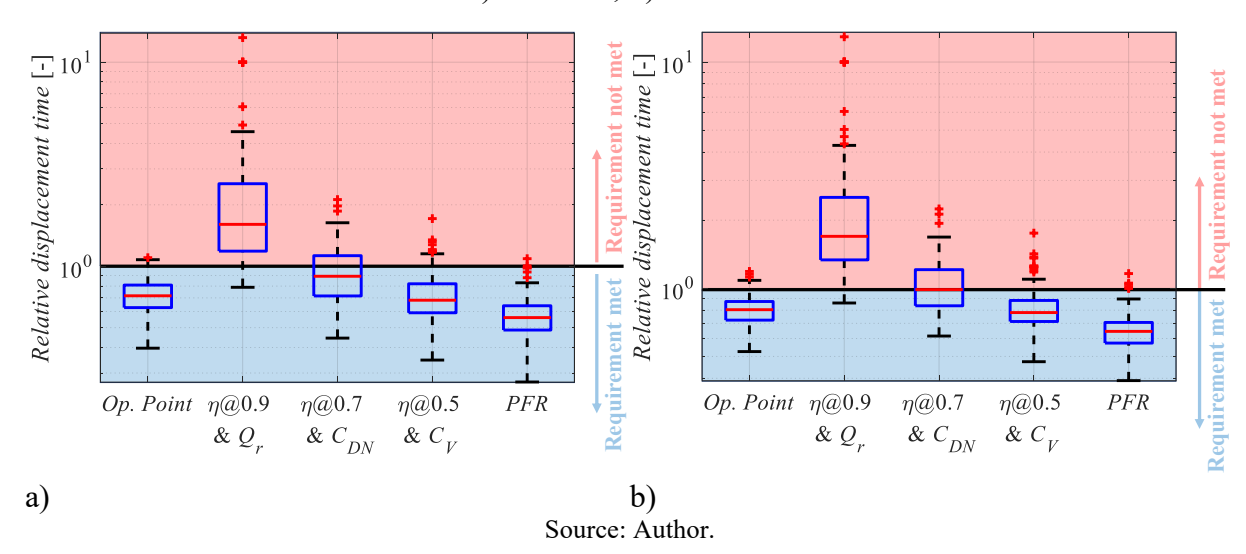


Figure 7.5 – Box plot results for the relative displacement time of the simulated systems: a) Meter-in; b) Meter-out

The main goal when designing a throttle valve is to ensure that its flow capacity is sufficient to complete the displacement in a time equal to or shorter than the design requirement. Therefore, for the results presented in Figure 7.5, a relative displacement time equal to or less than 1 is desirable. As shown, for the operating point method, the relative displacement time ranged from 0.4 to 1.1 for the meter-in configuration and from 0.52 to 1.18 for the meter-out configuration.

Compared to the other methods, the operating point method stands out by achieving a relative displacement time within the requirement for nearly 100% of the simulations and by having the smallest data range, as represented by the total height of the box plot, including outliers. These characteristics highlight the effectiveness of the developed method in properly designing the cylinder and valve set.

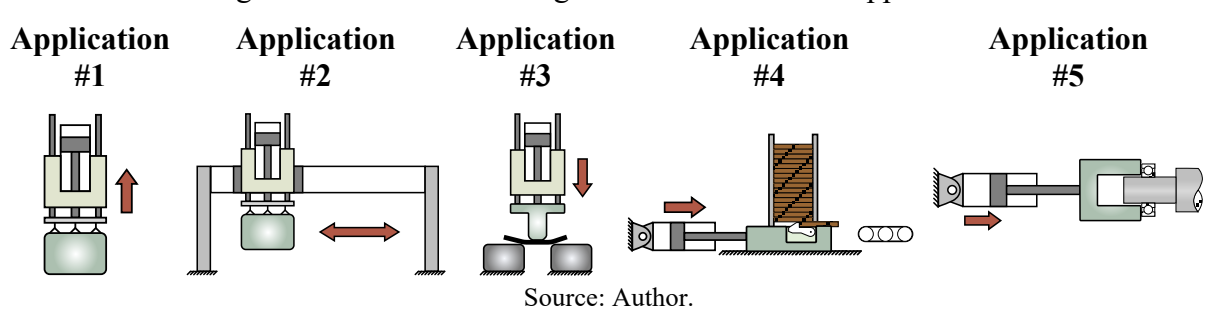
For the remaining methods, it can be observed that the combination of $\eta@0.9 \& Q_r$ fails to meet the requirements in nearly 100% of the cases, while $\eta@0.7 \& C_{DN}$ fails in about 50% of the cases. In contrast, both $\eta@0.5 \& C_V$ and the *PFR* method successfully achieved the required time in approximately 95% of the simulations. However, the *PFR* method tends to oversize the system valves, as indicated by the lower quartile results, leading to excessively fast displacements.

It can also be noted that, apart from the operating point method, the remaining methods resulted in a high number of outliers, highlighting their inability to provide consistent performance in valve sizing across a wide range of applications and loading conditions.

7.1.2 Experimental assessment of the sizing methods

The sizing methods presented in Table 7.1 were applied to determine the cylinder area and the flow capacity of the throttle valves for five different applications, represented by the schematic diagrams in Figure 7.6. Each application was selected to represent typical working conditions in which pneumatic drives are used to perform specific automation tasks. The Ybitú test rig, described in Appendix E was configured to replicate the expected load forces for each application.

Figure 7.6 – Schematic diagrams of the evaluated applications



The results of the experiments are presented in terms of: piston position and velocity measured by the test rig sensors; robustness calculated using Equation (4.10); relative air consumption, which measures the percentage of air consumed by each sizing method compared to the operating point method, with air consumption based on the cylinder and hose volume and supply pressure; and the required sonic conductance of the throttle valves, estimated based on the number of screw turns of the valve and compared with the designed sonic conductance of the throttle valve.

In the following subsections, the characteristics of each application, as well as the experimental results, are presented.

7.1.2.1 *Application #1*

The first application analyzed involved the vertical lifting of a 33 kg mass, which is supported by a suction cup attached to the cylinder rod. The lifting is achieved through the retracting movement of a cylinder with a 100 mm stroke, completed within a total time of 0.45 seconds. The cylinder is equipped with a double guide, which introduces a viscous force component with a viscous friction coefficient of 43.75 N.s/m. A reference supply pressure of 7 bar_{abs} was used for the sizing process. For this application, a kinetic energy of 3.26 J is expected (Equation (4.37)). Table 7.7 presents the dimensioned cylinder, supply pressure, throttle, and directional valves for each sizing method listed in Table 7.1.

Table 7.7 – Sizing methods results for Application #1

Parameters	Unit	Op. Point	η @0.9 & Q_r	η @0.7 & C_{DN}	η @0.5 & C_V	PFR
Sizing Load Force (F_L)	N	367	375.8	375.8	375.8	343.2
Piston Diameter (d_c)	mm	40	32	40	40	40
Supply pressure (p_S)	bar_{abs}	7.1	7.2	6.1	8.13	6.8
Design sonic conductance (C_{eq})	L/min.bar	49.3	25.1	29.3	28.6	37.4
Throttle valve (C_{TV})	L/min.bar	49.6	31.9	31.9	31.9	49.6
Directional valve (C_{DV})	L/min.bar	165.2	217.1	217.1	217.1	217.1
Hose length (L_h) / diameter (d_h)	m / m		0	0.35 / 0.00	55	

Source: Author.

The sizing load force (F_L) is different between the methods due to the different assumptions made in each approach. While the operating point method incorporates corrective factors for spring- and damper-based applications, empirical methods typically assume the most critical scenario involving the maximum load force. In the PFR method, the load force includes only gravity and viscous forces, as the inertial force is inherently accounted for through the pneumatic eigenfrequency and the pneumatic frequency ratio.

To select a commercially available throttle valve, the flow capacity from all methods was converted into sonic conductance using equations (5.24), (5.25), and (5.26). A valve model was chosen with a maximum sonic conductance at the throttling path equal to or greater than the design value. For the operating point method, the directional valve was selected with a sonic conductance equal to or greater than three times the required sonic conductance. For the remaining methods, since no specific guidelines are provided for selecting directional valves, the directional valve with the highest capacity available in the laboratory was used, ensuring it

offered minimal resistance to airflow. The throttle valves were assembled in a meter-in-out configuration at chamber B due to the resistive force during retraction and the assistive load force during extension.

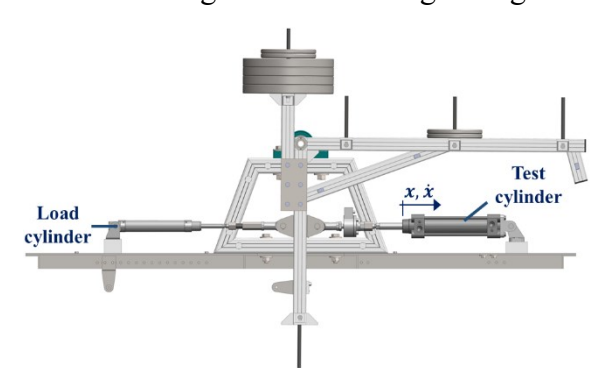
The hose diameter and length were selected in such a way that their sonic conductance is equal to or greater than three times the design sonic conductance, following the same principle used for the minimum flow resistance of the directional valve described in Section 5.2. To determine the sonic conductance of the hose (C_h) , the approach presented in ISO 6358-3 (ISO, 2014) was used, in which it is given by

$$C_h = \frac{\pi d_h^2}{2 \times 10^3 \sqrt{(2.35 \times 10^{-3} d_h^{-0.31}) \frac{L_h}{d_h} + 1}}$$
(7.2)

where L_h and d_h are the hose's length and diameter, respectively.

Figure 7.7 presents the configuration of the Ybitú test rig used in the experiments to replicate the load force characteristics of vertically lifting a mass with a double-guide cylinder.

Figure 7.7 – Test rig configuration for Application #1 experiments



Test rig mass (M): 27.4 kg

Moment of inertia (*I*): 1.2222 kg.m² Center of gravity (CG_x): 0.017607 m Center of gravity (CG_y): 0.119897 m

Load cylinder: Ø 25 mm

Load cylinder pressure: 8.05 bar_{abs} @ Ch. B

Expected kinetic energy (E_{kn}): 3.42 J Maximum load force (F_{L_max}): 376 N

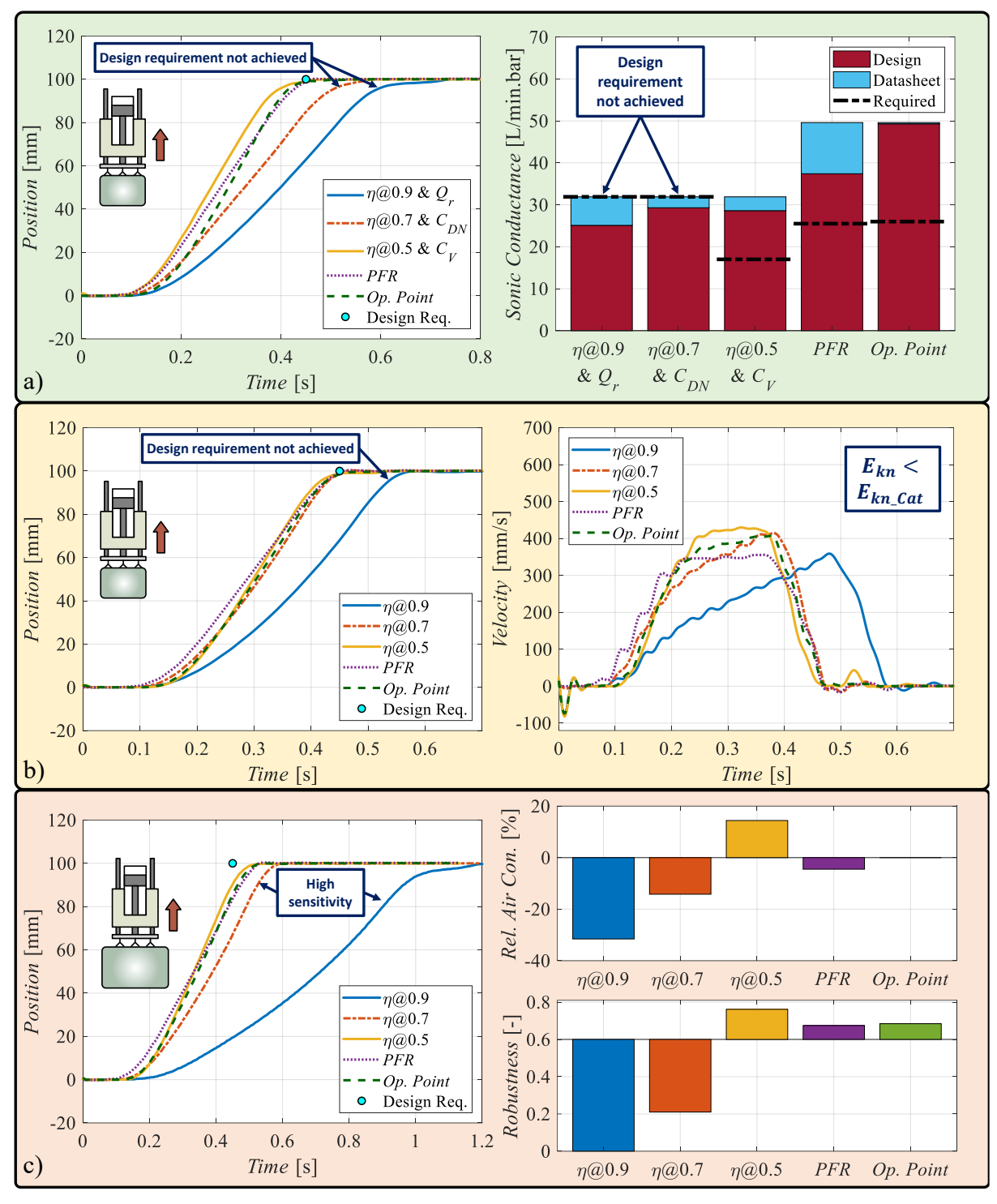
Source: Author.

Each sizing method was analyzed in three distinct scenarios. In the first, both the dimensioned cylinder and valves were tested. In the second scenario, a larger throttle valve was applied to verify the possible cases where the desired displacement time was not being achieved due to an undersized valve. A third scenario involved testing the system with the larger valve and an increased load force of about 10%, simulating the displacement of a slightly heavier mass in the same application, which enabled the assessment of the cylinder's robustness. The results of the performed tests are shown in Figure 7.8.

In Figure 7.8-a), the right chart shows the sonic conductance of each sizing method with red bars. The blue bar represents the actual sonic conductance of the valve used in the

experiment, while the dashed black line indicates the relative opening of the valve required on the experiment to achieve the required displacement time.

Figure 7.8 – Experimental results for Application #1: a) Tests with designed valves; b) Tests with oversized valves; c) Tests with oversized valves and $\Delta F_L \approx 10\%$



Source: Author.

Analyzing the results where the designed valves were used (Figure 7.8-a), it can be seen that the empirical methods with $\eta@0.9 \& Q_r$ and $\eta@0.7 \& C_{DN}$ were unable to meet the design requirement for displacement time, despite the throttle valve's flow capacity being higher than the designed value.

Using a throttle valve with higher capacity, as shown in Figure 7.8-b), solved the problem for the empirical method with $\eta @ 0.7$. However, for the empirical method with $\eta @ 0.9$, the system remained unable to achieve the required displacement time. By analyzing the displacement velocity and comparing it with the chart in Figure 4.28, it can be seen that all tested cylinders had kinetic energy lower than the value specified by the manufacturer.

The charts in Figure 7.8-c) present the results of a 10% average increase in the load force. As can be seen, the two variations of the empirical method with η @0.7 and η @0.9 resulted in increases of 28% and 105%, respectively, in displacement time, demonstrating the high sensitivity of these drives to small load changes. This aspect is further highlighted by the low robustness in the rightmost lower chart, where both methods resulted in robustness values of 0 and 0.21, respectively. Consequently, these two methods also led to higher energy efficiency, with relative air consumption 33% and 14% lower than the operating point method, respectively.

The empirical method with $\eta@0.5 \& C_V$, the *PFR*, and the Operating Point methods presented good results in meeting the design requirement for displacement time, as well as in ensuring robust operation. Regarding air consumption, the empirical method with $\eta@0.5 \& C_V$ consumed 14% more compressed air than the Operating Point method, while the *PFR* consumed 4.5% less.

7.1.2.2 *Application #2*

The second application analyzed was the no-contact horizontal displacement of the same 33 kg mass, typically performed by a rodless pneumatic cylinder. In this case, the required displacement time is 0.45 seconds, with a total displacement of 100 mm. Only inertial forces are expected in this application, and the same 3.26 J of kinetic energy is also expected. A reference supply pressure of 5 bar_{abs} is adopted for cylinder sizing. In Table 7.8, the results of the sizing methods for this application are presented.

In this application, since only inertial forces are expected, the sizing load force is the same for all methods, except for PFR, which does not require a sizing load force for such applications. Following Activity 4 of the operating point method presented in Figure 4.29, a

cylinder with Ø40 mm was chosen due to the inability of smaller cylinders to withstand the expected kinetic energy. For the remaining methods, this activity was intentionally skipped to evaluate the impact of this design choice. The throttle valves were assembled in a meter-in configuration, as it provides better dynamic behavior for high-inertia applications, as discussed in section 6.1.

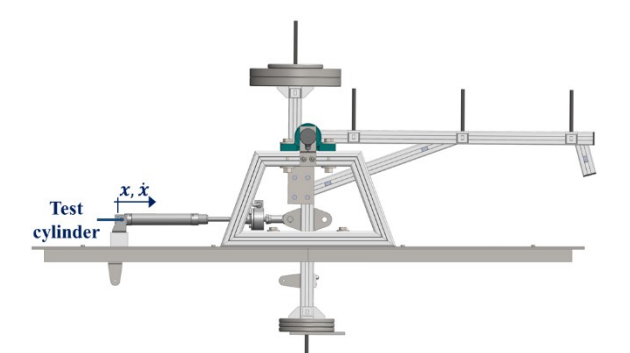
Table 7.8 – Sizing methods results for Application #2

Parameters	Unit	Op. Point	η @0.9 & Q_r	η @0.7 & C_{DN}	η @0.5 & C_V	PFR
Sizing Load Force (F_L)	N	32.6	32.6	32.6	32.6	0
Piston Diameter (d_c)	mm	40	12	12	16	25
Supply pressure (p_S)	bar_{abs}	30.7	4.22	5.13	4.25	3.96
Design sonic conductance (C_{eq})	L/min.bar	30.7	2.6	4.6	7.1	18.9
Throttle valve (C_{TV})	L/min.bar	31.9	11.3	11.3	11.3	31.9
Directional valve (C_{DV})	L/min.bar	129.8	217.1	217.1	217.1	217.1
Hose length (L_h) / diameter (d_h)	m / m		0.	35 / 0.003	55	

Source: Author.

The configuration chosen to replicate the load force characteristics of this application at the Ybitú test rig is described in Figure 7.9.

Figure 7.9 – Test rig configuration for Application #2 experiments



Test rig mass (M): 17.7 kg Moment of inertia (I): 1.1543 kg.m²

Center of gravity (CG_x) : 0.004514 m Center of gravity (CG_y) : -0.009483 m Expected kinetic energy (E_{kn}) : 3.23 J

Maximum load force (F_{L_max}): 37.6 N

Source: Author.

Similar to Application #1, three distinct scenarios were evaluated: the condition where both the dimensioned cylinder and valves were tested, a second scenario with an oversized valve, and a third scenario with an increase of approximately 7% in the load force, simulating the displacement of a slightly heavier mass. The results are presented in Figure 7.10.

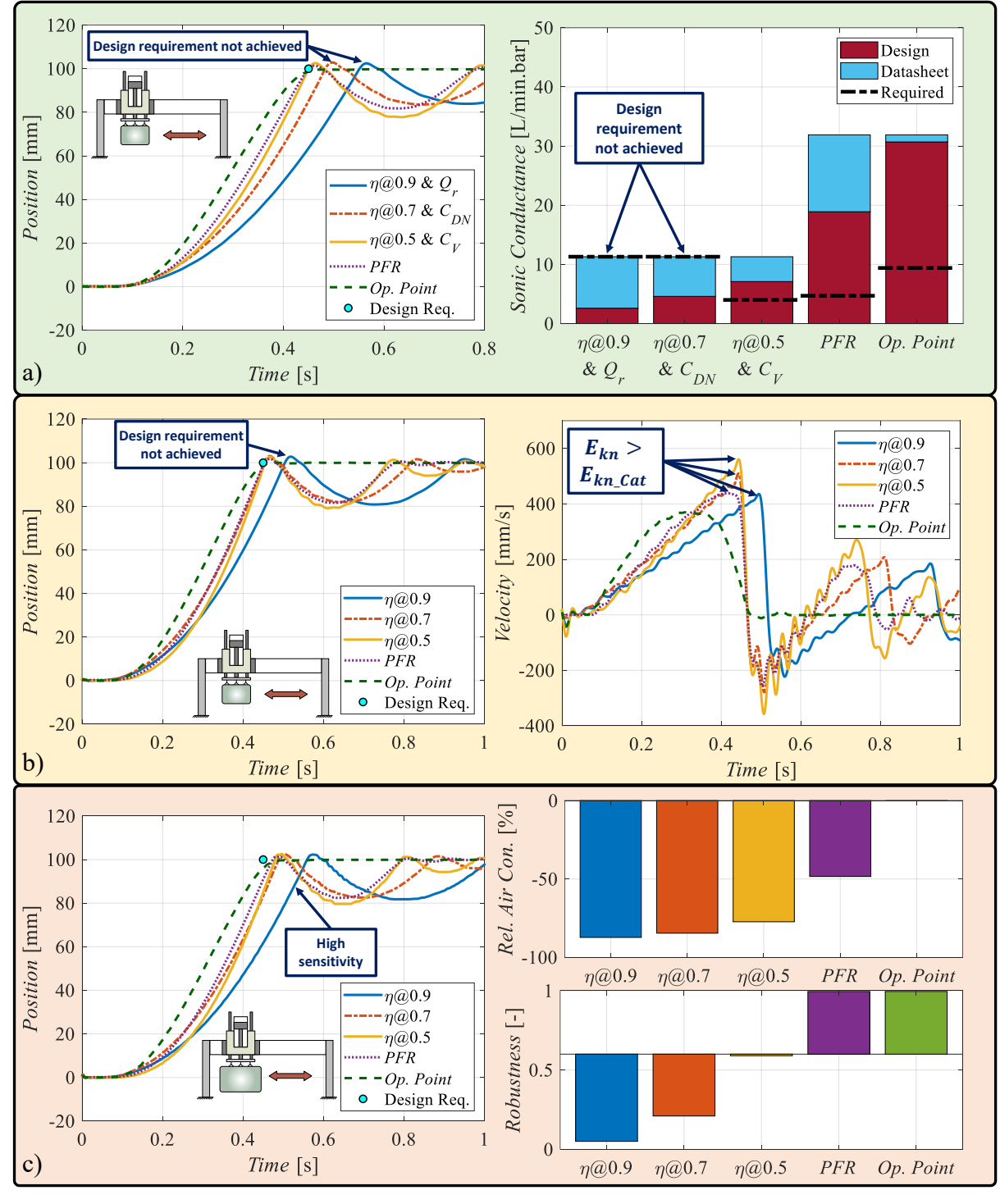


Figure 7.10 – Experimental results for Application #2: a) Tests with designed valves; b) Tests with oversized valves; c) Tests with oversized valves and $\Delta F_L \approx 7\%$

Source: Author.

The charts of Figure 7.10-a) show that, when the cylinder was assembled with the designed valves, two variations of the empirical method, $\eta@0.9 \& Q_r$ and $\eta@0.7 \& C_{VD}$, were unable to meet the design requirement, even though the valve had a substantially higher flow capacity than the designed value. The experiments presented at Figure 7.10-b), which used an

oversized valve, resulted in faster displacements for the $\eta @ 0.7$ method. However, the $\eta @ 0.9$ variation of the empirical method still failed to meet the requirement. This method also demonstrated high sensitivity to load changes, as shown in the position chart on Figure 7.10-c), resulting in robustness value of 0.05.

As expected, the three variations of the empirical method exceeded the allowable kinetic energy, causing the piston to hit the cylinder head strongly and creating a significant bouncing effect, as shown in the velocity chart of Figure 7.10-b). The *PFR* method also failed to meet this requirement, resulting in a kinetic energy greater than the allowable value.

All tested methods resulted in higher air consumption than the operating point method. However, it is also evident that these methods failed to meet the design requirement for displacement time or to complete the task without exceeding the maximum allowable kinetic energy, leading to bouncing effects at the end of the movement.

7.1.2.3 *Application #3*

The third evaluated application is the mechanical forming of steel plates using a double-guide linear actuator. This process involves stamping flat steel shapes with a die to produce U-shaped pieces. In this application, the load forces acting during the extension of the cylinder can be modeled as a combination of five components: a spring force effect due to steel forming, with a spring stiffness of 3,678 N/m; a viscous force from the cylinder guides, with a viscous coefficient of 24.6 N.s/m; a small magnitude of inertial and gravitational forces resulting from the vertical acceleration and displacement of the 4 kg piston and punch set; and a constant force of 120 N due to friction between the sheet metal and the die.

The stamping process is set to be completed in 0.6 seconds, with a total stamping stroke of 100 mm. A reference supply pressure of 7 bar_{abs} is used for the sizing process. The expected kinetic energy for this application is 0.22 J (Equation (4.37)). The actuation systems designed according to each of the sizing methods being analyzed are shown in Table 7.9.

Similar to Application #1, the sizing load force for the empirical method is higher due to the assumption of maximum load force. For the operating point method, the corrective factors K_d and K_s prevent the use of the maximum load force in spring- and damper-based applications. For the PFR method, the inertial force is not accounted for by the F_L . Moreover, the value of F_L exceeds 50% of the maximum cylinder force, which is the threshold suggested by the author of the PFR method. As a result, the dimensioned cylinder and supply pressure for both the PFR and $\eta@0.5$ methods achieved the same results. The throttle valves for this application were

assembled in a meter-out configuration due to the expected variable load force caused by the spring force.

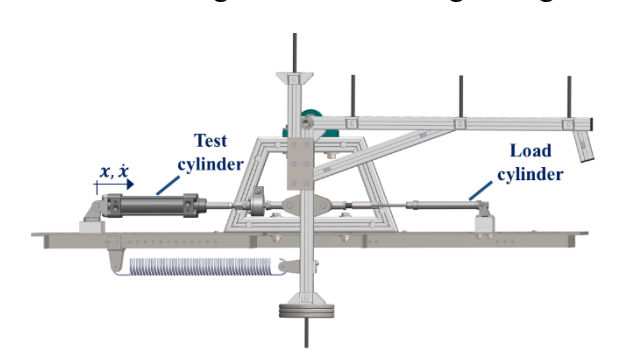
Table 7.9 – Sizing methods results for Application #3

Parameters	Unit	Op. Point	η @0.9 & Q_r	η @0.7 & C_{DN}	η @0.5 & C_V	PFR
Sizing Load Force (F_L)	N	423.4	537.5	537.5	537.5	535.2
Piston Diameter (d_c)	mm	40	40	40	50	50
Supply pressure (p_S)	bar_{abs}	6.78	5.75	7.12	6.49	6.49
Design sonic conductance (C_{eq})	L/min.bar	30.3	17.3	27.1	37.6	49.2
Throttle valve (C_{TV})	L/min.bar	31.9	31.9	31.9	49.6	49.6
Directional valve (C_{DV})	L/min.bar	129.8	217.1	217.1	217.1	217.1
Hose length (L_h) / diameter (d_h)	m / m		0	.25 / 0.00	4	

Source: Author.

The load force characteristics of this application were replicated at the Ybitú test rig with the following configuration.

Figure 7.11 – Test rig configuration for Application #3 experiments



Test rig mass (M): 6.4 kg

Moment of inertia (*I*): 0.84074 kg.m^2 Center of gravity (CG_x): 0.06395 mCenter of gravity (CG_y): -0.246816 m

Load cylinder: Ø 16 mm

Load cylinder pressure: 7 barabs @ Ch. A

Spring stiffness (K): 1,220 N/m Expected kinetic energy (E_{kn}): 1.32 J Maximum load force ($F_{L,max}$): 536.7 N

Source: Author.

The results of the three sets of experiments conducted for this application are shown in Figure 7.12. In the figure, in can be seen that the results of the experiments conducted with both the pneumatic cylinder and throttle valves designed by each method (Figure 7.12-a) show that the empirical method with $\eta@0.9 \& Q_r$ was not capable of achieving the specified displacement time. The operating point method met the requirement; however, a sonic conductance 5% higher than the designed value was necessary, as shown in the right chart of Figure 7.12-a). The empirical method with $\eta@0.7 \& C_{DN}$ also met the requirement, but with a slightly higher sonic conductance than the designed value. Both the *PFR* and the empirical method with $\eta@0.5 \& C_V$ resulted in good design values for the valve's sonic conductance.

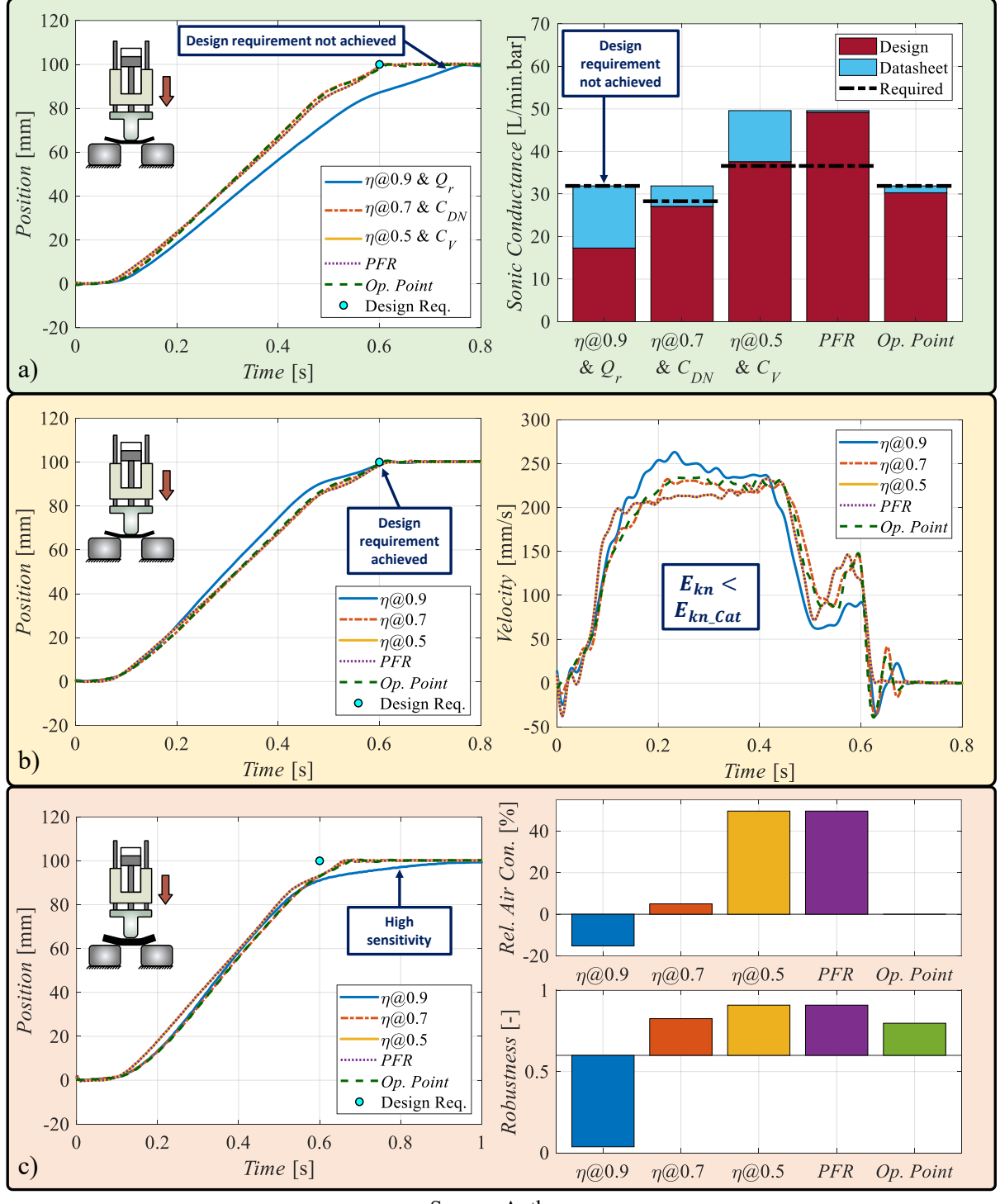


Figure 7.12 – Experimental results for Application #3: a) Tests with designed valves; b) Tests with oversized valves; c) Tests with oversized valves and $\Delta F_L \approx 11\%$

Source: Author.

The charts in Figure 7.12-b) show that all tested methods achieved the specified displacement time when an oversized valve was used. Moreover, the kinetic energy achieved during the experiments did not exceed the maximum allowable limit specified by the manufacturer.

The charts presented in Figure 7.12-c) result from an approximately 11% increase in the load force, simulating, for instance, the stamping of a slightly thicker steel sheet. Once again, the empirical method with $\eta@0.9 \& Q_r$ presented high sensitivity, increasing its displacement time by 53% and resulting in a robustness value of 0.04. The remaining methods demonstrated robustness values within an acceptable range.

In terms of air consumption, the variations of the empirical method with $\eta @ 0.7$ and $\eta @ 0.5$ consumed 5% and 49.6% more compressed air than the operating point method, respectively. Since the *PFR* method resulted in the same cylinder and supply pressure as the $\eta @ 0.5$ variation, it also consumed 49.6% more compressed air than the operating point method. On the other hand, the variation with $\eta @ 0.9$ consumed 15.2% less compressed air. However, this method showed deficiencies in meeting the design requirements of the application and in performing the task with robust operation.

7.1.2.4 *Application #4*

The goal of this application is to remove wood pieces from a magazine. The process is performed by a pusher attached to the cylinder rod, which pushes one wood piece during each extension movement. The moving load is estimated at 17 kg, and the sliding friction coefficient between the wood pieces is 0.33. The total extension stroke is 100 mm and must be completed within 0.8 seconds. A supply pressure of 6 bar_{abs} is used as a reference value for sizing, and the expected kinetic energy of the application is 0.53 J (Equation (4.37)). Table 7.10 presents the results of the five sizing methods applied to this application.

Table 7.10 – Sizing methods results for Application #4

Parameters	Unit	Op. Point	η @0.9 & Q_r	η @0.7 & C_{DN}	η @0.5 & C_V	PFR
Sizing Load Force (F_L)	N	60.3	60.3	60.3	60.3	55
Piston Diameter (d_c)	mm	20	12	16	16	16
Supply pressure (p_S)	bar_{abs}	4.15	6.95	5.3	7.01	6.5
Design sonic conductance (C_{eq})	L/min.bar	6.5	2.0	3.4	3.6	4.7
Throttle valve (C_{TV})	L/min.bar	11.3	11.3	11.3	11.3	11.3
Directional valve (C_{DV})	L/min.bar	47.2	217.1	217.1	217.1	217.1
Hose length (L_h) / diameter (d_h)	m / m		(0.4 / 0.00	4	

Source: Author.

The sizing load force for all methods was the same for this application, as no spring or viscous forces were involved. The exception was the *PFR* method, where the sizing load force did not include inertial forces, unlike the other methods. Additionally, in this application, the supply pressure of the system designed using the *PFR* method needed to be increased to ensure that the load force did not exceed the threshold of 50% of the maximum cylinder force. Meterin throttling was selected for this application due to the resistive and mostly constant expected load force.

To replicate the load force characteristics of this application on the Ybitú test rig, the following configuration was used.

Figure 7.13 – Test rig configuration for Application #4 experiments



Test rig mass (M): 4.4 kg Moment of inertia (I): 0.643016 kg.m² Center of gravity (CG_x): 0.234192 m Center of gravity (CG_y): -0.055228 m

Expected kinetic energy (E_{kn}) : -0.033228 m Expected kinetic energy (E_{kn}) : 0.5694 J Maximum load force $(F_{L\ max})$: 59.06 N

Source: Author.

The experimental results for the three distinct scenarios evaluated using the sizing methods tested in this application are shown in Figure 7.14.

When the designed valves and cylinder were employed (Figure 7.14-a), all sizing methods successfully met the design requirement. However, the empirical method with $\eta @0.9 \& Q_r$ benefitted from the fact that the only commercially available valve had a flow capacity 5 times greater than the design value. Otherwise, the design requirement would not have been met, as a sonic conductance 3.9 times bigger than the designed value was required, as shown in the right chart of Figure 7.14-a).

In terms of kinetic energy, the only method that was able to perform the task without exceeding the manufacturer's limitation was the operating point method. This was due to Activity #4 presented in Figure 4.29, which led to the selection of a larger cylinder capable of absorbing the kinetic energy required for the task according to the manufacturer's datasheet. The design Activity #5 helped optimize the supply pressure to a lower value for the selected cylinder.

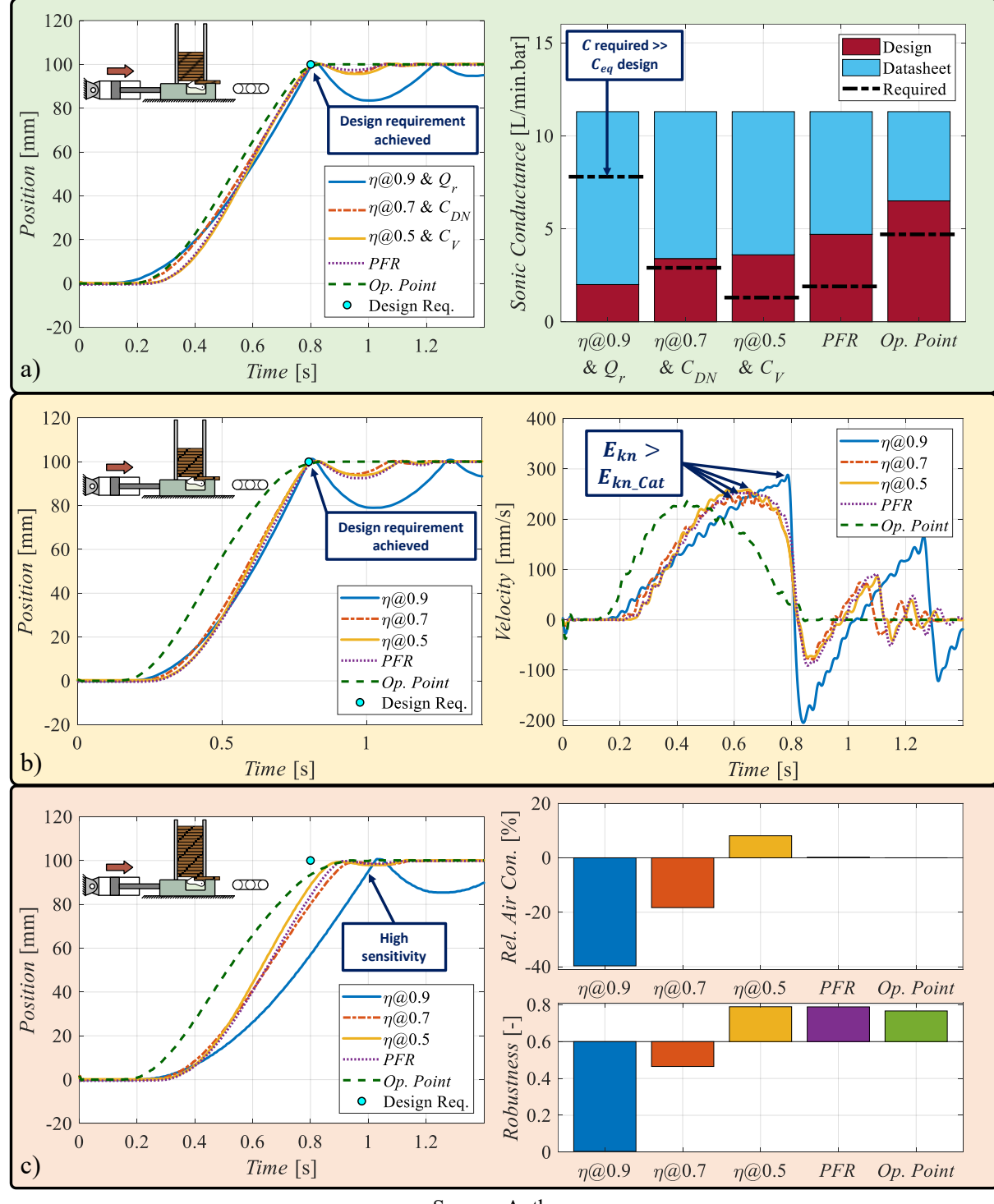


Figure 7.14 – Experimental results for Application #4: a) Tests with designed valves; b) Tests with oversized valves; c) Tests with oversized valves and $\Delta F_L \approx 9\%$

Source: Author.

The results shown on Figure 7.14-c) were obtained with an increase of approximately 9% in the load force, simulating a potential rise in the number of wood pieces in the magazine, which increases the friction force required to remove the piece from the bottom. As seen, the empirical method with $\eta@0.9$ resulted in a 30% increase in displacement time, leading to a

robustness value of 0.004. The remaining methods produced robustness values within an acceptable range.

In terms of air consumption, two variations of the empirical method (η @0.9 and η @0.7) consumed 39.7% and 18.3% less compressed air than the operating point method, respectively, while the empirical method with η @0.5 and the *PFR* method consumed 8.1% and 0.2% more compressed air than the operating point method, respectively. As with the previous applications, lower air consumption is also linked to lower robustness and kinetic energy exceeding the manufacturer's limits.

7.1.2.5 *Application #5*

The last analyzed application involves assembling bearings in a steel shaft. This task is characterized by a slow displacement velocity, with 100 mm of displacement occurring in 1 second. The main force acting on the cylinder rod is the friction between the bearing and the shaft, estimated at 193 N. A small inertial force results from the acceleration of a 5 kg tool attached to the piston rod. A supply pressure of 8 bar_{abs} is used as a reference for sizing the cylinders. In this application, only 0.1 J of kinetic energy are expected due to the low mass and low velocity displacement. The results of the sizing methods for this application are summarized in Table 7.11.

Table 7.11 – Sizing methods results for Application #5

Parameters	Unit	Op. Point	η @0.9 & Q_r	η @0.7 & C_{DN}	η @0.5 & C_V	PFR
Sizing Load Force (F_L)	N	194	194	194	194	193
Piston Diameter (d_c)	mm	25	20	25	25	25
Supply pressure (p_S)	bar_{abs}	7.35	7.9	6.7	8.94	8.94
Design sonic conductance (C_{eq})	L/min.bar	8.7	4.4	7.0	6.5	8.6
Throttle valve (C_{TV})	L/min.bar	11.3	11.3	11.3	11.3	11.3
Directional valve (C_{DV})	L/min.bar	47.2	217.1	217.1	217.1	217.1
Hose length (L_h) / diameter (d_h)	m / m		(0.7 / 0.004	4	

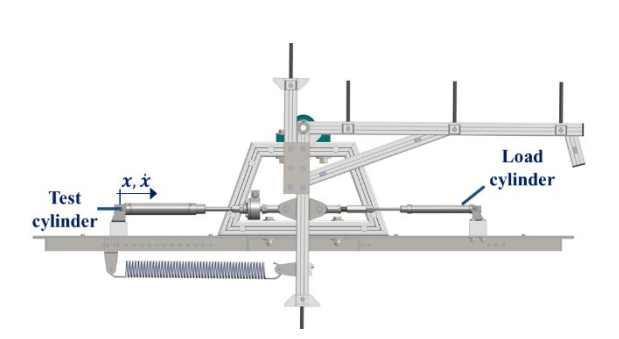
Source: Author.

Similar to Applications #3 and #4, the sizing load force (F_L) exceeded 50% of the cylinder's maximum force with the PFR method. As a result, the supply pressure was increased to keep the designed system within this threshold. A meter-out throttling was chosen due to the low displacement velocity, as stick-slip is more likely to occur with meter-in throttling in such

conditions. Moreover, meter-out throttling results in more stable displacement, which is desirable for assembly applications.

The Ybitú test rig was assembled using the configuration shown in Figure 7.15 to replicate the load force characteristics expected for this application.

Figure 7.15 – Test rig configuration for Application #5 experiments



Test rig mass (M): 3.4 kg Moment of inertia (I): 0.275524 kg.m² Center of gravity (CG_x): 0.121998 m Center of gravity (CG_y): -0.078016 m

Load cylinder: Ø 16 mm

Load cylinder pressure: 8 bar_{abs} @ Ch. A

Spring stiffness (K): 123 N/m

Expected kinetic energy (E_{kn}): 0.16 J Maximum load force ($F_{L,max}$): 195.8 N

Source: Author.

The spring was included in this experiment to counterbalance the force decomposition that occurs in the load cylinder as the rotating arm rotates, resulting in a constant load force acting on the piston rod during the extension of the testing cylinder. The results of the three sets of experiments performed with each sizing method are shown in Figure 7.16.

In this application, the empirical method with $\eta@0.5 \& C_V$, the *PFR*, and the operating point method successfully determined the required sonic conductance to complete the task within the design requirements, as shown by the right chart of Figure 7.16-a). The empirical method with $\eta@0.7 \& C_{DN}$ met the design requirements; however, it required a higher sonic conductance than the design value. The empirical method with $\eta@0.9 \& Q_r$ failed to achieve the required displacement time, even with the selected valve having a flow capacity 2.5 times greater than the design value.

Figure 7.16-b) shows that replacing the designed valve with an oversized valve enabled all design methods to meet the requirement of displacement time. The kinetic energy in all tests did not exceed the manufacturer's recommendation, as this was a low-inertia application.

The charts in Figure 7.16-c) present the results of an average 13% increase in the load force, simulating the assembly of a wider bearing model. As shown, the empirical method with η @0.9 resulted in a complete system stall, failing to complete the task. This result highlights the potential challenges of designing a low-robustness system, which does not compensate for the lower relative air consumption observed with this design method.

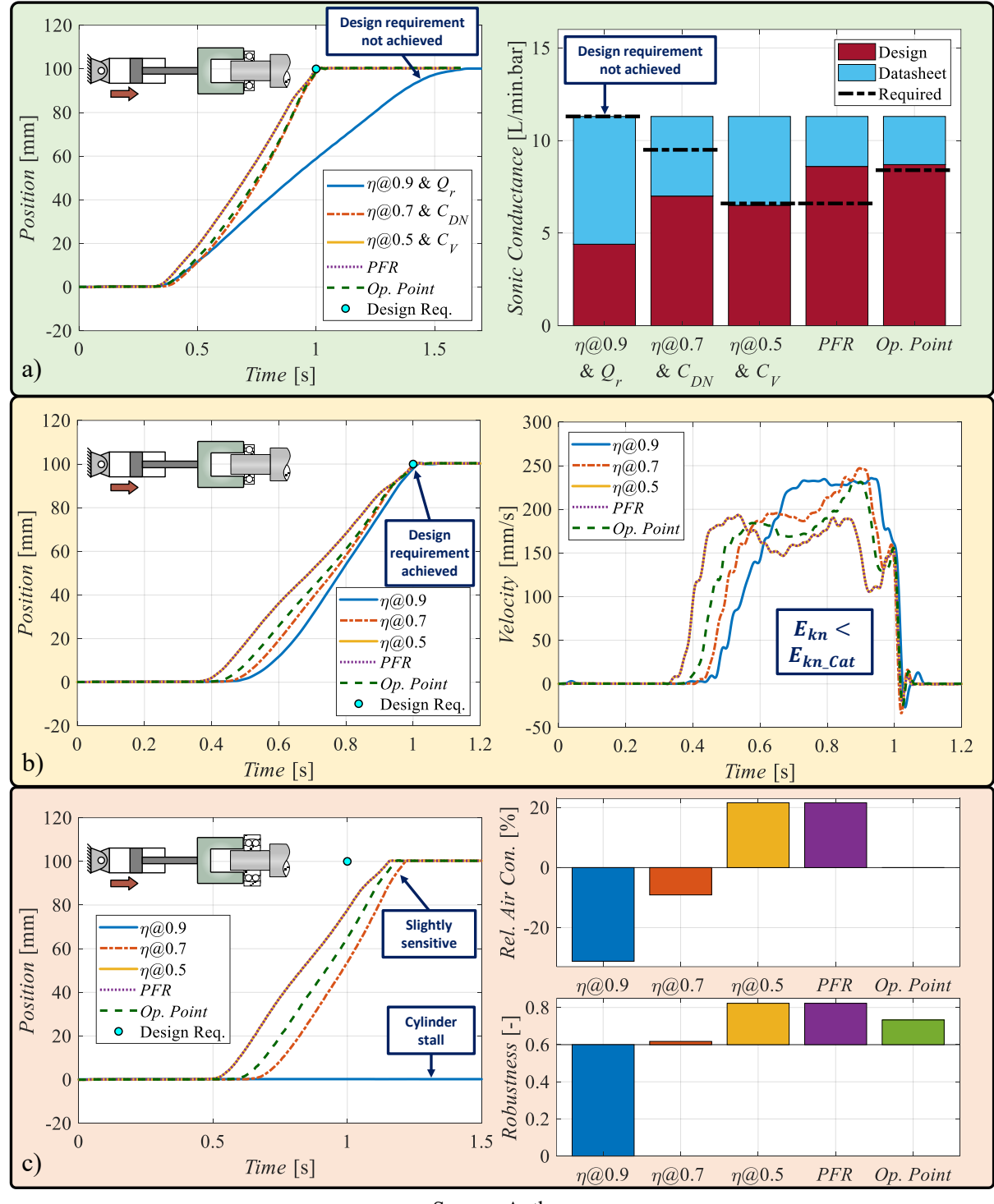


Figure 7.16 – Experimental results for Application #5: a) Tests with designed valves; b) Tests with oversized valves; c) Tests with oversized valves and $\Delta F_L \approx 13\%$

Source: Author.

In this application, the empirical method with $\eta @ 0.7$ consumed 9.1% less compressed air than the operating point method, with a slightly impact on robustness. However, when this method was combined with the C_{DN} method to design the throttle valve, it failed to determine the required sonic conductance to meet the displacement time requirement. On the other hand,

the empirical method with $\eta @ 0.5$ and the *PFR* method consumed 21.6% more compressed air than the operating point method.

7.1.2.6 Synthesis of experimental results

Throughout the analysis of these five distinct applications, it can be observed that, in some cases, one sizing method performs better than others in certain aspects, such as lower compressed air consumption, while robustness and the ability to meet design requirements might be compromised, or vice versa. Table 7.12 summarizes five characteristics of each sizing method based on the experimental results presented in this section. In the table, small bar graphs beneath each cell provide a visual breakdown of results across the five test applications, as represented by the icons at the bottom of the table. The numerical values within the cells indicate the average result across these five applications.

Design method $\eta@0.9 \& Q_r \mid \eta@0.7 \& C_{DN} \mid \eta@0.5 \& C_V$ Op. Point PFR1/5 2/5 5/5 5/5 5/5 Design requiment met? 0.441 0.837 1.658 2.127 1.703 Throttle Valve Characteristic $C_{Des.}/C_{Req.}$ 3/5 3/5 3/5 5/5 3/5 Kinetic energy $E_{kn} < E_{kn_Cat}$ -41.21% -24.24% 3.28% 3.72% 0% Relative air consumption 0.838 0.795 0.019 0.466 0.776 Robustness 000

Source: Author.

Table 7.12 – Summary of observed characteristics of each sizing method

The empirical method with $\eta@0.9 \& Q_r$ failed to design the sonic conductance of the valves for all applications ($C_{Des.}/C_{Req.} < 1$). The only application where it met the required displacement time was due to the higher flow capacity of the commercially available valve. It also presented low robustness across all scenarios. Although it consumed significantly less compressed air than the operating point method, its poor performance during operation does not justify the compressed air savings.

On the other hand, the empirical method with $\eta@0.5 \& C_V$ met all design requirements and demonstrated high robustness across all tests. However, it also resulted in higher compressed air consumption. The average relative air consumption of 3.28%, shown in Table 7.12, is significantly impacted by Application #2, where an oversized cylinder was selected by the operating method to withstand the high kinetic energy of the application. Excluding this application when determining the average relative air consumption results in a value of 23%, highlighting the higher air consumption trend of this method.

As an intermediate solution, the empirical method with $\eta @0.7 \& C_{DN}$ demonstrated good robustness in most applications while consuming around 9% less compressed air, assuming Application #2 is removed from the calculation. Nevertheless, this method also had limitations, showing high sensitivity to load changes in Application #1 and failing to determine the flow capacity of the valves in 4 out of the 5 performed tests.

Regarding the *PFR* method, it demonstrated good performance in terms of robustness and ability to meet the design requirements. Nonetheless, it showed a tendency to excessively oversize the valves, which corroborates with the simulation results presented in Section 7.1.1. Although this characteristic does not compromise the functionality of the system, it may lead designers to select disproportionately large valves, resulting in higher acquisition costs and a more challenging system setup. However, the main drawback of this approach is the empirical rule suggested by the author, which states that the load force of the application should not exceed 50% of the cylinder's maximum force. As observed, in 3 out of the 5 tested applications, the supply pressure had to be increased to keep the designed system within this threshold. Consequently, the *PFR* method consumed, on average, 16.7% more compressed air than the operating point method (excluding the outlier of Application #2). Furthermore, in two applications, the kinetic energy exceeded the manufacturer's recommendations, contradicting a primary goal of the PFR method. A possible explanation for this discrepancy is that Doll; Neumann and Sawodny (2015) determined the optimum Ω range using a Festo simulation tool, whereas the current study used cylinders from a different manufacturer (Camozzi).

Finally, the operating point method showed positive results in terms of achieving the design requirements of the applications and ensuring robust operation. The only application where it failed to determine the required nominal flow rate for the throttle valve was Application #3; however, the error was only about 5%. With the exception of Application #2, which required an oversized cylinder due to its higher kinetic energy, the robustness of the remaining applications stayed within the range of 0.68 to 0.8, with an average robustness of 0.75. As seen in Section 4.1.3, this range of robustness presents a good balance between air consumption and robustness, allowing the drive to meet the design requirements without consuming an excessive amount of compressed air and not being too sensitivity to load changes, as demonstrated by the experiments in this section.

7.2 EVALUATION OF THE HML MODEL FOR ONLINE PNEUMATIC SYSTEM OPTIMIZATION

As presented in Section 6.2, the HML was designed to overcome the uncertainties frequently encountered when determining the load force in applications where a pneumatic actuation system is being designed. To assess the effectiveness of the HML model in optimizing pneumatic actuation systems using real-time data, it was implemented in a test rig. The goal of the HML was to assist the user in properly adjusting the supply pressure and the throttle valve's opening, resulting in optimal operation in terms of air consumption and robustness.

7.2.1 Test rig for evaluating the HML model

The experimental evaluation of the HML was conducted using the test rig shown in Figure 7.17, which belongs to the Fluidtronik Chair at the Institut für Mechatronischen Maschinenbau, Technische Universität Dresden, Germany. The test rig consists of three distinct workstations. The first workstation performs the horizontal displacement of a mass on a low-friction surface (LC1), while the second workstation moves a mass horizontally using a Ø50 mm load cylinder that generates a spring-like force (LC2). The third workstation is designed for vertically lifting a load mass (LC3).

The measurement tools included pressure sensors (model 18S-0862180 from Norgren) and limit switches (model SMT-8M-A from Festo) for recording chamber pressures and displacement time, respectively. Additionally, a flow sensor (model SFAB-200-U-H-Q8 from Festo) was used to measure air consumption.

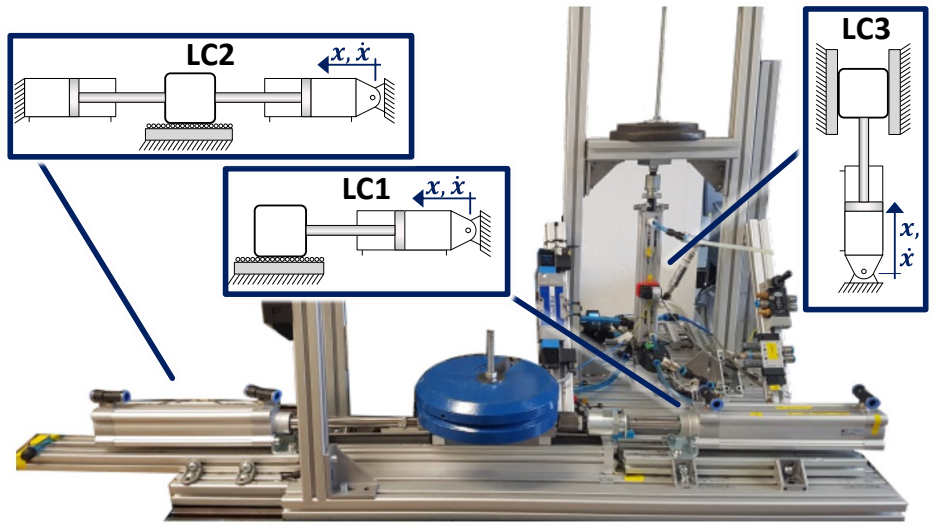


Figure 7.17 – General overview of the test rig and its workstations

Source: Author.

An application was developed in the LabVIEW environment for real-time data acquisition using an NI USB-6008 acquisition board operating at a frequency of 500 Hz. The LabVIEW application was designed to extract only the data corresponding to the actual piston displacement period. This subset of data was then transmitted to a MATLAB script responsible for feature extraction and running the HML model. The corrective action output from the HML was sent back to the LabVIEW environment, where it was displayed to the user. The time required for feature extraction and running the optimization strategy was approximately 500 ms, which is negligible during manual system setup.

Beyond the HML, two additional architectures were evaluated during the experiments, each utilizing different technologies that can be applied to meet the same requirements of a given application. The architectures analyzed were:

- 1) Conventional Setup: This setup consists of a standard actuation system with a linear actuator, two throttle valves, and a directional valve. The displacement time was adjusted using the throttle valves, while the supply pressure was kept constant at the value specified during the system design.
- 2) HML: This architecture, shown in Figure 7.18, uses the same standard actuation system from the conventional setup. It also temporally uses two pressure sensors to measure the chamber pressures during system setup. The displacement time and

- supply pressure were manually adjusted based on the corrective actions proposed by the HML.
- 3) Festo VTEM: The directional and throttle valves of the standard actuation system were replaced with a Festo Motion Terminal (Festo, 2017). The "ECO drive" app of the equipment was selected, and the extending time was adjusted using the slider available in the WebConfig interface.

NI USB-6008

Figure 7.18 – Schematic diagram of the HML system setup

Source: Author.

7.2.2 Experimental evaluation of the tested architectures

By utilizing the wide range of assembly options in the test rig, twenty-two different design requirements were generated by varying load weights, pressure on the load cylinder, and displacement time. For each requirement, a cylinder with a piston diameter of 25, 32, or 50 mm and a stroke of 200 mm was selected. The choice of cylinder diameters and load forces was structured to distinguish between overload and underload conditions, simulating scenarios where the cylinder was poorly designed due to uncertainties in the load force, resulting in both undersized and oversized drives, respectively. Additionally, a robustness test was conducted in which the load force was increased between 7% to 22% after the system was configured to properly meet the design requirements.

Specific details about the design requirements are provided in Table 7.13. In this table, the term load mass refers to the actual mass being moved by the pneumatic drive, while load

force represents the sum of all forces acting against the movement, including gravitational forces, inertial forces, and the load cylinder force.

Table 7.13 – Description of the design requirements for the performed tests

	General data					l operation	Robus	tness test	tness test Sensitivity data			ita
T	337 1		1		Load	Load	Load	Load	ΔF_{L}	Δ	$\Delta t_d/t_d$	[%]
Test #	Work	t_d	d_c	p_S	Mass	Force	Mass	Force	$/F_{L}$	Conv.	111/11	VTEM
#	Station	[s]	[mm]	[bar _{abs}]	[kg]	[N]	[kg]	[N]	[%]	Set.	HML	VTEM
1	LC1	1.40	25	4.00	15	4.33	18	4.94	14.1	-1.1	4.5	3.7
2	LC1	1.40	25	4.00	40	9.43	50	11.47	21.6	-0.6	7.2	1.5
3	LC2	1.30	25	7.60	7	121.06	8	140.93	16.4	11.6	37.5	31.3
4	LC2	1.30	25	8.00	15	260.40	18	280.74	7.8	84.9	14.3	12.3
5	LC2	0.50	25	5.00	15	107.60	18	128.10	19.1	20.8	14.7	14.7
6	LC3	0.70	25	8.00	7	94.22	8	104.84	11.3	6.2	13.9	17.0
_ 7	LC3	1.00	25	7.00	17	192.63	19	213.05	10.6	101.4	29.9	25.6
8	LC1	1.20	32	4.20	20	7.23	25	8.62	19.2	-0.4	5.9	4.6
9	LC1	1.20	32	4.20	40	12.78	50	15.56	21.7	3.2	6.3	9.9
10	LC2	0.50	32	7.00	10	105.00	12	127.84	21.7	11.7	17.1	23.6
11	LC2	0.50	32	7.00	30	333.35	33	402.95	20.9	38.2	32.3	33.3
12	LC3	0.80	32	4.80	13	192.63	15	213.05	10.6	66.7	20.8	10.9
13	LC3	0.80	32	6.00	10	121.83	12	142.70	17.1	8.8	27.7	27.8
14	LC3	0.80	32	6.00	25	260.88	30	313.05	20.0	136.1	46.7	45.4
15	LC1	1.20	50	4.20	30	10.15	40	12.93	27.4	-6.2	-4.0	2.8
16	LC1	1.20	50	4.20	100	29.59	115	33.76	14.1	-2.1	1.9	-3.7
17	LC2	1.00	50	7.00	10	303.31	12	363.01	19.7	11.0	29.0	18.2
18	LC2	1.00	50	7.20	40	888.65	50	1004.57	13.0	72.3	25.3	21.2
19	LC2	0.90	50	4.30	30	405.11	40	468.02	15.5	44.0	23.6	24.6
20	LC3	1.10	50	6.00	25	274.29	29	314.64	14.7	8.9	19.7	26.4
21	LC3	1.00	50	4.10	32	344.91	37	395.34	14.6	61.9	5.6	14.1
22	LC3	1.10	50	6.00	65	660.90	75	761.78	15.3	109.0	19.4	26.7

Gray Underloaded test
White Overloaded test

Source: Author.

The experimental results are presented in terms of robustness, calculated using Equation (4.10), and relative air consumption, which quantifies the percentage of compressed air each architecture consumed more or less than the conventional setup, used as the baseline solution. The compressed air consumption was determined by integrating the flow sensor measurements over time.

Figure 7.19 presents the results of the underloaded tests, in which the cylinder area was intentionally oversized for the actual load force applied to the system.

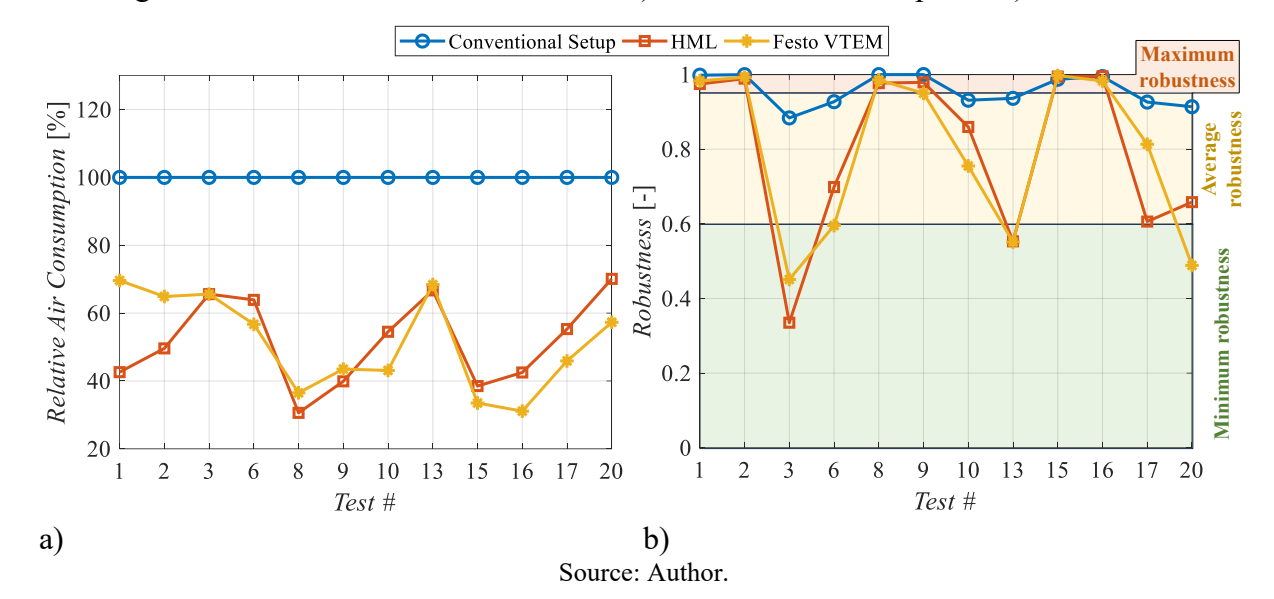


Figure 7.19 – Underloaded tests results: a) Relative air consumption; b) Robustness

As can be seen in Figure 7.19-a), in all 12 underloaded cases, the HML and Festo VTEM architectures significantly reduced compressed air consumption. On average, these strategies lowered air consumption by 48.4% and 48.7%, respectively. The main reason for this energy savings is the limitation of the supply pressure, which prevents unnecessary chamber filling after the task is completed, as exemplified by the driving chamber pressures in experiment #17, shown in Figure 7.21-a).

The Festo VTEM achieves greater energy savings by completely shutting off the supply pressure once the task is completed. In contrast, the 5/2-way valve and control strategy used in the HML architecture do not allow for this approach. Instead, the HML regulates the supply pressure to match the actual load force being applied on the cylinder rod, keeping just enough extra pressure to ensure robustness and dynamic performance of the drive.

In terms of robustness, Figure 7.19-b) shows that systems configured using the HML remained above the 0.6 threshold in 10 out of the 12 tests, with an average robustness of 0.8. Robustness values exceeding the 0.95 threshold occurred in high-inertia applications (LC1). In these cases, the load force was substantially low, requiring a supply pressure in the range of 1.5–2 bar_{abs}. Since such low pressure is not feasible for proper operation, the supply pressure was limited to 3 bar_{abs}, resulting in high robustness. Nevertheless, the HML effectively achieved a substantial reduction in compressed air consumption for high-inertia applications.

The Festo VTEM architecture resulted in robustness similar to the HML, with an average of 0.797, which is due to the same supply pressure used in both architectures. In contrast, the conventional setup resulted in unnecessarily high robustness, with an average value

of 0.96. Consequently, the conventional setup consumed, on average, 106% more compressed air than the HML.

In Figure 7.20, the results of the tests conducted under overloaded conditions are presented. These cases involve the cylinder area being intentionally undersized for the actual load applied to the system. Details of the loading conditions for each Test # are provided in Table 7.13.

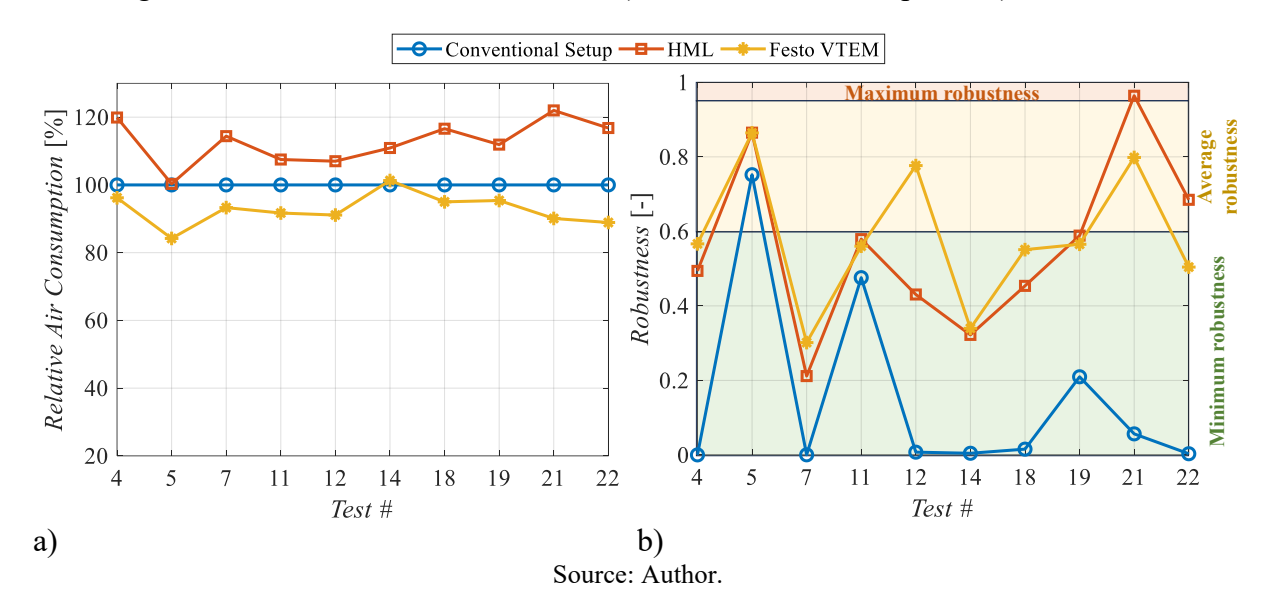


Figure 7.20 – Overloaded tests results: a) Relative air consumption; b) Robustness

In an overloaded condition, the HML consumed, on average, 12.7% more compressed air than the conventional setup. In such cases, the main advantage of the HML lies in its capacity to enable more robust operation. In this aspect, the HML succeeded in identifying critical loading conditions and maintaining higher supply pressure. As shown in Figure 7.20-b), the HML improved robustness across all performed tests. Although 6 tests remained below the 0.6 threshold, the robustness of these tests were close to the threshold, with an average robustness value of 0.56 across all 10 tests. These robustness values remain within an acceptable range and does not significantly impact displacement time of the cylinder.

The Festo VTEM architecture achieved robustness values similar to the HML, with an average of 0.58. This similarity is attributed to both architectures using the same supply pressure during the tests. On average, the Festo VTEM saved 7.3% more compressed air compared to the conventional setup in the overloaded tests.

On the other hand, for the conventional setup, in 7 out of 10 tests, the robustness remained near zero, which is a dangerous working condition for pneumatic drives. A small

change in the load force may cause a significant increase in displacement time or even a system stall. This effect is exemplified in Figure 7.21-b), where the piston displacement of test #7 is shown after a 10.6% increase in the load force.

The results presented in Figure 7.19 and Figure 7.20 demonstrate the HML's ability to effectively balance air consumption and robustness. Across the 22 tests conducted under various loading and operating conditions, the HML successfully assessed the loading condition in real time and improved the system's operation, achieving robustness values near or above the desired threshold.

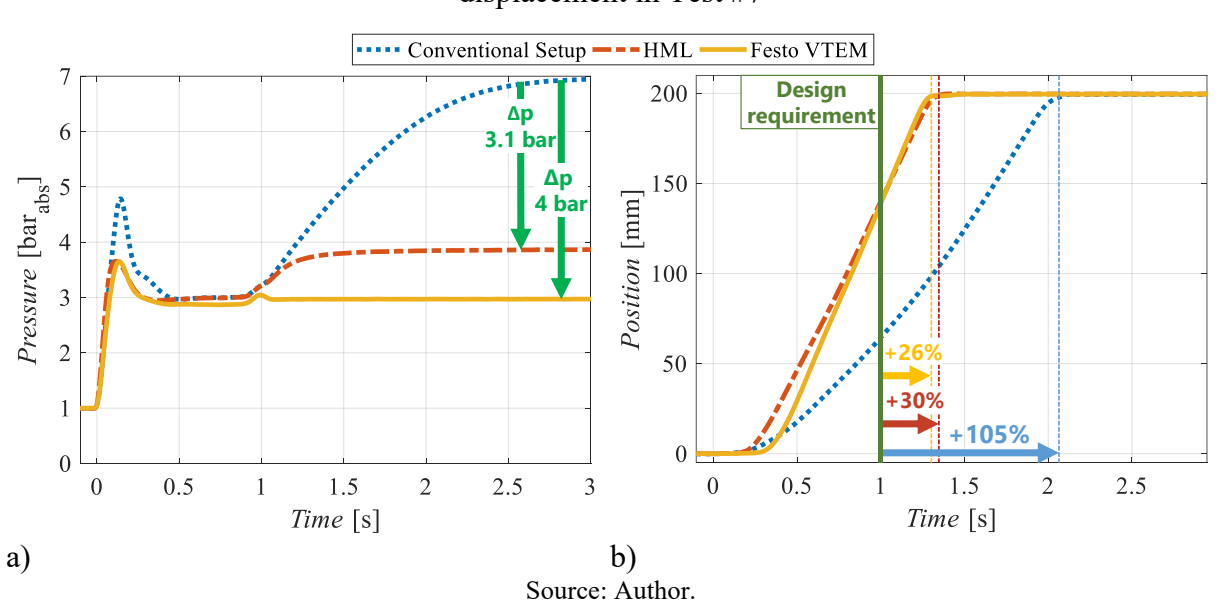


Figure 7.21 – Experiment analysis: (a) Chamber A pressures in Test #17; (b) Piston displacement in Test #7

Compared to the Festo VTEM, the key characteristics of the HML are as follows:

Assistive Setup Tool: The HML functions as a setup tool, specifically designed to set the supply pressure and adjust the throttle valves in a standard actuation system, without requiring continuous use. In such cases, the economic impact is minimal, as no additional components are needed, and the setup tool can be reused for multiple actuators.

Detection of Overloaded Conditions: The HML was designed to detect overloaded conditions. When such conditions are detected, the user is guided to increase the supply pressure to prevent issues like loss of dynamic performance or complete drive stall due to changes in load force. This capability is not available in the Festo VTEM.

Single Drive Operation: The HML was designed for single drive operation, making it suitable for applications with only one cylinder. Currently, the Festo VTEM is available only with a minimum of two valves.

Nevertheless, the results presented in this section indicate a higher energy-saving potential for the Festo VTEM. However, this advantage is associated with significant investment costs. Selecting the optimal solution requires a comprehensive total cost of ownership analysis, which should account for factors such as acquisition costs, cylinder dimensions, operating frequency, and the number of cylinders, as shown in Boyko *et al.* (2024). This analysis, however, is beyond the scope of this thesis.

7.3 FINAL CONSIDERATIONS ABOUT CHAPTER 8

This chapter presented a thorough analysis of the application of the operating point method for pneumatic actuation system sizing. The analysis included a comparison with three variations of a classical sizing approach, which assumes only a yield coefficient for the cylinder, and a method based on the eigenfrequency of a pneumatic cylinder, called the Pneumatic Frequency Ratio (*PFR*).

The analysis was first conducted in a simulative environment, where different loading conditions were individually and mutually considered for system sizing. The results indicate a consistent capability of the operating point method in designing pneumatic systems to operate within a desired robustness range of 0.6 to 0.95. Additionally, tests assessing the throttle valves' capability demonstrated the accuracy of the operating point method in determining the required flow capacity of the valves.

A set of five different applications was experimentally evaluated using all five sizing methods. Overall, the experimental results showed a notable agreement with the simulation results, confirming the capability of the operating point method to consistently design pneumatic actuation systems for robust and efficient operation.

This chapter also presented the experimental evaluation of the HML model in addressing the uncertainties encountered in determining the load force during the sizing of the actuation system. The HML was applied in a set of 22 experiments, encompassing both overloaded and underloaded operations. Across all tests, the HML successfully guided the user in configuring the system for improved operating conditions, effectively compensating for any miscalculations in load force estimation during system sizing.

8 CONCLUSIONS

The main objective of this PhD thesis was the development of a framework for the design and optimization of pneumatic actuation systems. The framework comprises a series of tools aimed at improving the sizing of pneumatic cylinders and valves, aiding in system assembly and setup, facilitating the selection of the most effective throttling method, and enabling online optimization of system parameters.

The motivation for developing this framework arises from the widespread use of empirical rules in pneumatic system design. These rules are commonly applied to account for system uncertainties, including friction forces, pressure fluctuations, and dynamic effects on system behavior and load forces. However, as demonstrated throughout this thesis, relying on empirical rules introduces several drawbacks, including excessive air consumption, failure to meet design requirements, and non-robust operation.

As the central component of the developed framework is the operating point method, which consists of a set of equations designed to correlate chamber pressures when the piston moves at steady state. By defining a reference operating point for the system, this method enables the determination of chamber pressures, reducing uncertainties in the sizing process.

By analyzing the piston velocity, it was possible to establish a reference operating point in which maximum velocity and dynamic performance are achieved. The development of sensitivity and robustness metrics demonstrated that this reference condition also resulted in robust operation. Therefore, the operating point method enabled the determination of chamber pressures for a reference operating condition that balances dynamic performance and robustness with reasonable air consumption.

Friction in pneumatic cylinders is another source of uncertainty that must be addressed during actuator design. Due to the current lack of friction models capable of generalizing pneumatic friction for cylinder sizing, a novel model has been proposed based on observations from approximately 1000 friction experiments. Friction force in pneumatic actuators is a challenging subject to align precision with generalization. Therefore, the derived model does not aim to precisely predict friction in all scenarios. Instead, in the absence of more precise data during the sizing process, it provides reasonable friction force estimates to be used during this phase of the design process.

Pneumatic drives are widely used in industrial applications, resulting in varied load force characteristics during operation. To address this, a detailed theoretical and experimental analysis of load force components was performed, including gravitational, inertial, spring, and

viscous forces. This analysis led to the development of simplified models for determining the sizing load force in variable load applications, where corrective factors were applied to replace the traditional engineering practice of sizing for worst-case scenarios. As a result, cylinder oversizing due to variable load profiles could be avoided.

Beyond pneumatic actuator design, empirical rules are also commonly used for valve sizing. To address this, a novel approach for determining the sonic conductance of pneumatic valves was developed. This approach was based on analyzing the characteristic phases of the velocity profile, allowing for the simplification of governing equations and the derivation of an analytical expression to size the equivalent sonic conductance of system valves. Further analysis of series-connected pneumatic restrictors enabled the determination of flow requirements for throttle and directional valves. Simulation and experimental results demonstrated that the proposed method meets design requirements without excessively oversizing the system valves, offering higher accuracy in determining their flow capacity compared to existing methods.

Despite the common assumption that meter-out throttling is the only viable method for pneumatic drives, this thesis demonstrates through theoretical and experimental analysis that meter-in throttling can offer advantages in specific applications, such as those involving high inertia and resistive load forces. These advantages include smoother piston deceleration at the stroke end and reduced system emptying time.

Uncertainties in determining load forces are among the most significant challenges in pneumatic system design. To address this, a Hybrid Machine Learning (HML) model was developed for online optimization. The HML model proved capable of assisting users during equipment setup by providing guidelines for adjusting the supply pressure and throttle valve openings, thereby meeting the requirements of displacement time, ensuring robust system operation, and minimizing air consumption.

The design and setup framework presented in this thesis was extensively tested in simulation-based and experimental environments and compared with alternative design methods from the literature. Results demonstrated that conservative empirical rules, which commonly oversize pneumatic cylinders to ensure proper operation of the system, consume approximately 20% more compressed air than the operating point method. While less conservative approaches do reduce air consumption, they often lead to operational issues, such as failure to meet design requirements and high sensitivity to load variations.

Experimental results also demonstrated the HML's capability to address uncertainties in determining sizing load forces, reducing compressed air consumption by up to 50% when

oversized cylinders are used. These findings show that the HML is a promising solution for developing portable monitoring devices, applicable as a one-time setup tool. This offers a cost-effective way to improve the energy efficiency of pneumatic drives.

Considering the objectives set out for this PhD thesis and the results obtained, it can be concluded that both the main and specific objectives were successfully achieved. Through extensive application of the developed framework in simulation environments and experimental setups, its ability to consistently meet the design requirements for displacement time was demonstrated. Moreover, the framework proved capable of designing and setting up pneumatic actuation systems to operate within a range of average robustness, where a balance between energy efficiency and robustness can be effectively achieved.

Finally, this thesis fills an existing gap in the design of pneumatic actuation systems by proposing a systematic alternative to traditional sizing methods, thereby enhancing the competitiveness of pneumatic technology compared to electromechanical drives while supporting more sustainable economic development.

8.1 FUTURE WORKS

There are still areas of pneumatic drive design that could not be addressed during the development of this thesis and could be further explored. Therefore, the following topics for future work are suggested:

- Design of pneumatic drives for closed-loop operation: As an initial attempt to apply the derived method for sizing pneumatic drives in closed-loop operation, it was observed that high-inertia applications are difficult to control with conventional PID controllers. Therefore, an analysis of the potential correlation between the drive's eigenfrequency and the system's controllability is suggested.
- Friction force model: Expand the range of cylinder manufacturers used to
 determine the parameters of the proposed friction models; evaluate the impact of
 different seal types on friction force; and assess the effect of non-filtered air on
 friction force.
- **Software implementation:** Development of a software or web tool that incorporates the developed framework, facilitating its application and use.

- Enhancements to the HML model: Expand the dataset used to train the multiclass classification model, improving its ability to configure systems under overloaded conditions.
- Load-sensing-based pressure regulator: Develop an auto-adjustable pressure regulator using pressure feedback from the cylinder chamber, similar to the load-sensing technology applied in variable displacement hydraulic pumps.
- **Total cost of ownership analysis:** Perform a cost analysis over the entire life cycle of a pneumatic actuation system to determine the best pneumatic solution for a given application.

REFERENCES

- AHMAD, T.; ZHANG, D. A critical review of comparative global historical energy consumption and future demand: The story told so far. **Energy Reports**, v. 6, p. 1973-1991, 2020.
- AL-BENDER, F.; LAMPAERT, V.; SWEVERS, J. The generalized Maxwell-slip model: a novel model for friction simulation and compensation. **IEEE Transactions on Automatic Control**, v. 50, n. 11, p. 1883-1887, 2005.
- ANDERSEN, B. W. **The analysis and design of pneumatic systems**. New York: Wiley, 1967. 302 p.
- ÅSTRÖM, K. J.; CANUDAS-DE-WIT, C. Revisiting the lugre model; stick-slip motion and rate dependence. **IEEE Control Systems Magazine**, v. 28, 2008.
- AVALLONE, E. A.; BAUMEISTER III, T.; SADEGH, A. Marks' standard handbook for mechanical engineers. 11 ed. New York, USA: McGraw-Hill Education, 2007. 2304 p.
- AZZI, A.; MAOUI, A.; FATU, A. *et al.* Experimental study of friction in pneumatic seals. **Tribology International**, v. 135, p. 432-443, 2019.
- BACCA, G. A.; DE NEGRI, V. J.; ASSAF, Y. Modelo Matemático No-Lineal para un Servosistema Neumático de Posicionamiento Preciso. **Tecno Lógicas**, n. 24, p. 11-37, 2010.
- BARBER, A. **Pneumatic Handbook**. 8 ed. Elsevier Science & Technology Books, 1997. 659 p.
- BEATER, P. **Pneumatic Drives**: System Design, Modelling and Control. Berlin, Germany: Springer, 2007. 323 p.
- BELFORTE, G.; BERTETTO, A. M.; MAZZA, L. Test rig for friction force measurements in pneumatic components and seals. **Proceedings of the Institution of Mechanical Engineers, Part J: Journal of Engineering Tribology**, v. 227, n. 1, p. 43-59, 2013.
- BELFORTE, G.; CONTE, M.; BERTETTO, A. M. et al. Experimental and numerical evaluation of contact pressure in pneumatic seals. **Tribology international**, v. 42, n. 1, p. 169-175, 2009.
- BELFORTE, G.; CONTE, M.; MANUELLO, A. *et al.* Determination of contact pressure at pneumatic seal/rod interface from radial force measurement. **WIT Transactions on Engineering Sciences**, v. 116, p. 161-168, 2017.
- BELFORTE, G.; CONTE, M.; MAZZA, L. Study on pneumatic cylinder piston seals behaviour. *In*: 15th International Sealing Conference, 2008, Stuttgart, Germany. **Proceedings** [...]
- BELFORTE, G.; CONTE, M.; MAZZA, L. Low friction multi-lobed seal for pneumatic actuators. **Wear**, v. 320, p. 7-15, 2014.

- BELFORTE, G.; D'ALFIO, N.; RAPARELLI, T. Experimental analysis of friction forces in pneumatic cylinders. **The Journal of Fluid Control**, v. 20, n. 1, p. 42-60, 1989.
- BELFORTE, G.; MATTIAZZO, G.; MAURO, S. *et al.* Measurement of friction force in pneumatic cylinders. **Lubrication Science**, v. 10, n. 1, p. 33-48, 2003.
- BERGMAN, T. L.; LAVINE, A. S.; INCROPERA, F. P. et al. Fundamentals of heat and mass transfer. New York: John Wiley & Sons, 2011.
- BIMBA. **Pneumatic application & reference handbook**. Monee, Illinois: Bimba Manufacturing Company, 2011. 46 p. Available at: https://www.bimba.com.
- BOLLMANN, A. Fundaments of Pneutronic Industrial Automation Design of Binary Electro-pneumatic Commands (in Portuguese). São Paulo, Brazil: ABHP, 1997. 278 p.
- BOYKO, V.; HÜLSMANN, S.; WEBER, J. Comparative Analysis of Actuator Dimensioning Methods in Pneumatics. *In*: BATH/ASME 2021 Symposium on Fluid Power and Motion Control (FPMC 2021), 2021, Online conference. **Proceedings** [...]
- BOYKO, V.; NAZAROV, F.; GAUCHEL, W. *et al.* Comprehensive Application-Based Analysis of Energy-Saving Measures in Pneumatics. **International Journal of Fluid Power**, v. 25, n. 1, p. 27-58, 2024.
- BOYKO, V.; WEBER, J. Combinations of energy saving measures in pneumatics. *In*: 12th International Fluid Power Conference (12 IFK), 2020, Dresden. **Proceedings** [...]
- BOYKO, V.; WEBER, J. Cycle Time-Based Fault Detection and Localization in Pneumatic Drive Systems. **Actuators**, v. 13, n. 11, p. 447, 2024a.
- BOYKO, V.; WEBER, J. Energy Efficiency of Pneumatic Actuating Systems with Pressure-Based Air Supply Cut-Off. **Actuators**, v. 13, n. 1, p. 44, 2024b.
- CAI, M.; KAGAWA, T.; KAWASHIMA, K. Energy conversion mechanics and power evaluation of compressible fluid in pneumatic actuator systems. *In*: 37th Intersociety Energy Conversion Engineering Conference, 2002, Washington. **Proceedings** [...]
- CAMOZZI. **Pneumatic Automation**: From basic principles to practical techniques. Brescia: Camozzi Automation S.p.A., 2019a. 215 p.
- CAMOZZI. **Series RFU and RFO flow control valves**. 2019b. Camozzi Automation. Available at: https://store.camozzi.co.uk/files//deddf3b1-718d-4de7-8cad-aafb00f16cf7/Series%20RFU%20RFO.pdf. Accessed on: 31 Jan. 2025.
- CAMOZZI. **Series SA shock absorbers**. 2019c. Camozzi Automation. Available at: https://store.camozzi.co.uk/files/91f96202-435a-4c6e-b64d-aaf000c53fe8/Series%20SA%20Shock%20Absorbers.pdf. Accessed on: 31 Jan. 2025.

- CANUDAS-DE-WIT, C.; OLSSON, H.; ASTROM, K. J. *et al.* A new model for control of systems with friction. **IEEE Transactions on Automatic Control**, v. 40, n. 3, p. 419-425, 1995.
- CARNEIRO, J.; DE ALMEIDA, F. G. Heat transfer evaluation of industrial pneumatic cylinders. **Proceedings of the Institution of Mechanical Engineers, Part I: Journal of Systems and Control Engineering**, v. 221, n. 1, p. 119-128, 2007.
- CARNEIRO, J. F.; DE ALMEIDA, F. G. Micro tracking and positioning using off-the-shelf servopneumatics. **Robotics and Computer-Integrated Manufacturing**, v. 30, n. 3, p. 244-255, 2014.
- CARNEIRO, J. F.; DE ALMEIDA, F. G. Lugre friction model: application to a pneumatic actuated system. *In*: 11th Portuguese Conference on Automatic Control (CONTROLO'2014), 2015, Porto, Portugal. **Proceedings** [...]
- ÇENGEL, Y. A.; BOLES, M. A. **Thermodynamics: An Engineering Approach**. 8 ed. New York, USA: McGraw-Hill Education, 2014. 1024 p.
- CHELLIAH, I. **Bagging Decision Trees Clearly Explanined**. Medium.com: Towards Data Science, 2021. Available at: https://towardsdatascience.com/bagging-decision-trees-clearly-explained-57d4d19ed2d3. Accessed on: Jan. 08, 2024.
- CLIMATE MANAGERS. **Energy efficiency best practice guide**: Compressed air systems. Melbourne, Australia: Sustentability Victoria, 2009. 28 p.
- CONTERATO, G. P.; SPADA, T. A. B.; VIGOLO, V. *et al.* Modeling a Pneumatic Speed Governor Using Electronic pressure valves and directional valves. *In*: 25th ABCM International Congress of Mechanical Engineering (COBEM 2019), 2019, Uberlândia. **Proceedings** [...]
- DAHL, P. R. A Solid Friction Model. Los Angeles, USA: Space and Missile Systems Organization Air Force Systems Command, p. 31. 1968.
- DAVIS, J. R. Concise metals engineering data book. Cleveland: ASM international, 1997. 245 p.
- DE GIORGI, R.; BIDEAUX, E.; SESMAT, S. Dynamic thermal model of a discharging process of a pneumatic chamber. *In*: 4th Fluid Power Net International PhD Symposium (FPNI 2006), 2006, Sarasota. **Proceedings** [...]
- DE NEGRI, V. J. Hydraulic and Pneumatic Systems for Automation and Control (in Portuguese): PART II Pneumatic Systems for Automation. Florianópolis: Federal University of Santa Catarina, 2001. 73 p.
- DEGEM SYSTEMS. **Instructor Manual**: Course PN 2100: Basic Pneumatics. 1990. Cat. No: 9021397010 p.
- DESTEK, M. A.; SINHA, A. Renewable, non-renewable energy consumption, economic growth, trade openness and ecological footprint: evidence from organisation for economic Co-

- operation and development countries. **Journal of Cleaner Production**, v. 242, p. 118537, 2020.
- DET, F.; SCAVARDA, S.; RICHARD, E. Simulated and experimental study of charging and discharging of a cylinder by using an electropneumatic servovalve. *In*: International Symposium on Fluid Power (JFPS), 1989. **Proceedings** [...]
- DOLL, M.; NEUMANN, R.; GAUCHEL, W. Sizing of Pneumatic Drives Under Energy Efficiency Aspects. *In*: 14th International Fluid Power Conference (IFK 2024), 2024, Dresden, Germany. **Proceedings** [...]
- DOLL, M.; NEUMANN, R.; SAWODNY, O. Energy efficient use of compressed air in pneumatic drive systems for motion tasks. *In*: 2011 International Conference on Fluid Power and Mechatronics, 2011, Beijing, China. **Proceedings** [...]
- DOLL, M.; NEUMANN, R.; SAWODNY, O. Dimensioning of pneumatic cylinders for motion tasks. **International Journal of Fluid Power**, v. 16, n. 1, p. 11-24, Mar. 2015.
- DONG, K.; DONG, X.; JIANG, Q. How renewable energy consumption lower global CO2 emissions? Evidence from countries with different income levels. **The World Economy**, v. 43, n. 6, p. 1665-1698, 2020.
- DRAPALA, J. **Kernel Density Estimator explained step by step**. Medium.com: Towards Data Science, 2023. Available at: https://towardsdatascience.com/kernel-density-estimation-explained-step-by-step-7cc5b5bc4517. Accessed on: Jan. 13, 2025.
- DU, H.; LIU, W.; BIAN, X. *et al.* Energy-saving for industrial pneumatic actuation systems by exhausted air reuse based on a constant pressure elastic accumulator. **Sustainability**, v. 14, n. 6, p. 3535, 2022.
- DUDIĆ, S.; RELJIĆ, V.; ŠEŠLIJA, D. *et al.* Improving Energy Efficiency of Flexible Pneumatic Systems. **Energies**, v. 14, n. 7, p. 1819, Mar. 2021.
- EMERSON. **ISO 6432, series MNI**. [S.1.]: Emerson Electric Co., 2020. Available at: https://www.emerson.com/documents/automation/catalog-iso-6432-series-mni-aventics-en-6907104.pdf. Accessed on: 31 Jan. 2025.
- ENDLER, L.; DE NEGRI, V. J.; CASTELAN, E. B. Compressed air saving in symmetrical and asymmetrical pneumatic positioning systems. **Proceedings of the Institution of Mechanical Engineers, Part I: Journal of Systems and Control Engineering**, v. 229, n. 10, p. 957-969, 2015.
- FAGOTTI, F.; PRATA, A. T. A new correlation for instantaneous heat transfer between gas and cylinder in reciprocating compressors. *In*: International Compressor Engineering Conference, 1998, Indiana, USA. **Proceedings** [...]
- FARIAS, N. M. d. Reuse of compressed air in discrete pneumatic actuation systems using an intermediate reservoir (in Portuguese). 2020. M. S. Thesis Mechanical Engineering Department, Federal University of Santa Catarina, Florianópolis, Brazil. Available at: http://laship.ufsc.br/site/en/. Accessed on: 31 Jan. 2025.

- FESTO. **Digital simplicity: New ways to increase productivity with "smart" systems**. 2017. Esslingen, Germany: Festo AG & Co. KG. Available at: https://www.festo.com/media/cms/media/editorial/downloads/wp_digitalsimplicity_en_v09_1. pdf. Accessed on: 31 Jan. 2025.
- FESTO. A new era of human-robot collaboration: the first pneumatic cobot. 2022. [S.l.]: Festo SE & Co. KG. Available at: https://www.pneumatictips.com/a-new-era-of-human-robot-collaboration-the-first-pneumatic-cobot/. Accessed on: 31 Jan. 2025.
- FESTO. **Round cylinders DSNU**. 2023. [S.l.]: Festo SE & Co. KG. Available at: https://stagewww.festo.com/media/pim/156/D15000100122156.PDF. Accessed on: 31 Jan. 2025.
- FESTO. **Pneumatic sizing**. 2024a. [S.l.]: Festo SE & Co. KG. Available at: https://www.festo.com/eac/en-us us/PneumaticSizing/. Accessed on: 25 Jan. 2025.
- FESTO. **Product Catalague**. 2024b. [S.l.]: Festo SE & Co. KG. Available at: https://www.festo.com/us/en/. Accessed on: 31 Jan. 2025.
- FESTO. **Standards-based cylinder DNC-V**. 2024c. [S.l.]: Festo SE & Co. KG. Available at: https://www.festo.com/se/en/p/standards-based-cylinder-id_DNCV_PUB/. Accessed on: 31 Jan. 2025.
- FESTO. **Shock absorber Type YSR-...-C.** s.d. [S.l.]: Festo SE & Co. KG. Available at: https://www.festo.com/net/en_en/SupportPortal/Files/44178/YSR-C.pdf. Accessed on: 31 Jan. 2025.
- FESTO, A. C. K.; HÜLSMANN, S.; KÖPSCHALL, M. *et al.* Energy efficiency in production in the drive and handling technology field. [S.l.]: EnEffAH Project Consortium, 2012. Available at: https://www.eneffah.de/EnEffAH_Broschuere_engl.pdf. Accessed on: 31 Jan. 2025.
- FIALHO, A. B. Pneumatic automation Design, dimensioning and analysis of circuits (in Portuguese). 2 ed. São Paulo: Érica Ltda, 2004. 324 p.
- FISCHER, G. S.; IORDACHITA, I.; CSOMA, C. *et al.* MRI-compatible pneumatic robot for transperineal prostate needle placement. **IEEE/ASME transactions on mechatronics**, v. 13, n. 3, p. 295-305, 2008.
- GAUCHEL, W.; HÜLSMANN, S.; MÜLLER, L. On the thermodynamics of pneumatic compression and expansion. *In*: 13th International Fluid Power Conference (IFK 2022), 2022, Aachen, Germany. **Proceedings** [...]
- GIECK, K.; GIECK, R. Engineering Formulas. 7 ed. Germering: McGraw-Hill, 1997. 630 p.
- GRYBOŚ, D.; LESZCZYŃSKI, J. Exergy Analysis for the Intermittent Air Supply in Pneumatic Machines. *In*: 14th International Fluid Power Conference (IFK 2024), 2024, Dresden, Germany. **Proceedings** [...]

- HARRIS, P.; NOLAN, S.; O'DONNELL, G. E. Energy optimisation of pneumatic actuator systems in manufacturing. **Journal of cleaner production**, v. 72, p. 35-45, Jun. 2014.
- HARRIS, P.; O'DONNELL, G. E.; WHELAN, T. Energy efficiency in pneumatic production systems: state of the art and future directions. *In*: 19th CIRP Conference on Life Cycle Engineering, 2012, Berkeley, USA. **Proceedings** [...]
- HARVEY, C. Sizing Pneumatics for Performance and Efficiency. [S. 1.]: Machine Design, 2009. Available at: https://www.machinedesign.com/archive/article/21829438/sizing-pneumatics-for-performance-and-efficiency. Accessed on: 22 Nov. 2024.
- HENÉ, M. D. Theoretical-experimental study of the operating point and proposition of a sizing method for pneumatic systems (in Portuguese). 2010. M.S. Thesis Mechanical Engineering Department, Federal University of Santa Catarina, Florianópolis, Brazil. Available at: http://laship.ufsc.br/site/en/. Accessed on: 31 Jan. 2025.
- HENÉ, M. D.; MENDONZA, Y. E. A.; OLIVEIRA, L. G. D. *et al.* Determination of operational point for penumatic system sizing. *In*: 7th International Fluid Power Conference (IFK 2010), 2010, Aachen, Germany. **Proceedings** [...]
- HEPKE, J. Energetische Untersuchung und Verbesserung der Antriebstechnik pneumatischer Handhabungssysteme. 2016. PhD thesis Fakultät Maschinenwesen, TU Dresden, Germany.
- HEPKE, J.; WEBER, J. Improving energy efficiency of pneumatic handling systems. *In*: 8th International Fluid Power Conference (IFK 2012), 2012, Dresden. **Proceedings** [...]
- HEPKE, J.; WEBER, J. Energy saving measures on pneumatic drive systems. *In*: The 13th Scandinavian International Conference on Fluid Power (SICFP 2013), 2013, Linköping, Sweden. **Proceedings** [...]
- HESSE, S. **99 Examples of Pneumatic Applications**. Esslingen: Festo AG & Company, 2001. 121 p.
- HILDEBRANDT, A.; SAWODNY, O.; NEUMANN, R. *et al.* Cascaded control concept of a robot with two degrees of freedom driven by four artificial pneumatic muscle actuators. *In*: American Control Conference, 2005, Portland. **Proceedings** [...]
- IEA. **Tracking Industry 2022: Energy**. Paris: International Energy Agency. 2022. Available at: https://www.iea.org/energy-system/industry. Accessed on: 31 Jan. 2025.
- ISO International Organization for Standardization. **ISO 6358:** Pneumatic Fluid Power, Components Using Compressible Fluids: Determination of flow rate characteristics. 1989
- ISO International Organization for Standardization. **ISO 15552:** Pneumatic Fluid Power: Cylinders with detachable mountings, 1 000 kPa (10 bar) series, bores from 32mm to 320mm Basic, mounting and accessories dimensions. 2004
- ISO International Organization for Standardization. **ISO 8573-1:** Compressed air: Part 1: Contaminants and purity classes. 2010

- ISO International Organization for Standardization. **ISO 6358-1:** Pneumatic Fluid Power: Determination of flow rate characteristics of components using compressible fluids -- Part 1: General rules and test methods for steady-state flow. 2013
- ISO International Organization for Standardization. **ISO 6358-3:** Pneumatic Fluid Power: Determination of flow rate characteristics of components using compressible fluids -- Part 3: Method for calculating steady-state flow-rate characteristics of systems. 2014
- ISO International Organization for Standardization. **ISO 6432:** Pneumatic Fluid Power: Single rod cylinders, 1 000 kPa (10 bar) series, bores from 8mm to 25mm -- Basic and mounting dimensions. 2015
- JIMENEZ, C. R.; REINERTZ, O.; SCHMITZ, K. A Comprehensive Study of Energy-Saving Strategies Through Combined Throttling. **International Journal of Fluid Power**, v. 25, n. 1, p. 1-26, 2024.
- KARPENKO, M.; SEPEHRI, N. Neural network classifiers applied to condition monitoring of a pneumatic process valve actuator. **Engineering applications of artificial intelligence**, v. 15, n. 3-4, p. 273-283, Jun. 2002.
- KAVITHA, M.; GNANESWAR, G.; DINESH, R. *et al.* Heart disease prediction using hybrid machine learning model. *In*: 2021 6th international conference on inventive computation technologies (ICICT), 2021, Coimbatore, India. **Proceedings** [...]
- KOSTURKOV, R.; NACHEV, V.; TITOVA, T. Diagnosis of Pneumatic Systems on Basis of Time Series and Generalized Feature for Comparison with Standards for Normal Working Condition. **TEM Journal**, v. 10, n. 1, p. 183, Feb. 2021.
- KRICHEL, S. V.; SAWODNY, O.; HILDEBRANDT, A. Tracking control of a pneumatic muscle actuator using one servovalve. *In*: American Control Conference, 2010, Baltimore. **Proceedings** [...]
- KRIVTS, I. L.; KREJNIN, G. V. Pneumatic actuating systems for automatic equipment: structure and design. Boca Raton: Crc Press, 2006. 345 p.
- LEE, J.; CHO, Y. National-scale electricity peak load forecasting: Traditional, machine learning, or hybrid model? **Energy**, v. 239, n. Part D, p. 122366, 2022.
- LESZCZYNSKI, J.; GRYBOS, D. Compensation for the complexity and over-scaling in industrial pneumatic systems by the accumulation and reuse of exhaust air. **Applied Energy**, v. 239, p. 1130-1141, 2019.
- LIERMANN, M.; FELLER, C.; LINDINGER, F. Real-Time Simulation of Fluid Power Systems. *In*: ASME/BATH Symposium on Fluid Power and Motion Control (FPMC 2021), 2021, Online. **Proceedings** [...]
- LOCATELI, C. C. Modeling and Development of a Pneumatic Position Control System Actuated by ON/OFF Valves (in Portuguese). 2011. M.S. Thesis Mechanical Engineering

Department, Federal University of Santa Catarina, Florianópolis, Brazil. Available at: http://laship.ufsc.br/site/en/. Accessed on: 31 Jan. 2025.

LOVE, L. J.; LANKE, E.; ALLES, P. Estimating the Impact (Energy, Emissions and Economics) of the U.S. Fluid Power Industry. Tennessee: U.S. Department of Energy, p. 45. 2012.

MADER. **Betriebsanleitung PCC Blue Sytem**. 2017. Leinfelden-Echterdingen, Germany: Mader GmbH & Co. KG. Available at: https://www.mader.eu/files/mader-ba-pcc-blue-system.pdf. Accessed on: 31 Jan. 2025.

MARKOWSKI, J.; GRYBOŚ, D.; LESZCZYŃSKI, J. *et al.* Exhaust Air Recovery System from the Utilisation Stage of Pneumatic System in Double Transmission Double Expansion Approach. **Energies**, v. 16, n. 23, p. 7840, 2023.

MASHAYEKHI, A.; BOOZARJOMEHRY, R. B.; NAHVI, A. *et al.* Improved passivity criterion in haptic rendering: influence of Coulomb and viscous friction. **Advanced Robotics**, v. 28, n. 10, p. 695-706, 2014.

MAZZA, L.; BELFORTE, G. Analytical/experimental study of the contribution of individual seals to friction force in pneumatic actuators. **Journal of Tribology**, v. 139, n. 2, p. 022202, 2017.

MEIXNER, H.; KOBLER, R. Introduction to pneumatics: Didactic Book (in Portuguese). 1977. 200 p.

MENDONZA, Y. E. A. **Development of a Servopneumatic System for Speed Regulation of Turbines in Small Hydropower Plants (in Portuguese)**. 2006. M.S. Thesis - Mechanical Engineering Department, Federal University of Santa Catarina, Florianópolis, Brazil. Available at: http://laship.ufsc.br/site/en/. Accessed on: 31 Jan. 2025.

MENDONZA, Y. E. A.; DE NEGRI, V. J.; SOARES, J. M. C. Pneutronic Speed Governor for Small Hydropower Plants – A New Application for Pneumatics. **Journal of the Brazilian Society of Mechanical Sciences and Engineering**, v. 38, n. 8, p. 2621-2633, 2014.

MENG, D.; TAO, G.; ZHU, X. Integrated direct/indirect adaptive robust motion trajectory tracking control of pneumatic cylinders. **International journal of control**, v. 86, n. 9, p. 1620-1633, 2013.

MERKELBACH, S.; MURRENHOFF, H. Exergy based analysis of pneumatic air saving measures. *In*: ASME/BATH Symposium on Fluid Power and Motion Control (FPMC 2015), 2015, Illinois. **Proceedings** [...]

MERKELBACH, S.; MURRENHOFF, I. H.; FEY, I. M. *et al.* Pneumatic or electromechanical drives - a comparison regarding their exergy efficiency. *In*: 10th International Fluid Power Conference (IFK 2016), 2016, Dresden. **Proceedings** [...]

MESSINA, A.; GIANNOCCARO, N. I.; GENTILE, A. Experimenting and modelling the dynamics of pneumatic actuators controlled by the pulse width modulation (PWM) technique. **Mechatronics**, v. 15, n. 7, p. 859-881, 2005.

- METAL WORK S.P.A. Easy Sizer. [S. 1.]: Metal Work Pneumática do Brasil, 2024. Available at: https://www.metalwork.com.br/ferramentas-de-engenharia. Accessed on: 31 Jan. 2025.
- MOUSAVI, S.; KARA, S.; KORNFELD, B. Energy efficiency of compressed air systems. **Procedia Cirp**, v. 15, p. 313-318, 2014.
- MUZY, G. A. A.; CAPORALI, A. S. Positioning system of a pneumatic actuator driven by proportional pressure regulator valves. *In*: 4th Workshop on Innovative Engineering for Fluid Power (WIEFP 2018), 2018, São Paulo. **Proceedings** [...]
- NAJAFI, F.; HEJRATI, B. Impedance control of a pneumatic actuator using fast switching on/off solenoid valves for tasks containing contact. *In*: 17th Annual International Conference on Mechanical Engineering (ISME 2009), 2009, Tehran, Iran. **Proceedings** [...]
- NAKUTIS, Z.; KASKONAS, P. Pneumatic cylinder diagnostics using classification methods. *In*: 2007 IEEE Instrumentation & Measurement Technology Conference (IMTC 2007), 2007, Warsaw, Poland. **Proceedings** [...]
- NAKUTIS, Z.; KAŠKONAS, P. An approach to pneumatic cylinder on-line conditions monitoring. **Mechanics**, v. 72, n. 4, p. 41-47, Apr. 2008.
- NAZAROV, F.; WEBER, J. Modelling, Simulation and Validation of the Pneumatic End-Position Cylinder Cushioning. *In*: Scandinavian International Conference on Fluid Power (SICFP 2021), 2021, Linköping. **Proceedings** [...]
- NAZAROV, F.; WEBER, J. Heat Transfer Model of Pneumatic End-Position Cylinder Cushioning. **International Journal of Fluid Power**, p. 1-18, 2022a.
- NAZAROV, F.; WEBER, J. Sensitivity Analysis and Robust Optimization of an Integrated Pneumatic End-Position Cushioning. *In*: 13th International Fluid Power Conference (IFK 2022), 2022b, Dresden, Germany. **Proceedings** [...]
- NFPA National Fluid Power Association. **NFPA T3.21.3:** Pneumatic Fluid Power: Flow Rating Test Procedure and Reporting Method For Fixed Orifice Componentes. 2008
- NORGREN. **Integrated Valve & Actuator (IVAC)**. [S.l.]: Norgren Ltd, 2024. Available at: https://www.norgren.com/en/products/actuators/integrated-valve-and-actuator. Accessed on: 31 Jan. 2025.
- NOURI, B. M.; AL-BENDER, F.; SWEVERS, J. et al. Modelling a pneumatic servo positioning system with friction. *In*: American Control Conference (ACC), 2000, Chicago, USA. **Proceedings** [...]
- NOVAKOVIC, M. M.; SESLIJA, D. D.; CAJETINAC, S. R. *et al.* Impact of capturing used air on the dynamics of actuator drive. **Journal of Control Engineering and Applied Informatics**, v. 17, n. 2, p. 82-89, 2015.

- NSK. **Rolling Bearings CAT. No. E1102m**. 2013. NSK Motion & Control. 283 p. Available at: https://www.nsk.com/common/data/ctrgPdf/bearings/e1102m.pdf. Accessed on: 31 Jan. 2025.
- OBERG, E.; JONES, F. D.; HORTON, H. L. et al. Machinery's Handbook. 30 ed. Norwal, USA: Industrial Press, 2016.
- OHLIGSCHLÄGER, O. Pneumatische Zylinderantriebe Thermodynamische Grundlagen und digitale Simulation. 1990. PhD thesis Fakultät für Maschinenwesen, RWTH Aachen University, Aachen, Germany.
- OLIVEIRA, L. G. **Determination of the operating points for pneumatic cylinder-valve set** (in **Portuguese**). 2009. M.S. Thesis Department of Mechanical Engineering, Federal University of Santa Catarina, Florianópolis, Brazil. Available at: https://laship.ufsc.br/. Accessed on: 31 Jan. 2025.
- OSHTORJANI, M. K.; MIKKOLA, A.; JALALI, P. Numerical treatment of singularity in hydraulic circuits using singular perturbation theory. **IEEE/Asme Transactions on Mechatronics**, v. 24, n. 1, p. 144-153, Feb. 2018.
- PADOVANI, D.; BARTH, E. J. Exploiting valve timing for pneumatic energy savings. *In*: BATH/ASME Symposium on Fluid Power and Motion Control (FPMC 2018), 2018, Bath, England. **Proceedings** [...]
- PARKER. Pneumatic Cylinders Ø10 to Ø25 mm P1A Series. 2020. Parker Hannifin Corporation.

 Available at: https://www.parker.com/Literature/Pneumatics%20Division%20Europe/PDE-Documents/Cylinders/Parker_Pneumatic_P1A_Mini_ISO_Cylinder_Catalogue_PDE2564TC UK.pdf. Accessed on: 31 Jan. 2025.
- PÉREZ, J. A. L. Force Control on Hydraulic Actuators Through Additional Hydraulic Compliance. 2019. PhD thesis Department of Mechanical Engineering, Federal University of Santa Catarina, Florianópolis, Brazil.
- PIANOSI, F. **SAFE Toolbox**. [S. l.]: GitHub, 2022. Available at: https://github.com/SAFEtoolbox/SAFE-matlab.
- POHJA, R.; NURMELA, A.; MOILANEN, P. *et al.* Multifunctional high precision pneumatic loading system (HIPS) for creep-fatigue testing. **Procedia Engineering**, v. 55, p. 573-577, 2013.
- PRITCHARD, P. J. Fox and McDonald's Introduction to Fluid Mechanics. Eighth edition ed. USA: John Wiley & Sons, 2011. 896 p.
- PRUDENTE, F. Industrial Pneumatic Automation Theory and Applications (in Portuguese). Rio de Janeiro: Grupo Gen-LTC, 2000. 263 p.
- RABIE, M. G. Fluid Power Engineering. USA: McGraw-Hill, 2009. 420 p.

- RADERMACHER, T.; MERX, M.; SITTE, A. *et al.* **Potenzialstudie Energie-/Kosteneinsparung in der Fluidtechnik**. Germany: TU Dresden, University of Stuttgart. 2021. Available at: https://www.umweltbundesamt.de/publikationen/potenzialstudie-energie-kosteneinsparung-in-der. Accessed on: 31 Jan. 2025.
- RADUENZ, H.; ERICSON, L.; UEBEL, K. *et al.* Energy Management Based on Neural Networks for a Hydraulic Hybrid Wheel Loader. **International Journal of Fluid Power**, v. 23, n. 03, p. 411-432, October 19-21 2020.
- RAISCH, A.; HÜLSMANN, S.; SAWODNY, O. Saving energy by predictive supply air shutoff for pneumatic drives. *In*: 2018 European Control Conference, 2018, Limassol, Cyprus. **Proceedings** [...]
- RAISCH, A.; SAWODNY, O. Analysis and optimal sizing of pneumatic drive systems for handling tasks. **Mechatronics**, v. 59, p. 168-177, 2019a.
- RAISCH, A.; SAWODNY, O. Modeling and Analysis of Pneumatic Cushioning Systems Under Energy-Saving Measures. **IEEE Transactions on Automation Science and Engineering**, v. 17, n. 3, p. 1388-1398, 2019b.
- RAKOVA, E.; HEPKE, J.; WEBER, J. EXonomy analysis for the Inter-domain comparison of electromechanical and pneumatic drives. *In*: 10th International Fluid Power Conference (IFK 2016), 2016, Dresden, Germany. **Proceedings** [...]
- RAKOVA, E.; WEBER, J. Exonomy Analysis for the Selection of the Most Cost-Effective Pneumatic Drive Solution. *In*: ASME 9th FPNI Ph.D Symposium on Fluid Power, 2016, Florianópolis, Brazil. **Proceedings** [...]
- RAO, Z.; BONE, G. M. Nonlinear modeling and control of servo pneumatic actuators. **IEEE transactions on control systems technology**, v. 16, p. 562-569, 2008.
- RAPARELLI, T.; MAZZA, L.; TRIVELLA, A. Study of a non-conventional sealing system for low-friction pneumatic cylinders. **WIT Transactions on Engineering Sciences**, v. 76, p. 55-64, 2012.
- REESE, C.; REINERTZ, O.; SCHMITZ, K. Feasibility Study and Experimental Validation of a Novel Combined Throttling Approach. *In*: 14th International Fluid Power Conference (IFK 2024), 2024, Dresden, Germany. **Proceedings** [...]
- RIGHETTINI, P.; GIBERTI, H. A nonlinear controller for trajectory tracking of pneumatic cylinders. *In*: 7th International Workshop on Advanced Motion Control, 2002, Maribor. **Proceedings** [...]
- SAGARA, H.; HOSONO, M.; YANG, Q.-h. An Approach for Low Speed Pneumatic Actuators. *In*: 4th International Symposium on Fluid Power (JFPS 1999), 1999, Tokyo, Japan. **Proceedings** [...]
- SAIDUR, R.; RAHIM, N.; HASANUZZAMAN, M. A review on compressed-air energy use and energy savings. **Renewable and sustainable energy reviews**, v. 14, n. 4, p. 1135-1153, 2010.

- SALTELLI, A.; RATTO, M.; ANDRES, T. *et al.* **Global sensitivity analysis: the primer**. Chichester, England: John Wiley & Sons, 2008.
- SANVILLE, F. E. A new method of specifying the flow capacity of pneumatic fluid power valves. *In*: Second Fluid Power Symposium, 1971, Guildford. **Proceedings** [...]
- SCHULZ, M.; VELICKOVIC, I.; ANDELKOVIC, S. *et al.* ML DESIGNER TM as simulation tool in robotics. *In*: 8th International Conference on Telecommunications in Modern Satellite, Cable and Broadcasting Services, 2007, Niš. **Proceedings** [...]
- ŠEŠLIJA, D.; DUDIĆ, S.; MILENKOVIĆ, I. Cost effectiveness analysis of pressure regulation method on pneumatic cylinder circuit. **International Energy Journal**, v. 17, n. 2, 2017.
- ŠEŠLIJA, D.; ŠULC, J.; RELJIĆ, V. Energy Efficient Pneumatic Control Scheme with Recirculation of the Used Air. *In*: 2nd regional conference Mechatronics in Practice and Education (MECHEDU 2013), 2013, Subotica, Serbia. **Proceedings** [...]
- ŠEŠLIJA, M.; RELJIĆ, V.; ŠEŠLIJA, D. *et al.* Reuse of exhausted air from multi-actuator pneumatic control systems. **Actuators**, v. 10, n. 6, p. 125, 2021.
- SHAMES, I. H. Fluid mechanics: Basic principles (in Portuguese). São Paulo, Brazil: Edgard Blücher, 1973. 192 p.
- SHEN, X.; GOLDFARB, M. Energy saving in pneumatic servo control utilizing interchamber cross-flow. **Journal of Dynamic Systems, Measurement, and Control**, v. 129, p. 303-310, 2007.
- SHI, Y.; CAI, M.; XU, W. et al. Methods to evaluate and measure power of pneumatic system and their applications. Chinese Journal of Mechanical Engineering, v. 32, n. 1, p. 1-11, 2019.
- ŠITUM, Ž. Control of a pneumatic drive using electronic pressure valves. **Transactions of the Institute of Measurement and Control**, v. 35, n. 8, p. 1085-1093, 2013.
- SKF. Rolamentos de esferas PUB BU/P1 10000/2 PT.BR. 2015. Grupo SKF. Available at: https://www.skf.com/binaries/pub45/Images/0901d19680416a2b-10000_2-PT-BR---Rolling-bearings tcm 45-121486.pdf. Accessed on: 31 Jan. 2025.
- SMC. **Basic Pneumatics**: A manual for fluid power components and practical applications. Indianapolis: SMC Pneumatics Inc., 1997. 120 p.
- SMC. **CVQ**, Compact Cylinder with Solenoid Valve. 2024a. SMC Corporation of America. Available at: https://www.smcusa.com/products/cvq-compact-cylinder-with-solenoid-valve~36025. Accessed on: 31 Jan. 2025.
- SMC. **Model Selection Software**. [S. 1.]: SMC Corporation, 2024b. Available at: https://www.smcworld.com/select/air/en-jp/index.html. Accessed on: 25 Jan. 2025.

- SMC. Air Cylinder MB Series ø32, ø40, ø50, ø63, ø80, ø100, ø125. s.d.-a. SMC Corporation. Available at: https://ca01.smcworld.com/catalog/en/actuator/MB-MDB-Z-E/7-3-2-p0477-0524-MB en/data/7-3-2-p0477-0524-MB en.pdf. Accessed on: 31 Jan. 2025.
- SMC. **Air Cylinder CJ2 Series ø6, ø10, ø16**. s.d.-b. SMC Corporation. Available at: https://ca01.smcworld.com/catalog/en/actuator/CJ2-CDJ2-Z-E/7-3-2-p0067-0183-CJ2 en/data/7-3-2-p0067-0183-CJ2 en.pdf. Accessed on: 31 Jan. 2025.
- SORLI, M.; GASTALDI, L. Thermic influence on the dynamics of pneumatic servosystems. **Journal of Dynamic Systems, Measurement, and Control**, v. 131, p. 024501, 2009.
- SPADA, T. A. B. Theoretical-experimental development of a system for actuating intake valves in small hydropower plants (SHPs) based on pneumatic technology (in Portuguese). 2020. M.S. Thesis Mechanical Engineering Department, Federal University of Santa Catarina, Florianópolis. Available at: http://laship.ufsc.br/site/en/. Accessed on: 31 Jan. 2025.
- SUBBARAJ, P.; KANNAPIRAN, B. Artificial neural network approach for fault detection in pneumatic valve in cooler water spray system. **International Journal of Computer Applications**, v. 9, n. 7, p. 43-52, Nov. 2010.
- SULLIVAN, J. A. **Fluid Power**: Theory and Application. 3 ed. New Jersey: Prentice-Hall Company, 1989. 532 p.
- SUN, X.; LING, K.-V.; SIN, K.-K. *et al.* Air Leakage Detection of Pneumatic Train Door Subsystems Using Open Set Recognition. **IEEE Transactions on Instrumentation and Measurement**, v. 70, p. 1-9, Jul. 2021.
- TADESE, M. A.; YUMBLA, F.; YI, J.-S. *et al.* Passivity guaranteed dynamic friction model with temperature and load correction: Modeling and compensation for collaborative industrial robot. **IEEE Access**, v. 9, p. 71210-71221, 2021.
- TEIXEIRA, P. L. Theoretical and Experimental Analysis of a Hydraulic Press Brake Controlled by a Variable-Speed Pump-Motor System (in Portuguese). 2015. M. S. Thesis Mechanical Engineering Department, Federal University of Santa Catarina, Florianópolis, Brazil.
- TERASHIMA, Y.; KAWAKAMI, Y.; ARINAGA, T. *et al.* An approach for energy-saving of pneumatic cylinders by meter-in circuit. *In*: The 6th Triennial International Symposium on Flow Control, Measurement and Flow Visualization (FLUCOME 2000), 2000, Québec, Canada. **Proceedings** [...]
- TRAN, X.; DAO, H.; TRAN, K. A new mathematical model of friction for pneumatic cylinders. **Proceedings of the institution of mechanical engineers, Part C: Journal of Mechanical Engineering Science**, v. 230, n. 14, p. 2399-2412, 2016.
- TRAN, X. B.; HAFIZAH, N.; YANADA, H. Modeling of dynamic friction behaviors of hydraulic cylinders. **Mechatronics**, v. 22, p. 65-75, 2012.
- TRAN, X. B.; NGUYEN, V. L.; TRAN, K. D. Effects of friction models on simulation of pneumatic cylinder. **Mechanical Sciences**, v. 10, n. 2, p. 517-528, 2019.

- TSAI, C.-F.; CHEN, M.-L. Credit rating by hybrid machine learning techniques. **Applied soft computing**, v. 10, n. 2, p. 374-380, 2010.
- UNGER, M.; RADGEN, P. Energy Efficiency in Compressed Air Systems A review of energy efficiency potentials, technological development, energy policy actions and future importance. *In*: 10th International Conference on Energy Efficiency in Motor Driven Systems, 2017, Rome, Italy. **Proceedings** [...]
- VALDIERO, A. C. Control of Hydraulic Robots with Friction Compensation (in Portuguese). 2005. PhD thesis Mechanical Engineering Department, Federal University of Santa Catarina, Florianópolis. Available at: https://laship.ufsc.br/site/en/. Accessed on: 31 Jan. 2025.
- VALDIERO, A. C. Mathematical Modeling of Hydraulic Robots (in Portuguese): Mathematical modeling applied to problem-solving in engineering (in Portuguese). Ijuí, Brazil: Editora Unijuí, 2012.
- VDI Verein Deutscher Ingenieure. **VDI 3290:** Parameters of Pneumatic Appliances for Control Systems: Directional Control Valves. 1962
- VIGOLO, V. Theoretical-experimental study to aid the sizing of pneumatic actuation systems (in Portuguese). 2018. M.S. Thesis Department of Mechanical Engineering, Federal University of Santa Catarina, Florianópolis, Brazil. Available at: https://laship.ufsc.br/site/en/. Accessed on: 31 Jan. 2025.
- VIGOLO, V.; BOYKO, V.; WEBER, J. et al. A Model-Based Approach for Online Optimization of Pneumatic Drives. **IEEE/ASME Transactions on Mechatronics**, 2024.
- VIGOLO, V.; BOYKO, V.; WEBER, J. *et al.* Online Monitoring of Pneumatic Actuation System for Energy Efficiency and Dynamic Performance. *In*: ASME/BATH 2023 Symposium on Fluid Power and Motion Control (FPMC 2023), 2023, Sarasota, USA. **Proceedings** [...]
- VIGOLO, V.; CONTERATO, G.; SPADA, T. *et al.* Energy efficiency and performance of servopneumatic drives for speed governors based on operating points. *In*: 12th International Fluid Power Conference (IFK 2020), 2020, Dresden. **Proceedings** [...]
- VIGOLO, V.; DE NEGRI, V. J. Sizing Optimization of Pneumatic Actuation Systems Through Operating Point Analysis. **Journal of Dynamic Systems, Measurement, and Control**, v. 143, n. 5, p. 051006, 2021.
- VIGOLO, V.; RODRIGUES, L. A.; VALDIERO, A. C. *et al.* HOPE-G: A Dual Belt Treadmill Servo-Pneumatic System for Gait Rehabilitation. **Journal of Intelligent & Robotic Systems**, v. 110, n. 3, p. 1-14, 2024.
- VIGOLO, V.; VALDIERO, A. C.; DE NEGRI, V. J. Sizing Directional Pneumatic Valves Based on the Characteristic Dynamic Behavior of Linear Actuators. *In*: BATH/ASME 2021 Symposium on Fluid Power and Motion Control (FPMC 2021), 2021, Online conference. **Proceedings** [...]

- VIGOLO, V.; VALDIERO, A. C.; DE NEGRI, V. J. Analysis of the operating point method for dimensioning of pneumatic drives under variable loading conditions. *In*: Advancements in Fluid Power Technology: Sustainability, Electrification, and Digitalization Proceedings of the Global Fluid Power Society PhD Symposium 2024, 2025, Hudiksvall, Sweden. **Proceedings** [...]
- VIRVALO, T. Modeling pneumatic position servo realized with commercial components. *In*: 2nd International Symposium on Fluid Power (JFPS 1993), 1993, Tokio, Japan. **Proceedings** [...]
- VON LINSINGEN, I. **Fundamentals of Hydraulic Systems (in Portuguese)**. 5 ed. Florianópolis, Brazil: Editora da UFSC, 2016. 398 p.
- WANG, J.; GORDON, T. Energy optimal control of servo-pneumatic cylinders through nonlinear static feedback linearization. **Journal of Dynamic Systems, Measurement, and Control**, v. 134, n. 5, p. 051005, 2012.
- WANG, J.; PU, J.; MOORE, P. Accurate position control of servo pneumatic actuator systems: an application to food packaging. **Control Engineering Practice**, v. 7, n. 6, p. 699-706, 1999.
- WANG, Z.; XIONG, W.; WANG, H. *et al.* Exergy analysis of the pneumatic line throwing system. **International Journal of Exergy**, v. 19, n. 3, p. 364-379, 2016.
- WANG, Z.; YANG, B.; MA, Q. *et al.* Facilitating Energy Monitoring and Fault Diagnosis of Pneumatic Cylinders with Exergy and Machine Learning. **International Journal of Fluid Power**, v. 24, n. 04, p. 643–682, Nov. 2023.
- XENERGY. Assessment of the Market for Compressed Air Efficiency Services. Massachusetts, USA, p. 63. 2001.
- YANADA, H.; SEKIKAWA, Y. Modeling of dynamic behaviors of friction. **Mechatronics**, v. 18, n. 7, p. 330-339, September 2008.
- YANADA, H.; TAKAHASHI, K.; MATSUI, A. Identification of dynamic parameters of modified LuGre model and application to hydraulic actuator. **Transactions of the Japan Fluid Power System Society**, v. 40, n. 4, p. 57-64, 2009.
- YANG, F.; TADANO, K.; LI, G. et al. Analysis of the Energy Efficiency of a Pneumatic Booster Regulator with Energy Recovery. **Applied Sciences**, v. 7, n. 8, p. 816, 2017.
- YIN, Y. **High Speed Pneumatic Theory and Technology Volume II**. Shanghai: Springer, 2020. 396 p.
- ZHAN, Y. J.; WANG, T.; WANG, B. Study on friction characteristics of energizing pneumatic cylinders. **Advanced Materials Research**, v. 904, p. 306-310, 2014.
- ZHU, S.; COX, T.; XU, Z. *et al.* Design considerations of fault-tolerant electromechanical actuator systems for more electric aircraft (MEA). *In*: IEEE Energy Conversion Congress and Exposition (ECCE 2018), 2018, Portland. **Proceedings** [...]

APPENDIX A – IDENTIFICATION OF FRICTION PARAMETERS

The friction parameters of the LuGre model were obtained from steady-state velocity-friction maps derived from experimental measurements. The tests involved moving the piston at different velocities, ranging from very low velocities (5-10 mm/s) to the maximum achievable velocity with the current valve set. A steady-state velocity is desirable to minimize acceleration forces on the drive, as acceleration values are challenging to be precisely determined due to the second derivative of position, which often introduces excessive noise into the measured data. Therefore, assuming a steady-state displacement without load, the piston's motion equation is

$$F_{fr} = p_A A_A - p_B A_B - p_0 A_r. (A.1)$$

For the pressure-dependent model, the same approach was applied to four different supply pressures ($p_S = 2, 4, 6, 8 \text{ bar}_{abs}$). As a result, four steady-state friction maps were generated, as shown in Figure A.1.

As shown in Section 3.2.5, the steady-state LuGre friction force is given by:

$$F_{fr_ss} = F_C + (F_S - F_C)e^{-(v/v_S)^{\alpha_S}} + \sigma_2 |v|^{\alpha_S}.$$
 (A.2)

The parameters of Equation A.2 can be obtained from each steady-state friction map through nonlinear regression. In this case, the '*Isqnonlin*' function in MATLAB was used. After estimating the parameters of Equation A.2 for each steady-state map, the pressure-dependent parameters (equations A.3-A.5) can be determined by performing a linear regression using the four pressure-based values.

$$F_C = F_{C \ 0} + p_s F_{C \ 1},$$
 (A.3)

$$F_S = F_{S_0} + p_S F_{S_1}, (A.4)$$

$$\sigma_2 = \sigma_{2,0} + p_s \sigma_{2,1}.$$
 (A.5)

Figure A.1 shows a comparison between the experimental steady-state friction points and the fitted curves from Equation A.2.

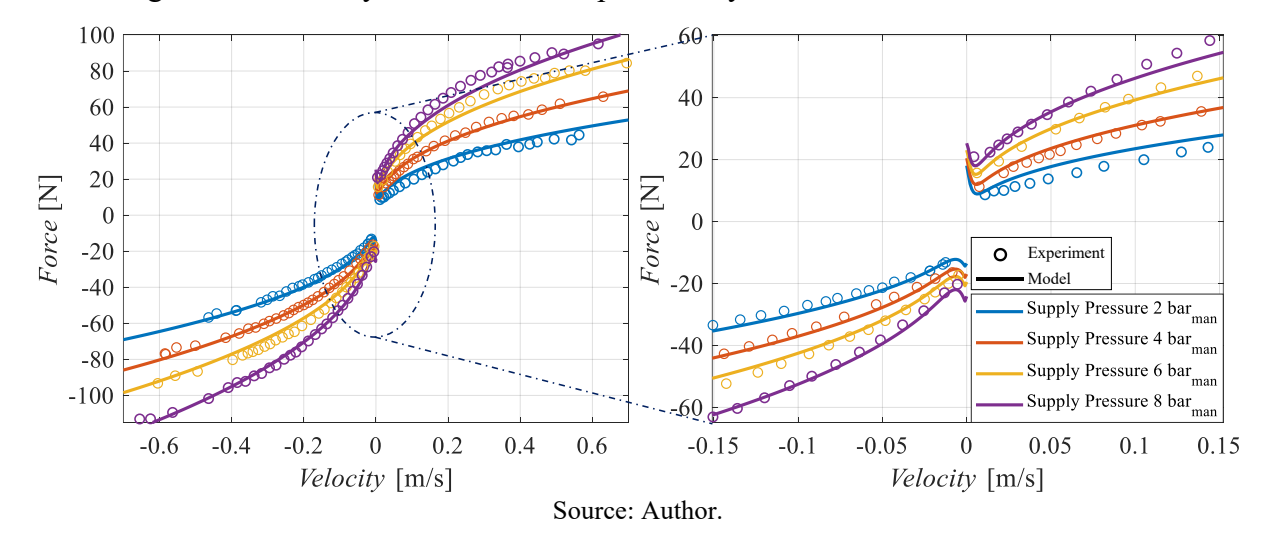


Figure A.1 – Steady-state friction map for the cylinder DSBC-32-200-PPVA-N3

As can be seen, pressure does influence the friction force of the cylinder, with the higher the supply pressure, the greater the friction force. This behavior can be explained by the pressing force exerted by the air pressure on the cylinder seals, which increases the piston's displacement resistance.

The determination of the dynamic parameters is less straightforward. As stated by Valdiero (2005), these parameters can be obtained iteratively through simulations until the desired value of micro-deformations during the pre-sliding regime is achieved, typically ranging from 1 to 50 µm. Another aspect to consider is the impact of the dynamic parameters on the friction force, as illustrated in Figure A.2, where the arrows indicate either increasing or decreasing velocity.

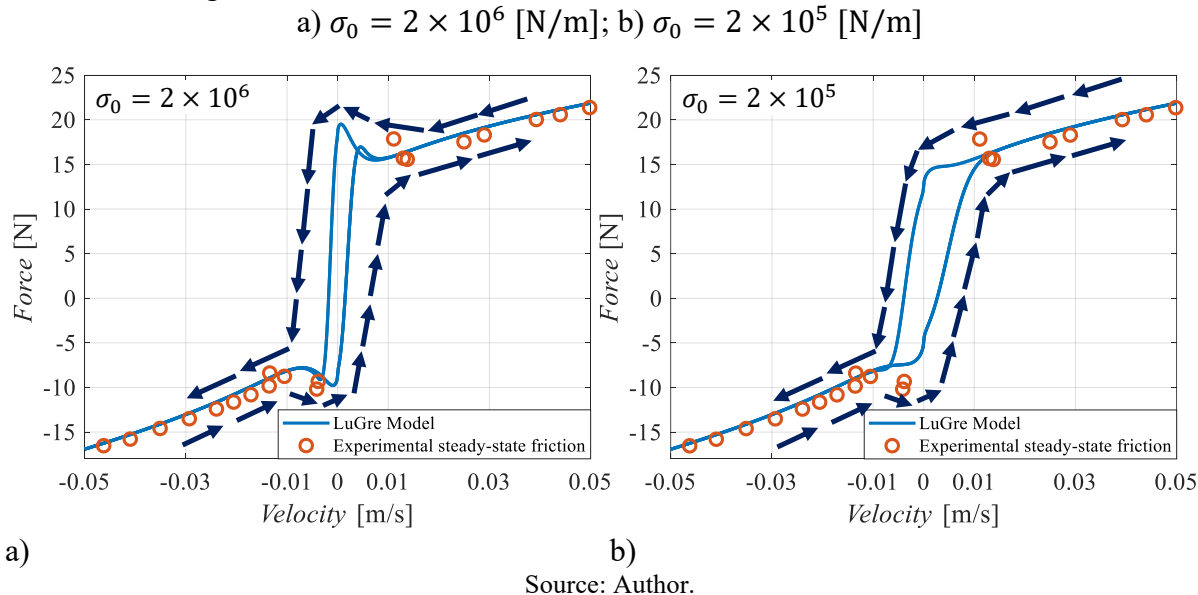


Figure A.2 – Effect of the stiffness coefficient on the friction force;

As can be seen, the stiffness coefficient (σ_0) influences the static friction region and friction hysteresis. Specifically, a smaller stiffness coefficient results in a lower static friction force and a larger hysteresis gap. Therefore, the procedure for setting σ_0 was based on the iterative adjustment of its value until the static friction region was properly defined, ensuring the Stribeck effect at low velocities, without excessively increasing the static friction.

The damping coefficient (σ_1) significantly affects systems with low-displacement velocities, such as microscopes and satellites. However, for systems with displacements on the order of millimeters, the influence of σ_1 is minimal (Åström; Canudas-de-Wit, 2008). For such systems where its influence is small, the approach proposed by Yanada; Takahashi and Matsui (2009) is applicable and should be used to adjust σ_1 to ensure passivity via the following expression:

$$\sigma_1 \le \frac{F_C}{(F_S - F_C)} \sigma_2,\tag{A.6}$$

which serves as the reference equation for determining the damping coefficient based on the static parameters of the model.

The identified parameters of the cylinder model DSBC-32-200-PPVA-N3, used during the validation of the model presented in Section 3.3, are listed in Table 3.3.

For the analysis performed in Chapter 4, the conventional LuGre friction model was used, which does not include the pressure-dependent parameters. Ten different cylinders were used in the analysis, with piston diameters ranging from 8 to 63 mm. The LuGre parameters for these cylinders were estimated using the approach previously mentioned, maintaining an average pressure of 6 bar_{abs} in the driving chamber, the opposing chamber connected to the atmosphere, and a load force applied to the cylinder rod to control the displacement velocity. Table A.1 presents the estimated parameters for the cylinders used in this thesis.

Cylinder Ø 08 mm Model: 16N2A08A100 **Dynamic Static parameters** parameters **Direction** σ_0 [N/m²] σ_I [Ns/m] σ_2 [Ns/m] v_s [m/s] $F_C[N]$ $F_S[N]$ α_s $4.0x10^6$ 1 v > 021.40 13.92 0.0024 0.83 1.37 $4.0x10^{6}$ v < 021.40 8.64 -0.0042 -5.15 -7.391.5 1

Table A.1 – LuGre friction parameters for the Camozzi cylinders

		Cylii	nder Ø 10 i	mm Model	: 16N2A10A	100			
Direction	Dynamic parameters		Static parameters						
	σ_{θ} [N/m ²]	σ_I [Ns/m]	σ ₂ [Ns/m]	v_s [m/s]	$F_C[N]$	$F_{S}[N]$	α_s	а	
v > 0	$8,0x10^6$	103.2	16.62	0.0027	4.78	5.55	2	1	
<i>v</i> < 0	$8,0x10^6$	103.2	12.43	-0.0123	-5.12	-5.43	2	1	
		Cyliı	nder Ø 12 i	mm Model	: 16N2A12A	100			
Direction	Dynamic parameters		Static parameters						
	σ_{θ} [N/m ²]	σ_I [Ns/m]	σ_2 [Ns/m]	v_s [m/s]	$F_{C}[N]$	$F_S[N]$	α_s	а	
v > 0	$9,0x10^6$	37.1	25.67	0.0029	2.56	4.33	1.5	1	
<i>v</i> < 0	$9,0x10^6$ 37.1		22.06 -0.0017 -8.13		-8.13	-9.03	1.5	1	
		Cyliı	nder Ø 16 i	mm Model	: 25N2A16A	100			
Direction	Dynamic parameters		Static parameters						
	σ_{θ} [N/m ²]	σ_l [Ns/m]	σ ₂ [Ns/m]	v_s [m/s]	$F_C[N]$	$F_S[N]$	α_s	а	
v > 0	$9,0x10^6$	648	25.11	0.0049	6.71	6.97	2	1	
<i>v</i> < 0	$9,0x10^6$	648	24.64	-0.0101	-5.99	-6.94	1.5	1	
		Cylin	nder Ø 20 i	mm Model	: 25N2A20A	100			
Direction	Dynamic parameters		Static parameters						
	σ_{θ} [N/m ²]	σ_I [Ns/m]	σ ₂ [Ns/m]	v_s [m/s]	$F_{C}[N]$	$F_S[N]$	α_s	а	
v > 0	$9,0x10^6$	94.7	38.23	0.0057	2.997	4.207	2	1	
<i>v</i> < 0	9.0×10^6 94.7		39.79	-0.0082	-5.132	-8.738	2	1	
		Cylii	nder Ø 25 i	mm Model	25N2A25A	100			
Direction	Dynamic parameters		Static parameters						
	σ_{θ} [N/m ²]	σ_I [Ns/m]	σ ₂ [Ns/m]	σ_{θ} [N/m ²]	σ_l [Ns/m]	$F_{S}[N]$	α_s	а	
v > 0	$9,0x10^6$	115.7	52.24	0.0042	3.578	5.193	2	1	
v < 0	$9,0x10^6$	115.7	43.75	-0.0072	-8.599	-12.69	2	1	
		Cylind	er Ø 32 mr	n Model: 6	3MT2C032	A0100			
Direction		amic neters			Static par	rameters			
	σ_{θ} [N/m ²]	σ_I [Ns/m]	σ_2 [Ns/m]	v_s [m/s]	$F_C[N]$	$F_{S}[N]$	α_s	а	
v > 0	$3,0x10^6$	2,788.4	100.04	0.0045	22.02	22.81	2	1	
, ,									

Cylinder Ø 40 mm Model: 63MT2C040A0100										
Direction	Dynamic parameters		Static parameters							
	σ_{θ} [N/m ²]	σ_l [Ns/m]	σ ₂ [Ns/m]	σ_{θ} [N/m ²]	σ_l [Ns/m]	$F_{S}[N]$	α_s	а		
v > 0	$5,0x10^6$	1,336.1	232.07	0.0014	19.23	22.57	2	1		
<i>v</i> < 0	$5,0x10^6$	1,336.1	228.37	-0.0015	-39.80	-42.69	2	1		
Cylinder Ø 50 mm Model: 63MT2C050A0100										
Direction	Dynamic parameters		Static parameters							
	σ_{θ} [N/m ²]	σ_l [Ns/m]	σ_2 [Ns/m]	v_s [m/s]	$F_C[N]$	$F_S[N]$	$\alpha_{\scriptscriptstyle S}$	а		
v > 0	$9,0x10^6$	1,934.1	587.15	0.0039	21.28	27.74	2	1		
v < 0	$9,0x10^6$	1,934.1	513.81	-0.0051	-41.62	-53.04	2	1		
Cylinder Ø 63 mm Model: 63MT2C063A0100										
Direction	Dynamic parameters		Static parameters							
	σ_{θ} [N/m ²]	σ_l [Ns/m]	σ_2 [Ns/m]	v_s [m/s]	$F_{C}[N]$	$F_{S}[N]$	α_s	а		
v > 0	$9,0x10^6$	4,487.5	1,095.40	0.0117	11.56	37.56	2	1		
v < 0	$9,0x10^6$	4,487.5	1,051.50	-0.0178	-35.62	-69.64	2	1		

Source: Author.

APPENDIX B – LINEARIZATION OF THE MASS FLOW RATE EQUATION

To linearize the mass flow rate equation from the ISO 6358-1 standard (ISO, 2013), a graphical method based on two known Cartesian points was chosen over a Taylor series expansion. The Taylor series expansion was avoided because it can result in a model that predicts mass flow rates when the pressure ratios exceed one. Furthermore, this method leads to complex first-order models, which would be unfeasible for coupling with the dynamics of chamber pressures discussed in 5.1.2.

For the graphical linearization, two distinct points on the mass flow rate curve are required to determine the angular (a_{ang}) and linear (b_{lin}) coefficients of the linear model $(y = a_{ang}x + b_{ang})$. To that end, the following points were chosen:

$$\left(\frac{p_2}{p_1}\right)_1 = 1 \qquad \left(\frac{p_2}{p_1}\right)_2 = b
(q_m)_1 = 0 \quad (q_m)_2 = p_1 C \rho_0 \sqrt{\frac{T_0}{T_1}}$$
(B.1)

The selection of these two points aims to characterize the zero mass flow rate (when there is no pressure difference across the valve) and the maximum mass flow rate (when the flow becomes choked).

The angular coefficient (a_{ang}) is expressed by

$$a_{ang} = \frac{y_2 - y_1}{x_2 - x_1},\tag{B.2}$$

where the points y_1 and y_2 represent the mass flow rate values $(q_m)_1$ and $(q_m)_2$, respectively. The points x_1 and x_2 correspond to the pressure ratios $(p_2/p_1)_1$ and $(p_2/p_1)_2$, respectively. Therefore

$$a_{ang} = \frac{p_1 C \rho_0 \sqrt{\frac{T_0}{T_1}}}{b - 1}.$$
(B.3)

To define the linear coefficient (b_{lin}) , any known point on the linear model can be used. Choosing point 2, as defined in Equation B.1, results in

$$p_1 C \rho_o \sqrt{\frac{T_0}{T_1}} = \frac{p_1 C \rho_o \sqrt{\frac{T_0}{T_1}}}{b - 1} b + b_{lin}.$$
(B.4)

Therefore, the linear coefficient is

$$b_{lin} = \frac{p_1 C \rho_o \sqrt{\frac{T_0}{T_1}}}{1 - b}.$$
 (B.5)

The resulting linearized mass flow rate model is

$$q_m = \frac{C\rho_o\sqrt{\frac{T_0}{T_1}}}{1-b}(p_1 - p_2).$$
(B.6)

In Figure B.1, a graphical comparison is presented between the derived linearized model and the ISO 6358-1 model.

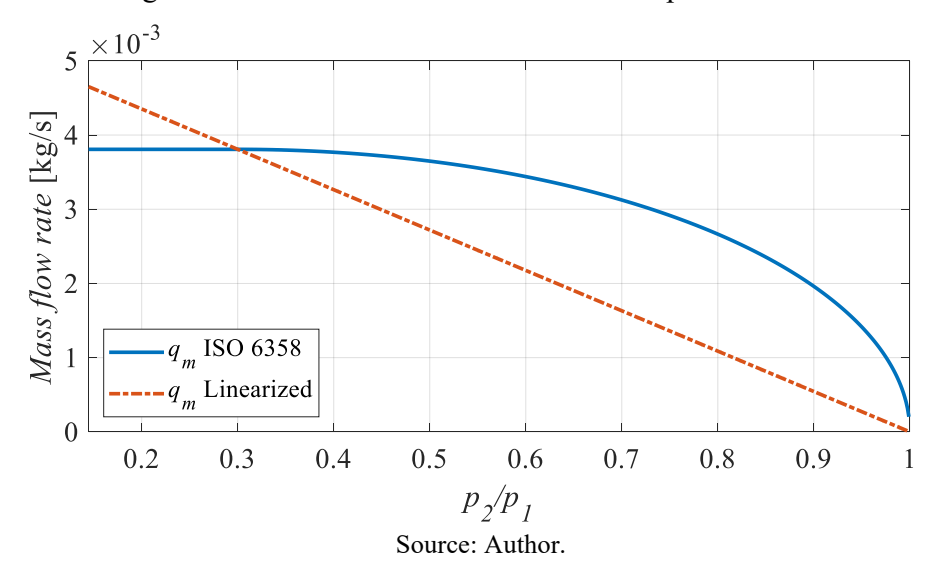


Figure B.1 – Mass flow rate as a function of pressure ratios

As can be seen, the linearized model provides an approximation of the expected mass flow rate. However, this model must be used with caution, as at certain pressure ratios, it may result in errors on the order of 100%. Nevertheless, this model has shown to be effective for the approach described in Chapter 5. A similar model is also presented in Beater (2007), which is used for the design of linear controllers.

APPENDIX C – AIR TEMPERATURE BEHAVIOR IN PNEUMATIC THROTTLE VALVES

According to Çengel and Boles (2014), throttle valves are small devices through which the flow can be assumed to be adiabatic, as there is insufficient time or surface area for heat exchange to occur. Additionally, no work is done, and the change in potential energy is negligible (or nonexistent). Although the output velocity is often significantly higher than the input velocity, the increase in kinetic energy can also be neglected. Therefore, the conservation of energy in a throttle valve states that the inlet enthalpy equals the outlet enthalpy. For ideal gases, this implies a constant temperature process, since enthalpy is a function of temperature.

On the other hand, this hypothesis contrasts with the isentropic assumption used to derive the general equation for modeling the mass flow rate of compressible fluids (Equation (3.1)), which is detailed in Appendix D. In this derivation, isentropic state changes are assumed, where the isentropic relationship between pressure and temperature is used to model the outflow temperature of the gas. In an isentropic process, there is a significant change in the gas temperature.

In order to evaluate both phenomena, an experimental assessment of the temperature change across a throttle valve was performed to determine which hypothesis better describes the behavior of compressed air flow through a throttle valve. The experiment was conducted using the test rig from the Fluidtronik Chair at the Institut für Mechatronischen Maschinenbau, Technische Universität Dresden, Germany.

The following components were used: a throttle valve (Festo model GR-QS-8) assembled in a meter-out configuration with its throttle needle fully opened. An Aventics throttle valve (model QR1-DBS-DA08) was used as a control valve to regulate the downstream pressure of the system. The measuring equipment consisted of pressure sensors (model PU5414) from IFM and thermocouples (model 5TC-TT-KI-40-1M) from Omega. The thermocouples had thin wires with a diameter of 0.08 mm, and their signal conditioning was performed using a TM1-2-3-0-100 °C amplifier from LEG. Signal acquisition was carried out using a Yokogawa oscilloscope (model DL708E) with an acquisition rate of 1 kHz. The test rig setup is shown in Figure C-1.

Upstream Temperature (T_1) Test Throttle valve

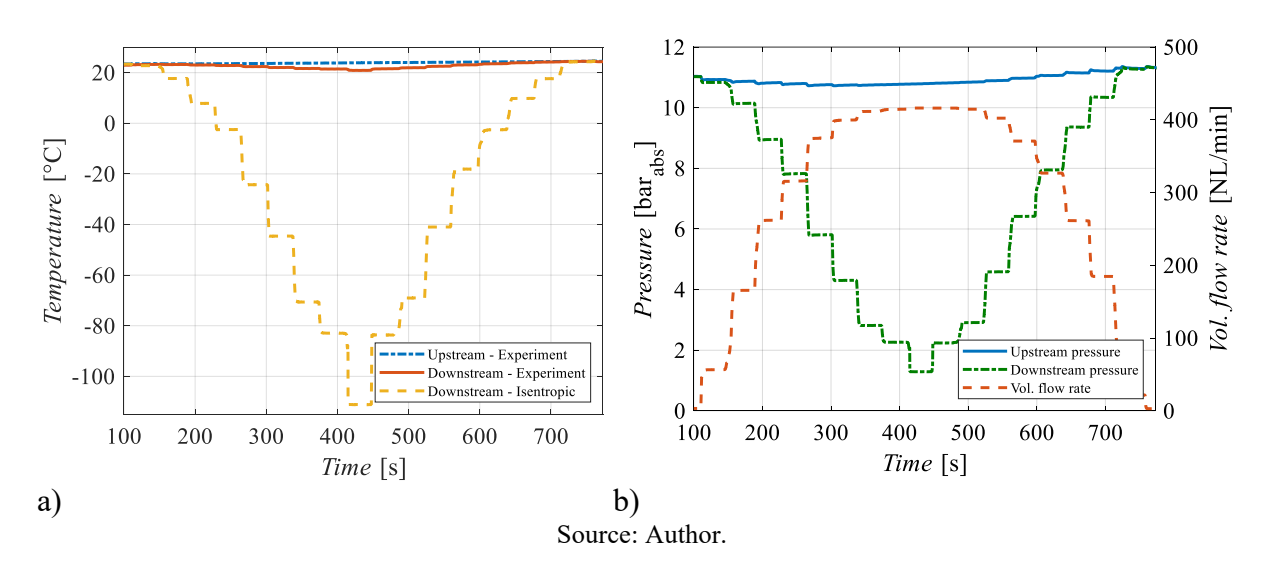
Upstream Downstream Temperature (T_2) Temperature (T_2) Downstream Pressure (p_1) Temperature (T_2) Downstream Pressure (p_2)

Figure C.1 – Experiment Setup.

Source: Author.

Prior to the test, the reservoir of the supply system was filled, and a waiting period of five hours was applied to ensure that the stored compressed air reached thermal equilibrium with the surrounding environment. The test was conducted using different openings of the downstream throttle valve, resulting in variations in pressure, temperature, and mass flow rate. The time interval between adjustments was approximately 30 seconds. The results of the experiments are presented in Figure C.2.

Figure C.2 - Experiment results; a) Upstream and downstream temperatures; b) Upstream and downstream pressures and volumetric flow rate



As can be seen, the downstream temperature remained nearly constant throughout the test, with a temperature drop of about 3 °C corresponding to a pressure drop of 10 bar_{abs}. According to thermodynamics, the temperature change across throttle valves for real gases is governed by the Joule-Thomson coefficient. For air at room temperature (20°C) and 1 bar, this coefficient is approximately 0.22 K/bar, which theoretically leads to a temperature drop of 2.2 °C for a pressure drop of 10 bar, closely matching the measured behavior.

According to the obtained results, the hypothesis of an isentropic process is not suitable for modeling the temperature behavior of throttle valves. This is because an isentropic process requires both adiabatic and reversible conditions. While throttling can indeed be considered adiabatic, it is not reversible due to flow friction within the valve. In other words, the frictional effects cancel out the temperature drop that would be expected in an isentropic process.

Even though the modeling of the mass flow rate of compressible fluids assumes an isentropic process, the constants determined empirically from experimental results (such as the discharge coefficient or the sonic conductance) are likely to account for deviations from this assumption. Nonetheless, when modeling pneumatic systems, it is more reasonable to assume an isenthalpic process (constant enthalpy and temperature for ideal gases) rather than an isentropic process through a throttle valve.

APPENDIX D – DERIVATION OF THE MASS FLOW RATE MODEL FOR COMPRESSIBLE FLOW

The modeling of compressed air flow through an orifice is based on the principle of mass conservation. Considering the differential control volume shown in Figure D.1, the mass flow rate at any given section is given by

$$q_m = A_x v_x \rho_x, \tag{D.1}$$

where A_x is the cross-section area, v_x is the fluid velocity and ρ_x is the specific mass on the x-direction.

Figure D.1 – Differential control volume

Source: Adapted from Pritchard (2011).

The velocity at any cross-section of the nozzle depends on the fluid's stagnation properties. To derive the fluid velocity as a function of the stagnation pressure, the approach presented by Pritchard (2011) was adopted and is presented below.

The continuity equation for a general control volume is given by

$$\frac{\partial}{\partial t} \int_{CV} \rho dV + \int_{CS} \rho \vec{v} \cdot d\vec{A} = 0. \tag{D.2}$$

Since the control volume is fixed, the left-hand side of Equation (D.2) is zero. The specific mass (ρ) can be assumed constant at the control surfaces. The area vector (\vec{A}) is always perpendicular to and oriented outward from the control surface, while the velocity vector (\vec{v}) is always aligned with the flow direction. Therefore

$$\rho v_x A \cos(180^\circ) + (\rho + d\rho)(v_x + dv_x)(A + dA)\cos(0^\circ) = 0, \tag{D.3}$$

therefore

$$\rho v_x A = (\rho + d\rho)(v_x + dv_x)(A + dA). \tag{D.4}$$

The momentum equation for a general control volume is given by

$$\overrightarrow{F_T} + \overrightarrow{F_B} = \frac{\partial}{\partial t} \int_{CV} \vec{v} \rho dV + \int_{CS} \vec{v} \rho \vec{v} \cdot d\vec{A}, \tag{D.5}$$

where F_T is the surface force, and F_B is the body force.

Since there is no body force acting on the control volume ($F_B = 0$), the change within the control volume is zero ($\partial/\partial t = 0$), and the fluid displacement occurs solely in the x-direction, the momentum equation results in

$$F_{T_X} = \int_{CS} v_X \rho \vec{v} \cdot d\vec{A}. \tag{D.6}$$

There are three surface forces acting on the control volume. Two of them act on the inflow and outflow control surfaces and result from the product of pressure and control surface area. The third acts on the side of the control volume and is denoted by dR_x . Therefore,

$$F_{T_x} = dR_x + pA - (p + dp)(A + dA).$$
 (D.7)

The dR_x is given by the average pressure change multiplied by the differential area.

$$dR_x = \left(p + \frac{dp}{2}\right)dA. \tag{D.8}$$

Therefore, the surface force is

$$F_{T_X} = pdA + \frac{dpdA}{2} + pA - pA - pdA - dpA - dpdA. \tag{D.9}$$

The terms involving the product of two differentials (dpdA) can be neglected, as their values are negligible. This leads to

$$F_{T_X} = -dpA. (D.10)$$

Applying Equation (D.10) to the momentum equation yields

$$-dpA = \int_{CS} v_x \rho \vec{v} \cdot d\vec{A}. \tag{D.11}$$

The velocity (v_x) is considered constant at the control surfaces, therefore

$$-dpA = v_x(-\rho v_x A) + (v_x + dv_x)[(\rho + d\rho)(v_x + dv_x)(A + dA)].$$
 (D.12)

Based on the continuity equation, it can be stated that

$$\rho v_x A = (\rho + d\rho)(v_x + dv_x)(A + dA). \tag{D.13}$$

This simplifies Equation (D.12) to:

$$\frac{dp}{\rho} + v_x dv_x = 0. ag{D.14}$$

The next step is to establish a relationship between pressure and density. Since the process is assumed to be isentropic, the isentropic equation of state is used.

$$\frac{p}{\rho^{\gamma}} = Cte, \tag{D.15}$$

therefore

$$\rho = \left(\frac{p}{Cte}\right)^{1/\gamma}.\tag{D.16}$$

Applying Equation (D.16) to Equation (D.14) results in a differential equation that relates pressure to the velocity of the fluid.

$$\left(\frac{p}{Cte}\right)^{-1/\gamma}dp + v_x dv_x = 0. \tag{D.17}$$

To obtain the stagnation pressure, Equation (D.17) is integrated from a generic point (2) to the stagnation point (1), where the velocity is zero.

$$\int_{p_2}^{p_1} \left(\frac{p}{Cte}\right)^{-1/\gamma} dp + \int_{v_2}^{0} v_x \, dv_x = 0.$$
 (D.18)

Applying the definite integrals leads to

$$Cte^{1/\gamma} \left(\frac{\gamma}{\gamma - 1}\right) p_2^{\frac{\gamma - 1}{\gamma}} \left(\left(\frac{p_1}{p_2}\right)^{\frac{\gamma - 1}{\gamma}} - 1\right) = \frac{v_2^2}{2}.$$
 (D.19)

Given that the process is isentropic, the following relationship holds

$$\frac{p_2}{\rho_2^{\gamma}} = Cte. \tag{D.20}$$

Which leads to

$$\frac{p_2^{1/\gamma}}{\rho_2} \left(\frac{\gamma}{\gamma - 1} \right) p_2^{\frac{\gamma - 1}{\gamma}} \left(\left(\frac{p_1}{p_2} \right)^{\frac{\gamma - 1}{\gamma}} - 1 \right) = \frac{v_2^2}{2}. \tag{D.21}$$

It can be further rearranged as follows

$$\left(\frac{\gamma}{\gamma-1}\right)\frac{p_2}{\rho_2}\left(\left(\frac{p_1}{p_2}\right)^{\frac{\gamma-1}{\gamma}}-1\right) = \frac{v_2^2}{2}.$$
(D.22)

Since air behaves as an ideal gas, the ideal gas law can be used to express the specific mass as a function of pressure, as follows

$$\frac{p_2}{\rho_2} = RT_2. \tag{D.23}$$

Therefore,

$$\left(\frac{\gamma}{\gamma-1}\right)RT_2\left(\left(\frac{p_1}{p_2}\right)^{\frac{\gamma-1}{\gamma}}-1\right) = \frac{v_2^2}{2}.$$
(D.24)

The temperature T_2 also needs to be expressed as a function of the reference (stagnation) condition. Therefore, the isentropic relations and the ideal gas law are employed

$$T_2 = T_1 \left(\frac{p_1}{p_2}\right)^{\frac{1-\gamma}{\gamma}}.$$
 (D.25)

Applying Equation D.25 to D.24 leads to

$$\left(\frac{\gamma}{\gamma - 1}\right) RT_1 \left(1 - \left(\frac{p_1}{p_2}\right)^{\frac{1 - \gamma}{\gamma}}\right) = \frac{{v_2}^2}{2}.$$
 (D.26)

From Equation (D.26), it is possible to isolate the velocity v_2 , which corresponds to the fluid velocity at any section of the differential control volume shown in Figure D.1. This velocity is a function of the stagnation pressure (p_1) and the static pressure (p_2) .

$$v_2 = \sqrt{2RT_1\left(\frac{\gamma}{\gamma - 1}\right)\left(1 - \left(\frac{p_1}{p_2}\right)^{\frac{1 - \gamma}{\gamma}}\right)}.$$
 (D.27)

From Equation D.1, it is also possible to determine the specific mass at any point within the differential control volume. Once again, the isentropic relations and the ideal gas law are employed, leading to

$$\rho_2 = \frac{p_1}{RT_1} \left(\frac{p_2}{p_1}\right)^{\frac{1}{\gamma}}.$$
 (D.28)

Applying Equations (D.28) and (D.27) to Equation (D.1) leads to a general equation for modeling the mass flow rate of compressible fluids through a nozzle, which is given by Equation D.29.

$$q_{m} = A_{0} p_{1} \sqrt{\frac{2}{RT_{1}}} \sqrt{\left(\frac{\gamma}{\gamma - 1}\right) \left(\left(\frac{p_{2}}{p_{1}}\right)^{\frac{2}{\gamma}} - \left(\frac{p_{2}}{p_{1}}\right)^{\frac{\gamma + 1}{\gamma}}\right)}.$$
 (D.29)

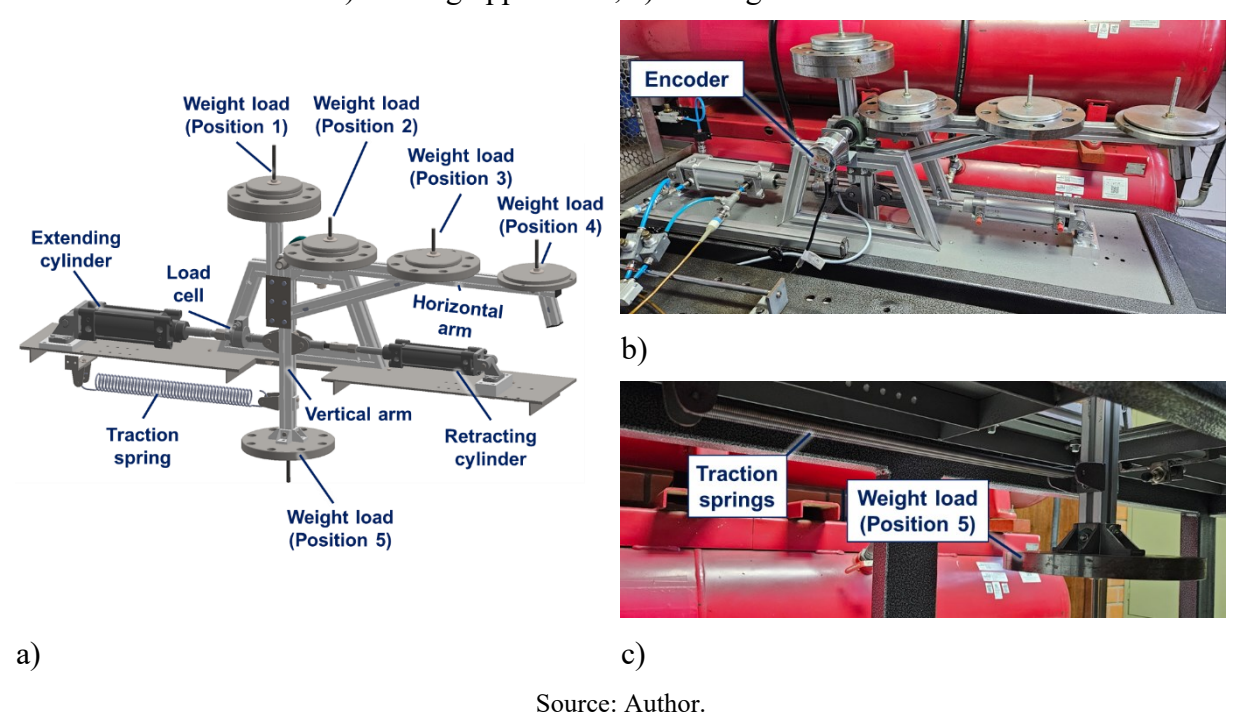
For application in pneumatic orifices, Equation (D.29) requires the use of a discharge coefficient (C_d), typically ranging from 0.53 to 0.98. This coefficient accounts for unmodeled phenomena such as friction flow and the vena contracta that occurs due to sharp edges (Beater, 2007).

APPENDIX E – THE YBITÚ TEST RIG

As discussed in section 4.3.2, there are several components that may compose the load force acting on the piston rod. Among these components, the following can be highlighted: inertial forces caused by the acceleration of the system mass, gravity forces caused by the vertical displacement of objects, spring forces resulting from the compression/stretching of elastic components, and the displacement of viscous materials.

Therefore, a test rig structure was designed to allow the evaluation of several working conditions. The structure consists of a rotating mechanism capable of moving a set of weights attached to its vertical and/or horizontal arm, thereby generating gravity and inertial forces. Up to three traction springs can be connected to the structure via an articulation located on the vertical arm. Additionally, the structure was designed to accommodate two pneumatic actuators operating simultaneously, allowing the effect of viscous forces to be added to the actuator under test. A general overview of the test rig structure is presented in Figure E.1.

Figure E.1 – General overview of the test rig structure: a) 3D Model section view; b) Test rig upper view; c) Test rig lower view



As can be seen, the structure allows weights to be positioned in various distinct locations. On the horizontal arm, for example, there are four positions for attaching the weights. When the weights are placed near the rotational axis (Position 1), the inertial effect is minimized

while the gravitational effect is preserved, mimicking the vertical displacement of weights. As the weights are moved to Positions 2, 3, and 4, a mechanical advantage is introduced, amplifying the force applied to the cylinder rod and increasing the inertial effect due to the larger rotational radius of the structure's center of gravity. When the weights are attached to Position 5 (on the vertical arm), the system results mostly in inertial forces, simulating the movement of objects on low-friction surfaces, such as bearing treadmills. Additionally, the inclusion of traction springs and/or a second actuator enables the incorporation of spring and viscous forces during the experiments.

The structure was designed to test pneumatic actuators with a 100 mm stroke and standardized piston diameters ranging from 8 to 63 mm. Extending and retracting movements can be performed since the actuator can be assembled on either side of the structure. The piston displacement is measured using a Hohner encoder, model 6410-4032-0014, installed on the axis of the rotating arm. A load cell, model U2A/200KG from HBM, measures the load force applied to the cylinder rod. Additionally, three pressure sensors (model K-P8AP-218-14-A5-0-K-1 from HBM) are used to monitor the pressures in the cylinder chambers and the supply line.

The structure was designed to withstand a load of 20 kg placed at Position 4 of the horizontal arm, resulting in a gravitational load force of 625 N applied to the cylinder rod. Under these conditions, the structure can sustain an angular acceleration of approximately 10 rad/s², generating an additional inertial force of 375 N and reaching the maximum load force of 1,000 N.

The structure's dimensions were designed to fit the Ybitú test rig, located at the Laboratory of Hydraulic and Pneumatic Systems (LASHIP). The Ybitú test rig is equipped with two compressed air reservoirs, each with a capacity of 460 L. These reservoirs are supplied by the compressed air network of the Mechanical Engineering Department at the Federal University of Santa Catarina (UFSC), which operates at an average supply pressure of 10 bar_{abs}.

The Ybitú test rig is equipped with a dSPACE data acquisition system, model DS1103, which connects to a desktop computer via an optical fiber cable. For handling input and output signals, the rig includes a connection expansion board with 20 analog-to-digital inputs and 8 digital-to-analog outputs. Sensors requiring signal conditioning and amplification, such as pressure sensors and the load cell, are supported by an HBM signal conditioning system, model MGCplus, which amplifies the signals before sending them to the connection expansion board.

The interface between the dSPACE board and the CPU is managed using the *ControlDesk* software, which enables real-time monitoring of the acquired data. For the experiments conducted in this thesis, a data acquisition rate of 1 kHz was used.

Considering that the articulated movement between the piston rod and the rotating arm results in a vectorial force decomposition, the law of cosines can be used to model the relationship between the measured angle (β), read by the encoder, and the other dimensional parameters of the structure. Figure E.2 presents the key parameters and angles used in modeling the structure's kinematics.

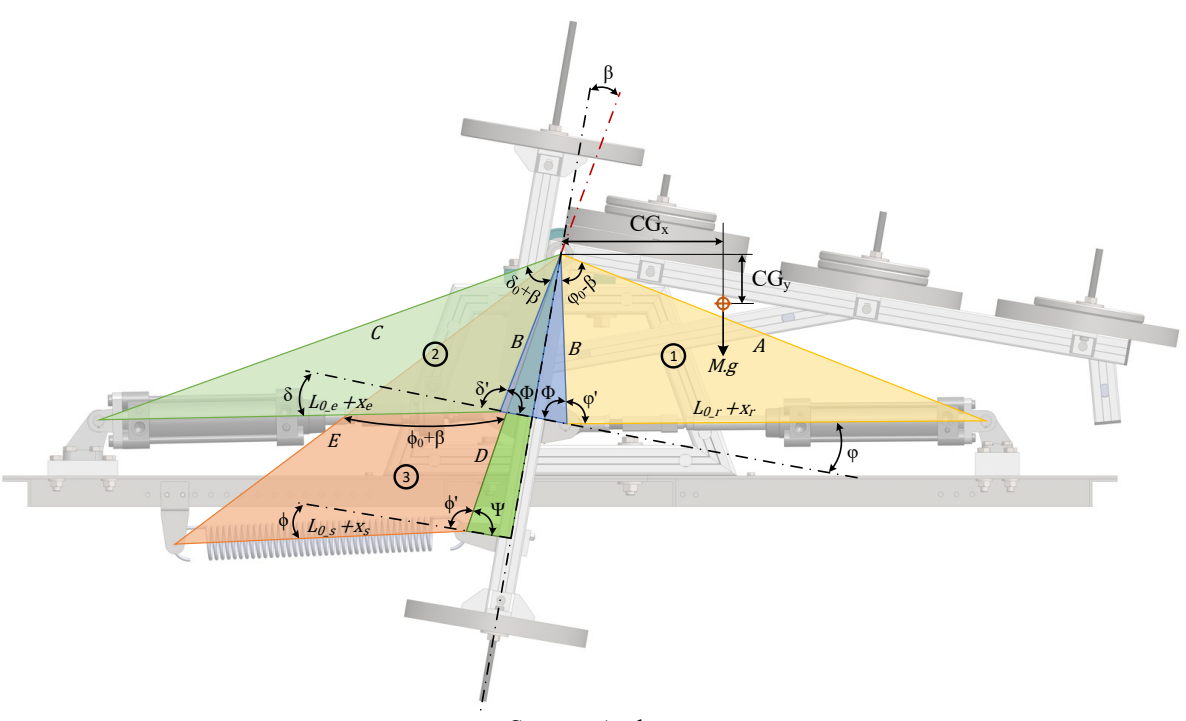


Figure E.2 – Dimensional parameters of the test rig's structure

Source: Author.

The reference position for measuring angle β is the retracted position, where the left cylinder is fully retracted, the right cylinder is fully extended, and the mechanical end-stop attached to the horizontal arm contacts the test rig's surface. At this reference angle, indicated by the red dash-dotted line, β is set to zero.

By applying the law of cosines to triangles 1, 2, and 3, the mathematical models for the linear displacement of the extending (x_e) and retracting (x_r) cylinders, as well as for the spring deformation (x_s) , are derived and given by:

$$x_e = -L_{0_e} + \sqrt{B^2 + C^2 - 2.B.C.\cos(\delta_0 + \beta)},$$
 (E.1)

$$x_r = -L_{0_r} + \sqrt{B^2 + A^2 - 2.B.A.\cos(\varphi_0 - \beta)},$$
 (E.2)

$$x_{s} = -L_{0 \ s} + \sqrt{D^{2} + E^{2} - 2.D.E.\cos(\phi_{0} + \beta)}, \tag{E.3}$$

where L_{0_e} , L_{0_r} , and L_{0_s} represent the initial lengths of the extending and retracting cylinders, and the spring deformation at the beginning of the test, respectively. The segments A, B, C, D, and E have fixed lengths, which depend on the geometric characteristics of the cylinders and springs being used. The angles δ_0 , φ_0 , and φ_0 correspond, respectively, to the angles between segments B and C, B and A, and D and E at the beginning of the test, when $\beta = 0$. The values of these parameters are given in Table E.1 and Table E.2.

The magnitude of the pneumatic force and the spring force, which effectively generate torque at the rotating axis, depends on the angles δ , φ , and φ , which result from the inclination of the respective components relative to the line perpendicular to the vertical arm. Therefore, the cosine law can be applied again to determine the respective angles:

$$\delta = 180^{\circ} - \Phi - \cos^{-1} \left(\frac{\left(x_e + L_{0_e} \right)^2 + B^2 - C^2}{2 \cdot \left(x_e + L_{0_e} \right) \cdot B} \right), \tag{E.4}$$

$$\varphi = 180^{\circ} - \Phi - \cos^{-1} \left(\frac{\left(x_r + L_{0_r} \right)^2 + B^2 - A^2}{2 \cdot \left(x_r + L_{0_r} \right) \cdot B} \right), \tag{E.5}$$

$$\phi = 180^{\circ} - \Psi - \cos^{-1} \left(\frac{\left(x_s + L_{0_s} \right)^2 + D^2 - E^2}{2 \cdot \left(x_s + L_{0_s} \right) \cdot D} \right), \tag{E.6}$$

where the angles Φ and Ψ have fixed values, as they result from the perpendicular distance between the pivot point of the articulations and the centerline passing through the rotation center of the vertical arm.

Figure E.3 presents the free body diagram of the test rig structure, which is used to perform the balance of forces acting on the system and to describe the rotational dynamics of the rotating arm, resulting in

$$F_{pn_e}. (L_{AT}.\cos\delta + L_{\phi}.\sin\delta) - F_{pn_r}. (L_{AT}.\cos\varphi + L_{\phi}.\sin\varphi) - F_{Kx}. ((L_{AT} + L_{SP})\cos\varphi + L_{\psi}.\sin\varphi) - M.g. (CG_{x}\cos\beta' - CG_{y}\sin\beta') = I.\alpha_{a},$$
(E.7)

where F_{pn_e} and F_{pn_r} are the pneumatic forces produced by the extending and retracting actuators, respectively. F_{Kx} is the spring traction force, while CG_x and CG_y represent the x- and y-distances between the center of gravity and the rotation point. β' is the vertical inclination angle of the rotating arm, I is the moment of inertia of the rotating arm, and α_a is the angular

acceleration. The viscous force acting on the rotating arm has been neglected due to the low friction provided by the bearings of the rotating arm's shaft.

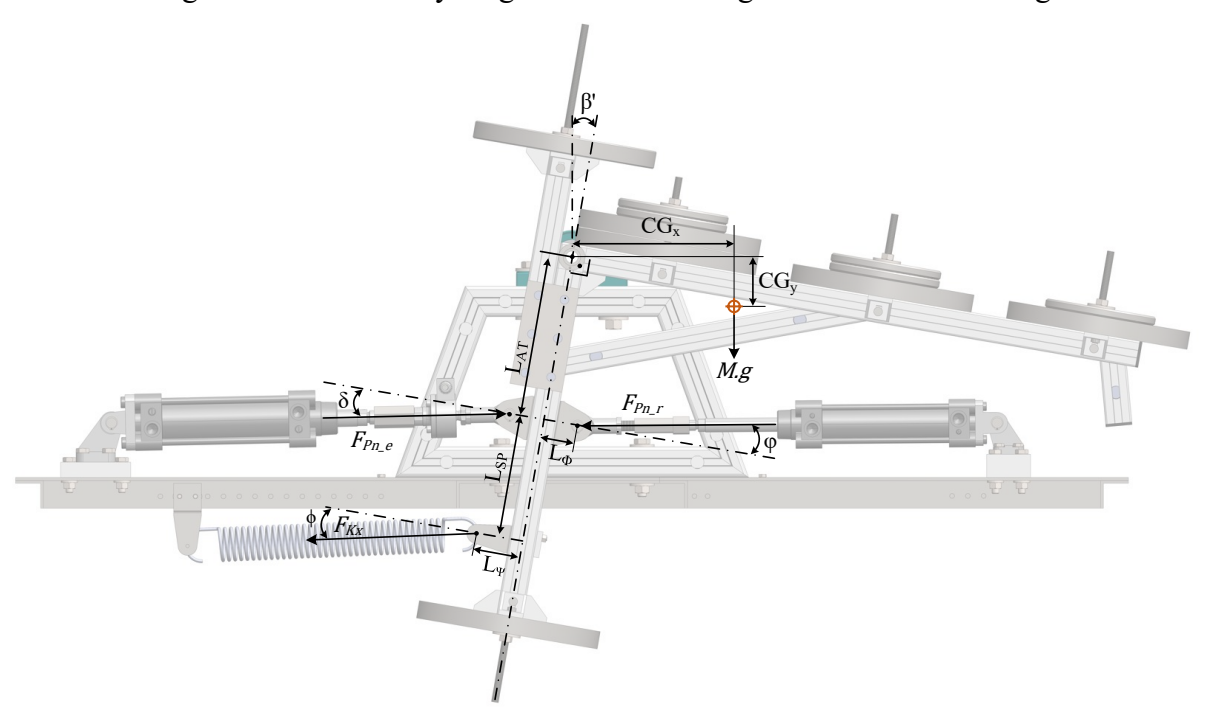


Figure E.3 – Free body diagram of the rotating structure of the test rig

Source: Author.

Equation (E.7) was used to determine the expected load force applied to the cylinder rod. The values for the moment of inertia and the distances from the center of gravity to the rotation point of the structure were obtained from the 3D model of the rotating arm in SolidWorks. This model was carefully developed to include the aluminum profiles of the structure, bolts, fittings, accessories, and the materials of each component.

The dimensional parameters with fixed values, that is, the parameters that are independent on the cylinder model being used, are listed in Table E.1.

				1					
Parameters	Unit	Value	Parameters	Unit	Value	Parameters	Unit	Value	
В	m	0.194	Ф	0	78.3	L_{SP}	m	0.141	
D	m	0.335	ϕ_0	0	28.7	$L_{\mathbf{\Phi}}$	m	0.393	
E	m	0.552	L_{0_S}	m	0.304	L_{Ψ}	m	0.054	
Ψ	0	80.8	L_{AT}	m	0.190				

Table E.1– Fixed dimensional parameters values of the test rig

Source: Author.

Table E.2 presents the parameter values that depend on the cylinder installed on the test rig. The reference point for the data in the table is the retracted condition, where the mechanical end-stop attached to the horizontal arm of the rotating structure contacts the test rig's surface.

Table E.2 – Actuator dependent dimensional parameters values of the test rig

Cylinder Ø [mm]	Parameters	Unit	Value	Cylinder Ø [mm]	Parameters	Unit	Value
8, 10	A, C	m	0.426		A, C	m	0.522
	L_{0_e}	m	0.293	32, 40	L_{0_e}	m	0.398
	L_{0_r}	m	0.393		L_{0_r}	m	0.498
	δ_0	0	36.4		δ_0	0	41.6
	$arphi_0$	0	67.2		$oldsymbol{arphi}_0$	0	72.3
12, 16	A, C	m	0.447		A, C	m	0.559
	L_{0_e}	m	0.317		L_{0_e}	m	0.437
	L_{0_r}	m	0.417	50, 63	L_{0_r}	m	0.537
	δ_0	0	37.7		δ_0	0	43.0
	$arphi_0$	0	68.5		$oldsymbol{arphi}_0$	0	73.8
	A, C	m	0.468				
20, 25	L_{0_e}	m	0.340				
	L_{0_r}	m	0.440				
	δ_0	0	39.0				
	$arphi_0$	0	69.8				

Source: Author.